Ventilation of the Arctic Ocean and the Gulf of St. Lawrence

Dissertation

zur Erlangung des Doktorgrades

der Mathematisch-Naturwissenschaftlichen Fakultät

der Christian-Albrechts-Universität zu Kiel

vorgelegt von

Lennart Gerke

Kiel, 2024

Erster Gutachter: Prof. Dr. Arne Körtzinger

Zweiter Gutachter: Prof. Dr. Hermann Bange

Tag der mündlichen Prüfung: 16.09.2024

Acknowledgements

First and foremost, I would like to thank Dr. Toste Tanhua for his supervision during my PhD and for making this work possible through a DFG grant. Thank you for introducing me into chemical tracer analysis and letting me be part of the tracer group at GEOMAR. Thanks a lot for all your scientific feedback and quick responses all throughout the years, which significantly improved the outcome of this thesis.

Special thanks go to Prof. Dr. Arne Körtzinger, head of the chemical oceanography department, for allowing me to write my thesis in this department and for his constructive and helpful feedback on my research results and questions during the numerous thesis committee meetings. Here, I would also like to thank Dr. Johannes Karstensen, the third member of my committee alongside Arne and Toste. Thank you all for the valuable discussions and the relaxing and productive atmosphere during our meetings.

A big thanks goes to the technicians Tina Schütt, Boie Bogner and Tim Steffens for their assistance in the laboratory during and prior to this thesis, helping me with any technical difficulties and providing me with insights on handling and repairing the different measuring instruments.

I would also like to thank the many colleagues, who participated with me on the research expeditions 'SAS-Oden 2021', 'TReX2' and 'TReX4' for all the experiences we shared onboard. Also, thanks to the entire chemical oceanography department for creating a great working environment and for our excellent combined work, particularly during the move of the GEOMAR into the new building.

Last but not least I would like to thank my family and friends for all their support during this time. Their help during stressful periods, assistance with proofreading this thesis, and especially for not allowing my absence and lack of time during these past years affect our relationships. A special thank you to all of you for the great time we spent together distracting me from this thesis every once in a while, whether on vacations, playing sports, enjoying a beer, or simply spending time together chatting.

Thank you all!

Manuscript contributions

Manuscript I: <u>Lennart Gerke</u>, Yannis Arck, and Toste Tanhua: ***Temporal Variability of Ventilation in the Eurasian Arctic Ocean***, *Journal of Geophysical Research: Oceans*, 2024 (accepted for publication).

Author contribution: LG carried out the sampling during the 'SAS-Oden 2021', measured tracer concentrations, performed the data processing and analysis, wrote the paper and prepared all figures and tables. TT obtained funding and contributed to data analysis and writing. YA helped with the sampling during the cruise and proofread the paper.

Manuscript II: <u>Lennart Gerke</u>, William A. Nesbitt, Samuel W. Stevens, Douglas W. R. Wallace and Toste Tanhua: ***Changing composition of the Gulf of St. Lawrence Inflow Waters***, *Geophysical Research Letters*, 2024 (in revision).

Author contribution: LG carried out the sampling, measured tracer concentrations (TReX 2), performed the data processing and analysis, wrote the paper and prepared all figures and tables. WN participated in sampling and measured tracer concentrations (TReX 2). DW and TT obtained funding and all authors supported the writing process, analyzed and discussed the results.

Manuscript III: <u>Lennart Gerke</u> and Toste Tanhua: ***Multiple tracer approach to analyze Arctic Ocean Ventilation***, manuscript in preparation, 2024.
Author contribution: LG carried out the sampling during the 'SAS-Oden 2021' cruise, performed the tracer measurements and data analyses, prepared all figures and tables, and wrote the paper. TT obtained funding and contributed to data analysis and writing of the manuscript.

Abstract

Ocean ventilation describes the physical process that transports surface waters into the ocean's interior. The process thereby links surface waters with deep waters, contributing significantly to the global ocean conveyer belt and affecting global water mass circulation.

The Arctic Ocean is a region known to play a vital role in driving global ocean circulation by moving recently subducted waters at intermediate depths and exporting them as deep water towards the Atlantic Ocean. Thus, changes in this region, for instance those inflicted by climate change which are amplified in this area due to decreasing sea ice coverage and increasing freshwater inflow, may impact ventilation patterns and consequently affect global ocean circulation.

Ocean ventilation patterns can be determined using transient tracer measurements combined with the transit time distribution (TTD) method. Transient tracers are gases with known atmospheric histories or radioactive decay rates, which dissolve in surface waters following air-sea gas exchange and are then transported via ventilation processes into the interior ocean. Because these tracers have no inner water interactions, measurements of their concentrations in subsurface water samples allow to estimate the age of that respective water parcel, defined as the time since it was last in contact with the atmosphere. By assuming an inverse Gaussian distribution of ages to represent the TTD, the method accounts for water masses of varying ages within the single water parcel, in which tracer concentrations are measured. The mean age derived from these distributions serves to determine the ventilation rates and the relationship between the mean age (Γ) and the width of the age distribution (Δ) provides insights into the advective vs. diffusive flow characteristic of the respective water parcel.

This thesis analyzed transient tracer measurements, primarily focusing on the tracers CFC-12 and SF_6, to examine ocean ventilation patterns. In addition, the potential of new ocean tracers, such as the hydrochlorofluorocarbons HCFC-22, HCFC-141b, HCFC-142b and the hydrofluorocarbon HFC-134a (referred to as 'Medusa'-tracers), was explored to aid ventilation analyses. The investigation of ventilation patterns focused on two regions. First, the Arctic Ocean and the primary aims here were (1) to analyze ventilation patterns and their temporal variability, and (2) to evaluate the use of the 'Medusa'-tracers to improve the ventilation

analysis. Second, the Gulf of St. Lawrence, where the main objective was to analyze deep water ventilation and hereby predict changes in the composition of the water mass flowing into the Gulf.

The general ventilation analysis using data collected in 2021 for CFC-12 and SF_6 in the Arctic Ocean indicated characteristics typical for this region. Specifically, the data revealed the presence of the Arctic Ocean Boundary Current near the North Pole on the Eurasian side of the Lomonosov Ridge. This current is present at depth between 250 and 800 m and transports Atlantic Water around the Arctic Ocean along the ocean ridges. The presence of this current was inferred from higher tracer concentrations in this area, compared to measurements within the central Nansen and Amundsen Basins. Furthermore, computed mean age data derived from CFC-12 and SF_6 measurements indicated an older age of the deep water in the Makarov Basin relative to the Nansen and Amundsen Basins. This finding highlights the slow ventilation of deep water masses on the Canadian side of the Lomonosov Ridge.

The examination of Arctic Ocean ventilation patterns at intermediate depths (250 – 1500 m) over the past three decades (1991 - 2021) revealed a significant temporal variability. The analysis identified a multidecadal variability in ventilation throughout this 30-year time period, showing reduced ventilation (higher mean ages) in 1991 and 2021 in comparison to 2005 and 2015. Additionally, it was observed that during the past 16 years (2005 until 2021) the ventilation slowed down on the Eurasian side of the Arctic Ocean, with increasing mean ages observed from 2005 over 2015 to 2021.

The ventilation analysis was also expanded using 'Medusa'-tracers collected in the Arctic Ocean in 2021. This approach enhanced precision in the characterization of ventilation patterns and thereby revealed that these tracers, whose concentrations can be accurately determined by mass spectrometry, can be used as new ocean tracers in this region. Employing multiple tracer pairs alongside the TTD unveiled that in general the flow within the Atlantic layer of the Arctic Ocean is dominated by advective forces, with diffusive characteristics increasing at lower depths. Additionally, it showed that in some areas of the Arctic Ocean two water masses with similar densities but distinct age histories undergo mixing. Given the slight disparities observed in these regions between different tracer pairs in mean age and Δ/Γ-ratio, the TTD approach was expanded. This involved the assumption that not a single inverse Gaussian distribution but two inverse Gaussian distributions have to be considered to describe

the age distribution. Consequently, the ventilation analysis was expanded, enabling a more detailed examination of each water layer in various regions.

Transient tracer measurements, coupled with the TTD method, were also utilized to analyze deep water ventilation in the Gulf of St. Lawrence, a semi-enclosed region located on the east coast of Canada, which is connected to the Atlantic Ocean. Recent studies in this area had shown a significant decline in the oxygen concentration, which was partly attributed to a shift in the composition of the deep water inflow, being increasingly dominated by deoxygenated waters. The deep water entering the Gulf consists of a mix of older, less oxygenated North Atlantic Central Water (NACW) and younger, oxygen-rich Labrador Current Water (LCW). By employing transient tracer measurements around an isopycnal of $\sigma_\Theta = 27.26$ kg/m^3, the deep water mean age was assessed employing the TTD method. The data identified the presence of older water in the eastern part compared to the western edge of the Gulf, contrary to the expected flow pattern of the water. This underscored the increasing influence of older, less oxygenated NACW in recent times, which limits the influence of recently ventilated, oxygenated water coming from the Labrador Sea. As this trend appears to be ongoing, it is anticipated that the Gulf and the St. Lawrence Estuary will experience further deoxygenation.

Zusammenfassung

Die Meeresventilation beschreibt den physikalischen Prozess, mit dem Oberflächenwasser in die Tiefen des Ozeans transportiert wird. Somit bildet sie das Bindeglied zwischen Oberflächenströmungen und Tiefenwasserströmungen und ist ein entscheidender Faktor des sogenannten ‚Conveyer belts', eines Zirkulationssystems, das Wassermassen durch die Ozeane dieser Welt bewegt und diese so miteinander verbindet.

Der Arktische Ozean ist eine Region, die eine wichtige Rolle bei der Zirkulation kürzlich abgesunkener Wassermassen in mittleren Tiefen und deren Export als Tiefenwasser in den Atlantik spielt. Hierdurch beeinflusst der Arktische Ozean die globale Ozeanzirkulation. Für die Forschung ist der Arktische Ozean darüber hinaus von besonderer Bedeutung, da sich in diesem Gebiet klimabedingte Veränderungen, wie z.B. schmelzendes Meereseis und zunehmender Süßwasserzufluss, in zunehmendem Maße manifestieren. Inwieweit diese Veränderungen Einfluss auf die Meeresventilation der Region haben und somit Veränderungen in der globalen Zirkulation hervorrufen können, steht im Interesse der Forschung.

Eine Möglichkeit, Meeresventilation und ihre Veränderungen zu untersuchen, besteht in der Messung von im Wasser gelösten Spurengasen in Kombination mit der sogenannten ‚Transit Time Distribution' (TTD) Methode. Spurengase, die für die Analysen genutzt werden, weisen eine über die letzten Jahre bekannte atmosphärische Konzentration auf oder besitzen eine bekannte radioaktive Zerfallsrate. Sie lösen sich im Oberflächenwasser und gelangen über Ventilationsprozesse in das Innere des Ozeans. Da diese Substanzen keine chemischen Reaktionen eingehen sobald sie sich im Inneren des Ozeans befinden, ermöglichen Messungen von Spurengaskonzentrationen in Wasserproben eine Bestimmung des Alters einer Wassermasse, d. h. der Zeit, die vergangen ist, seit das Wasser zum letzten Mal mit der Atmosphäre in Kontakt war. Bei dieser Bestimmung wird eine inverse Gauß'sche Altersverteilung angenommen, um die TTD zu beschreiben und so direkte und indirekte Transportwege des Wassers in tiefere Schichten des Ozeans zu berücksichtigen. Dabei stellt das Durchschnittsalter den Durchschnitt der Altersverteilungen einer Wassermasse dar, und fließt so in die Analyse der Ventilation ein. Das Verhältnis des Durchschnittsalters (Γ) zur Breite der Altersverteilung (Δ) liefert zudem Informationen über die advektive bzw. diffusive Strömung der Wassermasse.

Zusammenfassung

Die vorliegende Arbeit nutzt hauptsächlich Konzentrationsmessungen der beiden Spurengase CFC-12 und SF_6, um die Meeresventilation im Arktischen Ozean zu beschreiben. Darüber hinaus werden bislang weniger untersuchte Spurengase, die Fluorchlorkohlenwasserstoffe HCFC-22, HCFC-141b, HCFC-142b und der Fluorkohlenwasserstoff HFC-134a (die sogenannten ‚Medusa'-Gase), analysiert. Hauptziele der Arbeit waren zum einen die Charakterisierung der Ventilation sowie möglicher zeitlicher Ventilationsveränderungen im Arktischen Ozean und zum anderen die Fragestellung, ob sich die neuen ‚Medusa'-Gase zur Bestimmung von Ventilationsprozessen in dieser Region eignen und diese möglicherweise verbessern.

Die Ventilationsanalyse mit Hilfe der im Jahr 2021 ermittelten CFC-12 und SF_6 Daten führte einige Charakteristika des Arktischen Ozeans zutage. Zum einen wiesen die gemessenen Konzentrationen auf den ‚Arctic Ocean Boundary Current' in der Region um den Nordpol auf der eurasischen Seite des Lomonossow Rückens hin. Diese Strömung bewegt sich in einer Tiefe von 250 bis 800 m entlang der Meeresrücken durch den Arktischen Ozean. Erhöhte Spurengaskonzentrationen in diesen Regionen und Tiefen im Vergleich zu Messungen in ähnlichen Tiefen in den mittleren Bereichen des Nansen und Amundsen Beckens sind Indizien für diese Strömung. Zum anderen lieferte die Analyse des Durchschnittsalters Befunde für sehr altes Wasser in den Tiefen des Makarov Beckens im Vergleich zum Tiefenwasser in den Becken auf der eurasischen Seite der Arktis. Dies deutet auf die langsame Ventilation des Tiefenwassers auf der amerasischen Seite des Lomonossow Rückens hin.

Die Analyse der Ventilation im Arktischen Ozean über die letzten drei Jahrzehnte (1991 – 2021) in mittleren Tiefen von 250 bis 1500 m zeigte eine signifikante zeitliche Veränderung. Die Daten sprechen für eine multidekadische Variabilität der Ventilation über die genannten drei Jahrzehnte, wobei im Vergleich zu 2005 und 2015 eine reduzierte Ventilation (älteres Durchschnittsalter) in den Jahren 1991 und 2021 detektiert wurde. Zudem konnte ermittelt werden, dass sich die Ventilation in den letzten 16 Jahren (2005 bis 2021) insbesondere auf der eurasischen Seite des Arktischen Ozeans verlangsamt hat. Das berechnete Durchschnittsalter nahm von 2005 über 2015 bis 2021 kontinuierlich zu.

Die Probennahme und Bestimmung der ‚Medusa'-Gase zeigte einerseits, dass sich diese sehr gut für die Ventilationsanalyse im Arktischen Ozean eignen. Die Bestimmung der Konzentrationsverhältnisse verschiedener Tracer-Paare unter der Annahme einer einfachen inversen Gauß'schen Altersverteilung der Wasserpakete zeigte generell die Dominanz der

advektiven Strömung bei Wassermassen in mittleren Tiefen, welche mehr und mehr diffusiven Charakter in größeren Tiefen entwickelte. Andererseits deuteten die Ergebnisse auch darauf hin, dass in einigen Regionen des Arktischen Ozeans eine mögliche Vermischung von zwei Wassermassen gleicher Dichte aber unterschiedlichen Alters vorliegt. Aufgrund der Menge an analysierten Spurengasen konnte hier das Durchschnittsalter mithilfe einer Ausweitung der TTD-Methode quantifiziert werden, wobei die Annahme einer einzelnen inversen Gauß'schen Verteilung auf eine zweifache inverse Gauß'sche Verteilung erweitert wurde.

Spurengasmessungen in Kombination mit der TTD-Methode wurden im Rahmen der Arbeit auch zur Ventilationsanalyse des Tiefenwassers im Sankt-Lorenz-Golf genutzt, einem halbgeschlossenen Meeresgebiets an der Ostküste Kanadas, das mit dem Atlantischen Ozean verbunden ist. Jüngste Studien zeigten in dieser Region einen starken Rückgang der Sauerstoffkonzentration. Dieser Rückgang wurde in Teilen auf eine veränderte Zusammensetzung des Tiefenwasserzuflusses und hieraus resultierend einem Zustrom von zunehmend sauerstoffarmem Wasser in den Golf zurückgeführt. Es ist bekannt, dass das Tiefenwasser, welches vom Atlantischen Ozean in den Golf fließt, aus älterem, sauerstoffarmem ‚North Atlantic Central Water' (NACW) und jüngerem, sauerstoffreichem ‚Labrador Current Water' (LCW) besteht. Mithilfe der Spurengasmessungen rund um die Dichteschicht von $\sigma_\Theta = 27.26$ kg/m^3 wurde das Durchschnittsalter des Tiefwassers im Rahmen dieser Arbeit berechnet. Hierüber konnte ermittelt werden, dass - im Vergleich zum westlichen Rand des Golfs - im Osten ältere Wassermassen auftreten. Dieses Resultat steht im Widerspruch zu der angenommenen Altersverteilung des Tiefenwassers, da auf Grund der von Ost nach West verlaufende Wasserströmung älteres Wasser im Westen zu erwarten gewesen wäre. Die Analyse zeigte somit, dass der Einfluss von älterem, sauerstoffarmem NACW in den letzten Jahren zugenommen hat, wodurch sich der Eintrag von sauerstoffreichem, jüngerem Wasser aus der Labradorsee (LCW) verringerte. Da sich dieser Trend zu verstetigen scheint, ist davon auszugehen, dass die Sauerstoffarmut im Golf sowie in der Sankt-Lorenz-Mündung stärker zunehmen wird.

Table of contents

1. Introduction

The world's oceans encompass 71 % of the Earth's surface with up to 6 % being covered by sea ice (Grassl, 2001). All oceans are interconnected by the global thermohaline circulation, also referred to as the conveyor belt (see Figure 1.1). This circulation pattern involves the movement of warm surface water towards the poles and the transport of cold, more dense water from the poles to the tropics at deeper levels. Surface water circulation is primarily driven by wind, heat and freshwater fluxes, along with ocean currents, which play a crucial role in the deep water circulation as well.

Figure key:
- Surface flow
- Deep flow
- Bottom flow
- Deep Water Formation
- ⊙ Wind-driven upwelling
- ⊙ Mixing-driven upwelling
- Salinity > 36 ‰
- Salinity < 34 ‰
- L — Labrador Sea
- G — Greenland Sea
- W — Weddell Sea
- R — Ross Sea
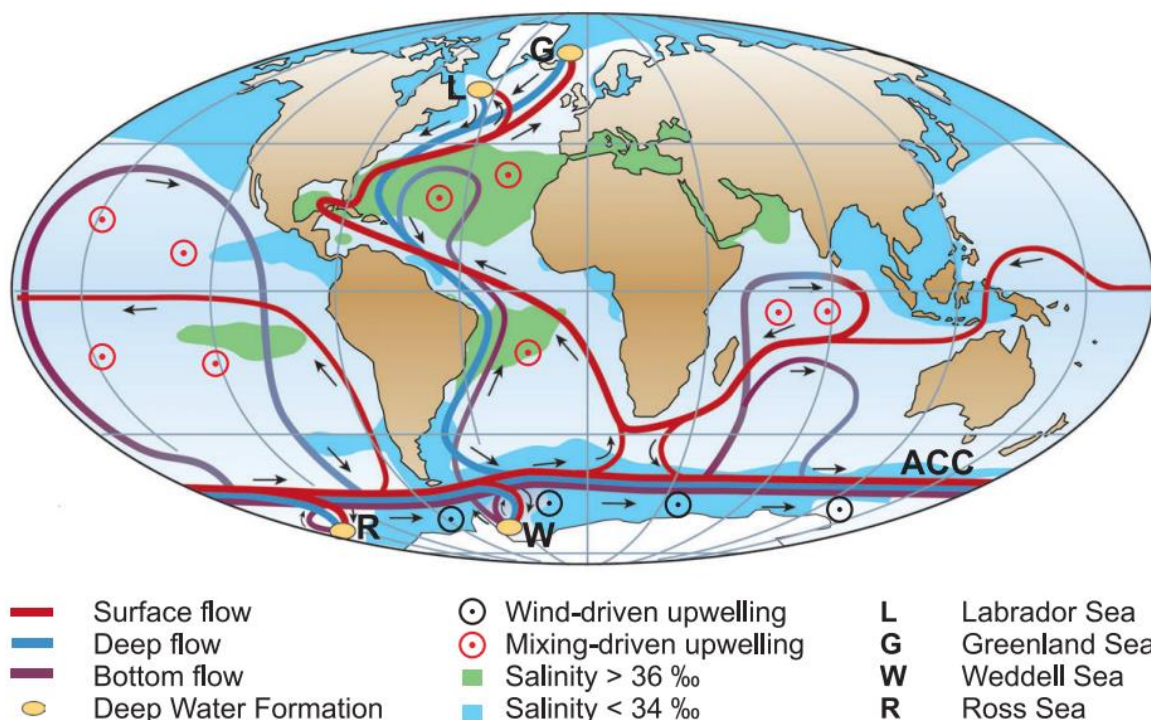
Figure 1.1: Display of the global thermohaline circulation within in the world's oceans. Locations of deep water formation are marked by yellow dots. The surface flow is represented in red and the deep water flow in blue (Kuhlbrodt et al., 2007).

As water moves towards the poles it increases in density due to a reduction in temperature (thermo) and a rise in salinity (haline) because of ice formation, causing it to sink into the interior. The process that describes the mixing of water masses on their way from the surface to the deeper layers of the ocean is referred to as ventilation.

1.1 Ventilation

Ocean ventilation is a physical process describing the dynamic exchange of parameters and variables, such as heat, salinity and dissolved gases, between the atmosphere and the ocean's interior (e.g. Azetsu-Scott et al., 2005; Krysell & Wallace, 1988; Talley et al., 2016; Tanhua et al., 2009; Thiele & Sarmiento, 1990; Wallace et al., 1987). The transfer of water masses from the surface mixed layer to the deep ocean establishes an important connection between the atmosphere and the interior ocean. In the surface mixed layer, water masses develop distinct characteristics through interactions with the atmosphere, however, when these water masses are transported beneath the surface, they become shielded from the atmosphere and are only subjected to mixing processes within the interior ocean with minor effects on the water mass composition. Hence, the ventilation process shapes long-term properties of the ocean interior, characterized by enduring parameters compared to the fast changing surface mixed layer (Williams, 2001).

Ventilation itself is driven by a combination of several mechanisms, including the above-mentioned thermohaline circulation, wind-driven mixing, tidal mixing, subduction, upwelling and deep ocean currents.

Surface winds generate wind-driven mixing and the resulting surface currents distribute and transport surface waters with all their dissolved components. Intense winds even induce surface waves, which deepen the mixed layer and enhance the air-sea gas exchange between the atmosphere and the ocean. Surface currents and waves can also disturb the density field within the mixed layer, generating internal waves that propagate water masses horizontally and vertically into deeper layers (D'Asaro, 1985; Ferrari & Wunsch, 2009; Rainville et al., 2011).

Tidal mixing significantly influences ventilation dynamics in coastal areas and estuarine environments. Generated by the gravitational force of moon and sun, tides influence vertical water movement affecting the exchange between the surface and deep layers. This process also produces internal waves affecting ventilation as described for the wind-driven mixing (Bowden, 1963; Ferrari & Wunsch, 2009; Griffin & LeBlond, 1990).

Within the above described thermohaline circulation, two major components are the subduction of surface water and the upwelling of deep water. Subduction transports dissolved atmospheric gases and other components/properties of the surface layer into the ocean interior, while upwelling exposes typically nutrient-rich water to the surface. These processes

are driven by density variations, with denser water sinking beneath lighter water and vice versa.

Ocean subduction significantly influences the ventilation within the upper ocean as well as in deeper layers, and it is particularly affected by seasonal variations and regional characteristics. As previously mentioned, surface water undergoes subduction to deeper layers as it moves towards the poles, driven by rapid cooling and subsequent density increase. This process is referred to as deep water convection and in the northern hemisphere is observed in regions like the Greenland Sea and the Labrador Sea (Clarke & Gascard, 1983; Gascard et al., 2002; Marshall & Schott, 1999; Watson et al., 1999). Deep water convection is not only affected by cooling events (Marshall & Schott, 1999) but also by deep convective eddies (Gascard et al., 2002; Watson et al., 1999). In the Greenland Sea, intermediate and deep water formation is affected by sea ice formation and fresh water outflow from the Arctic Ocean (AO), along with the formation of sub-mesoscale eddies through diapycnal mixing (mixing across density surfaces) (Aagaard & Carmack, 1989; Gascard et al., 2002). The generation of such sub-mesoscale eddies has also been observed in the Labrador Sea (McWilliams, 1988). Another mechanism involved in the formation of intermediate and deep-water masses at high latitudes is boundary convection of brine-enriched waters (Aagaard, 1989; Anderson et al., 1999). This process occurs in the AO, where ice formation at the shelfs produces brine-enriched water. As this water characterized by higher density flows off the shelfs into the basins, it mixes with surrounding water masses, leading to the generation of regional deep water (Anderson et al., 1999).

Subduction also occurs as a consequence of seasonal variations. The surface mixed layer is highly homogenous during winter time and resides above the thermocline, thereby forming a pronounced vertical temperature gradient. Surface water warming in spring and summer reduces this gradient and generates a seasonal thermocline, which is separated from the atmosphere only by a thin wind-exposed layer. As autumn and winter temperatures cool the water, the mixed layer expands again, forming a thicker barrier between the thermocline and the atmosphere. This annual variation mixes water masses, also affecting the ocean interior (Williams, 2001). Strong subduction processes form thick, widely distributed near-surface layer water masses. These are characterized by homogeneous physical properties covering a large volume vertically and horizontally, and are called mode waters (Hanawa & Talley, 2001). Mode waters propagate within boundary currents and gyres well beyond their origin of

formation, contributing to overall ventilation processes (McCartney & Talley, 1982; Sallée et al., 2012).

Upwelling processes primarily result from bottom boundary mixing, occurring at ocean ridges and coast lines. Additionally, strong winds move surface water, which is subsequently replaced by upwelled water from deeper layers. Upwelling transports nutrient (phosphate, silicate and nitrate) rich waters to the ocean surface, supporting phytoplankton growth and production of organic material (NOAA, 2023).

Another crucial component affecting ventilation processes are deep-water currents. These transport subducted waters, along with their inherent compositions at different density levels supporting the distribution of these waters across all ocean regions (e.g. Warren & Owens, 1987).

In all processes mentioned above, transport occurs via advective and diffusive pathways, as illustrated in Figure 1.2. These are particularly evident in phenomena such as subduction, upwelling and deep water circulation.
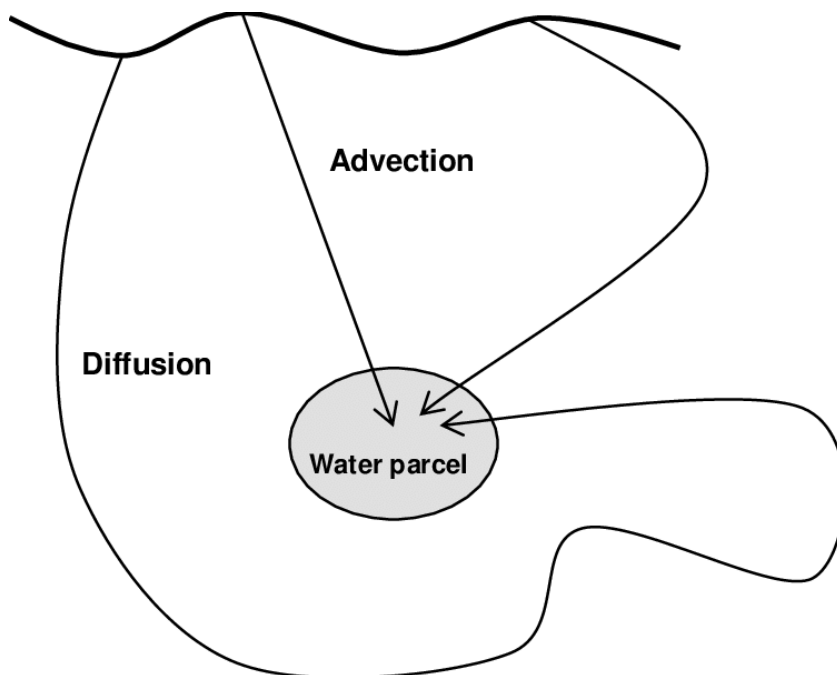
Figure 1.2: Ocean ventilation via diffusive and advective pathways affects the composition of a given water parcel in the ocean interior (Khatiwala et al., 2001).

Ventilation itself can be examined using a variety of different techniques that involve direct measurements and proxy studies. Due to the complexity of various mechanisms influencing ventilation, direct measurements are often limited. Therefore, different approaches to study

water mass ventilation are often combined, including transient tracer measurements, the analysis of physical properties conducted via ships or autonomous floats and drifters, satellite observations, modelling techniques and direct measurements of specific parameters, such as the velocity of water masses.

Satellite observations provide information mainly on the wind-driven mixing and the upwelling of nutrient rich waters, often described through surface water observations. Sea surface temperature, ocean color and the presence of gyres are variables used to determine these processes. They can reveal a cooling of surface waters before subduction or through measuring the width and strength of ocean eddies, can give insight on vertical mixing (e.g. Feldman & McClain, 2012; Papadopoulos et al., 2015; Raitsos et al., 2011).

The oldest technique examining ventilation relies on the measurements of physical properties, such as temperature and salinity, using ship-based instruments and nowadays also floats and drifters with attached sensors. These surveys help to describe different water masses by their properties, thereby obtaining information on their movement and mixing and their site of formation (e.g. Gordon, 1981). Measurement of dissolved oxygen concentrations and the calculation of apparent oxygen utilization (AOU), by subtracting the measured concentration from the calculated saturated concentration, is another approach to describe ocean ventilation, which is also conducted using ship-based measurements (e.g. Mecking et al., 2006; Shao et al., 2016).

Direct approaches, which are applied to determine vertical and horizontal velocities and turbulent mixing, include techniques like the Acoustic Doppler Current Profiler (ADCP) (e.g. Thomson et al., 2017). They provide direct information on the movement of water masses at the measuring point and especially can help to identify ocean eddies.

In the recent past biogeochemical modelling has become increasingly important to understand ocean processes and predict future ocean behavior and anomalies. The models are validated by comparing the results to measurements of the variables mentioned above. The validated models can then help to characterize ventilation changes of the past and predict future variabilities in ventilation. A model widely applied for the analysis of ocean ventilation is the Flexible Ocean and Climate Infrastructure (FOCI) – Earth System Model (ESM) (e.g. Flato, 2011; Matthes et al., 2020).

The predominant method used to determine ventilation involves transient tracer measurements in combination with the transit time distribution (TTD) concept (e.g. Hall & Plumb, 1994; Khatiwala et al., 2001; Stöven & Tanhua, 2014; Waugh et al., 2002). This approach (see Chapter 2 for details) assesses the age of different water masses, with 'age' referring to the time this water parcel was last at the ocean surface in contract with the atmosphere. The concept either assumes a one-inverse Gaussian (1-IG TTD) or two-inverse Gaussian (2-IG-TTD) distribution of ages to account for water masses of varying ages merging to form a single water parcel, where tracer concentrations are measured. Here, the mean age represents the average of all distributions. Another frequently used age parameter is the mode age, describing the most probable age within the distribution (see Figure 1.3) (Smith et al., 2011; Wefing, 2021). These two ages often yield different ventilation and circulation timescales, influenced significantly by the long tail in the distribution towards older ages. The mean age is favored for estimating ocean ventilation timescales, variability in ventilation and potentially assessing anthropogenic carbon uptake values, including all inputs from water of varying ages within the distribution. The mode age, on the other hand, is more commonly used when estimating the propagation of biogeochemical pulses, such as phytoplankton blooms (Wefing, 2021).
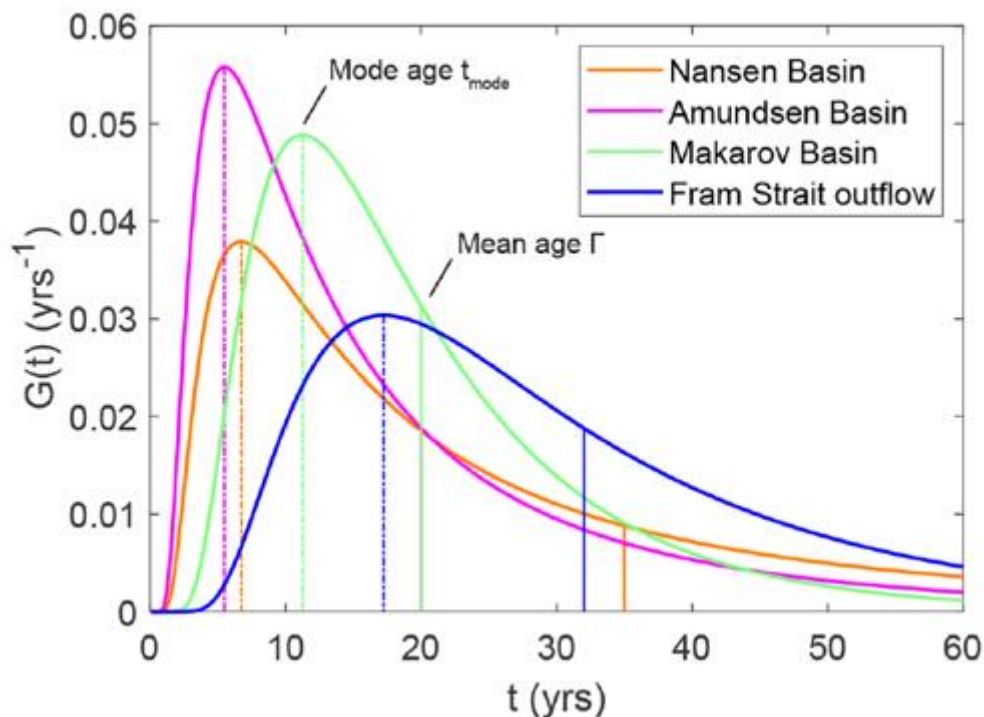
Figure 1.3: One-Inverse Gaussian TTDs, showing the distribution of ages for a water parcel with the mean age and mode age displayed. In this case the most probable functions for different basins in the AO are shown (Wefing et al., 2021).

1.2 Transient Tracers

Transient tracers can be chemical molecules, elements or isotopes characterized by a time-varying source or sink or a radioactive decay rate. These tracers originate from various sources, including radioactive tracers of natural origin (e.g. ^{39}Ar), those released from nuclear reprocessing plants (^{129}I; ^{236}U) or anthropogenically produced chronological tracers such as the artificial halogenated compounds chlorofluorocarbons (CFC's), hydrochlorofluorocarbons (HCFC's), hydrofluorocarbons (HFC's) and sulfur hexafluoride (SF_6).

The two main chronological transient tracers extensively used in the past and also in this study are CFC-12 (dichlorodifluoromethane) and SF_6. Other tracers and their individual potential of being used in ocean applications are discussed below. CFC-12 and SF_6 have been pivotal to understand ventilation processes in ocean sciences since the 1980s and 1990s, respectively (Fine, 2011; Talley et al., 2016). This is due to their characteristics of being stable in seawater (Tanhua & Olsson, 2005), having no inner water interactions and well documented atmospheric concentrations (Bullister & Warner, 2017). Moreover, their solubility in seawater has been well studied (Bullister et al., 2002; Warner & Weiss, 1985). In general, these characteristics are crucial for transient tracers to be effectively used in ocean ventilation studies.

1.2.1 CFC's & SF_6

CFC's, also known as freons, are organic compounds of low molecular weight composed of hydrocarbons with hydrogen atoms substituted by halogens, notably chlorine and fluorine. CFC's were primarily used as refrigerants, gas propellants and in foaming and cleaning agents in the past, thereby being introduced anthropogenically into the atmosphere. The best known and one of the most widely produced CFC's is CFC-12, which consists of two chlorine and two fluorine atoms replacing the hydrogen atoms in methane (see Figure 1.4). CFC-12 was initially produced in the 1920s, with its atmospheric concentration showing a gradual increase until

the 1960s, followed by an exponential rise until 2002. Subsequently, atmospheric concentrations declined because production was banned by an environmental agreement signed in the late 1980s, which prohibited the production of ozone depleting gases such as CFC-12 (The Montreal Protocol) (see Figure 1.4). Due to its atmospheric lifespan of 90 years, the reduction in concentrations occurs at a slow rate, resulting in sustained high values within the atmosphere until now (Fine, 2011; Stöven et al., 2015).

CFC-12 is primarily used to assess the ventilation rates of waters of young to intermediate ages. However, its use in determining highly ventilated waters has become increasingly challenging over the past two decades, given its declining atmospheric concentration. Nonetheless, it still serves important purposes in detecting temporal variability, due to its extensive historical database.

SF_6 (see Figure 1.4) was first synthesized at the beginning of the 20th century and since the 1950s it is applied as an insulating and quenching gas for high voltage systems. The gas shows inert properties with low UV degradation rate, contributing to its atmospheric lifetime of 3200 years (Ravishankara et al., 1993; Stöven et al., 2015). Historical data of this transient tracer reveal an initial detection in the late 1900s, followed by a profound increase in its atmospheric concentration as a consequence of the start of production and subsequent atmospheric pollution in the 1950s. Atmospheric concentrations of SF_6 exhibited a gradual increase until around 1980, followed by a more pronounced rise, as shown in figure 1.4. SF_6 is still produced although it shows a high global warming potential of 23500, i.e. one ton will contribute 23500 times more to global warming than one ton of CO_2 (Dincer et al., 2018).

The use of SF_6 as a transient tracer is limited to highly ventilated water masses because its concentrations measured in the atmosphere are still relatively low.
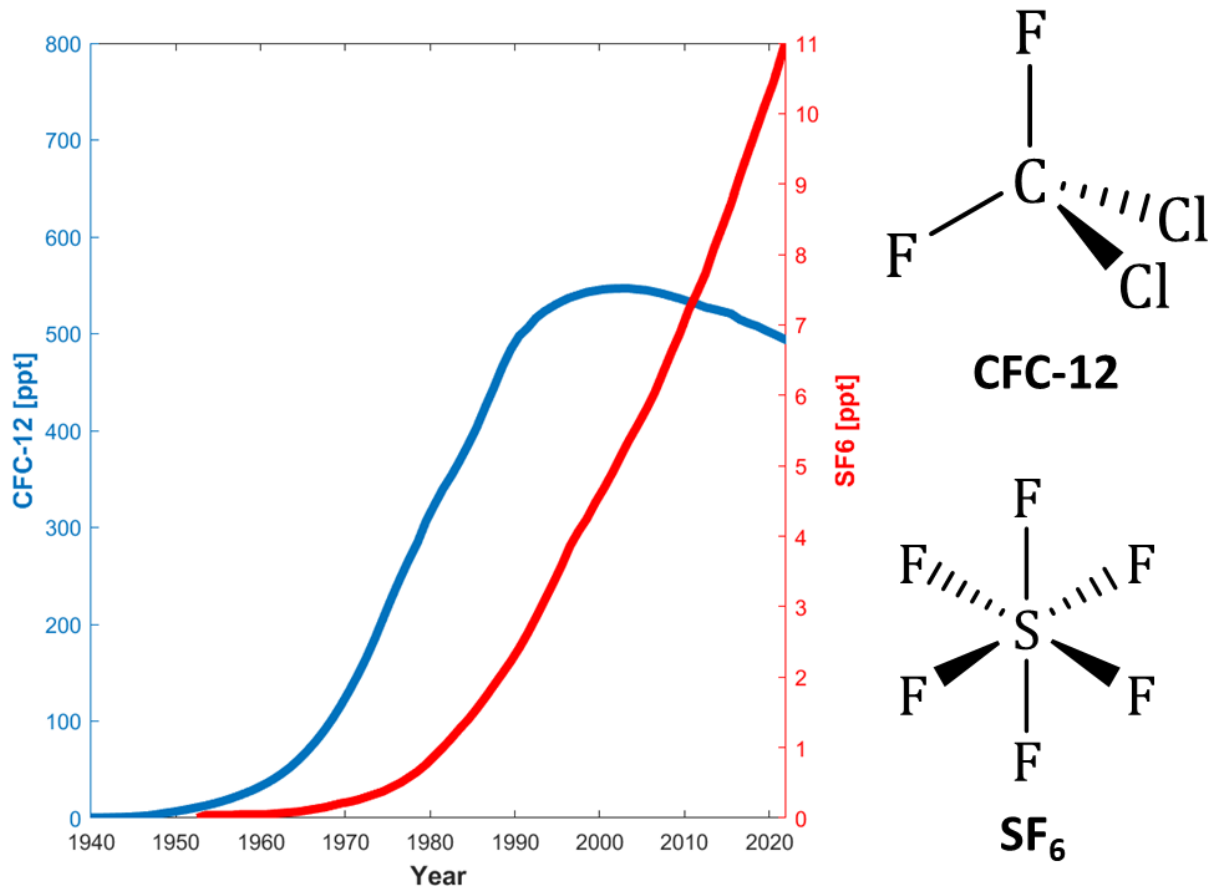
Figure 1.4: Atmospheric concentrations of the two transient tracers mainly used in this study (Bullister & Warner, 2017), CFC-12 (blue) and SF_6 (red). Both tracer concentrations are given in ppt (parts per trillion). The chemical structures of both tracers are depicted on the right. CFC-12 shows a trigonal pyramidal structure with chluoro and fluoro atoms surrounding a carbon atom, and SF_6 a square bipyramidal structure of six fluoro atoms bonding to the sulfur atom.

As the transient tracer CFC-12 is starting to fade out of the atmosphere (see above), there is a growing need to identify alternative gases that can serve as tracers in the near future for estimating oceanic ventilation and circulation timescales. Furthermore, these new tracers should help determine a broader range of water ages.

1.2.2 Iodine-129 & Uranium-236

Especially in the AO, the two radioactive nuclides Iodine-129 (^{129}I) and Uranium-236 (^{236}U) serve as valuable ocean tracers. With very long half-lives of $16*10^6$ and $23*10^6$ years, respectively, they show stable tracer characteristics suitable for tracing ocean movements. Their atmospheric concentrations, which are related to their input functions into the ocean,

are primarily linked to two nuclear fuel reprocessing plants situated at La Hague and Sellafield, near the English Channel. Here these tracers are directly introduced into Atlantic waters, and then move towards the AO within the Norwegian Coastal Current (NCC) (Christl et al., 2015; Edmonds et al., 2001; Gascard et al., 2004; Wefing, 2021). Another source of these radionuclides is the global fallout from nuclear bomb tests (Casacuberta et al., 2016), mainly influencing the ^{236}U concentration. Temporal changes in the atmospheric concentrations of the two tracers are illustrated in figure 1.5.
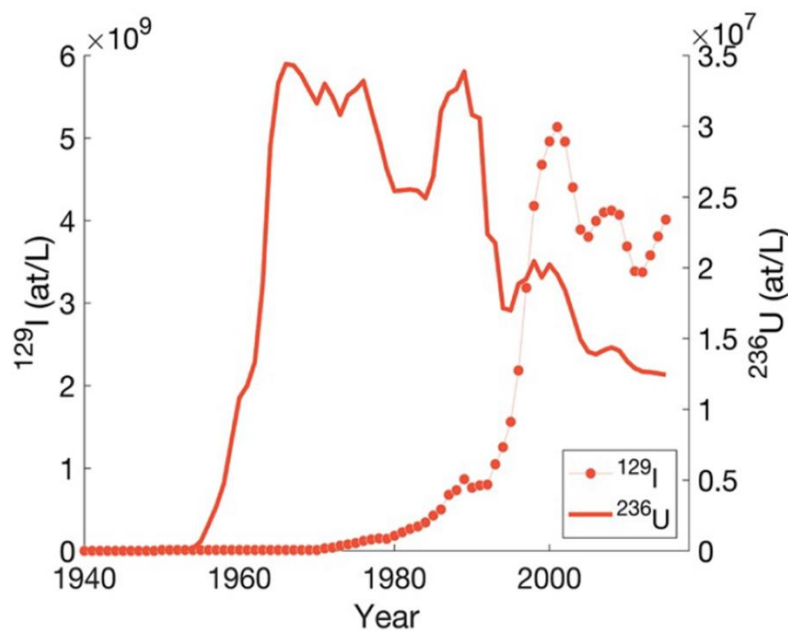
Figure 1.5: Atmospheric concentrations of the two radionuclide transient tracers ^{129}I (red dots) and ^{236}U (solid red line). Both tracer concentrations are displayed in at/L (Raimondi et al., 2023).

As concentrations of these two radionuclides can be measured precisely in seawater samples, they meet all criteria for serving as a transient tracer in ocean sciences. They possess a known input function, are stable in seawater (due to their long half-lives) and have well documented sources (two reprocessing plants). As the tracers enter the Atlantic Water (AW) travelling northwards towards the Arctic, ^{129}I and ^{236}U have significant potential in the analysis of AO circulation and ventilation (Wefing, 2021).

1.2.3 Argon-39

Calculation of ventilation timescales for the deep ocean layers requires a tracer with long-reaching time histories. Radioactive isotopes, such as ^{39}Ar and ^{14}C are prime candidates

due to the consistent atmospheric ratios to their stable isotopes and well-defined half-lives, enabling the measurement of seawater concentrations to determine ages. Until recently the use of the radioactive isotope ^{39}Ar was hindered due to challenging analytics. However, these have significantly improved in recent times, resulting in a reduction of the seawater volume required for accurate measurements by over 95 % and a shortening in the measurement times from up to 60 days to just 1 day per sample (Ritterbusch et al., 2014). Traditionally, ^{39}Ar was measured using Low Level Counting (LLC), but a new technique, called Atom Trap Trace Analysis (ATTA) (explained in detail in Data and Methods, below) has emerged recently, allowing accurate measurements of ^{39}Ar concentrations within a water sample of approximately 5-10 L (Ebser et al., 2018; Lu et al., 2014). With its half-life of 268 years (Golovko, 2023), ^{39}Ar serves as an effective ocean tracer, enabling water dating within the time range of 50-1000 years, significantly improving age determination for deep waters (Ritterbusch et al., 2014). The new measuring approach, a known input function (radioactive decay rate), stability in seawater, and the absence of inner water interactions, render ^{39}Ar an excellent ocean tracer.

1.2.4 HCFC's & HFC's

The use of chronological transient tracers other than CFC-12 and SF_6 in ocean science has also expanded and now includes HCFC's and HFC's. These compounds are of anthropogenic origin and have known atmospheric concentrations, similar to the well-established ocean tracers CFC-12 and SF_6. Over the past few years, there has been increasing interest in the use of these compounds as future ocean tracers (Li et al., 2019). Owing to their atmospheric lifetimes these tracers, initially produced in the mid 1900s (see Figure 1.6), could significantly improve the study of ventilation processes in surface and intermediate waters.
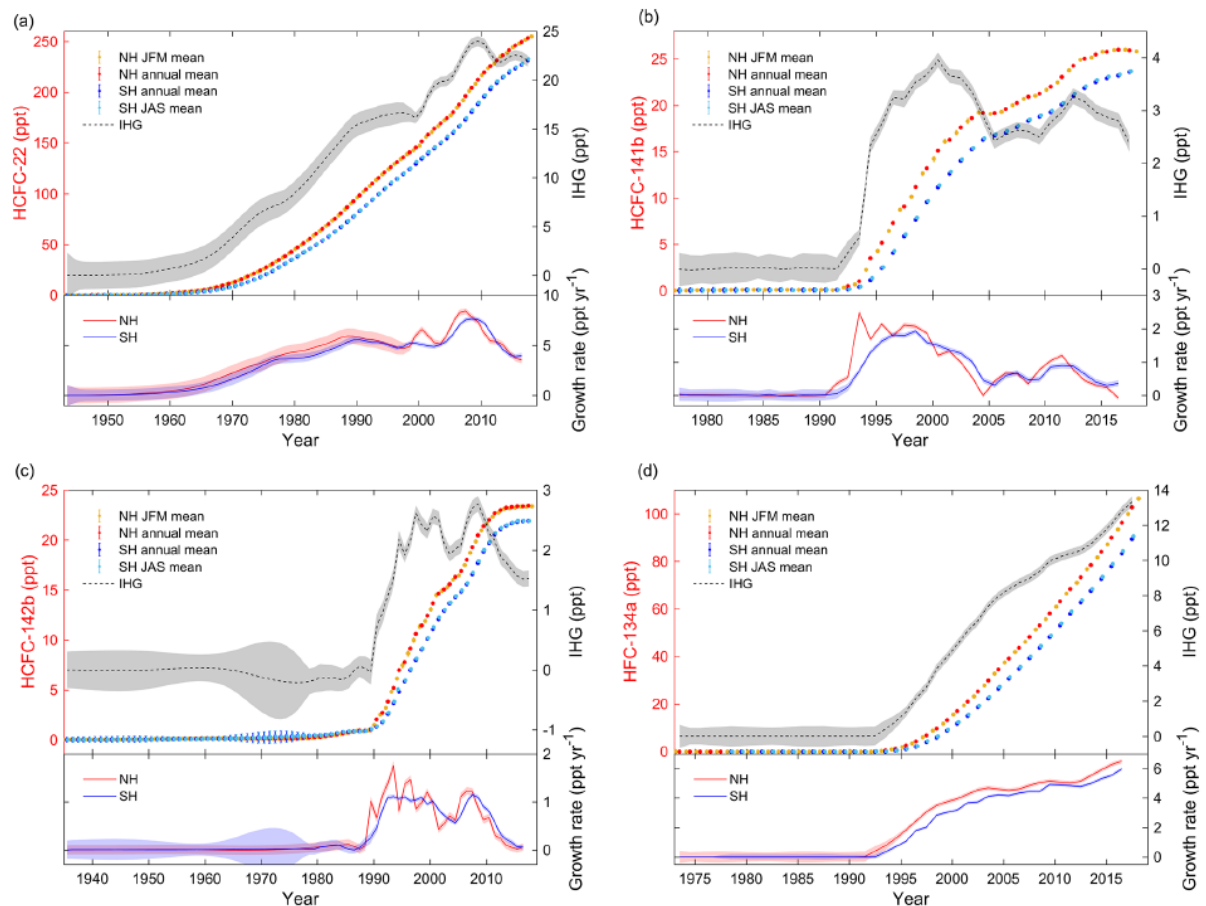
Figure 1.6: Display of the atmospheric concentrations of (a) HCFC-22, (b) HCFC-141b, (c) HCFC-142b and (d) HFC-134a (Li et al., 2019). The top of each panel shows the northern hemisphere means (red), southern hemisphere means (blue) of atmospheric mole fractions and the interhemispheric gradients (IHG, in black, using the right axes). The lower sections show the annual growth rates in ppt yr^{-1}, with the shadings reflecting the uncertainties.

These tracers are currently still evaluated for their potential in ocean studies as their solubility and stability in seawater have not been experimentally determined yet. However, they show well established atmospheric records, have no natural background and can be measured precisely, making them ideal candidates for ocean tracers. In this study we will focus on HCFC-22 (chlorodifluoromethane), HCFC-141b (1,1-dichloro-1-fluoroethane), HCFC-142b (1-chloro-1,1-difluoroethane) and HFC-134a (1,1,1,2-tetrafluoroethane), as they show potential for future use (Li & Tanhua, 2021).

Given their time and application range, a combined use of the different tracers can help assess ventilation processes within the entire water column.

1.3 Study regions

This thesis focusses on the analysis of some of the above-mentioned transient tracers in two regions of the world's oceans, the Arctic Ocean (AO) and the Gulf of St. Lawrence (GSL).

1.3.1 Arctic Ocean

The AO is an area where the process of ventilating waters is highly significant (see Figure 1.7). Here the thermohaline circulation can be described in more detail taking into account the Atlantic Meridional Overturning Circulation (AMOC) and the influence of winds as an additional driving factor for circulation and ventilation processes (Rahmstorf, 2006).
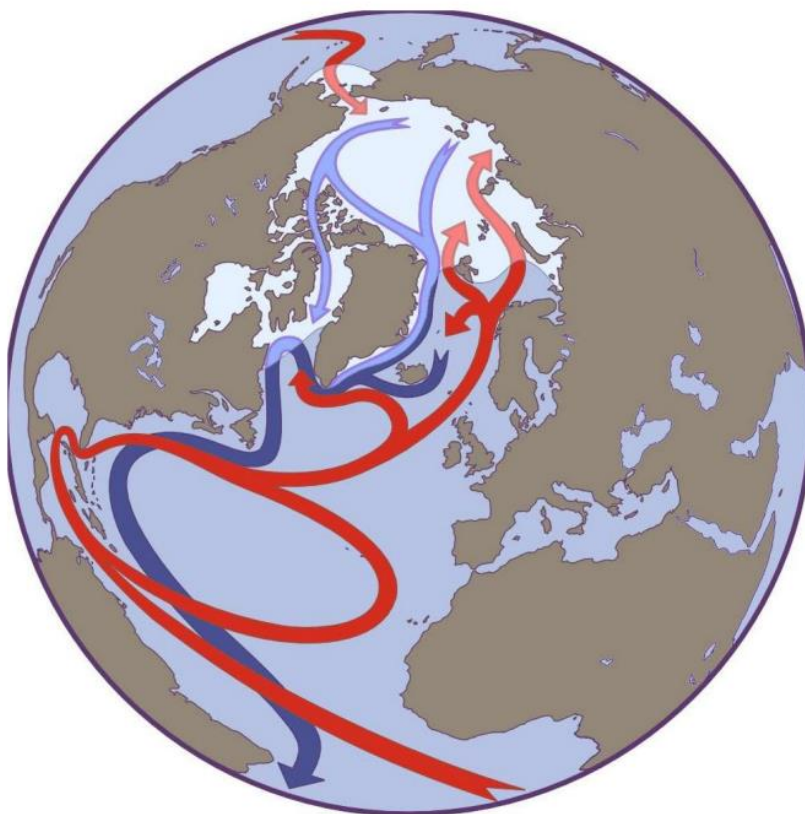
Figure 1.7: Display of the thermohaline circulation in the northern Atlantic Ocean and the AO, with warmer water flowing at the surface towards the pole (red arrows) and colder water being transported south out of the AO (blue arrows) (Rahmstorf, 2006).

The AMOC describes the movement of water masses within the Atlantic Ocean driven by four factors: upwelling processes of warm waters to the surface, wind-driven surface circulation of light waters, formation of deep waters at high latitudes and the circulation of deep water currents (Kuhlbrodt et al., 2007). In the AO and the Nordic Seas, we observe three of these

four components, the wind-driven flow of warm waters at the surface towards the pole, the formation of deep water and the outflow of cold, dense bottom waters. This underscores the significance of this region within the global circulation system and highlights that changes within the ventilation in the AO can have a far reaching, global impact. This is particularly relevant in light of the fact that the AO is one of the areas in the world experiencing the most drastic impact of climate changes (Wassmann, 2015; Woodgate, 2013). It's sea ice coverage has decreased by 12.8 ± 2.4 % per decade since 1979 (Meredith et al., 2019), and overall, temperatures in the Arctic have risen approximately three times faster than the global average air temperatures (Polyakov et al., 2023).

The AO is a largely landlocked sea with connections to the Pacific and Atlantic Oceans through the Bering Strait, and the Fram Strait, the Barents Sea and Canadian Archipelago, respectively (e.g. Jones, 2001; Rudels et al., 1996). It is divided into four different basins by four ocean ridges, the Nansen and Amundsen Basins within the Eurasian AO (the area on the European and Asian side connected to the Atlantic Ocean) separated by the Gakkel Ridge, and the Makarov and Canada Basin separated via the Alpha and Mendeleev Ridge on the Amerasian side (the area connected to the Pacific Ocean and thus the American and Asian continent). The Lomonosov Ridge generally separates the Amerasian and Eurasian Basins. The deep basins form the Central AO, while large shelf areas all around providing the transition to the respective land masses (see Figure 1.8).
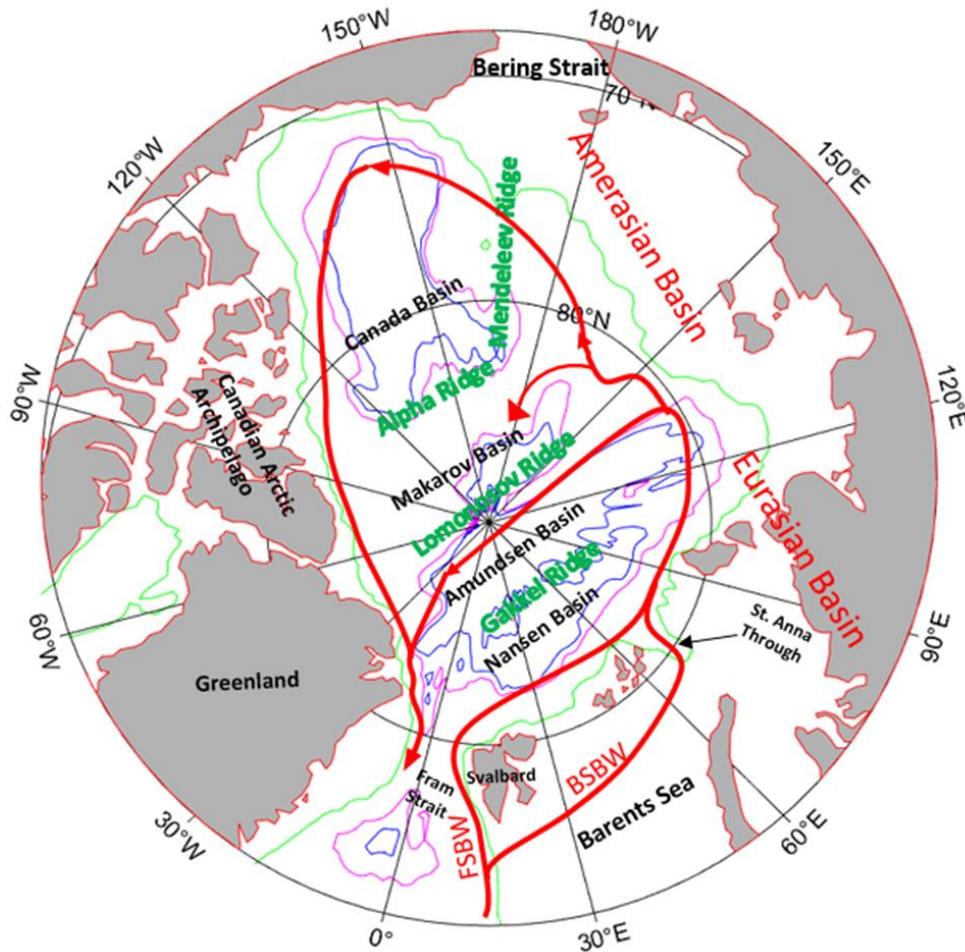
Figure 1.8: The AO and its individual Basins divided by ocean ridges with contour lines at 500m (green), 3000m (magenta) and 3500m (blue). The red arrows show a simplified Atlantic Water (AW) circulation in the AO.

1.3.1.1 Water masses and circulation

The water column within the AO can be divided into four different water mass layers: surface, halocline, intermediate and deep layer.

The wind driven surface layer mainly circulates horizontally. However, with increasing temperatures, decreasing sea-ice coverage and increasing freshwater input, the vertical mixing is likely to increase in this layer (Frolov et al., 2005; Nansen, 1902; Pfirman, 2004; Rigor et al., 2002). It is characterized by near freezing temperatures and a high fresh water content from river runoff, precipitation and iceberg calving (Ekwurzel et al., 2001; Haine, 2021). The halocline layer is found below the surface layer, mainly formed via vertical movement of dense and saline shelf water that is produced during freezing. This layer acts as a barrier between

the surface water above and the intermediate layer below, preventing upward heat flux (Aagaard et al., 1981; Bauch et al., 2014). The intermediate layer is dominated by water entering from the Atlantic Ocean primarily at depths between 250 and 800 m. The water coming from the Atlantic, also called Atlantic Water (AW), circulates as part of the Arctic Ocean Boundary Current (AOBC) which mainly follows the ocean ridges (see Figure 1.8, red arrows) (Aagaard, 1989; Aksenov et al., 2011; Rudels et al., 1999). The AW enters the AO both west and east of Svalbard through the Fram Strait and Barents Sea, respectively. The water then circulates through the AO at depth between 250 and 800 m, rotating counter clockwise and being referred to as mid depth Atlantic layer (Karcher et al., 2012; Rudels et al., 1994; Wefing et al., 2021). On its way through the AO, some AW enters the Amerasian basin. Here, a larger fraction flows around the Canadian Basin and circulates back along the Canadian archipelago, whereas a smaller part enters the Makarov Basin. On the Eurasian side of the Lomonosov Ridge, the AW flows back towards the east Greenland shelf along the Gakkel, but mainly the Lomonosov Ridge. During this movement, the water mass increases in density due to mixing with colder ambient water masses along the way. After the circulation in the AO the AW flows south through the Fram Stait, as part of the East Greenland Current, and enters the Atlantic Ocean as part of the dense Denmark Strait Overflow Water (DSOW) (Swift & Aagaard, 1981; Tanhua et al., 2005). This completes the AOBC within the central AO and describes a ventilation process within the AMOC. Apart from the DSOW, other dense water masses from the AO also flow south through the Faroe-Shetland Strait/Faroe-Bank Channel (850 m) (Beaird et al., 2012) and through the Denmark Strait (650 m) (Macrander et al., 2007). Nonetheless, the DSOW is considered the major deep outflow contributor of water from the AO into the Atlantic and is responsible for the outflow of cold, dense bottom water within the AMOC. The water found below the Atlantic layer at depths between ≈ 800 and 1500 m, which is still considered part of the intermediate layer, is referred to as the upper Polar Deep Water (uPDW) (Rudels et al., 2012; Ulfsbo et al., 2018). The fourth water mass within the AO are the deep water layers below 1500 m. These ventilate via boundary convection processes that transport brine-enriched water formed at the shelfs into the deep Basins (Aagaard & Carmack, 1989; Anderson et al., 1999; Wallace et al., 1992).

1.3.2 Gulf of St. Lawrence

The second major research area, where transient tracer concentration and water masses were analyzed in this thesis is the GSL. This region is located in eastern North America, connected to the Atlantic Ocean and Labrador Sea through the Cabot Strait and Strait of Belle Isle, respectively (see Figure 1.9). The GSL is composed of three major parts: the Upper St. Lawrence Estuary (USLE) ranging from Ile d'Orleans to Tadoussac, the Lower St. Lawrence Estuary (LSLE) spanning from Tadoussac to Pointe-des-Monts, and finally the main Gulf itself consisting of three main channels (Laurentian Channel, Anticosti Channel and Esquiman Channel) and shelf areas.
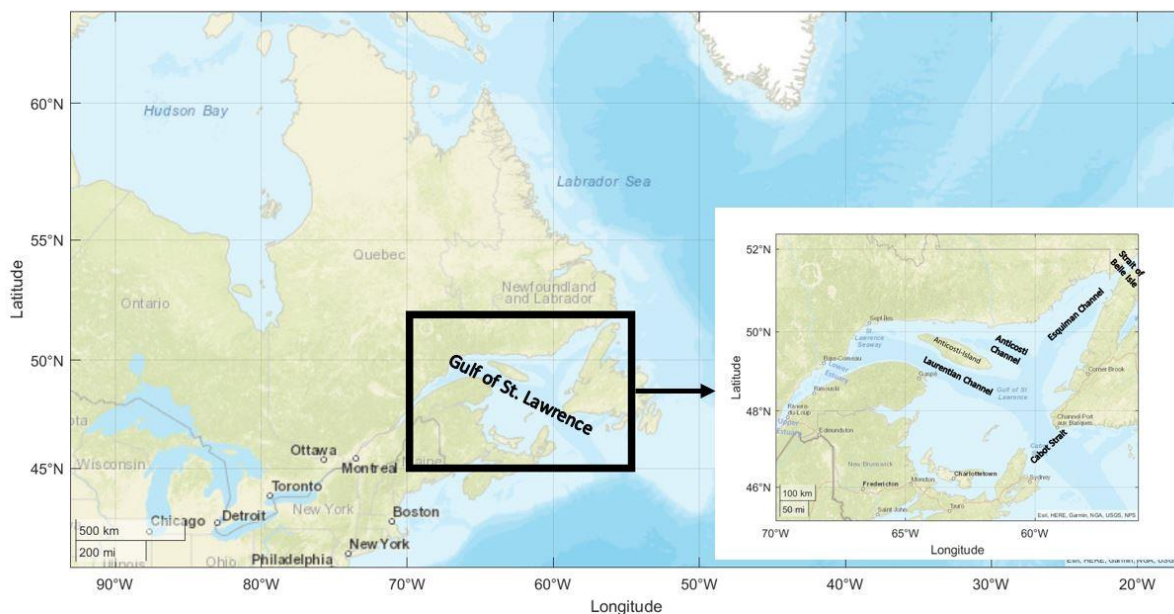
Figure 1.9: Map showing the location of the GSL with the neighboring Labrador Sea and Atlantic Ocean. The zoomed in map shows the channels and straits of the GSL.

The Labrador Sea is the second area, besides the AO and Nordic Seas, where water ventilation due to rapid cooling is apparent in the northern hemisphere (see Figure 1.1 and 1.7). Here oxygen-rich, dense Labrador Current Water (LCW) is formed and transported southward below the surface (Brandt et al., 2006; Gascard & Clarke, 1983). Historically, this water has supplied the GSL bottom waters with high oxygen contents. Interestingly, recent studies have revealed a significant decrease in oxygen concentrations within the GSL, which was proposed to partly be attributed to a change in the composition of the entering deep water (Gilbert et al., 2010; Jutras et al., 2023). This water mass comprises the LCW and water with less oxygen concentrations that is transported from intermediate depths in the North Atlantic; it is

referred to as North Atlantic Central Water (NACW). A possible connection between the composition of water entering the GSL and decreasing oxygen content in the GSL was examined in this thesis using transient tracer data and the TTD method (see manuscript II/chapter 4).

1.3.2.1 Water masses and circulation

Three different water layers are observed in the GSL: surface, intermediate and deep water layer.

The surface layer, which consists of warm water (> 2 °C) with low salinity (27-31.5 psu) is formed by upwelled deep water, the continental freshwater runoff from the Estuary, and water from the north shore rivers (Galbraith, 2006; Gilbert & Pettigrew, 1997). This water mass flows mainly seaward towards the Atlantic leaving through the Cabot Strait on top of the more dense, intermediate and deep waters (Dickie & Trites, 1983; Jutras et al., 2020). The intermediate layer is characterized by cold (-1.5°-2°C) and saline (31.5-33 psu) waters entering through the Strait of Belle Isle from the Labrador Sea and through the Cabot Strait at intermediate depths during wintertime. In addition, deep water mixing occurs north of Anticosti Island every winter, when surface water is transported to intermediate depth supplying the LSLE and USLE with cold and saline waters (Saucier et al., 2003; Smith et al., 2006). The deep water enters through the Cabot Strait from the Atlantic Ocean at depths below 200 m. Two major currents feed this relatively warm (2-7 °C) and saline (33-35 psu) deep water mass, the LCW and the NACW (Dickie & Trites, 1983; Jutras et al., 2023). While the LCW contributes colder, and oxygen rich water with lower salinity, the NACW supplies warm, saline waters with lower oxygen concentrations. The deep water flows landwards within each channel of the GSL and is vertically mixed at the edges by bottom-boundary mixing processes (Cyr et al., 2015; Ingram, 1983; Jutras et al., 2020; Saucier et al., 2003).

1.4 Aim of the thesis

The overall objective of this thesis was to analyze the ventilation in the Arctic Ocean (AO) and the Gulf of St. Lawrence (GSL). This involved the analysis of general ventilation patterns, as well as temporal variability in ventilation dynamics within the two regions.

In the AO, transient tracer data and information on the ventilation patterns are relatively scarce. Furthermore, this area is increasingly affected by climate change resulting in possible ventilation changes within the oceans interior. Therefore, the primary objective of this thesis was to analyze general ventilation patterns and potential temporal variabilities in these patterns within the AO. To achieve this, transient tracer measurements of CFC-12 and SF$_6$, conducted during a cruise in 2021, were employed in combination with the TTD method. Moreover, historical data of these tracers, collected over the last three decades (1991, 2005 and 2015), were included to assess temporal changes in ventilation.

The analysis of ventilation using the TTD relies on a variety of assumptions that can be further confined using additional experimental data. Therefore, a second goal of this thesis comprised the introduction of a multiple tracer approach. Several different tracers measured simultaneously at the same location and time in the AO were employed to analyze ventilation patterns in more detail and obtain more information on the mixing of water masses as well as the relationship of advective and diffusive water flow in different regions of the AO. Alongside the well explored and commonly used transient tracers CFC-12 and SF$_6$, additional tracers known as 'Medusa'-tracers were sampled, measured and included in the analysis. These tracers encompassed other HFC's and HCFC's which are characterized by distinct input functions, permitting the application of a 2-IG-TTD method in the ventilation analysis.

The GSL has experienced a rapid decrease in oxygen concentrations over the last decades. This decline was proposed to stem from an alteration in the composition of the deep water entering the Gulf. Therefore, another aim of this thesis was to investigate whether such change in the deep water composition is indeed observed. To achieve this, transient tracer data (CFC-12 and SF$_6$) collected during two field campaigns in 2022, were analyzed utilizing the TTD method. As the deep water supply of this Gulf by water entering from the Atlantic Ocean, comprises a mix of recently ventilated, oxygen-rich water and older water with lower oxygen content, an analysis of the mean age of the deep water within the GSL was conducted to obtain detailed information on the inflowing water.

2. Data and Methods

2.1 Collection of data

Transient tracer data used to analyze ventilation in this thesis were primarily obtained from seawater samples collected during various research expeditions in 2021 and 2022. Measurements of CFC-12 and SF_6 concentrations were conducted directly on-board of the research vessels during the Synoptic Arctic Survey expedition in 2021 on the Icebreaker Oden ('SAS-Oden 2021'), as well as during two cruises in the Gulf of St. Lawrence (GSL) (TReX 2 & TReX 4) in 2022 on the research vessel Coriolis II, with calibrations carried out in the laboratory at the GEOMAR in Kiel. Other tracers, such as ^{39}Ar or HCFC's and HFC's, were analyzed in different laboratories using samples collected during the 'SAS-Oden 2021' expedition. HCFC's and HFC's were measured at the GEOMAR in Kiel and the radioisotope ^{39}Ar at the University of Heidelberg.

Additional historical transient tracer data for CFC-12 and SF_6 were taken from the Global Ocean Data Analysis Project (GLODAP) data portal, in particular GLODAPv2.2021 and GLODAPv2.2022 (Lauvset et al., 2022; Lauvset et al., 2021).

2.2 Determination of transient tracer concentrations

2.2.1 CFC-12 & SF_6

The chronological transient tracers CFC-12 and SF_6, were measured using a purge and trap system in combination with a gas chromatograph equipped with an electron capture detector (PT-GC-ECD). Such measurements can be conducted either directly on board of the research vessel or in the laboratory, after sampling and shipping of the probes. On board samples were collected from Niskin bottles using calibrated 250 mL glass syringes. After brief storage in a cold water bath to prevent outgassing, the water was inserted into the purge and trap unit under atmospheric exclusion. For the analysis approximately 200 mL of the 250 mL water sample were injected into the purge and trap unit, ensuring it was free from atmospheric contamination. Subsequently, the sample was purged with pure nitrogen gas, and the analytes were transferred to a cooled trap consisting of 100 cm 1/16" tubing packed with 70 cm Heysep D. The trap was kept as temperatures of -60 to -70 °C by placing over liquid nitrogen. After

purging the sample, the trap was desorbed by heating it to 100 °C, and the analytes were transferred into the gas chromatograph, separated within a pre-column, composed of 30 cm Porasil C and 60 cm Molsieve 5A, and then a main column consisting of 200 cm Carbograph 1AC and 20 cm Molsieve 5A, before being analyzed with the Electron Capture Detector (ECD). A detailed description of this experimental setup can be found in manuscript I/chapter 3, and in Tanhua et al. (2004) and Bullister et al. (2002). The system has a detection limit of approximately 0.05 fmol/kg for SF_6 and 0.01 pmol/kg for CFC-12, respectively (Stöven et al., 2015).

In this study, 709 samples collected during the research expedition 'SAS-Oden 2021' were all analyzed using an on-board system, enabling direct measurements of CFC-12 and SF_6 concentrations. The data had a precision of 0.03 fmol/kg (2.6 %) and 0.02 pmol/kg (1.5 %) for SF_6 and CFC-12, respectively, as determined from duplicates measured throughout the mission at various depths and locations.

During TReX 2, tracer concentrations were again measured using an on-board system; they exhibited a precision of 0.03 fmol/kg (2.8 %) for SF_6 and 0.02 pmol/kg (1.3 %) for CFC-12, as determined from duplicate samples. During TReX 4, the data showed relatively high variations and overall higher concentrations, when compared to measurements during TReX 2 at similar density and location. Therefore, these data were shifted by -20 % for CFC-12 and -14 % for SF_6 to achieve more plausible values (see Figure S1 in supplemental material to manuscript II/chapter 4). The measurements from TReX 2 were considered to be more accurate, as they showed surface water tracer concentrations being close to 100 % saturated with the atmosphere.

In the laboratory, the gaseous standard containing known SF_6 and CFC-12 concentrations (see Table D1 - DS3) was calibrated against and referenced to the SIO (Scripps Institution of Oceanography) calibration scale.

2.2.2 HCFC's & HFC's

Samples for analyzing HCFC's and HFC's were collected in 1.3 L glass ampoules and measured using a GC-Mass spectrometer (MS), referred to as the 'Medusa-Aqua' analytical system.

The 'Medusa'-GC-MS system was developed at the Scripps Institute of Oceanography to provide high precision and simultaneous measurements of approximately 40 atmospheric compounds, including CFC's, HCFC's and HFC's (Miller et al., 2008). A network of 'Medusa'-systems placed around the world provides high accuracy measurements of atmospheric concentrations of these compounds in the northern and southern hemisphere every 2 hours. The system operates by trapping the analytes on two differently packed traps kept at controlled low temperature (≈ -165 °C) (Miller et al., 2008). These separate the less volatile analytes from the most volatile ones in the sample. By individually heating each trap to 100 °C for desorption, the compounds of each trap are transferred and separated within a pre and a main column in the GC. Finally, the analytes are measured using the quadrupole MS (see Figure 2.1).
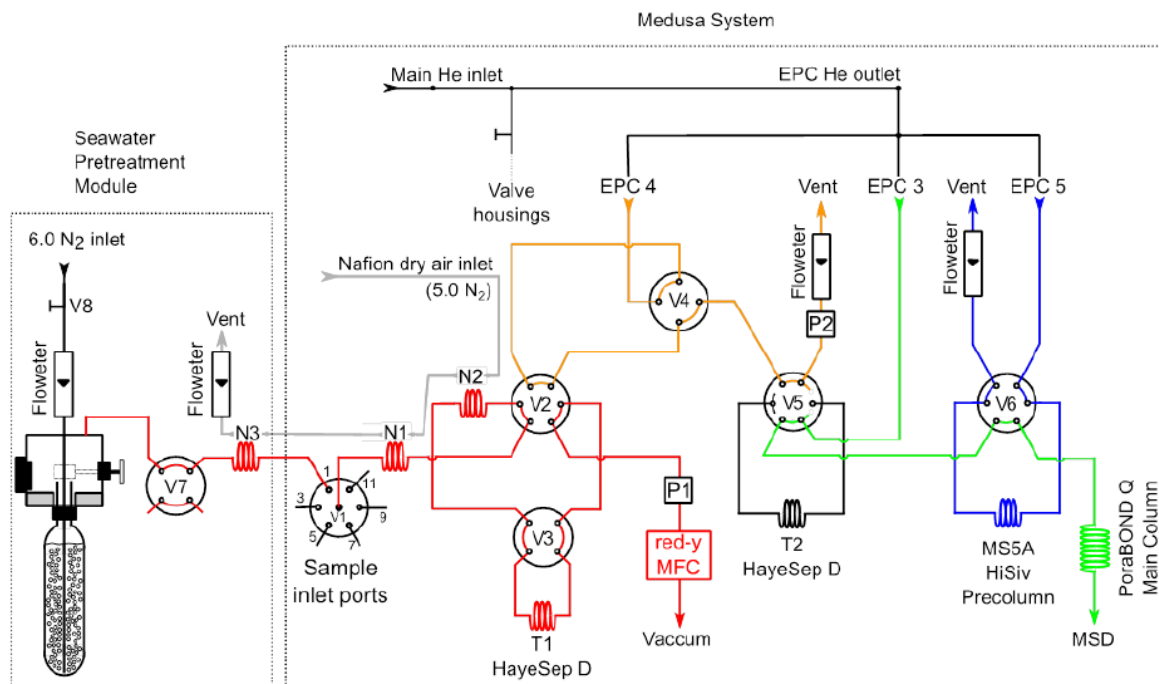
Figure 2.1: Display of the 'Medusa-Aqua'-system flow scheme. The system comprises the seawater pretreatment module and the 'Medusa'-GC-MS analyzing system (Li & Tanhua, 2021).

The 'Medusa'-system was adapted to analyze water samples by installing a purge and trap unit replacing the original air sampling device with an Ampoule-Cracker-System (Li & Tanhua, 2021; Stöven, 2011; Vollmer & Weiss, 2002). This modification permits to crack open and purge the water samples collected in ampoules, absorbing and transporting the analytes with pure nitrogen gas onto the two traps as described previously. This final design is called, 'Medusa-Aqua' analytical system (see Figure 2.1) (Li & Tanhua, 2021).

During the 'SAS-Oden 2021' expedition, samples for the measurement of HCFC's and HFC's concentrations were collected at six station. At each station, samples were obtained at seven different depths spanning from 30 to 2000 m. The 1.3 L ampoule was connected to the Niskin bottle via a stainless steel mounting system (Stöven, 2011). When filling of the ampoule with seawater, it was overflowed by at least twice the amount of seawater to ensure removal of any previous atmospheric contaminations. After sampling, the ampoules were flame-sealed immediately. In this step, a continuous nitrogen flow was connected to the mounting system, providing a headspace of nitrogen gas only, and the ampoule was flame sealed using a torch (see Figure 2.2). The water samples were analyzed using the 'Medusa-Aqua'-system in the laboratory at the GEOMAR shortly after the cruise.

Figure 2.2: Picture of a flame sealed ampoule showing the headspace filled with pure nitrogen.

In the laboratory, each ampoule was placed in a 65 °C water bath for a minimum of 24 h before being inserted into the Ampoule-Cracker-System. This increased the purge efficiency by forcing more gas molecules into the gas phase. Despite this precaution, each sample was measured at least four times to ensure optimal purge efficiency. Following the measurement,

the ampoules were weighted once with seawater and once without to determine the exact volume of each sample.

Calibration procedures involved the measurement of standard curves every two weeks using a gaseous standard with known concentrations of the analytes (see Table D1 – Gold). The standard curves were used to determine the concentrations of the measured gases and provided information about possible detector drifts.

For reasons outlined below, the concentrations obtained in the initial measurements required some corrections. First, determination of the exact concentrations in each sample involved an adjustment to previously measured standard curves. This was necessary because the standard curves generated during the actual analysis process did not fully cover the range of concentrations found in the measured samples. In other words, the areas determined in the chromatograms for each analyte, which indicate the amount of tracer injected at varying volumes of gaseous standard, did not sufficiently cover the tracer-analyte amount detected in the water sample. Therefore, standard curves encompassing higher amounts of tracers-analytes, which were measured on the 'Medusa' prior to the sample analysis, were also considered. These curves were adjusted to align closely with values measured from standard curves during the actual sample analysis, especially at lower area values (see Figures 2.3a, D1a, D2a & D3a). This enabled an extension of the standard curves to cover a wider concentration/area range. Consequently, biases at high values were reduced and comparable areas to those measured in the water samples were obtained (see Figures 2.3b, D1b, D2b & D3b). The corrected standard curves were then used to calculate concentrations of each tracer.
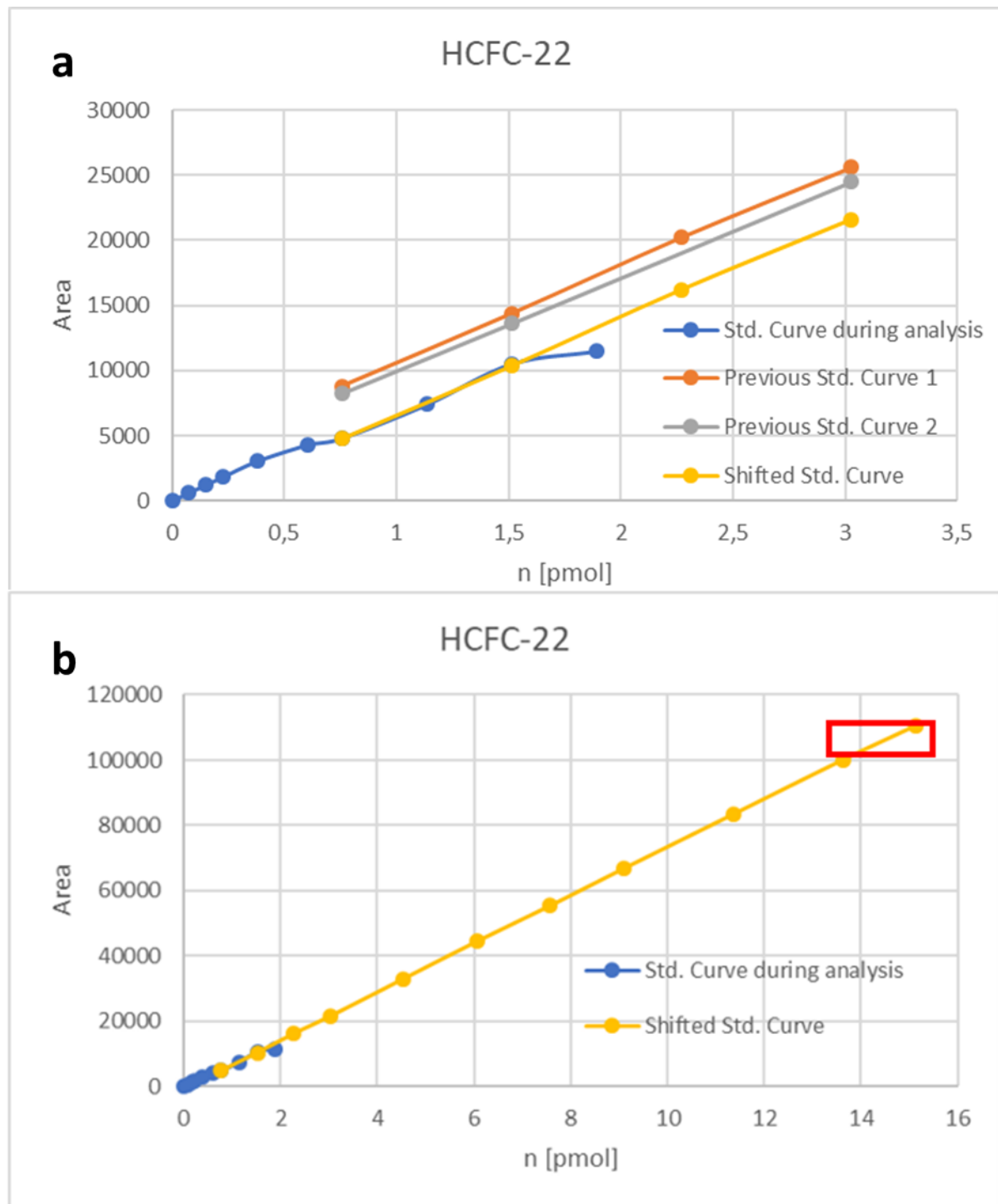
Figure 2.3: Graph of the shift (a) and extension (b) of the standard curve used to determine HCFC-22 concentrations. The shifted standard curve in the top graph only shows the lower concentration ranges to fit it more precisely to the standard curve measured during the actual sample analysis. The actual concentrations measured in the ocean surface water samples are found in the high concentration range shown in the red box.

Furthermore, the concentrations obtained for HCFC-22 after this adjustment were multiplied by a factor of 1.5 and the HFC-134a data by 0.9 to align the values observed in surface water

samples with the atmospheric concentrations measured in the corresponding year (2021) in the northern hemisphere. To compare the values, the measured concentrations were converted from mol/L to partial pressure (ppt - parts per trillion) values, the unit which is typically used for atmospheric concentrations. This conversion took into account the solubility of each tracer in seawater. Due to unsatisfying results from a laboratory experiment aimed to determine the solubility of HCFC's and HFC's in seawater (described below), the calculated Ostwald solubility of each tracer was used in the conversion (Li et al., 2019). Following these corrections all tracer concentrations measured in the surface water samples were found to be consistent with the respective atmospheric concentrations observed in 2021 (see Figure 2.4).
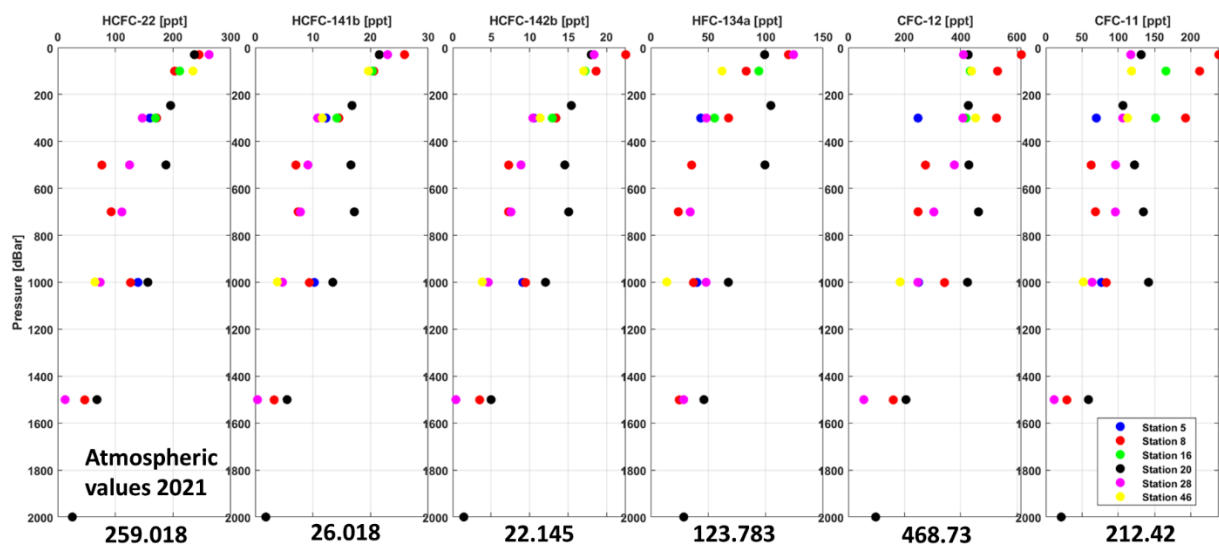
Figure 2.4: Calculated partial pressures of different tracers as a function of depth (given as pressure values). Calculations involved using the Ostwald solubility of each tracer (Li et al., 2019) and implementing the adjustments described in the text. The different colors represent the samples collected at each of the six stations. The atmospheric partial pressures of each tracer the northern hemisphere in 2021 are displayed at the bottom.

2.2.2.1 Solubility of HCFC's & HFC's

To determine the solubility of some 'Medusa'-tracers, tracer concentrations were investigated in water samples of varying temperature and salinity, aiming to establish solubility as a function of temperature and salinity. To quantify the amount of tracers dissolved in the sample, a procedure was developed that involved insertion of known amounts of tracer into

a seawater sample and subsequently equilibration under atmospheric exclusion, before the samples were measured on the 'Medusa-Aqua'-system.

The final experimental setup involved filling a 330 mL glass ampoule with 250 mL of water of varying salinity values (0, 18, 26.2 & 34.4 psu). This sample was then purged with pure nitrogen gas for two hours and 0.5 bar pressure to extract any previous gases and contaminants from the water. Next, the 80 mL headspace of the ampoule was filled with standard gas containing known tracer concentrations (see Table D1 – DS4) for one minute at 1 bar pressure. Subsequently, the ampoule was tightly sealed and placed in a water bath at the respective temperatures (4, 10, 15 or 20 °C) for 24 h to establish equilibrium between the gas and water phase. Throughout this period, the samples were intermittently shaken to ensure mixing and speed up the equilibration process. Once the samples were saturated, the headspace was purged with pure nitrogen to remove the residual standard gas, leaving only the dissolved gases in the water sample before the ampoule was flame-sealed and analyzed.

The measured concentration in each sample (in pmol/L) was divided by the concentration of tracer injected into the headspace at the beginning yielding the fraction of tracer dissolved in the sample relative to the amount initially injected into the headspace (headspace ppt) (see Equation 2.1). The partial pressure of the tracer injected into the headspace was determined using the ideal gas law (see Equation 2.2).

$$F[\frac{pmol}{L*atm}] = \frac{measured\ pmol/L}{headspace\ ppt} \qquad \textbf{2.1}$$

$$headspace\ ppt = amount\ of\ substance\ in\ pmol * \frac{R*T}{p*V} \qquad \textbf{2.2}$$
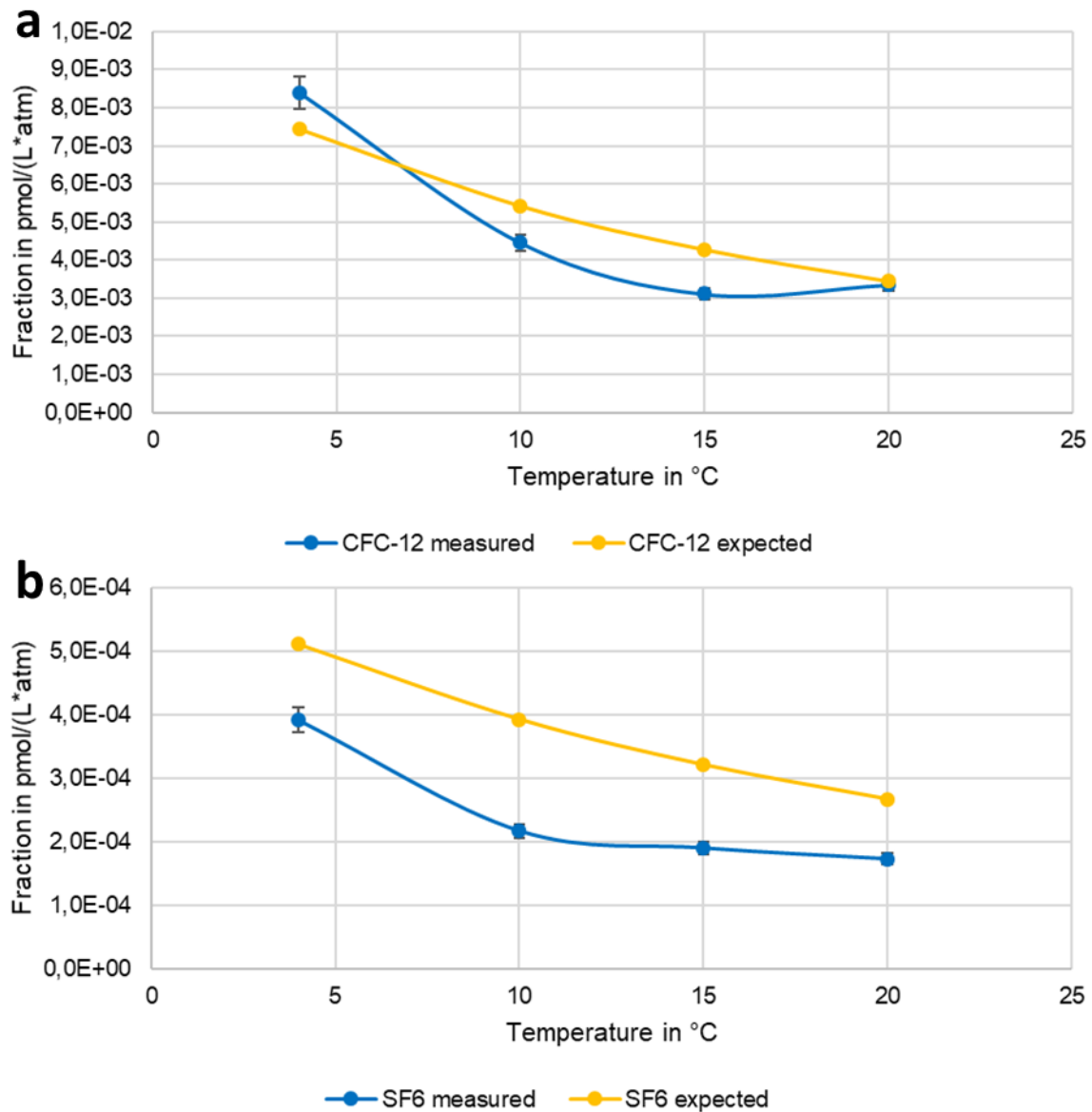
Figure 2.5: Solubility of (a) CFC-12 and (b) SF$_6$ in MilliQ water (0 psu). Comparison of the measured results (CFC-12 and SF$_6$ measured) to those calculated using the solubility functions from Warner & Weiss (1985) and Bullister et al. (2002) (CFC-12 and SF$_6$ expected).

To determine the accuracy of the experiment, the results of tracers with known solubility functions, such as CFC-12 or SF$_6$, were compared to literature values at varying temperatures and salinities, revealing a close comparability (see Figures 2.5, and D4, D5 & D6 in Appendix D). For HCFC-22, results of the dissolved fractions as a function of temperature and salinity levels (0 psu and 34.4 psu) are shown in Figure 2.6. Here measured values were compared to values calculated based on self-determined solubility functions which included all measurement results from varying temperatures and salinities. The results for HCFC-22

measurements at salinity values of 18 psu and 26.2 psu and for HFC-134a can be found in the Appendix D2 (see Figures D7 – D9).
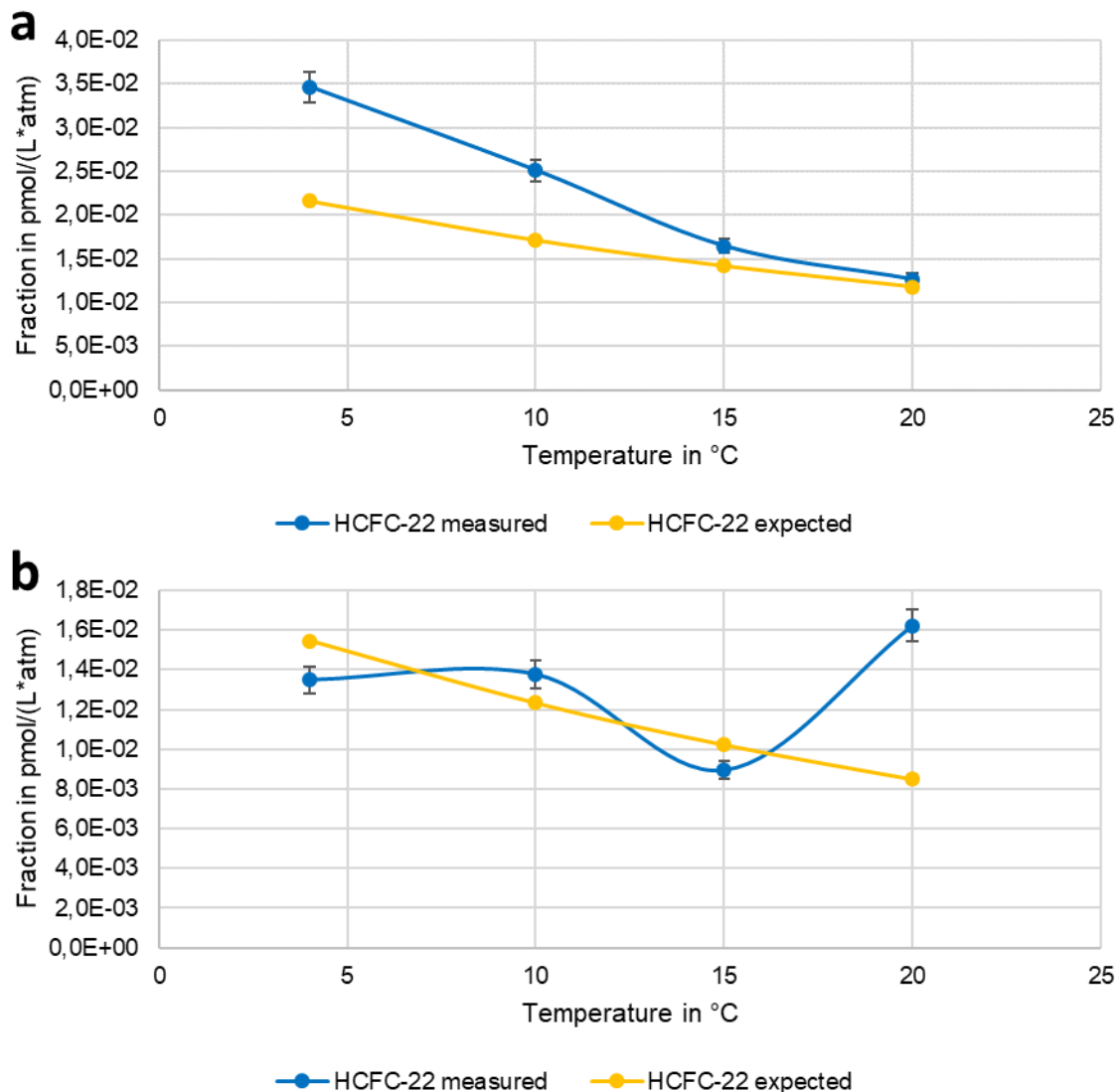
Figure 2.6: Solubility fraction of HCFC-22 in (a) MilliQ water (0 psu) and (b) 34.4 psu water. Shown is a comparison of the results measured (blue) to those calculated using self-determined solubility functions, which included all measurement results from varying temperatures and salinities (yellow).

The measurements fall within the expected solubility range, but somewhat varying results underscore the challenge of constraining outcomes using this experimental setup. To improve the determination of the solubility of the 'Medusa'-tracers in future experiments, it could be beneficial to purge the sample continuously throughout the saturation process in a contamination free chamber. Combining this with constant stirring could ensure that the water reaches full 100 % gas saturation. Additionally, to obtain consistent results at

temperatures around 0 °C or even below 0 °C, a mixture of glycol and water and a recirculating chiller bath could be considered to maintain colder temperatures (Warner & Weiss, 1985).

The solubility functions derived from these experiments showed reasonable results for measurements conducted at temperatures above 4 °C; however, applying them at lower temperatures resulted in higher uncertainties. Thus, given that the samples analyzed in this study were collected in the AO, where temperatures are commonly at and below 0 °C, we used the mathematically determined Ostwald solubility functions to calculate the partial pressure of the 'Medusa'-tracers, providing more reasonable results (Li et al., 2019).

2.2.3 Argon-39

Due to the low abundance of the ^{39}Ar isotope, with a ratio of ^{39}Ar/^{40}Ar $= 8.1*10^{-16}$ in atmospheric argon (Collon et al., 2004), 5 to 10 L of water are required per sample for high-quality measurements. Consequently, samples for the measurements were collected solely from one entire Niskin bottle at each depth using empty industry-standard propane gas bottles during the 'SAS-Oden 2021' expedition. The propane gas bottles, with volumes of 6 and 12 L, were evacuated and flushed with pure nitrogen prior to sampling to prevent any potential contamination. Finally, they were evacuated, facilitating the intake of the water sample.

Each propane gas bottle was attached to a Niskin bottle using a 3-way-valve for sampling. Some water was first rinsed through one side of the valve to eliminate any contamination risk or bubbles in the tubing, before switching the valve and filling the gas bottle. Throughout this process, the bottles were placed on a scale to determine the volume through weight measurement (Snoeijs-Leijonmalm & Party, 2022). After shipment, the samples underwent preparation for analysis on the ATTA (Atom Trap Trace Analysis) system at the University of Heidelberg.

The preparation yielded a few milliliters of purified argon gas from each 5-10 L water sample. This was achieved via a special purification setup, which was connected to the propane bottle absorbing the gas via a trap during degassing of the water sample. The trapped gas was passed through a titanium sponge getter, which efficiently removes all reactive gases from the noble gases, eventually yielding pure argon. The concentrated sample was then subjected to and

analyzed within the ATTA ((Ebser et al., 2018; Snoeijs-Leijonmalm & Party, 2022), Y. Arck, personal communication).

The ATTA uses laser-based atom counting to record noble gas radionuclides, including isotopes such as [81]Kr, [85]Kr and [39]Ar. Originally designed to measure rare krypton isotopes (Chen et al., 1999), the system was expanded to [39]Ar measurements (e.g. Jiang et al., 2011; Lu et al., 2014; Ritterbusch et al., 2014). ATTA uses a magneto-optical trap (MOT) and laser beams of precise frequencies to capture the desired isotope within a vacuum chamber. Gas recirculation within this vacuum system is crucial for the small sample size used. The laser frequency is selected to match the resonance frequency of the atomic transition specific to each isotope. The method separates the rare isotopes from the abundant ones by exploiting the high selectivity of resonant photon scattering in laser cooling.

In detail, a specific isotope (here [39]Ar) is slowed down using laser cooling, where a laser with the exact resonance to the atomic transition of the isotope is fired straight at the incoming sample. Through momentum transfer of several million photons, the speed is slowed down efficiently to capture the respective isotope within the MOT for a short time, before it is replaced by the next isotope or falls back into the ground state. Hereby, the analyte re-emits the photons, which are measured with a photosensor, analyzing the laser-induced fluorescence emitted by each individual trapped atom. After leaving the MOT, the analytes are recycled to the beginning (Lu et al., 2014; Ritterbusch et al., 2014). However, an [39]Ar isotope cannot be initialized from the ground state, but only from a meta-stable state. Therefore, the sample is initially discharged using a plasma ignition, generating some atoms that enter the meta-stable phase for a short time. The ATTA technique counts each single atom and not the radioactive decays, which are measured in the Low Level Counting technique (Loosli, 1983; Schlosser et al., 1994). This reduces the analysis time enormously.

Samples for [39]Ar were collected at the same locations as samples for the 'Medusa'-tracers during the 'SAS-Oden 2021' cruise. The sampling depths ranged from the surface to the bottom of the water column at the six stations.

2.3 Transit Time Distribution

One approach to assess ventilation timescales and rates employs the Transit Time Distribution (TTD) concept. This well-established method (Hall & Plumb, 1994; Khatiwala et al., 2001; Schneider et al., 2012; Sonnerup et al., 2013; Stöven & Tanhua, 2014; Waugh et al., 2002) is used to characterize the age distribution of individual water parcels within the ocean interior using transient tracer measurements. The 'age' in these analyses refers to the time since a water parcel was last at the ocean surface interacting with the atmosphere.

The TTD method takes into account that oceanic water movement isn't solely governed by advective processes, but also involves diffusion and mixing with surrounding water masses. This is achieved by assuming not a single age for the transit time, but a distribution of ages. To account for such distributions, the Green's function ($G(t',r)$) is applied, which describes the propagation of a tracer boundary condition into the interior ocean in the form of an age spectrum. Green's function is linked to the concentration of a dissolved substance (tracer) at a certain location and time ($c(t,r)$) by the following function (Hall & Plumb, 1994; Holzer & Primeau, 2010).

$$c(t,r) = \int_0^\infty c_0(t - t')e^{-\lambda t'} * G(t',r)\, dt' \qquad \textbf{2.3}$$

Here, the input function of each tracer ($c_0(t-t')e^{-\lambda t'}$) is known due to its atmospheric history and characteristics. The unknown is Green's function, which is commonly described by an inverse Gaussian (IG) shape of the distribution, providing the probability density function (PDF) (see equation 2.4).

$$G(t) = \sqrt{\frac{\Gamma^3}{4\pi\Delta^2 t^3}} * \exp\left(\frac{-\Gamma(t-\Gamma)^2}{4\Delta^2 t}\right) \qquad \textbf{2.4}$$

Within equation 2.4, Γ describes the mean age, whereas Δ represents the width of the distribution of the PDF. The relationship between these two parameters is used to provide information on the advective and diffusive characteristics within the water parcel. A Δ/Γ-ratio < 1 indicates dominance of advective processes, and a Δ/Γ-ratio > 1 characterizes a more diffusive flow.

The TTD-method relies on several assumptions to serve as a framework for understanding ocean ventilation. These include:

1. Steady state conditions

2. A single source region for the tracer

3. No inner water interaction of the tracer

4. A one-dimensional flow

2.3.1 1-IG TTD approach

The commonly used TTD approach to describe ocean ventilation and achieve information on the advective and diffusive characteristics is based on the one-inverse Gaussian (1-IG) assumption (Stöven & Tanhua, 2014). Here a combination of two tracers with significantly different input functions (e.g. CFC-12 and SF_6) is used to determine a Δ/Γ-ratio with the lowest uncertainty for the region of interest, by comparing the resulting mean ages from each tracer and identifying the ratio, where the mean ages show the best comparability (see Figure S1 in supplemental material to manuscript I/chapter 3).

Equation 2.3 and 2.4 are used to effectively constrain matrices of simulated tracer concentrations each associated to mean ages (Γ), Δ/Γ-ratio and their respective input functions, maintaining a fixed Δ/Γ-ratio.

Generally, a preset range of mean ages (e.g. 0-2000 years) and Δ/Γ-ratios ranging from 0.2 and 1.8 are considered to constrain the width of the distribution (Δ). Γ and Δ are then used to obtain the PDF across all ranges of mean ages for each Δ/Γ-ratio (see Figure 1.3). Combined with the input functions of the individual tracers, this approach provides all possible concentrations of each tracer at a certain location and time within the defined age spectrum and fixed Δ/Γ-ratio.

For the actual analysis, the measured concentrations of each tracer sample are correlated with the simulated concentrations from a fixed Δ/Γ-ratio and their respective mean ages. These mean ages computed for tracers with significantly different input functions are then compared and where they show the best match, this TTD is fixed for the respective region (see Figure S1 in supplemental material to manuscript I/chapter 3).

2.3.2 Smith's TTD approach

An alternative approach to determine the best suitable Δ/Γ-ratio and obtain information on advection and diffusion is the so-called 'Smith' method, initially introduced by Smith et al.

(2011) and used in Raimondi et al. (2023) and Wefing et al. (2021). This method is particularly advantageous when water masses are analyzed that are characterized by significant Δ/Γ-ratio differences in neighboring locations, and where small-scale circulations have to be constrained. Similar to the 1-IG TTD approach, 'Smith's' method assumes an inverse Gaussian shape of the TTD. However, 'Smith's' TTD method does not fix the Δ/Γ-ratio, but allows for variability in both, the mean age (Γ) and width of the distribution (Δ), permitting individual Γ and Δ values for each water sample. Similar to the 1-IG TTD approach a range of mean ages (Γ) is preset, but 'Smith's' method also permits a range of the distributions (Δ), thus not fixing the ratio between Δ and Γ. However, only combinations of Δ and Γ within the range of ratios between 0.2 to 1.8 are permitted. For each combination allowed, the PDF is determined and the input function of each tracer is incorporated, thereby calculating the modelled tracer concentrations for each potential PDF. Considering all possible Δ/Γ-ratios, the resulting simulated concentrations of two tracers with significantly different input functions are plotted against each other. This generates a grid of all possible modelled concentration pairs, who each include a specific predetermined Γ and Δ value, as well as a Δ/Γ-ratios in the range from 0.2 to 1.8 (see Figure 2.7a). The measured tracer data are then plotted onto this grid and each sample point is referred to the nearest grid point, revealing an individual mean age, width of the distribution and Γ/Δ-ratio for each measurement (Raimondi et al., 2023; Wefing et al., 2021) (see Figure 2.7b).
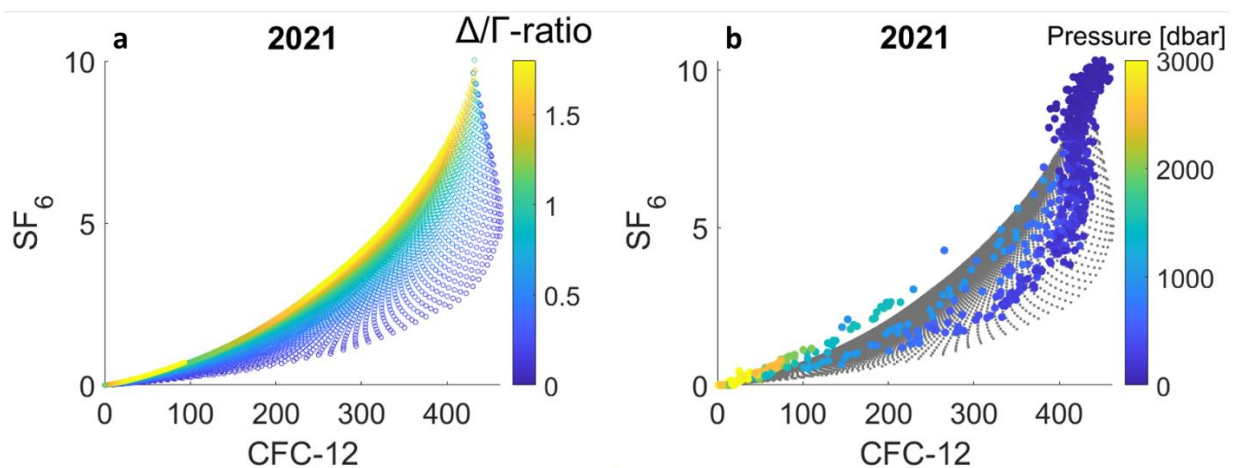
Figure 2.7: (a) A grid of modelled CFC-12 and SF_6 concentration pairs constrained with 'Smith's' TTD method, showing the varying Δ/Γ-ratios within the grid. The saturations used for the tracers were 85 % for CFC-12 and 100 % for SF_6. (b) Display of the same grid in grey, with actual measured tracer concentrations in ocean water samples plotted on top. The colors show the pressure (depth) at which the samples were collected.

2.3.3 2-IG TTD approach

If the assumption of a one-inverse Gaussian distribution is predicted to be not sufficiently accurate to determine the TTD for the analysis of water masses within a specific region, this assumption can be expanded to a two-inverse Gaussian distribution to represent the TTD. This extended approach accounts for the influence of two water masses with similar densities but distinct ages histories on the ventilation of a certain area. The revised approach uses the following equation, including two Green functions (G_1 & G_2) with distinct Γ and Δ values.

$$c(t,r) = \int_0^\infty c_0(t - t')e^{-\lambda t'} * [\alpha * G_1(\Gamma_1, \Delta_1, t', r) + (1 - \alpha) * G_2(\Gamma_2, \Delta_2, t', r)] \, dt' \qquad \textbf{2.5}$$

In addition to the two individual Green functions, this equation includes the input function of each tracer ($c_0(t\text{-}t')e^{-\lambda t'}$) as well as a factor α to calculate the simulated tracer concentrations at a specific location and time ($c(t,r)$). Here, α is the distribution factor between the two water masses, which, in turn, determines the combined mean age of the mixed water mass at that location and time (see equation 2.6).

$$\Gamma = \alpha * \Gamma_1 + (1 - \alpha) * \Gamma_2 \qquad \textbf{2.6}$$

Equation 2.5, which incorporates each tracer's input function along with varying values for Γ_1, Γ_2, Δ_1, Δ_2 and α, yields a matrix of simulated concentrations. This matrix can be constructed for each specific α, Δ_1/Γ_1-ratio and Δ_2/Γ_2-ratio, representing the relationship between two assumed mean ages as a function of the simulated tracer concentrations (see Figure 2.8).
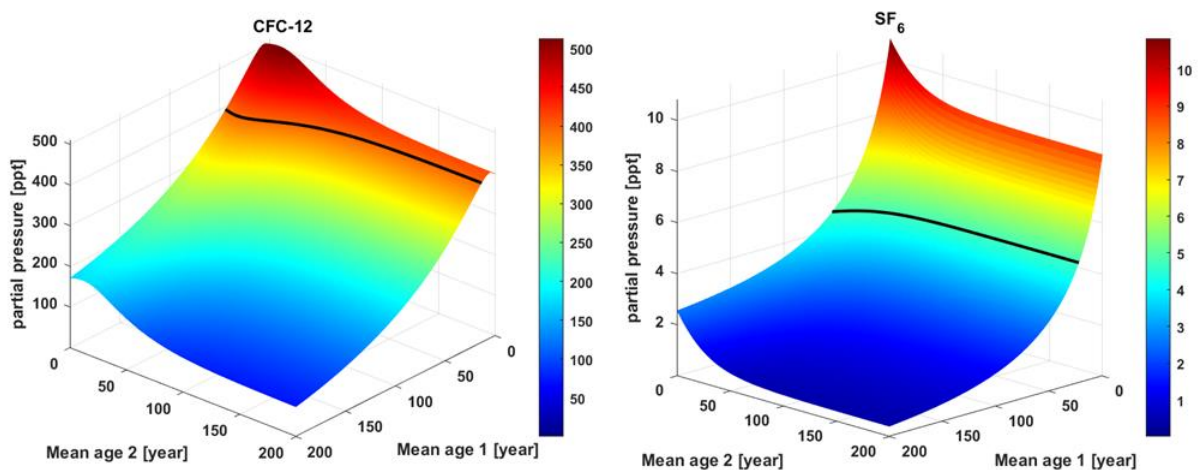
Figure 2.8: Example of mean age matrices for CFC-12 and SF$_6$ with a Δ_1/Γ_1-ratio = 0.9, a Δ_2/Γ_2-ratio = 0.4 and α = 80 %. The black line represents a simulated tracer concentration of 393 ppt and 4.7 ppt for CFC-12 and SF$_6$, respectively.

To effectively apply this method, more than two tracers with distinct input functions are required.

Measurements of multiple tracers then permit to correlate simulated concentrations, which are computed using this method, to actual samples. This involves the application of an Euclidean distance error calculation (Dokmanic et al., 2015) for the correlation, which yields the best match for all measured samples to simulated concentrations corresponding to a specific set of Γ_1, Γ_2, Δ_1, Δ_2 and α values.

Together, employing the TTD method to determine mean ages of water parcels at different depths within a water column permits the assessment of general ventilation time scales and potential temporal changes, and thereby can reveal important information, e.g., on pathways of climate anomalies. In addition, this approach allows to answer the question whether the water transport is predominantly advective or diffusive within specific regions.

Summary of results

The main results of this thesis are presented in three manuscripts; one article accepted for publication, one paper in revision and one manuscript to be submitted.

Manuscript I (Chapter 3) entitled 'Temporal Variability of Ventilation in the Eurasian Arctic Ocean' analyzes the temporal variability of ventilation in intermediate waters (250 - 1500 m) of the Eurasian Arctic Ocean (AO), using CFC-12, SF_6, and oxygen data collected over the last three decades. The results show temporal changes in the ventilation in this region, with a significant decrease between 2005 and 2021. Additionally, evidence for multidecadal variability in ventilation of the intermediate waters is obtained, as higher mean ages are observed in 1991 and 2021 compared to 2005 and 2015.

Gerke, L., Arck, Y. and Tanhua, T., ***Temporal Variability of Ventilation in the Eurasian Arctic Ocean***, *Journal of Geophysical Research: Oceans*, 2024, manuscript accepted for publication.

Manuscript II (Chapter 4) entitled 'Changing composition of the Gulf of St. Lawrence Inflow Waters' analyzes the deep water inflow into the Gulf of St. Lawrence (GSL). With the help of transient tracer data in combination with the TTD, mean ages of the GSL deep water were determined showing ages not matching the regional flow patterns. This can be explained by a recent shift in the composition of the source water entering the GSL, towards a larger fraction of older North Atlantic Central Waters at the expense of younger, more oxygenated Labrador Current Waters. The results also suggest that the deoxygenation of the deep water in the Gulf and St. Lawrence Estuary is likely to increase in the future, as the shift towards less oxygenated, older water is increasingly evident at the entrance point.

Gerke, L., Tanhua, T., Nesbitt, W. A., Stevens, S. W., Wallace, D. W. R., ***Changing composition of the Gulf of St. Lawrence Inflow Waters***, *Geophysical Research Letters*, 2024, manuscript in revision.

Manuscript III (Chapter 5) entitled 'Multiple tracer approach to analyze Arctic Ocean Ventilation' attempts to increase accuracy in the ventilation analysis of water masses in the

AO by using multiple transient tracers, including CFC-12, SF$_6$, and 'Medusa'-tracers (HCFC-22, HCFC-141b, HCFC-142b, and HFC-134a). The results reveal that the 'Medusa'-tracers are suitable for determining ventilation parameters in the Arctic region. Furthermore, they show that reasonable TTD's can be obtained using different tracer combinations. The multiple tracers combined with the concept of a 2-IG TTD identify distinct ventilation patterns in specific areas of the Eurasian AO, specifically, a more advective flow pattern in the upper 1000 m and an increase in the diffusive component in deeper water masses.

Gerke, L. and Tanhua, T., ***Multiple tracer approach to analyze Arctic Ocean Ventilation***, manuscript in preparation.

Additional information and results of this thesis are given in the appendices.

Appendix A expands the analysis on the temporal variability presented in chapter 3 to the Makarov Basin of the AO and the Svalbard Shelf area.

Appendix B discusses the presence of elevated SF$_6$ concentrations measured in 2021 at a certain density interval, which most likely can be attributed to a tracer release experiment in 1991 in the Greenland Sea.

Appendix C presents preliminary results of ^{39}Ar measurements conducted at three stations along the cruise track of the 'SAS-Oden 2021' expedition.

Appendix D shows supporting figures to the main Introduction and the Data and Methods chapters of this thesis.

3. Manuscript I

Temporal Variability of Ventilation in the Eurasian Arctic Ocean

L. Gerke[1], Y. Arck[2], T. Tanhua[1]

1 GEOMAR Helmholtz Centre for Ocean Research Kiel, Kiel, Germany
2 Institute of Environmental Physics, Heidelberg University, Heidelberg, Germany

Temporal Variability of Ventilation in the Eurasian Arctic Ocean

Lennart Gerke[1][*] (https://orcid.org/0000-0002-5783-1070)**, Yannis Arck[2]**

(https://orcid.org/0009-0004-1038-2564)**, Toste Tanhua[1]** (https://orcid.org/0000-0002-0313-2557)

[1]GEOMAR Helmholtz Centre for Ocean Research Kiel, Kiel, Germany

[2]Institute of Environmental Physics, Heidelberg University, Heidelberg, Germany

* Corresponding author: Lennart Gerke (lgerke@geomar.de)

Key Points:

- Temporal variability of ventilation in the Eurasian Arctic Ocean during the past 30 years is estimated by observations of transient tracers
- We found a slow down of the ventilation between 2005 and 2021 in the intermediate waters
- Evidence of multidecadal variability of ventilation in the intermediate waters of the Eurasian Arctic Ocean is present

Abstract

The Arctic Ocean plays an important role in the regulation of the earth's climate system, for instance by storing large amounts of carbon dioxide within its interior. It also plays a critical role in the global thermohaline circulation, transporting water entering from the Atlantic Ocean to the interior and initializing the southward transport of deep waters. Currently, the Arctic Ocean is undergoing rapid changes due to climate warming. The resulting consequences on ventilation patterns, however, are scarce. In this study we present transient tracer (CFC-12 and SF_6) measurements, in conjunction with dissolved oxygen concentrations, to asses ventilation and circulation changes in the Eurasian Arctic Ocean over three decades (1991 to 2021). We constrained transit time distributions of water masses in different areas and quantified temporal variability in ventilation. Specifically, mean ages of intermediate water layers in the Eurasian Arctic Ocean were evaluated, revealing a decrease in ventilation in each of the designated areas from 2005 to 2021. This intermediate layer (250-1500 m) is dominated by Atlantic Water entering from the Nordic Seas. We also identify a variability in ventilation during the observation period in most regions, as the data from 1991 shows mean ages comparable to those from 2021. Only in the northern Amundsen Basin, where the Arctic Ocean Boundary Current is present at intermediate depths, the ventilation in 1991 is congruent to the one in 2005, increasing thereafter until 2021. This suggests a reduced ventilation and decrease in the strength of the Boundary Current during the last 16 years.

Plain Language Summary

The Eurasian Arctic Ocean, the region of the Arctic Ocean connected to the European and Asian continents, is an important pathway for recently ventilated water from the Nordic Seas. These waters are exported back to the North Atlantic following their travel through the Arctic Ocean. Ventilation describes the process of surface waters being transported into the interior ocean due to increasing density, which affects the underlying water masses.

In this study we investigate how the ventilation patterns have evolved in the Eurasian Arctic Ocean over the past three decades, using transient tracer (CFC-12 and SF_6) measurements. We observed a significant change in the intermediate layer (250 - 1500 m) with older waters found in measurements in 1991 and 2021 compared to 2005 and 2015. Moreover, our data suggest a

49 slowdown in ventilation throughout the three decades in the northern Amundsen Basin, implying

50 a decrease in the circulation time-scale of the Arctic Ocean Boundary Current over the past 16

51 years. This has potentially important implications for the transport of, e.g., heat, salt or oxygen

52 from the Atlantic Ocean around the Arctic Ocean, and back.

53

1 Introduction

55 The Arctic Ocean (AO), one of the most rapidly changing environments on earth, has recently

56 garnered significant scientific interest due to the undeniable climate-related changes that are well

57 observable in the Arctic region (e.g. Wassmann, 2015; Woodgate, 2013). As the AO is also of high

58 importance for the climate system, observing and understanding this region has become

59 increasingly relevant. This relates not only to the large ecosystem of the AO, consisting of

60 biological matter from phytoplankton to bigger mammals, but also concerns the global climate for

61 a number of reasons (e.g. Wassmann, 2006; Wassmann, 2011).

62 Most known is probably the sea ice coverage of the AO, which is an important factor of the climate

63 system (e.g. Singarayer et al., 2006). It acts as a shield for the surface water because its white color

64 reflects sun light (high albedo), thereby prevents heat exchange with the atmosphere and restricts

65 the air-sea exchange of gases. Since 1979, sea ice coverage has decreased rapidly at an average

66 rate of 12.8 ± 2.4 % per decade (Meredith et al., 2019; Nghiem et al., 2006), resulting in the AO

67 surface water absorbing more heat. In addition to general global warming, one reason for the

68 decreasing sea ice in the Arctic is the increasing heat flux driven by warm Atlantic Water (AW)

69 flowing towards the AO. Due to its ventilation and circulation patterns (e.g. Fabry et al., 2009;

70 Terhaar et al., 2020), the AO stores a large amount of anthropogenic carbon (2.5 to 3.3 PgC,

71 normalized to 2005 (Tanhua et al., 2009)). Surface water sinks to the interior ocean in the Nordic

72 Seas at latitudes close to Svalbard (~80 °N) (e.g. Jeansson et al., 2023; Karstensen et al., 2005;

73 Mauritzen, 1996; Swift et al., 1980; Talley, 1996), before entering the AO, circulating around and

74 back into the Atlantic Ocean as deep water with higher density due to cooling (e.g. Karcher et al.,

75 2012; Smith et al., 2011). Thereby the carbon dioxide (CO_2), which has been taken up by the water

76 via air-sea gas exchange, is transported within the ventilating water masses and is either stored in

77 the AO or exported with the outflowing deep water (MacGilchrist et al., 2014). This CO_2 uptake

78 is likely to increase due to a larger proportion of the surface ocean being exposed as a result of the

79 melting sea ice (Arrigo & Van Dijken, 2011; Loose et al., 2014). The increasing sea surface
80 temperature (Steele et al., 2008) exacerbated by the decreasing sea ice coverage and the general
81 warming of ocean waters most likely has an influence on the ventilation, circulation and
82 composition of water masses in the AO. Although primary production has already been observed
83 under the sea ice (Arrigo et al., 2012), more exposed surface ocean could further enhance primary
84 production and lead to increased CO_2 uptake. On the other hand, increasing temperatures and a
85 concomitant reduction in vertical mixing could result in a decline of nutrient supply, algae growth
86 and thereby reduced primary production and in general influence seasonal cycles (Lavoie et al.,
87 2010; Slagstad et al., 2015).

88 The AO plays an important role for the global climate and water movement in the world's oceans,
89 mediated through the Atlantic Meridional Overturning Circulation (AMOC). The most northern
90 component of this circulation is found in the AO where it circulates the ventilated AW and exports
91 subsurface and deep waters into the Nordic Seas (Rudels et al., 1994). The AMOC is a component
92 of the global thermohaline circulation, therefore changes occuring in the AO have global impact.
93 Despite the high relevance of these processes, ventilation patterns in the AO and the role of the
94 AMOC in these patterns are still incompletely understood. With the exception of Rajasakaren et
95 al. (2019), who evaluated changes focusing on the anthropogenic carbon uptake, data on
96 ventilation changes over time in the recent period of increased global warming and reduction in
97 sea ice coverage are lacking. Consequently, we attempted to assess such changes in circulation
98 and ventilation patterns in the AO by measuring different key variables throughout the water
99 column. We focused on the distribution of the transient tracers sulphur hexafluoride (SF_6) and
100 chlorofluorocarbon-12 (CFC-12), as they can be utilized to calculate the movement and ventilation
101 of water masses in the ocean. This investigation should shed light on the impact of climate change
102 on the inflowing AW and reveal possible changes occurring in the AO (e.g. Lauvset et al., 2018;
103 Smedsrud et al., 2022).

104 Ventilation is a process that transports signals and perturbations related to gas exchange between
105 the atmosphere and the surface ocean, to the ocean's interior (e.g. Tanhua et al., 2013; Waugh et
106 al., 2006). Thus, it is a measurable parameter for the transport of atmosphere-ocean boundary
107 perturbations, such as temperature, oxygen or CO_2, to the deep ocean. By utilizing the transit time
108 distribution (TTD) concept to quantify ventilation, it is possible to assess ventilation timescales

109 and to obtain knowledge on the ratio between advective and diffusive transports of water masses

110 from the surface into the interior of the ocean (Stöven & Tanhua, 2014; Waugh et al., 2003).

111

2 Hydrographic settings

113 The AO is mainly landlocked, with connections to the Pacific Ocean via the shallow Bering Strait

114 (50 m) and to the Atlantic Ocean via the deeper Fram Strait (2600 m), the shallow Barents Sea and

115 the Canadian Arctic Archipelago. Volumetrically, the main water inflow into the AO is almost

116 completely composed of AW (90 % (Woodgate, 2013)). This water enters via two branches that

117 are combined at the St. Anna Through with one branch flowing throught the Fram Strait (Fram

118 Strait Branch Water (FSBW)) and the other through the Barents Sea (Barents Sea Branch Water

119 (BSBW)) (e.g. Rudels et al., 1994; Woodgate, 2013).

120 Several ocean ridges divide the Central AO into a number of different ocean basins. First and

121 foremost, the Lomonosov Ridge, separates the Eurasian Basin from the Amerasian Basin. The

122 Eurasian Basin is located on the European/Asian side of the Arctic and the Amerasian Basin on

123 the American/Asian side. Within the Eurasian Basin, the Gakkel Ridge separates the Nansen Basin

124 from the Amundsen Basin, and the Amerasian Basin is divided into the Makarov and Canada Basin

125 by the Alpha and Mendeleev Ridges (see Figure 1a).

126
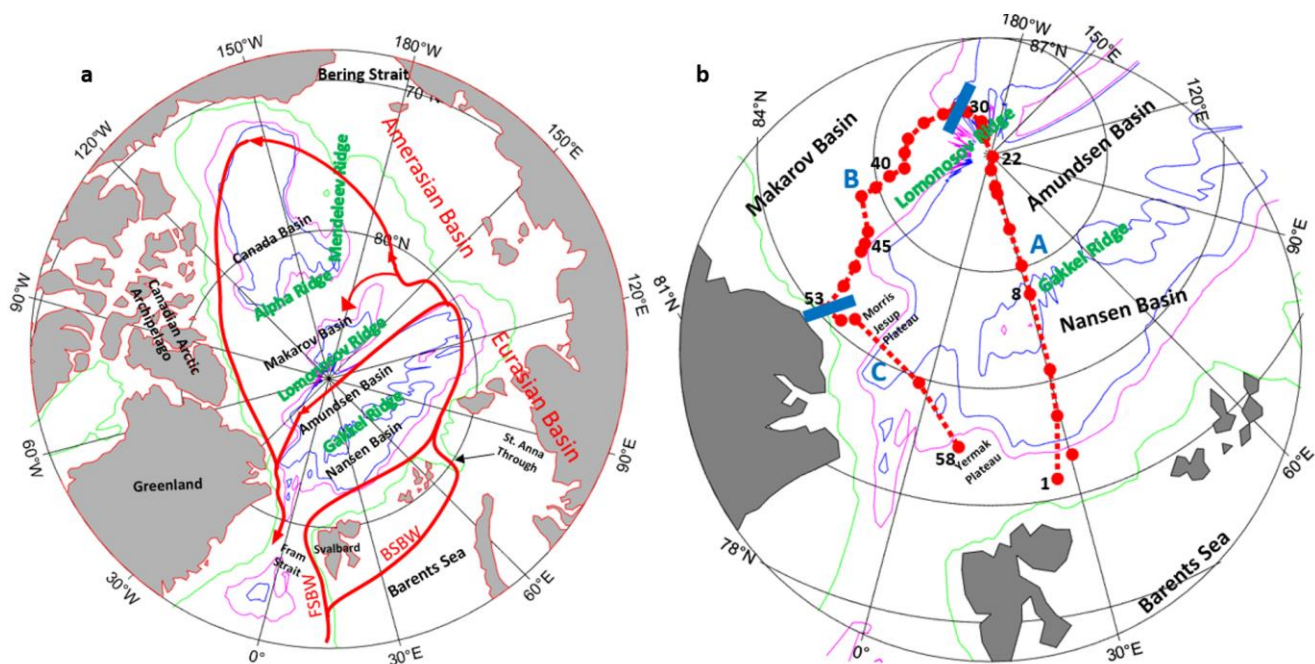
127

128   **Figure 1.** (a) The AO and its individual basins divided by ocean ridges with contour lines at 500 m (green),

129   3000 m (magenta) and 3500 m (blue). The red arrows show a simplified Atlantic Water (AW) circulation

130   in the AO. (b) Map of the SAS-Oden 2021 expedition with the red dots indicating CTD stations, separated

131   into sections A, B and C by the blue lines at station 30 and 53. In this study we focus only on section A

132   crossing the Nansen and Amundsen Basin.

133

134   The AO has a volume of approximately 18,750,000 km^3 (Eakins & Sharman, 2007), which

135   accounts for ≈ 1 % of the total world's oceans. Roughly 53 % of the AO lies over extensive

136   continental shelves (Jakobsson, 2002). The AO serves an important role in the earth's response to

137   rising CO_2 levels as up to 2 % of all anthropogenic carbon is stored within Arctic waters, thus

138   acting as a larger sink than anticipated from its volume (Tanhua et al., 2009). Recently, studies

139   have shown that the CO_2 uptake in the AO has increased even further (4-8 % of the global CO_2

140   uptake) and thereby its role in counteracting climate change has grown significantly (DeVries et

141   al., 2023; Yasunaka et al., 2023).

142   Historically, AO research was hampered due to heavier ice conditions, especially during winter.

143   Recently, however, the rapid decline in the sea-ice coverage in the AO (Meredith et al., 2019), has

144   made research in this region more accessible. Although more extensive sampling has been

145   conducted than in other areas, e.g. the South Pacific or the Southern Ocean, the AO is still a region

146   where data are relatively scarce. This is due to seasonal limitations on when research is feasible

147   (summer months), and the small number of suitable research vessels (i.e. research icebreakers).

148

149   **2.1 Water masses and circulation**

150   Four different water mass layers are present in the Eurasian AO: surface, halocline, Atlantic, and

151   deep.

152   The wind driven surface layer primarily circulates horizontally. Nonetheless, vertical mixing is

153   likely to increase in the surface layer due to decreasing sea-ice coverage and increasing freshwater

154   input (Frolov et al., 2005; Nansen, 1902; Pfirman, 2004; Rigor et al., 2002). The surface layer is

155   characterized by near freezing temperatures and a high freshwater content from river runoff,

156   precipitation and iceberg calving (Ekwurzel et al., 2001; Haine, 2021). The halocline layer forms

157   via vertical movement of dense and saline shelf water produced during freezing and initiates a

158   barrier between the surface water and the AW, preventing an upward heat flux (Aagaard et al.,

159 1981; Bauch et al., 2014). The circulation of AW, as part of the Arctic Ocean Boundary Current

160 (AOBC), is both the main and best studied circulation in the AO. It occurs at a depth between 250

161 and 800 m (Atlantic layer), mainly following the ocean ridges (see Figure 1a, red arrows)

162 (Aagaard, 1989; Aksenov et al., 2011; Rudels et al., 1999). The AW enters the AO both west and

163 east of Svalbard through the Fram Strait (FSBW) and Barents Sea (BSBW), respectively. It

164 proceeds in a counter clockwise rotation around the entire AO at depths between 250 and 1500 m,

165 where it is referred to as mid-depth Atlantic layer (Karcher et al., 2012; Rudels et al., 1994; Wefing

166 et al., 2021). On the Amerasian side, some AW enters the Makarov Basin, while a larger fraction

167 flows around the Canadian Basin, circulating back along the Canadian Arctic Archipelago. Most

168 of the AW flows back towards the east Greenland shelf already on the Eurasian side along the

169 Gakkel and the Lomonosov Ridges, becoming increasingly dense due to mixing with colder

170 ambient water masses. After circulating within the AO, the AW flows south through the Fram

171 Stait, as part of the East Greenland Current, and enters the Atlantic Ocean as part of the dense

172 Denmark Strait Overflow Water (DSOW) (Swift & Aagaard, 1981; Tanhua et al., 2005b). This

173 completes the AOBC within the central AO. The transport of AW from the Barents Sea through

174 the AO and back into the Nordic Seas at the Fram Strait is estimated to take approximately 15

175 years when circulating within the Eurasian AO and up to 30 years via the Canadian side (Karcher

176 et al., 2011; Smith et al., 2011). The deep water layers of the AO (below 1500 m) ventilate via

177 boundary convection processes that transport brine-enriched water formed at the shelfs into the

178 deep basins (Aagaard & Carmack, 1989; Anderson et al., 1999; Wallace et al., 1992). This

179 ventilation was observed to be slower on the Amerasian side, showing deep water mean ages that

180 are approximately 100 years older than on the Eurasian side (Tanhua et al., 2009). Nonetheless,

181 this deep water layer is difficult to examine properly due to increasing uncertainty in the age

182 determination, which is a consequence of the low concentrations measured at these depths of our

183 selected tracers in this study. Therefore, this work focusses solely on the intermediate depths

184 between 250 and 1500 m.

185

186 3 Materials and Methods

187 3.1 Chronological transient tracers

_____

188   Based on temporally varying atmospheric concentrations, chronological transient tracers (tracers

189   that have no sources or sinks within the ocean (Stöven & Tanhua, 2014)), such as CFCs and SF_6,

190   can be used to estimate the age of a water parcel and help understand ventilation and circulation

191   processes in the ocean (Fine, 2011). The input function of a tracer dissolving in surface water via

192   air-sea gas exchange is based on its solubility (a function of temperature, salinity, and the physical

193   nature of the molecule), the degree of saturation, and the variation of its atmospheric concentration

194   over time. CFCs and SF_6 are conservative in seawater, and thanks to measurements over time

195   (Bullister & Warner, 2017; Walker et al., 2000), together with production estimates, atmospheric

196   concentrations of these gases are well known. Therefore, they are extremely useful to estimate

197   rates and pathways of ocean circulation and mixing processes as well as rates and variabilities of

198   water mass formation (Fine, 2011). In this paper, we focus on two tracers, CFC-12 and SF_6, first

199   produced and released to the atmosphere in the late 1940s and early 1960s, respectively (Maiss &

200   Brenninkmeijer, 1998; Walker et al., 2000). Due to the regulation of CFC-12 production in 1990

201   (Montreal Protocol, 1987), its atmospheric concentration started to decrease by 2002.

202   Consequently, CFC-12 becomes an increasingly limited tracer for young water masses as the

203   measured concentration is inconclusive, represented by the cut-off area in Figure 2. In contrast, as

204   the SF_6 atmospheric concentration is steadily increasing, it is the preferable tracer for younger

205   water.

_____
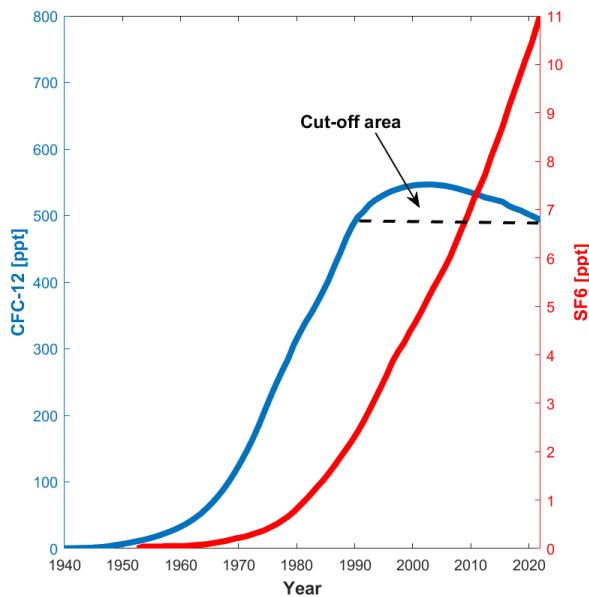
Figure 2. Atmospheric concentrations of the two transient tracers used in this study (Bullister & Warner, 2017). CFC-12 (blue) and SF_6 (red), both tracer concentrations in ppt (parts per trillion). The dashed line represents the cut-off area of inconclusive translation of concentrations to ventilation ages.

Since there is a significant global data set of CFC-12 observations, recent monitorings are helpful for comparison with older data (Fine, 2011) in order to detect temporal variability of ventilation, and CFC-12 provides useful information on older water masses due to higher concentrations in seawater and atmosphere compared to SF_6. In addition, using a tracer couple (e.g. CFC-12 and SF_6) provides the ability to constrain a TTD and thereby add valuable information in understanding the ventilation patterns in the water column.

Transient tracer concentrations in water are often reported as partial pressure values with units in ppt (parts per trillion). This eliminates the effect of changing temperature and salinity on the tracer solubility and allows for direct comparison to atmospheric concentrations (Bullister et al., 2002; Warner & Weiss, 1985).

3.2 Contemporary data

Samples were collected during the "SAS-Oden 2021" expedition on the Swedish icebreaker Oden (see Figure 1b). The cruise contributed to the Synoptic Arctic Survey (SAS), which consisted of 29 expeditions carried out in the AO spanning years 2020-2022. The SAS focused on three major

226   research areas: (1) Physical drivers of importance to the ecosystem and carbon cycle, (2) the

227   ecosystem response, and (3) the carbon cycle and ocean acidification (Snoeijs-Leijonmalm &

228   Party, 2022).

229   The cruise took place in 2021 between July 24th and September 20th. Starting just north of Svalbard

230   (81.5 °N, 30 °E), the Nansen and Amundsen Basins were crossed until reaching 89 °N and

231   150 °W, i.e. shortly past the Lomonosov Ridge in the Makarov Basin (Section A – Figure 1b).

232   This was followed by a short section parallel to the Lomonosov Ridge in the Makarov Basin before

233   reaching a previously unstudied area close to the north coast of Greenland (Section B – Figure 1b).

234   Finally, the vessel then sailed a direct route from the Morris Jesup Plateau to the Yermak Plateau

235   (Section C – Figure 1b). This study focuses on the first section (Section A) as we can compare

236   data obtained here to historical observations to evaluate temporal changes.

237

238   **3.3 Historical data**

239   The data collected along Section A in 2021 were compared with data included in the data product

240   GLODAPv2.2021 (Global Ocean Data Analysis Project version 2) (Lauvset et al., 2021). We

241   extracted transient tracer data from three earlier years (1991, 2005 and 2015) from locations

242   proximal to Section A of the SAS-Oden cruise having transient tracer data (see Figure 3 and Table

243   1).

244   **Table 1.** Information on the cruises from the repeats in 1991, 2005 and 2015.

Cruise Name	Year	Ship	Chief Scientist	Transient Tracer PI	Expocode	References
Oden-91	1991	Oden	L. Anderson	P. Jones	77DN19910726	(Anderson et al., 1994) (Anderson & Party, 1998)
ODEN05	2005	Oden	A. Karlqvist	T. Tanhua	77DN20050819	(Karlqvist & Party, 2010)
TransArc-II	2015	Polarstern	U. Schauer	M. vd Loeff	06AQ20150817	(Schauer & Party, 2016)

245

246

_____
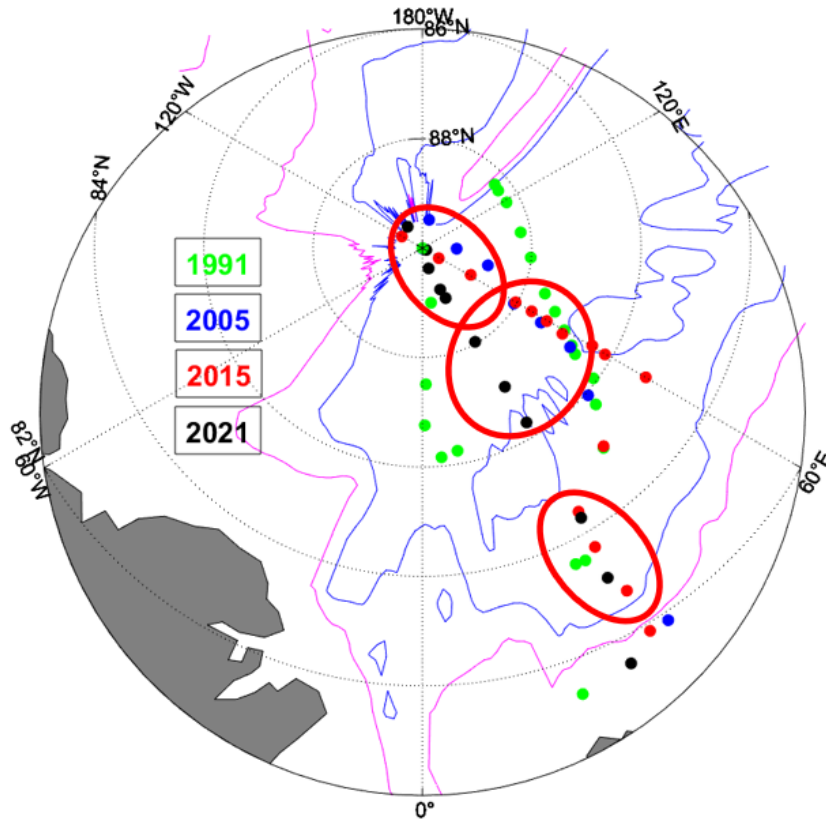
247

248 **Figure 3.** CTD stations at locations similar to those of SAS-Oden in 2021 (black): 1991 (green), 2005

249 (blue) and 2015 (red). Only stations where samples for transient tracer analysis were taken are shown. The

250 contour lines display depths of 3000 m (magenta) and 3500 m (blue), showing the deep basins, the Gakkel

251 Ridge, and the Lomonosov Ridge. The red circles indicate the stations included in each area analyzed.

252

253 **3.4 Analysis method**

254 During the SAS-Oden cruise, the two transient tracers CFC-12 and SF_6, were measured on-board

255 using a gas chromatographic – electron capture detector system in combination with a purge and

256 trap unit (Bullister et al., 2002; Snoeijs-Leijonmalm & Party, 2022; Tanhua et al., 2005a; Tanhua

257 et al., 2004). Water samples were drawn from Niskin bottles in 250 mL glass syringes and briefly

258 stored in a 0 °C water bath to prevent outgassing prior to measurement. For the analysis

259 approximately 200 mL of the 250 mL water sample were injected into the purge and trap unit,

260 while being devoid of atmospheric contamination. Using nitrogen as a carrier gas, the samples

261 were purged and the analytes were trapped on a column consisting of 100 cm 1/16" tubing packed

262 with 70 cm Heysep D. Suspended over liquid nitrogen, the trap was kept at a temperature of -60

263 to -70 °C. The trap was subsequently desorbed by heating to 100 °C whereby the analytes were

264 separated within a pre-column, consisting of 30 cm Porasil C and 60 cm Molsieve 5A followed by

265 a main column of 200 cm Carbograph 1AC and 20 cm Molsieve 5A. The columns were kept

266 isothermal at 50 °C and detection was performed with the Electron Capture Detector (ECD).

267 Calibration was carried out by injecting small volumes of a gaseous standard containing SF_6 and

268 CFC-12, which was obtained from the company Deuste-Steiniger (Germany). Prior to the mission,

269 this standard was calibrated against and referenced to the SIO (Scripps Institution of

270 Oceanography) calibration scale in the lab at the GEOMAR (Kiel). In addition to a full calibration

271 curve, which was recorded every 2 weeks, point calibrations were performed at every station to

272 quantify detector drifts.

273 The system has a detection limit of 0.04 fmol/kg for SF_6 and 0.2 fmol/kg for CFC-12 and provided

274 data with a precision of 0.03 fmol/kg (2.6 %) and 0.02 pmol/kg (1.5 %) for SF_6 and CFC-12,

275 respectively. Analytic precision was determined from duplicates measured throughout the mission

276 at various depths and locations. Considering the precision and detection limit of the system, the

277 limit of quantification was set to 0.1 ppt for CFC-12 and 0.3 ppt for SF_6, respectively (three times

278 the detection limit).

279 Transient tracer measurements acquired during the historical cruises in 1991 and 2005 were

280 conducted with the help of similar on-board purge and trap gas chromatographic systems.

281 However, in these measurements, samples with a volume of $\approx$ 30 ml were analyzed, potentially

282 resulting in lower precision and higher detection limits as compared to 2021, in particular for

283 waters with low concentrations of the tracers. In 2015, samples were drawn from the Niskin bottles

284 and after being stored, measured in the laboratory back on shore. Here, the samples were also

285 measured with a GC-ECD system in combination with a purge and trap unit. In contrast to the

286 2021 methodology, samples were split into two aliquots to measure each gas individually. Separate

287 gas lines and separate ECDs were used with one 30 ml sample for CFC-12 and one 200 mL sample

288 for SF_6 (Smith et al., 2022).

289

290 **3.5 Transit Time Distribution (TTD)**

291 The transit time distribution (TTD) method (Hall & Plumb, 1994) is used to calculate the mean

292 age of a water parcel. It statistically describes an age distribution of a water mass in the ocean's

293 interior and thereby gives information on the time it was last in contact with the atmosphere. It

294 includes not only the constant advective velocity but also the diffusive processes, which transport

295 water from the surface to the ocean's interior.

296 The TTD method is based on Green's function (Eq. 1). The concentration of a single tracer at a

297 specific location and at a given time ($c(t_s,r)$) is calculated via the boundary concentrations, which

298 are related to the input function multiplied by Green's function ($G(t,r)$).

299

300
$$c(t_s,r) = \int_0^\infty c_0(t_s - t)e^{-\lambda t} \times G(t,r)dt \qquad \textbf{1}$$

301

302 Including the following assumptions of (1) a steady state, (2) a single surface source region

303 dominating, (3) no changes in the concentration due to inner water interactions, and (4) assuming

304 a one-dimensional flow, one solution to Green's function is the inverse Gaussian TTD (IG-TTD)

305 (Eq. 2) (Khatiwala et al., 2001; Schneider et al., 2012; Sonnerup et al., 2013; Stöven & Tanhua,

306 2014; Waugh et al., 2002). Here the ratio of mean age (Γ) to the width of a distribution (Δ) over a

307 specified time range is analyzed in more detail. This ratio provides information on the share of

308 advection and diffusion, determining the shape of the TTD. A Δ/Γ-ratio < 1 describes

309 predominantly advective ventilation, whereas a Δ/Γ-ratio > 1 suggests more diffusive ventilation.

310 The validity of the IG-TTD has been evaluated by various studies (e.g. Shao et al., 2016), e.g. by

311 using the Bayesian statistical method and comparing the TTD results to model-based solutions on

312 the ventilation (Trossman et al., 2012; Trossman et al., 2014).

313

314
$$G(t) = \sqrt{\frac{\Gamma^3}{4\pi\Delta^2 t^3}} \times \exp(\frac{-\Gamma(t-\Gamma)^2}{4\Delta^2 t}) \qquad \textbf{2}$$

315

316 In this study we compare the mean age relationship of two tracers with significantly different input

317 functions sampled concurrently at the same location.

318 To define the input function, an estimate of the saturation in the surface water of each tracer is

319 required. It is difficult to obtain this information on this in the AO due to sea ice coverage, which

320 introduces biases in saturation times when comparing surface water concentrations to atmospheric

321 concentrations. As we focus our analysis on the intermediate water, which consists mainly of AW

322 entering from the Greenland Sea and last being in contact with the atmosphere at this location, we

323 utilized the historic surface saturations estimated in the Greenland Sea by Jeansson et al. (2023)

324   for our analysis. Jeansson et al. (2023) estimated that the saturation varies over time by analyzing

325   samples just below the summer thermocline, to reduce biases araising from seasonal

326   summer/winter variations. Due to the availability of historical CFC-12 measurements in the

327   Greenland Sea, a time-dependent saturation was established for this tracer. We used the observed

328   temporal variability of CFC-12 surface saturation on the atmospheric concentration to calculate

329   the input function of the tracer at the ocean surface during wintertime. The same time dependency

330   was applied for the SF_6 saturation, as Jeansson et al. (2023) were not able to constrain an individual

331   time dependency due to an uncertainty caused by a SF_6 tracer release experiment in 1996 in the

332   Greenland Sea (Watson et al., 1999).

333   To determine the Δ/Γ-ratio, we calculated mean ages from CFC-12 and SF_6 measurements using

334   various ratios and the saturation listed above to have a detailed look on their relationship. The

335   measured tracers (CFC-12 and SF_6) only show comparable estimates of mean ages for depths from

336   250 to 3000 m. Below 3000 m (approx. 400 years) the SF_6 measurements and corresponding mean

337   ages reach their quantification limit. Conversely, above 300 m (approx. 15-20 years) the declining

338   atmospheric concentration of CFC-12 influences values in the surface waters (see Figure S1a).

339   The analysis shows that the best constrained TTD for the intermediate water column is obtained

340   when using a Δ/Γ-ratio = 1.0. Some ratios bias calculated mean ages based on SF_6 (CFC-12) low

341   (high) values, e.g. Δ/Γ-ratios < 1.0 tend to show more mean age values of lower SF_6 and higher

342   CFC-12 and Δ/Γ-ratios > 1.0 exhibit the opposite trend, each of which imply suboptimal

343   comparability (see Figure S1b).

344   As we were able to constrain mean ages from both tracers in 2021, we used those calculated from

345   CFC-12 data if the measured concentrations were below 410 ppt (approx. 23 years of mean age).

346   Conversely, for samples showing higher CFC-12 concentrations (i.e. younger waters), we utilized

347   mean ages from corresponding SF_6 concentrations. For the years 1991, 2005 and 2015, mean ages

348   were solely calculated from CFC-12 concentrations, due to a lack of SF_6 measurements. Assuming

349   the shape of the TTD remained unchanged with time, the Δ/Γ-ratio = 1.0 was adopted for all years.

350

351   **3.6 Apparent Oxygen Utilization (AOU)**

352   Another parameter to analyze ocean ventilation, and assess changes in ventilation, is the apparent

353   oxygen utilization (AOU). AOU is calculated by subtracting the measured oxygen concentration

354   from the calculated saturation concentration. The main advantage AOU has over the CFC-12 and

355 SF_6 derived water mass ages is its time independency of the surface water concentrations. AOU

356 can be used as a ventilation tracer, under the assumption that its surface concentration, saturation,

357 and biological activity does not change with time, so that a decrease or increase in AOU in the

358 interior is a sign of changes in ventilation. For example, an increase in AOU at specific depths

359 over the years (i.e. decrease in oxygen), would suggest a decrease in ventilation and vice versa.

360

361 **3.7 Uncertainties**

362 The uncertainty in the derived mean ages, which are used to analyze ventilation changes over the

363 last three decades, arise from several sources. These include errors in the measurements of the

364 transient tracer concentrations, the uncertainties in constraining the TTD, and uncertainties in the

365 input function (i.e. atmospheric concentration and saturation level during winter). The uncertainty

366 in the transient tracer concentration include analytical uncertainties of the measurements. These

367 represent systematic biases during calibration routines (using values of a calibrated standard gas,

368 calibrated standard loops and temperature and pressure measurements) ($\approx$ 1 %), and precision

369 errors ermerging from factors such as the determined purge efficiency (for CFC-12: $\approx$ 2 %) (Stöven

370 & Tanhua, 2014).

371 The uncertainty in the atmospheric concentration has a bias of < 1 %, resulting from the use of a

372 mean atmospheric concentration derived from measurements across different facilities in the

373 northern hemisphere (Walker et al., 2000). Additionally, for the measurements in the AO, we used

374 a saturation determined in the Greenland Sea rather than directly from the sampling area.

375 Uncertainties in the saturation pose a potentially significant error in tracer applications (Raimondi

376 et al., 2023; Shao et al., 2013). Nevertheless, the saturation typically varies over time at higher

377 latitudes due to fluctuations in the winter mixed layer depth and the atmospheric growth rate of

378 the tracers (Jeansson et al., 2010; Tanhua et al., 2008). As reported by Rajasakaren et al. (2019),

379 mean saturation for CFC-12 were estimated to be 93 % $\pm$ 10 % and for SF_6 at = 85 % $\pm$ 9 % in the

380 AO. Comparing this to the data analyzed in 2021, where we evaluated the mean surface saturation

381 from water samples of the upper 20 m, we calculated slightly different saturations (CFC-12 =

382 87.7 % $\pm$ 2.8 % and SF_6 = 86 % $\pm$ 3.7 %). Another factor of uncertainty is the non-linearity in the

383 solubility of the tracers, as they are affected by mixing with different water masses in different

384 ways. Collectively and consistent with previous reports, we estimate that the input function

385   contribute a bias in the calculations of up to 10 % (DeGrandpre et al., 2006; Haine & Richards,

386   1995; Stöven & Tanhua, 2014; Tanhua et al., 2008).

387   The challenge in constraining the TTD adds another source of uncertainty to the calculation of

388   mean ages. While we assume that the TTD follows an Inverse Gaussian (IG) distribution, the actual

389   distribution may deviate, especially considering the mixing of various water masses with different

390   histories. For the IG distribution, the selection of a specific Δ/Γ-ratio represents another factor of

391   uncertainty, as the value between advective and diffusive flows are set. A Δ/Γ-ratio of 1 has often

392   been used in previous studies and has therefore been adopted many times. This, however, is usually

393   due to difficulties of constraining the correct ratio (Tanhua et al., 2008; Waugh et al., 2004). Smith

394   et al. (2011) proposed a changing Δ/Γ-ratio, particularly ≤ 1 for the AW, and also questioned

395   whether the TTD might differ from an inverse Gaussian function within the AO. Rajasakaren et

396   al. (2019) reported that the Δ/Γ-ratio differs between the Amerasian and Eurasian Basins and

397   among water masses. On the Eurasian side, a Δ/Γ-ratio of 1 for the AW was constrained, but the

398   Δ/Γ-ratio for the water masses below could not be defined. Conversely, on the Amerasian side, the

399   Δ/Γ-ratio for all water masses was determined to have a mean value of 1.2. Limitations exist in

400   using the TTD approach to estimate changes in ventilation, such as it requires, for instance, steady-

401   state transport and a single source region. However, the approach yields a framework that permits

402   a comparison of historical surveys on a standardized scale (i.e. the mean age). The bias of using a

403   specific Δ/Γ-ratio is shown in the results, by displaying errorbars in the profile plots, depicting the

404   differences in the calculated mean ages when using a ratio of 0.8 or 1.2.

405   Moreover, given that transient tracer data are only available from four years (1991, 2005, 2015,

406   2021) within a 30-year time span, an uncertainty in evaluating temporal changes due to scarcity of

407   data, in particular in the period between 1991 and 2005, needs to be taken into consideration.

408   The potential uncertainty arising from varying sampling locations, due to fluctuating sea ice

409   coverage and possible eddies, was mitigated by focusing the analysis only on the intermediate

410   layer and selecting areas where multiple stations were sampled within the same basin.

411   Furthermore, the results of stations sampled each year were averaged. This was performed

412   similarly to the manually generated crossover analysis used in GLODAP (Tanhua et al., 2010),

413   by averaging all stations from one cruise in a defined area to one depth profile, and then comparing

414   to data in this same area from another year. By focusing solely on the intermediate layer, the

415   uncertainty due to varying sea ice coverage was addressed, as the surface layer does not directly

416   affect the intermediate layer. This water mass primarily consists of water originating in the Nordic

417   Seas, where sea ice does not have an influence.

418   Uncertainties affecting AOU changes are likely dominated by the assumption of a constant

419   equilibrium of the sea surface and constant biology over time, which is not necessarily the case

420   (Olsen et al., 2010). Temporal variability in the AOU is not always a sign of ventilation changes,

421   but could also be caused by changes in, e.g., respiration rates. To account for this uncertainty, we

422   calculated the standard deviation at each depth across all samples measured in each selected area

423   each year, yielding a value of approximately 5 %.

424

425   **3.8 Analysis of temporal variability**

426   To estimate ventilation changes in the intermediate layer (250 - 1500 m) during the last decades,

427   the observed mean ages in the AO were compared. The water layer below 1500 m was excluded

428   due to the quantification limit mentioned above and the upper 250 m were not taken into account

429   due to the uncertainty in the mean ages calculated from CFC-12 measurements (dashed lines in

430   Figures 5-7 and S3). Apart from analyzing each sample at certain depths within the designated

431   area throughout the years the average mean ages (average profile of all profiles in this area) of

432   each year were compared to the average mean ages in 2021 (see Figure 5 - right panel). Here the

433   relative difference, i.e. average mean age X/average mean age 2021, was calculated and shifted,

434   by subtracting all values by one, so that values < 0 indicates a slower ventilation in 2021 in

435   comparison to the historical cruise in year X, and vice versa.

436   As the different cruises followed slightly different cruise tracks towards the Lomonosov Ridge

437   (mostly due to variable ice-conditions), it is difficult to compare the observations along a section.

438   Therefore, we divided the Eurasian Basin into three different areas, characterized by a number of

439   stations in the different years and compared them using profile plots (see Figures 5-7, S3). By

440   calculating an average of all stations in each area, we overcome the issue of small Eddies in the

441   AO effecting the results. The three designated locations are: (1) the Nansen Basin, (2) the southern

442   Amundsen Basin, and (3) the northern Amundsen Basin. The Nansen Basin was not subdivided

443   into a southern and northern section due to scarcity of observations.

444

_____

445 **4 Results and Discussion**

446 **4.1 General ventilation pattern**

447 Before evaluating possible temporal variability in the ventilation, we provide information on the

448 general ventilation patterns based on the 2021 tracer measurements along the section from

449 Svalbard to the North Pole and into the Makarov Basin (see Figures 4a,b).

450

451 **Figure 4.** Distribution of the partial pressure of (a) CFC-12 and (b) SF_6 along Section A of the 2021 Oden

452 cruise. The upper panel of each plot shows the upper 1500 m, while depths below 1500 m are shown in the

453 lower panel. The red line in (b) at 0.3 ppt represents the quantification limit for SF_6 concentrations. (c)

454 Distribution of the calculated mean age along Section A of the 2021 cruise. In all plots the station numbers

455 are displayed on top in black and the white dots within each plot represent the sampling depths.

456

457 CFC-12 is detected at all depths, but show low partial pressure values (< 50 ppt) below about

458 2000 m, particularly in the Makarov Basin (10 ppt at 2000 m) (see Figure 4a). Here, the

459 concentration in the deep water is significantly lower compared to what is found in the deep water

460 in the Nansen and Amundsen Basins. This indicates a slower deep water ventilation on the

461 Amerasian side of the Lomonosov Ridge as compared to the Eurasian side, as previously noted by

462 Macdonald & Carmack (1991) and Jones et al. (1995). This is also reflected in the calculated mean

463 ages (see Figure 4c), where very old water is present in the Makarov Basin. It is important to note

464 that the calculations only display ages up to a depth of 2500 m, as the tracers used in this study

465 cannot effectively quantify water ages beyond this depth due to its old age, i.e. CFC-12

466 concentrations are close to the limit of quantification. Although we could estimate the mean age

467 of all waters in the Nansen and Amundsen Basins, we refrain from using these deep water data to

468 estimate temporal variability of ventilation, due to the high uncertainties at these depths.

469 At depths above 1500 m (upper panels), higher concentrations of SF_6 are found on the Eurasian

470 side of the Lomonosov Ridge and near the southern end of the section, close to Svalbard. This

471 distribution is the characteristic of the AOBC, with AW entering close to Svalbard from the Nordic

472 Seas and flowing in a counter clockwise circulation back along the Lomonosov Ridge (Coachman

473 & Barnes, 1963; Rudels et al., 1999; Wefing et al., 2021). This AW is also visible in the

474 temperature profile (see Figure S2), with higher temperatures being measured in these areas. Along

475 its path, the AW expands its vertical extent due to mixing: it enters the AO at depths between

476 150 m and 300 m while it penetrates to depths of 1000 m close to the North Pole. The cooling

477 resulting from mixing with colder ambient waters is evident in the temperature section as well,

478 with measured values of approximately 1 °C near the Lomonosov Ridge and > 2 °C at the entrance

479 close to Svalbard. The mean ages of this intermediate water at the shelf and near the North Pole

480 show values of 10 years and approximately 20 years, respectively, suggesting a 10-year transit

481 time for the water transported within the AOBC. This fits precisely with the transport rates reported

482 by Smith et al. (2011).

483   In general, we observed ages of more than 50 years below 900 m near Svalbard and in the Makarov

484   Basin, whereas water in the Amundsen Basin exhibits mean ages of maximally 30 years at these

485   depths.

486   The generally low tracer concentrations and corresponding old mean ages in the bottom waters in

487   all three basins, coupled with a steady decrease from surface to bottom indicate slow ventilation

488   and show that the AOBC does not reach these bottom waters to a significant extent. The deep

489   water is most likely formed by boundary convection processes that transport brine-enriched water

490   formed at the shelfs into the deep basins (Aagaard & Carmack, 1989; Anderson et al., 1999;

491   Tanhua et al., 2009; Wallace et al., 1992).

492

493

494   **4.2 Temporal variability of ventilation in the intermediate layer**

495   Here we present a detailed analysis of the temporal variability of ventilation in specific areas within

496   the Eurasian AO, focusing on intermediate depths (250 - 1500 m). We assessed changes by

497   analyzing variations in calculated mean ages and differences in AOU considering measurements

498   conducted over three decades (1991-2021).

499

500

_____
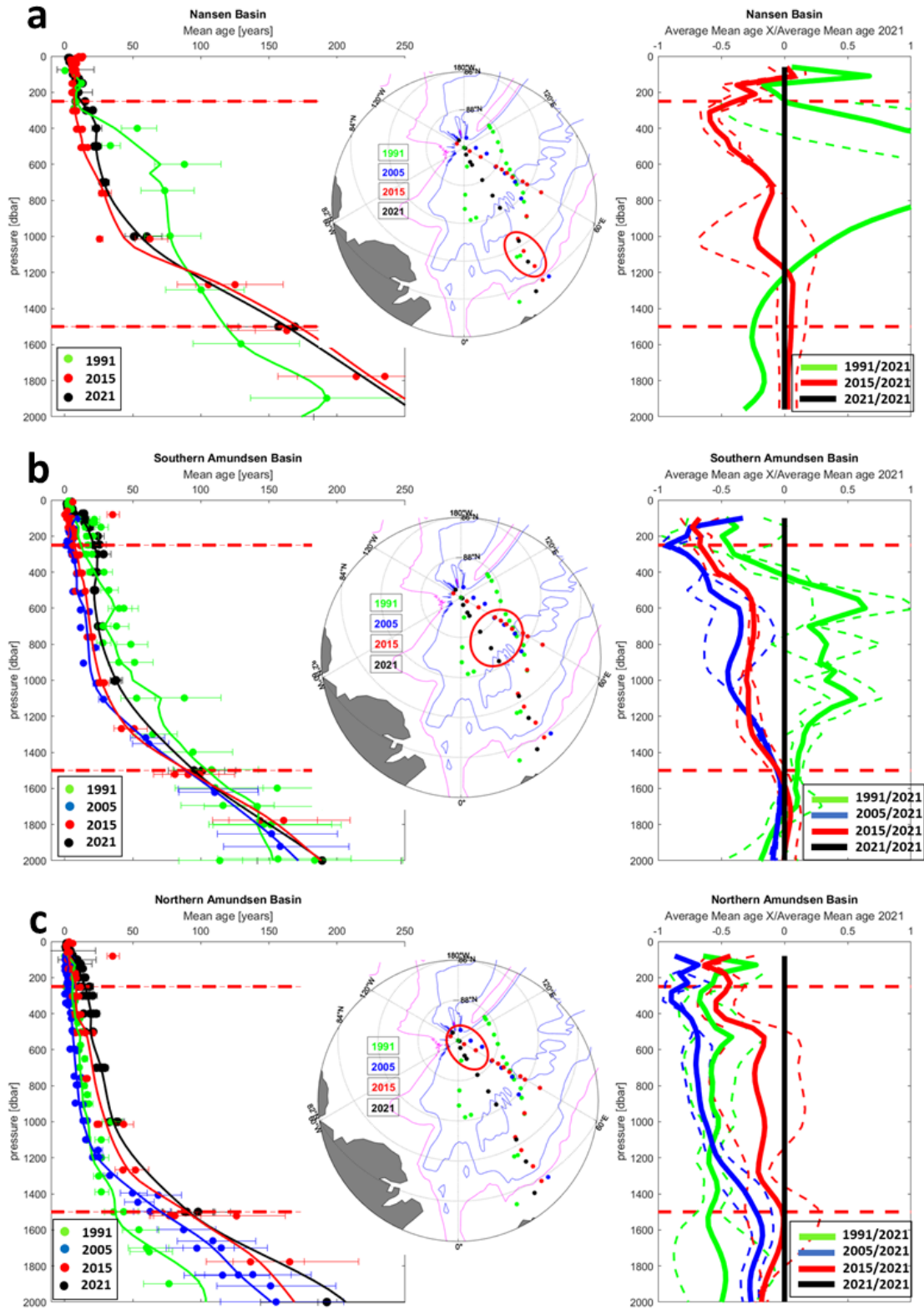
Figure 5. Mean age comparison of stations from year X: 1991 (green), 2005 (blue), 2015 (red) and 2021 (black) in (a) the Nansen Basin, (b) the southern Amundsen Basin and (c) the northern Amundsen Basin. The left figures show data points from each station and depth above 2000 m in the respective basin, with the mean values demonstrated by the solid lines. The right figures show the average relative mean age difference with respect to the data from 2021, with the dashed lines showing the standard deviation of the crossover analysis used for computing the mean values. The dashed red lines represent the focus area of this study, the intermediate layer (250 - 1500 m).

4.2.1 Nansen Basin

In the Nansen Basin we compared data from five stations from 1991 and 2015 to data from two stations in 2021 (see Figure 5a).

The mean age in 2021 is higher at depths between 250 and 1200 m (except around 700 m) compared to the mean ages observed in 2015, indicating a ventilation decrease within these six years in the intermediate waters of the Nansen Basin. In 1991, waters between about 300 and 1000 m depth are significantly older than the waters in 2021 even considering that the 1991 measurements have a larger uncertainty. This was supported by considering mean ages derived from CFC-11 concentrations in 1991 (see Figure S3, CFC-11 has higher concentrations in seawater, rendering the measurements of this tracer less uncertain). The similar high mean ages observed with CFC-11 data show that elevated mean ages in 1991 compared to 2015 and 2021 are not caused by errors in the CFC-12 data. Therefore, the higher mean ages in 1991 compared to 2015 and 2021 indicate slower ventilation at these intermediate depths in the past. In contrast, below 1200 m, mean age values from 1991 are younger compared to 2015 and 2021. As younger water is present in 2015 compared to 2021 and 1991 in the upper 1200 m, this suggests multidecadal variability in ventilation at these depths, i.e. the ventilation seems to have increased from 1991 until 2015 and decreased thereafter again.

When considering changes in AOU in the Nansen Basin, the values show comparable but slightly different results (see Figure 6a). Specifically, the comparison shows higher values, i.e. likely older water, in the intermediate water in 1991 and 2021 compared to 2015, which indicates a decrease in ventilation in the past six years. Notable differences emerge in similar values observed in 1991 and 2021, where only minor ventilation changes in the upper 800 m are evident. Below 1000 m

532 the AOU results show similar concentrations in all years, implying no variability in ventilation

533 below these depths.

534 The findings obtained from both, transient tracer data and AOU measurements, indicate increased

535 ventilation in 2015 and more poorly ventilated water in 1991, in comparison to 2021 within this

536 region. However, the transient tracer data distinctly illustrates the poorly ventilated water in 1991,

537 with data from 2015 and 2021 falling within comparable ranges. In contrast, the AOU comparison

538 shows nearly aligned data in 1991 and 2021, while the 2015 data indicate well-ventilated waters

539 with a more pronounced difference. This discrepancy in the two variables (mean age and AOU)

540 can be attributed to uncertainties in the transient tracer data from 1991, as previously mentioned,

541 and to changes in respiration rates over the years, which influence the AOU concentrations.

542 Possibly decreasing respiration rates might have shifted the 2015 and 2021 data towards higher

543 levels, closer to those observed in 1991, resulting in similar values in 1991 and 2021.

544 Focusing on changes in the water mass properties (temperature and salinity) (see Figure 7 – left

545 panels), we observe slightly higher temperatures and salinity values in the upper area of the

546 intermediate layer (250 - 600 m) in 2015 compared to 1991 and 2021. This indicates a significantly

547 increased influence of AW during this year, especially considering that this water represents the

548 youngest water mass in 2015 as well. The variability is only present in the upper 600 m, which

549 may be attributed to the AW being confined to these depths in the Nansen Basin. While traversing

550 throught the AO, the AW mixes with ambient water masses, leading to increasing densities and an

551 expansion to lower depths along its path. The salinity values from 1991 align with those of 2021,

552 but the temperature indicates the coldest water being present at these depths in 1991. This

553 variability is again only observed at depths above 600 m, with consistent temperatures and salinity

554 values below, throughout the years. This once more implies that the variability of AW in the

555 Nansen Basin primarily affects the upper part of the intermediate layer. It is possible that the AW

556 has not significantly increased in density due to cooling by mixing with ambient water masses;

557 hence, changes in the entering AW only impact the upper 600 m in this region.

558

559

_____
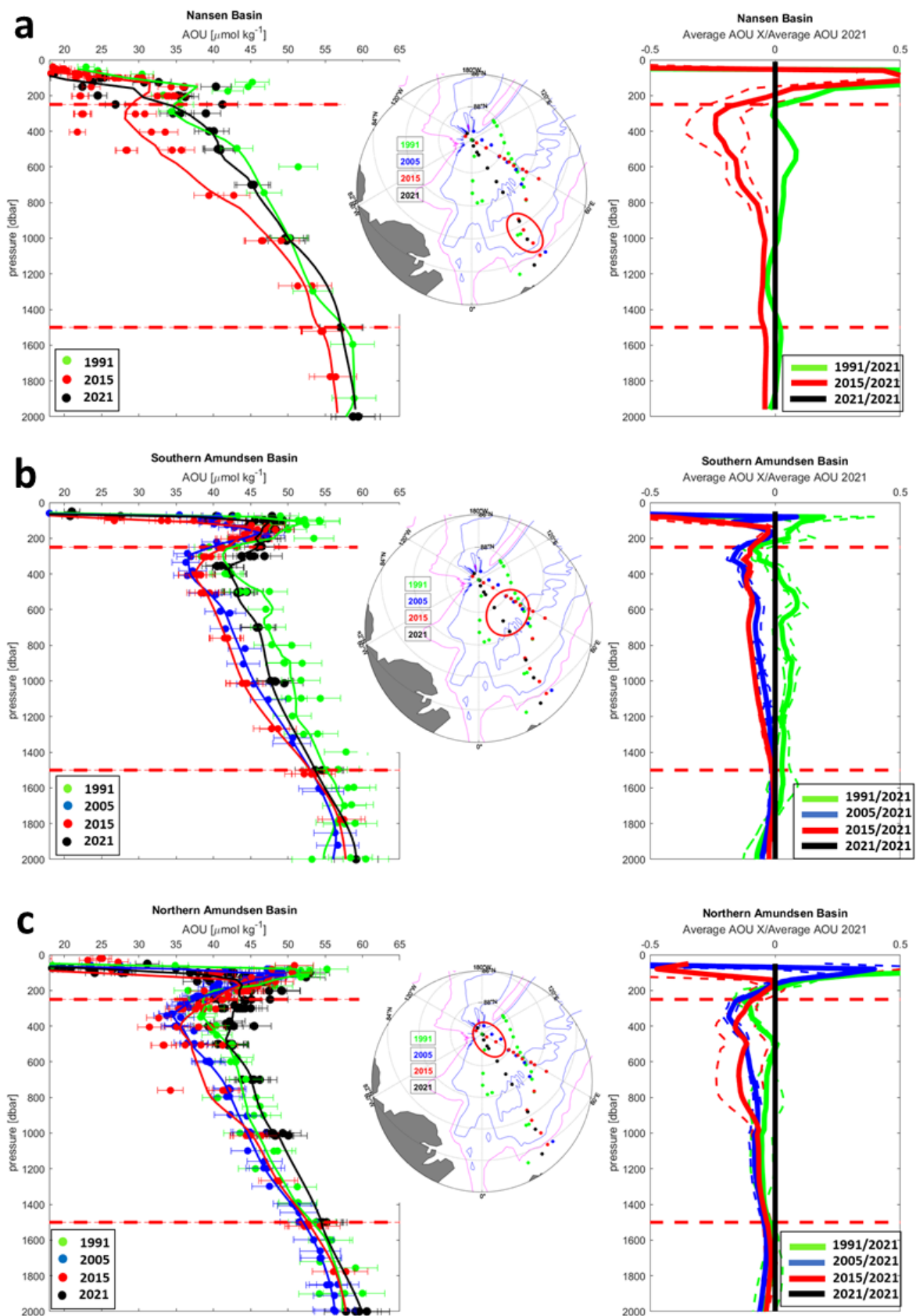
561 **Figure 6.** Display of the calculated AOU concentrations in µmol/kg from year X: 1991 (green), 2005 (blue),

562 2015 (red) and 2021 (black) in (a) the Nansen Basin, (b) the southern Amundsen Basin and (c) the northern

563 Amundsen Basin. The left figures show data points from each station and depth in the respective basin,

564 with the mean values demonstrated by the thin lines. The right figures show the average AOU difference

565 with respect to the data from 2021, with the dashed lines showing the standard deviation of the crossover

566 analysis used for computing the mean values. Average AOU X/Average AOU 2021 < 0 indicates a slower

567 ventilation in 2021 in comparison to the historical cruise in year X, and vice versa. The dashed red lines

568 represent the focus area of this study, the intermediate layer (250 - 1500 m).

569

570
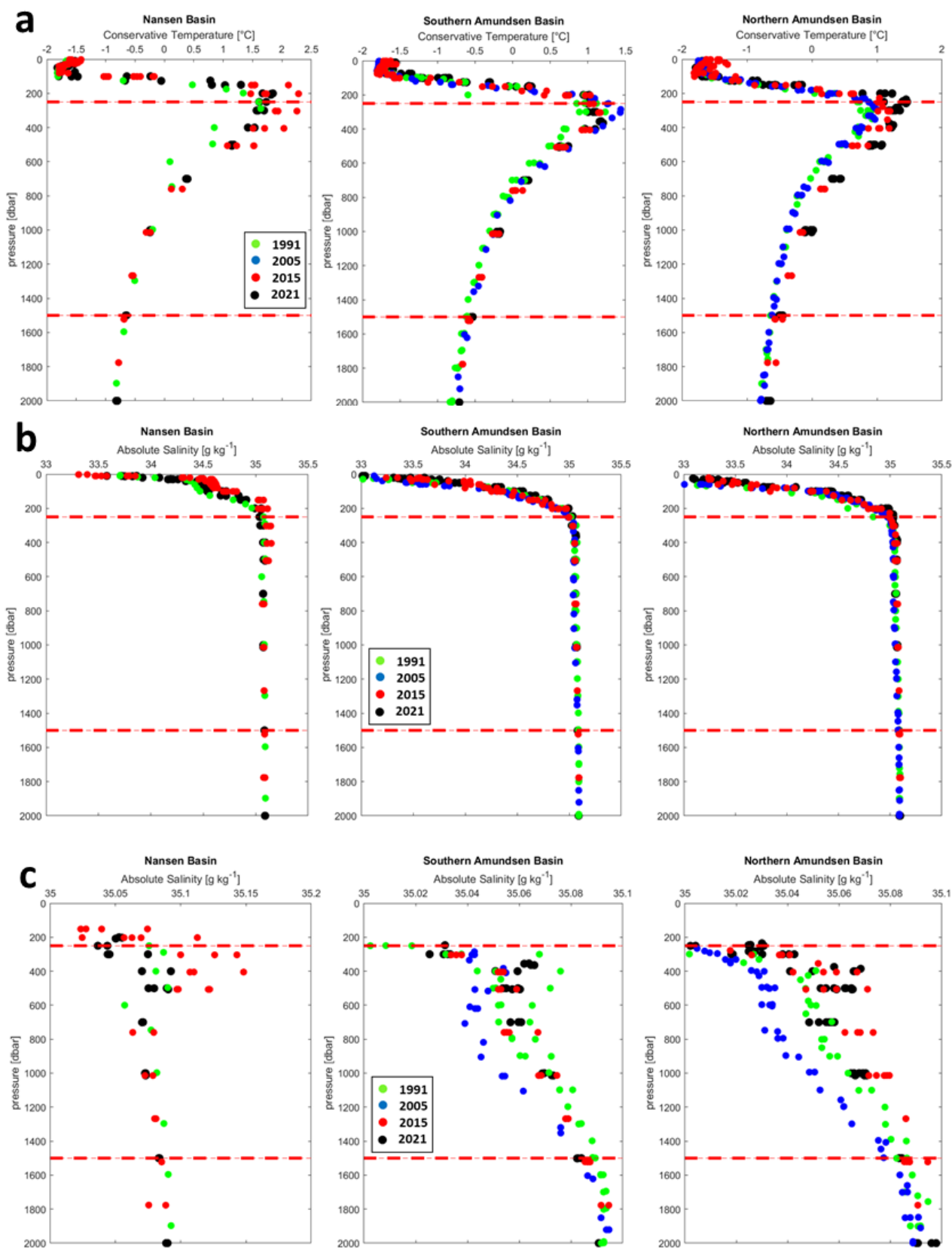
Figure 7. Display of (a) conservative temperature in °C, (b) absolute salinity in g/kg and (c) a zoom of salinity data from each year X: 1991 (green), 2005 (blue), 2015 (red) and 2021 (black) in the Nansen Basin (left panels), the southern Amundsen Basin (middle panels) and the northern Amundsen Basin (right panel). The dashed red lines represent the focus area of this study, the intermediate layer (250 - 1500 m).

4.2.2   Southern Amundsen Basin

A large number of stations are found in the southern Amundsen Basin (12 in total) throughout the sampling years from 1991 until 2021 that can be used to compare temporal changes (see Figures 5b and 6b).

Similar to the results in the Nansen Basin, the oldest water is present in 1991 in the intermediate water column between 400 to 1500 m, although the difference to the mean ages observed in 2021 is not as large. Mean ages observed in 2005 and 2015 show the youngest values across this layer. Throughout the intermediate waters, the mean age in 2021 is approximately 10 to 20 years older compared to 2005 and 2015, indicating slower ventilated water in 2021. Additionally, a slight increase in the mean age is visible from 2005 until 2015. The generally higher mean ages in 1991 compared to 2021 and those from 2021 being higher compared to 2005 and 2015 again indicate a multidecadal variability in ventilation as observed in the Nansen Basin.

The AOU comparison qualitatively confirms the tracer data with similar results until a depth of 1200 m (see Figure 6b). This again indicates slower ventilation in 1991 and 2021 compared to 2005 and 2015, although the values from 1991 and 2021 are more in line again, showing only minor variability. Nonetheless, as both transient tracers and oxygen show comparable results, this is a strong indication for a variability in ventilation throughout the period analyzed.

As seen in the Nansen Basin, both variables (mean age and AOU) show consistent results, however, with some variation in their magnitude. Again the AOU data from 1991 and 2021 show closer alignment compared to the transient tracer data from the same years. This discrepancy most likely can be attributed to uncertainties in the transient tracer measurements in 1991 and possible changes in respiration rates over the 30-year time frame.

Temperature and salinity values across the observed period (see Figure 7 - middle panels) show the coldest water at intermediate depth (especially in the upper 800 m) in 1991 and the warmest in 2005, whereas salinity is lowest in 2005 and similar salinity values are found in 1991, 2015, and 2021.

603

604 *4.2.3   Northern Amundsen Basin*

605   Similar to the southern Amundsen Basin, the northern Amundsen Basin also harbors a large

606   number of stations for comparison (15 in total) (see Figures 5c and 6c). Additionally, one station

607   was located at the same position each year (the North Pole).

608   The mean age results show variability in the intermediate water column with the youngest found

609   in 2005 and the oldest in 2021. There is a significant increase in mean age from 2005 via 2015 to

610   2021. The difference in the northern Amundsen Basin, as opposed to the other observed regions,

611   are the mean age values from 1991. These are more in line with those from 2005 and 2015 rather

612   than with the values from 2021.

613   The variability observed in the mean age data is, to some extent, also seen in the AOU plot (see

614   Figure 6c). The data from 2021 displays higher AOU values in comparison to 2005 and 2015,

615   which confirms the results shown in the mean age data, but the data from 1991 here are more in

616   line with the 2021 values. Also, the magnitude of the variability is minor compared to what is seen

617   in the tracer-based mean age calculations. These differences in the variables most likely can be

618   attributed to the aforementioned uncertainties in the calculation of each parameter.

619   Examining the water properties, we observe a change in temperature over the years at this location,

620   with increasing values within the intermediate layer from 2005 over 2015 until 2021 (see Figure

621   7a - right panel). The data from 1991 are generally in agreement with temperatures measured in

622   2005. A similar increase is also visible in the salinity data (see Figure 7c - right panel), with the

623   freshest water found in 2005 and the most saline in 2015 and 2021. As the AOBC is present in this

624   area and the AW is therefore affected less by ambient colder water masses within the AO, this

625   suggests an increase in the temperature of the AW entering the AO.

626   The increasing mean age over the past 16 years also indicates a slower circulation of the AW

627   around the AO within the AOBC, possibly even affected by a slowdown of the AMOC as reported

628   by Caesar et al. (2021). As the AOBC transports recently ventilated waters from the Nordic Seas

629   through the AO and along the Lomonosov Ridge at intermediate depths, the time it takes for this

630   water to travel from the Nordic Seas towards the North Pole is represented by the mean age. An

631   increased velocity of the AOBC in one year as compared to the precious one would reflect itself

632   by the presence of younger mean ages of waters at the North Pole in the later year. For example,

633   Heukamp et al. (2023) reported that before entering the AO, the AW recirculating inside the Fram

634 Strait has accelerated. This reflects in a deceleration of the AW flowing into the AO and thereby

635 increases the time needed for AW to travel to the North Pole. Possibly this is caused by rising sea

636 surface temperatures in the Nordic Seas, stronger southeastward winds and a westward shift of the

637 West Spitzbergen Current (current running poleward west of Spitzbergen, transporting AW) to

638 areas of deeper ocean inside the Fram Strait as described by Heukamp et al. (2023).

639 The difference in the 1991 data, which show increased ventilation in the northern Amundsen Basin

640 compared to poor ventilation in the other two sections analyzed, is likely caused by the influence

641 of the AOBC, resulting in generally younger water in the intermediate layer, as shown and

642 described in section 4.1. This suggests, on the one hand, that the multidecadal variability in

643 ventilation, as reflected by less ventilated waters in 1991 and 2021 compared to 2005 and 2015,

644 might not influence the intermediate layer in the northern Amundsen Basin. This could, in turn, be

645 attributed to the observation that circulation of AW from the Fram Strait to the North Pole only

646 takes approximately 9 to 12 years (Smith et al., 2011) (see section 4.1), whereas the multidecadal

647 change is seen here, ranging over a period of at least 14 years (from 1991 until 2005). While there

648 is variability in the ventilation among the years analyzed, the 1991 data do not show these

649 comparably high mean ages observed in the other regions. On the other hand, the ventilation data

650 indicate that the decrease in the circulation speed of the AW started within the past 15 years, with

651 the mean ages showing the youngest values in 2005 and increasing thereafter until 2021.

652

653 5 Conclusion and Outlook

654 This study analyzed ventilation changes in the Eurasian AO between 1991 and 2021, based on

655 transient tracer measurements, i.e. TTD-derived mean ages, as well as AOU. Changes in

656 ventilation in the intermediate water layer (250 - 1500 m depth) in both the Nansen and Amundsen

657 Basins are observed. In the Amundsen Basin, higher mean ages, indicating a decrease in

658 ventilation, are observed in the entire intermediate layer in 2021 compared to 2005 and 2015. Due

659 to a lack of comparable stations, we were only able to identify this decrease between 2015 and

660 2021 in the Nansen Basin, and only being present in the intermediate layer between 250 and

661 1200 m. This suggests that this ventilation change is linked to a variability in the transport of AW

662 into the AO. That the variability is observed at deeper depth in the Amundsen Basin compared to

663 the Nansen Basin can be linked to the increasing density of the AW moving further into the AO

664   (Richards et al., 2022). Data from 1991 confirm a decrease in ventilation within the AOBC in the

665   northern Amundsen Basin close to the North Pole, as they show similar results to measurements

666   of 2005 and 2015. This suggests that the ventilation decrease happened primarily over the past 16

667   years. It also implies a possible decrease in the strength of the AOBC as the mean age comparison

668   shows these increasing ages, which represent the transport time of the AW from subduction to this

669   location. In contrast, the southern Amundsen Basin and the Nansen Basin exhibit poorly ventilated

670   water in the intermediate layer from 1991 data, with mean ages even surpassing those measured

671   in 2021. This implies a multidecadal ventilation change within the intermediate layer in these parts

672   of the Eurasian AO. Despite limited data points (data are only available for 1991, 2005, 2015 and

673   2021), this change is evident in two distinct areas of the Eurasian AO and is detected by two

674   independent variables (mean age and AOU). Notably, the area close to the Lomonosov Ridge does

675   not follow this trend, likely due to the influence of the AOBC. This current has a circulation time

676   of 9-12 years from the Fram Strait to the North Pole (Karcher et al., 2011; Raimondi et al., 2023;

677   Smith et al., 2011) and therefore rejuvenates water masses in this area quicker than the observed

678   multidecadal change. This suggests that the multidecadal variability in ventilation surpasses the

679   time it takes for the AW to reach the North Pole. Moreover, this multidecadal variability could

680   also be caused by a change in the recirculating AW inside the AO, being more pronounced along

681   the Lomonosov Ridge for some time-period, and in other years along the Gakkel Ridge. However,

682   the lack of transient tracer data, especially in the Nansen Basin close to the Gakkel Ridge, limits

683   such conclusions.

684   Both derived variables, mean ages and AOU, yield comparable results, however, with variations

685   in their magnitude. In the Nansen Basin and the southern Amundsen Basin, transient tracer data

686   distinctly show the poorly ventilated intermediate water layer in 1991 compared to all other years.

687   Conversely, AOU data indicates that the 1991 data are in closer alignment with the 2021 data, with

688   noticeably increased ventilation evident in 2005 and 2015. In the northern Amundsen Basin, AOU

689   values from 1991 again align closely with those measured in 2021, showing no significantly

690   increased ventilation compared to 2021, as indicated by TTD-derived mean age data. This

691   discrepancy may stem from measurement uncertainties in the 1991 data and changes in respiration

692   rates affecting AOU values. A decline in respiration rates may have shifted the 2005, 2015 and

693   2021 data towards higher levels, closer to those observed in 1991, thus resulting in similar values

694 between 1991 and 2021, thereby not reflecting the poorer ventilation observed in 1991 compared
695 to the later years in the Nansen and southern Amundsen Basin.

696 Changes in the water properties, already present in the Nordic Seas, affect the ventilation. The
697 temperature increase identified in the northern Amundsen Basin from 2005 until 2021, likely
698 reflects increasing surface water temperature in the Nordic Seas as measurements at this location
699 solely represent AW being transported within the AOBC. As changes in the water mass anomaly
700 in the Nansen Basin are only visible in the upper 600 m and in the southern Amundsen Basin until
701 depths of around 800 to 1000 m, this can be attributed to the density increase of the AW when
702 mixing with ambient colder water along its path through the AO. Another factor influencing
703 ventilation in the AO is the decreasing sea ice coverage and the impact of fresh water affecting the
704 surface layer and thereby weakening the cold halocline. However, as we still see a steep
705 thermocline and halocline in all regions examined, this effect has no impact on the intermediate
706 layer yet.

707 The combined findings of the all variables shed light on the dynamic changes in the Eurasian AO
708 and its impact on the larger scale circulation patterns.

709 The variability in ventilation observed within the last three decades, calls for future observation in
710 the Eurasian AO, including regular transient tracer and oceanographic measurements. These are
711 crucial for understanding the observed changes and identifying potential trends in this region. For
712 instance, long-term measurements in the outflow region of the AO south of the Fram Strait and
713 close to the Greenland shelf could help to understand decadal scale variability of the circulation,
714 ventilation and outflow of subsurface and deep waters. Moreover, continued observations in the
715 Central Arctic Ocean and its shelf areas are required to obtain sufficient information on the
716 variability in ventilation in this region.

717

Data Availability Statement

719 The data used from the GLODAPv2.2021 data product can be found at
720 https://www.ncei.noaa.gov/access/ocean-carbon-acidification-data-
721 system/oceans/GLODAPv2_2021/. The data from the 2021 cruise on the IB Oden can be found
722 on the GLODAPv2.2023 data product at https://www.ncei.noaa.gov/access/ocean-carbon-
723 acidification-data-system/oceans/GLODAPv2_2023/.

74

724 **Acknowledgments**

725 This study would not have been possible without support of the DFG (Deutsche

726 Forschungsgesellschaft), financing the project 'Der arktische Ozean 2020 –

727 Ventilationszeitskalen, anthropogener Kohlenstoff und Variabilität in einer sich verändernden

728 Umgebung' (TA 317/8-1 and AE 93/21-1) and also providing the opportunity to participate in the

729 SAS-Oden 2021 cruise. We would also like to extend our thanks to ARICE (Arctic Research

730 Icebreaker Consortium) (grand number 730965), the Hasselblad Foundation (Contract No. 2019-

731 1218) and the Swedish Polar Research Secretariat (SPRS) for their support during the 2021 cruise.

732 In this regard, we would also like to thank the captain, crew and all the other researchers on board

733 for their assistance. Additionally, we would like to acknowledge the impressive work and data

734 collection of all scientists and technicians contributing to the data in GLODAPv2.2021. Finally,

735 we would like to thank the editor and our four anonymous reviewers for their helpful and

736 constructive comments which lead to the improvement of the quality of the manuscript. A sincere

737 thank you to William A. Nesbitt from Dalhousie University, Halifax, for thoroughly proofreading

738 the manuscript for language and grammar issues.

739

740 **References**

741

742 Aagaard, K. (1989), A synthesis of the Arctic Ocean circulation, *Rapports et Proces-verbaux Reunion Conseil*
743 *Internationale Exploration de la Mer*, *188*, 11-22, doi:10.17895/ices.pub.19279133.
744 Aagaard, K., & Carmack, E. (1989), The role of sea ice and fresh water in the Arctic circulation, *J. Geophys. Res.*,
745 *94*(14), 485-498.
746 Aagaard, K., Coachman, L. K., & Carmack, E. C. (1981), On the halocline of the Arctic Ocean, *Deep Sea Research*,
747 *28*, 529-545.
748 Aksenov, Y., Ivanov, V. V., Nurser, A. J. G., Bacon, S., Polyakov, I. V., Coward, A. C., Naveira Garabato, A. C., &
749 Beszczynska-Möller, A. (2011), The arctic circumpolar boundary current, *Journal of Geophysical Research:*
750 *Oceans*, *116 (C9)*, doi:https://doi.org/10.1029/2010JC006637.
751 Anderson, L., & Party, S. (1998), Cruise Report: Arctic Ocean Expedition 1991 (ODEN-91)*Rep.*
752 Anderson, L. G., Björk, G., Holby, O., Jones, E. P., Kattner, G., Koltermann, K. P., Liljeblad, B., Lindegren, R.,
753 Rudels, B., & Swift, J. (1994), Water masses and circulation in the Eurasian Basin - Results from the Oden 91
754 Expedition, *J. Geophys. Res.*, *99*(C2), 3273-3283.
755 Anderson, L. G., Jones, E. P., & Rudels, B. (1999), Ventilation of the Arctic Ocean estimated by a plume
756 entrainment model constrained by CFCs, *J. Geophys. Res.*, *104*(C6), 13423-13429.
757 Arrigo, K. R., et al. (2012), Massive Phytoplankton Blooms Under Arctic Sea Ice, *Science*, *336*,
758 doi:https://doi.org/10.1126/science.1215065.
759 Arrigo, K. R., & Van Dijken, G. L. (2011), Secular trends in Arctic Ocean net primary production, *J. Geophys. Res.*,
760 *116*(C9), doi:10.1029/2011jc007151.
761 Bauch, D., Torres-Valdes, S., Polyakov, I., Novikhin, A., Dmitrenko, I., McKay, J., & Mix, A. (2014), Halocline
762 water modification and along-slope advection at the Laptev Sea continental margin, *Ocean Science*, *10*(1), 141-154,
763 doi:10.5194/os-10-141-2014.

764 Bullister, J., & Warner, M. J. (2017), Atmoshperic Histories (1765-2022) for CFC-11, CFC-12, CFC-113, CCl4,
765 SF6, N2O (NCEI Accession 0164584). An update to Bullister (2015) NDP-09, *NOAA Nathional Centers for*
766 *Environmental Information. Dataset*, doi:https://doi.org/10.3334/cdiac/otg.cfc_atm_hist_2015.
767 Bullister, J. L., Wisegarver, D. P., & Menzia, F. A. (2002), The solubility of sulfur hexafluoride in water and
768 seawater, *Deep-Sea Res. I*, *49*(1), 175-187.
769 Caesar, L., McCarthy, G. D., Thornalley, D. J. R., Cahill, N., & Rahmstorf, S. (2021), Current Atlantic Meridional
770 Overturning Circulation weakest in last millennium, *Nature Geoscience*, doi:10.1038/s41561-021-00699-z.
771 Coachman, L. K., & Barnes, C. A. (1963), The Movement of Atlantic Water in the Arctic Ocean, *Arctic*, *16*(1), 8,
772 doi:10.14430/arctic3517.
773 DeGrandpre, M. D., Kortzinger, A., Send, U., Wallace, D. W. R., & Bellerby, R. G. J. (2006), Uptake and
774 sequestration of atmospheric CO2 in the Labrador Sea deep convection region, *Geophys. Res. Letters*, *33*(21),
775 doi:https://doi.org/10.1029/2006GL026881.
776 DeVries, T., et al. (2023), Magnitude, Trends, and Variability of the Global Ocean Carbon Sink From 1985 to 2018,
777 *Global Biogeochem Cycle*, *37*(10), doi:10.1029/2023gb007780.
778 Eakins, B. W., & Sharman, G. F. (2007), Volumes of the World's Oceans from ETOPO1, *AGU Fall Meeting*
779 *Abstracts*.
780 Ekwurzel, B., Schlosser, P., Mortlock, R. A., Fairbanks, R. G., & Swift, J. H. (2001), River runoff, sea ice
781 meltwater, and Pacific water distribution and mean residence times in the Arctic Ocean, *J. Geophys. Res.*, *106*(C5),
782 9075-9092.
783 Fabry, V. J., McClintock, J. B., Mathis, J. T., & Grebmeier, J. M. (2009), Ocean acidification at high latitudes: The
784 Bellwether, *Oceanography*, *22*, 160-171, doi:https://doi.org/10.5670/oceanog.2009.105.
785 Fine, R. A. (2011), Observations of CFCs and SF(6) as Ocean Tracers, *Annual Review of Marine Science, Vol 3*, *3*,
786 173-195, doi:10.1146/annurev.marine.010908.163933.
787 Frolov, I. E., Gudkovich, Z. M., Radionov, V. F., Shirochkov, A. V., & Timokhov, L. A. (2005), The Arctic Basin,
788 *Springer Praxis Books*, doi:10.1007/3-540-37665-8.
789 Haine, T. W. N. (2021), A Conceptual Model of Polar Overturning Circulations, *J. Phys. Oceanogr.*, *51*(3), 727-
790 744, doi:10.1175/jpo-d-20-0139.1.
791 Haine, T. W. N., & Richards, K. J. (1995), The influence of the seasonal mixed layer on oceanic uptake of CFCs, *J.*
792 *Geophys. Res.*, *100*(C6), 10727-10744.
793 Hall, T. M., & Plumb, R. A. (1994), Age as a diagnostic of stratospheric transport, *Journal of Geophysical*
794 *Research: Atmospheres*, *99*(D1), 1059-1070, doi:10.1029/93JD03192.
795 Heukamp, F. O., Kanzow, T., Wang, Q., Wekerle, C., & Gerdes, R. (2023), Impact of Cyclonic Wind Anomalies
796 Caused by Massive Winter Sea Ice Retreat in the Barents Sea on Atlantic Water Transport Toward the Arctic: A
797 Model Study, *Journal of Geophysical Research: Oceans*, *128*, doi:https://doi.org/10.1029/2022JC019045.
798 Jakobsson, M. (2002), Hypsometry and volume of the Arctic Ocean and its constituent seas, *Geochemistry*
799 *Geophysics Geosystems*, *3*, doi:https://doi.org/10.1029/2001GC000302.
800 Jeansson, E., Olsson, K. A., Tanhua, T., & Bullister, J. L. (2010), Nordic Seas and Arctic Ocean CFC data in
801 CARINA, *Earth Syst. Sci. Data*, *2*(1), 79-97.
802 Jeansson, E., Tanhua, T., Olsen, A., Smethie, W. M., Rajasakaren, B., Ólafsdóttir, S. R., & Ólafsson, J. (2023),
803 Decadal Changes in Ventilation and Anthropogenic Carbon in the Nordic Seas, *Journal of Geophysical Research:*
804 *Oceans*, *128*(3), doi:10.1029/2022jc019318.
805 Jones, E. P., Rudels, B., & Anderson, L. G. (1995), Deep waters of the Arctic Ocean: origins and circulation, *Deep-*
806 *Sea Res. I*, *42*(5), 737-760.
807 Karcher, M., Beszczynska-Möller, A., Kauker, F., Gerdes, R., Heyen, S., Rudels, B., & Schauer, U. (2011), Arctic
808 Ocean warming and its consequences for the Denmark Strait overflow, *J. Geophys. Res.*, *116*(C2),
809 doi:10.1029/2010jc006265.
810 Karcher, M., Smith, J. N., Kauker, F., Gerdes, R., & Smethie, W. M. (2012), Recent changes in Arctic Ocean
811 circulation revealed by iodine-129 observations and modeling, *Journal of Geophysical Research: Oceans*, *117*(C8),
812 doi:10.1029/2011jc007513.
813 Karlqvist, A., & Party, S. (2010), Cruise Report: ODEN05*Rep.*
814 Karstensen, J., Schlosser, P., Wallace, D. W. R., Bullister, J. L., & Blindheim, J. (2005), Water mass transformation
815 in the Greenland Sea during the 1990s, *J. Geophys. Res.*, *110*, C07022, doi:doi:10.1029/2004JC002510.
816 Khatiwala, S., Visbeck, M., & Schlosser, P. (2001), Age tracers in an ocean GCM, *Deep-Sea Res. I*, *48*(6), 1423-
817 1441.

818 Lauvset, S. K., Brakstad, A., Våge, K., Olsen, A., Jeansson, E., & Mork, K. A. (2018), Continued warming,
819 salinification and oxygenation of the Greenland Sea gyre, *Tellus A: Dynamic Meteorology and Oceanography*, *70*
820 *(1)*, 1-9, doi:https://doi.org/10.1080/16000870.2018.1476434.
821 Lauvset, S. K., et al. (2021), An updated version of the global interior ocean biogeochemical data product,
822 GLODAPv2.2021, *Earth Syst. Sci. Data Discuss.*, *2021*, 1-32, doi:10.5194/essd-2021-234.
823 Lavoie, D., Denman, K. L., & Macdonald, R. W. (2010), Effects of future climate change on primary productivity
824 and export fluxes in the Beaufort Sea, *J. Geophys. Res.*, *115*(C4), doi:10.1029/2009jc005493.
825 Loose, B., McGillis, W. R., Perovich, D., Zappa, C. J., & Schlosser, P. (2014), A parameter model of gas exchange
826 for the seasonal sea ice zone, *Ocean Science*, *10*(1), 17-28, doi:10.5194/os-10-17-2014.
827 Macdonald, R. W., & Carmack, E. C. (1991), Age of Canada Basin Deep Waters - a Way to Estimate Primary
828 Production for the Arctic-Ocean, *Science*, *254*(5036), 1348-1350.
829 MacGilchrist, G. A., Naveira Garabato, A. C., Tsubouchi, T., Bacon, S., Torres-Valdés, S., & Azetsu-Scott, K.
830 (2014), The Arctic Ocean carbon sink, *Deep Sea Research Part I: Oceanographic Research Papers*, *86*(0), 39-55,
831 doi:http://dx.doi.org/10.1016/j.dsr.2014.01.002.
832 Maiss, M., & Brenninkmeijer, C. A. M. (1998), Atmospheric SF6: Trends, sources, and prospects, *Environ. Sci.*
833 *Technol.*, *32*(20), 3077-3086.
834 Mauritzen, C. (1996), Production of dense overflow waters feeding the North Atlantic across the Greenland-
835 Scotland Ridge. Part 1: Evidence for a revised circulation scheme, *Deep-Sea Res. I*, *43*(6), 769-806.
836 Meredith, M., et al. (2019), Polar Regions. In: IPCC Special Report on the Ocean and Cryosphere in a Changing
837 Climate.
838 Nansen, F. (1902), The oceanography of the North Polar Basin. The Norwegian North Polar Expedition 1893-1896,
839 *Scientific Results 3*.
840 Nghiem, S. V., Chao, Y., Neumann, G., Li, P., Perovich, D. K., Street, T., & Clemente-Colón, P. (2006), Depletion
841 of perennial sea ice in the East Arctic Ocean, *Geophys. Res. Letters*, *33*(17), doi:10.1029/2006gl027198.
842 Olsen, A., Omar, A. M., Jeansson, E., Anderson, L. G., & Bellerby, R. G. J. (2010), Nordic seas transit time
843 distributions and anthropogenic CO_2, *J. Geophys. Res.*, *115*(C5), C05005.
844 Pfirman, S. (2004), Variability in Arctic sea ice drift, *Geophys. Res. Letters*, *31*(16), doi:10.1029/2004gl020063.
845 Raimondi, L., Wefing, A. M., & Casacuberta, N. (2023), Anthropogenic Carbon in the Arctic Ocean: Perspectives
846 From Different Transient Tracers, *Journal of Geophysical Research: Oceans*, *129*(1),
847 doi:https://doi.org/10.1029/2023JC019999.
848 Rajasakaren, B., Jeansson, E., Olsen, A., Tanhua, T., Johannessen, T., & Smethie, W. M. (2019), Trends in
849 anthropogenic carbon in the Arctic Ocean, *Prog. Oceanogr.*, *178*, 102177,
850 doi:https://doi.org/10.1016/j.pocean.2019.102177.
851 Richards, A. E., Johnson, H. L., & Lique, C. (2022), Spatial and Temporal Variability of Atlantic Water in the
852 Arctic From 40 Years of Observations, *Journal of Geophysical Research: Oceans*, *127*(9),
853 doi:10.1029/2021jc018358.
854 Rigor, I. G., Wallace, J. M., & Colony, R. L. (2002), Response of Sea Ice to the Arctic Oscillation, *J Climate*,
855 *15*(18), 2648-2663.
856 Rudels, B., Friedrich, H. J., & Quadfasel, D. (1999), The Arctic Circumpolar Boundary Current, *Deep-Sea Res. II*,
857 *46*(6-7), 1023-1062.
858 Rudels, B., Jones, E. P., Anderson, L. G., & Kattner, G. (1994), On the Intermediate Depth Waters of the Arctic
859 Ocean, in *The Polar Oceans and Their Role in Shaping the Global Environment*, edited by R. Muench and O. M.
860 Johannesson, pp. 33-46, American Geophysical Union, Washington D.C.
861 Schauer, U., & Party, S. (2016), The Expedition PS94 of the Research Vessel POLARSTERN to the central Arctic
862 Ocean in 2015*Rep*.
863 Schneider, A., Tanhua, T., Körtzinger, A., & Wallace, D. W. R. (2012), An evaluation of tracer fields and
864 anthropogenic carbon in the equatorial and the tropical North Atlantic, *Deep Sea Research Part I: Oceanographic*
865 *Research Papers*, *67*(0), 85-97, doi:10.1016/j.dsr.2012.05.007.
866 Shao, A. E., Mecking, S., Thompson, L., & Sonnerup, R. E. (2013), Mixed layer saturations of CFC-11, CFC-12,
867 and SF6 in a global isopycnal model, *Journal of Geophysical Research: Oceans*, *118*(10), 4978-4988,
868 doi:10.1002/jgrc.20370.
869 Shao, A. E., Mecking, S., Thompson, L., & Sonnerup, R. E. (2016), Evaluating the use of 1-D transit time
870 distributions to infer the mean state and variability of oceanic ventilation, *Journal of Geophysical Research: Oceans*,
871 *121*(9), 6650-6670, doi:10.1002/2016jc011900.
872 Singarayer, J. S., Bamber, J. L., & Valdes, P. J. (2006), Twenty-First-Century Climate Impacts from a Declining
873 Arctic Sea Ice Cover, *J Climate*, *19*(7), 1109-1125, doi:10.1175/jcli3649.1.

874 Slagstad, D., Wassmann, P., & Ellingsen, I. (2015), Physical constrains and productivity in the future Arctic Ocean,
875 *Frontiers in Marine Science*, *2*, 1-23, doi:10.3389/fmars.2015.00085.
876 Smedsrud, L. H., et al. (2022), Nordic Seas Heat Loss, Atlantic Inflow, and Arctic Sea Ice Cover Over the Last
877 Century, *Rev. Geophys.*, *60*(1), doi:10.1029/2020rg000725.
878 Smith, J. N., McLaughlin, F. A., Smethie Jr., W. M., Moran, S. B., & Lepore, K. (2011), Iodine-129, 137Cs, and
879 CFC-11 tracer transit time distributions in the Arctic Ocean, *Journal of Geophysical Research: Oceans*, *116*(C4),
880 doi:10.1029/2010jc006471.
881 Smith, J. N., Smethie Jr., W. M., & Casacuberta, N. (2022), Synoptic 129I and CFC–SF6 Transit Time Distribution
882 (TTD) Sections Across the Central Arctic Ocean From the 2015 GEOTRACES Cruises, *Journal of Geophysical*
883 *Research: Oceans*, *127*(9), e2021JC018120, doi:https://doi.org/10.1029/2021JC018120.
884 Snoeijs-Leijonmalm, P., & Party, S.-O. S. (2022), Expedition Report SWEDARCTIC Synoptic Arctic Survey 2021
885 with icebreaker Oden*Rep.*, 300 pp.
886 Sonnerup, R. E., Mecking, S., & Bullister, J. L. (2013), Transit time distributions and oxygen utilization rates in the
887 Northeast Pacific Ocean from chlorofluorocarbons and sulfur hexafluoride, *Deep Sea Research Part I:*
888 *Oceanographic Research Papers*, *72*, 61-71, doi:http://dx.doi.org/10.1016/j.dsr.2012.10.013.
889 Steele, M., Ermold, W., & Zhang, J. (2008), Arctic Ocean surface warming trends over the past 100 years, *Geophys.*
890 *Res. Letters*, *35*(2), doi:10.1029/2007gl031651.
891 Stöven, T., & Tanhua, T. (2014), Ventilation of the Mediterranean Sea constrained by multiple transient tracer
892 measurements, *Ocean Sci.*, *10*(3), 439-457, doi:10.5194/os-10-439-2014.
893 Swift, J. H., & Aagaard, K. (1981), Seasonal transitions and water mass formation in the Iceland and Greenland
894 seas, *Deep-Sea Res. A*, *28*(A10), 1107-1129.
895 Swift, J. H., Aagaard, K., & Malmberg, S.-A. (1980), The contribution of the Denmark Strait overflow to the deep
896 North Atlantic, *Deep-Sea Res. A*, *27*(1A), 29-42.
897 Talley, L. D. (1996), North Atlantic circulation and variability, reviewed for the CNLS conference, *Physica D:*
898 *Nonlinear Phenomena*, *98*(2-4), 625-646.
899 Tanhua, T., Bulsiewicz, K., & Rhein, M. (2005a), Spreading of overflow water from the Greenland to the Labrador
900 Sea, *Geophys. Res. Letters*, *32*(10), L10615, doi:10.1029/2005GL022700.
901 Tanhua, T., Jones, E. P., Jeansson, E., Jutterstrom, S., Smethie, W. M., Wallace, D. W. R., & Anderson, L. G.
902 (2009), Ventilation of the Arctic Ocean: Mean ages and inventories of anthropogenic CO$_2$ and CFC-11, *J. Geophys.*
903 *Res.*, *114*(C1), C01002, doi:doi:10.1029/2008JC004868.
904 Tanhua, T., Olsson, K. A., & Fogelqvist, E. (2004), A first study of SF$_6$ as a transient tracer in the Southern Ocean,
905 *Deep-Sea Res. II*, *51*, 2683-2699.
906 Tanhua, T., Olsson, K. A., & Jeansson, E. (2005b), Formation of Denmark Strait Overflow Water and its hydro-
907 chemical composition, *J. Mar. Systems*, *57*, 264-288, doi:10.1016/j.jmarsys.2005.05.003.
908 Tanhua, T., van Heuven, S., Key, R. M., Velo, A., Olsen, A., & Schirnick, C. (2010), Quality control procedures and
909 methods of the CARINA database, *Earth Syst. Sci. Data*, *2*(1), 35-49, doi:10.5194/essd-2-35-2010.
910 Tanhua, T., Waugh, D. W., & Bullister, J. L. (2013), Estimating changes in ocean ventilation from the early 1990s
911 CFC-12 and late 2000s SF$_6$ measurements, *Geophys. Res. Lett*, *40*, 1-6, doi:10.1002/grl.50251.
912 Tanhua, T., Waugh, D. W., & Wallace, D. W. R. (2008), Use of SF$_6$ to estimate anthropogenic carbon in the upper
913 ocean., *J. Geophys. Res.-Oceans*, *113*, C04037, doi:10.1029/2007JC004416.
914 Terhaar, J., Kwiatkowski, L., & Bopp, L. (2020), Emergent constraint on Arctic Ocean acidification in the twenty-
915 first century, *Nature*, *582*(7812), 379-383, doi:10.1038/s41586-020-2360-3.
916 Trossman, D. S., Thompson, L., Mecking, S., & Warner, M. J. (2012), On the formation, ventilation, and erosion of
917 mode waters in the North Atlantic and Southern Oceans, *Journal of Geophysical Research: Oceans*, *117*(C9),
918 C09026, doi:10.1029/2012jc008090.
919 Trossman, D. S., Thompson, L., Mecking, S., Warner, M. J., Bryan, F. O., & Peacock, S. (2014), Evolution of
920 oceanic transport parameters using transient tracers from observations and model output, *Ocean Modelling*, *74*, 1-
921 21, doi:http://dx.doi.org/10.1016/j.ocemod.2013.11.001.
922 Walker, S. J., Weiss, R. F., & Salameh, P. K. (2000), Reconstructed histories of the annual mean atmospheric mole
923 fractions for the halocarbons CFC-11, CFC-12, CFC-113 and carbon tetrachloride, *J. Geophys. Res.*, *105*(C6),
924 14285-14296.
925 Wallace, D. W. R., Schlosser, P., Krysell, M., & Bönisch, G. (1992), Halocarbon ratio and tritium/3He dating of
926 water masses in the Nansen Basin, Arctic Ocean, *Deep Sea Research I*, *39*(S2A), 435-458.
927 Warner, M. J., & Weiss, R. F. (1985), Solubilities of chlorofluorocarbons 11 and 12 in water and sea water, *Deep-*
928 *Sea Res.*, *32*(12), 1485-1497.

929 Wassmann, P. (2006), Structure and function of contemporary food webs on Arctic shelves: An introduction, *Prog.*
930 *Oceanogr.*, *71*, 123-128, doi:https://doi.org/10.1016/j.pocean.2006.09.008.
931 Wassmann, P. (2011), Arctic marine ecosystems in an era of rapid climate change, *Prog. Oceanogr.*, *90*, 1-17,
932 doi:https://doi.org/10.1016/j.pocean.2011.02.002.
933 Wassmann, P. (2015), Overarching perspectives of contemporary and future ecosystems in the Arctic Ocean, *Prog.*
934 *Oceanogr.*, *139*, 1-12, doi:https://doi.org/10.1016/j.pocean.2015.08.004.
935 Watson, A. J., et al. (1999), Mixing and convection in the Greenland Sea from a tracer-release experiment, *Nature*,
936 *401*(6756), 902-904.
937 Waugh, D. W., Hall, T. M., & Haine, T. W. N. (2003), Relationship among tracer ages, *J. Geophys. Res.*, *108*(C5),
938 doi:10.1029/2002JC001325.
939 Waugh, D. W., Hall, T. M., & Haine, T. W. N. (2004), Transport Times and Anthropogenic Carbon in the Subpolar
940 North Atlantic Ocean, *Deep Sea Research I*, *51*, 1471-1491, doi:10.1016/j.dsr.2004.06.011.
941 Waugh, D. W., Hall, T. M., McNeil, B. I., Key, R., & Matear, R. J. (2006), Anthropogenic CO_2 in the Oceans
942 estimated using transit-time distributions, *Tellus*, *58B*, 376-389, doi:10.1111/j.1600-0889.2006.00222.x.
943 Waugh, D. W., Vollmer, M. K., Weiss, R. F., Haine, T. W. N., & Hall, T. M. (2002), Transit time distributions in
944 Lake Issyk-Kul, *Goephysical Research Letters*, *29*(24).
945 Wefing, A. M., Casacuberta, N., Christl, M., Gruber, N., & Smith, J. N. (2021), Circulation timescales of Atlantic
946 Water in the Arctic Ocean determined from anthropogenic radionuclides, *Ocean Sci.*, *17*(1), 111-129,
947 doi:10.5194/os-17-111-2021.
948 Woodgate, R. A. (2013), Arctic Ocean Circulation: Going Around the Top Of the World, *Nature Education*
949 *Knowledge*, *4*.
950 Yasunaka, S., et al. (2023), An Assessment of CO2 Uptake in the Arctic Ocean From 1985 to 2018, *Global*
951 *Biogeochem Cycle*, *37*(11), doi:10.1029/2023gb007806.
952

3.1 Supplemental Material Manuscript I

Temporal Variability of Ventilation in the Eurasian Arctic Ocean

L. Gerke[1], Y. Arck[2], T. Tanhua[1]

1 GEOMAR Helmholtz Centre for Ocean Research Kiel, Kiel, Germany
2 Institute of Environmental Physics, Heidelberg University, Heidelberg, Germany

_____

Journal of Geophysical Research: Oceans

Supporting Information for

Temporal Variability of Ventilation in the Eurasian Arctic Ocean

Lennart Gerke[1], Yannis Arck[2] ,Toste Tanhua[1]

[1]GEOMAR Helmholtz Centre for Ocean Research Kiel, Kiel, Germany

[2]Institute of Environmental Physics, Heidelberg University, Heidelberg, Germany

Contents of this file

Figures S1 to S3

_____
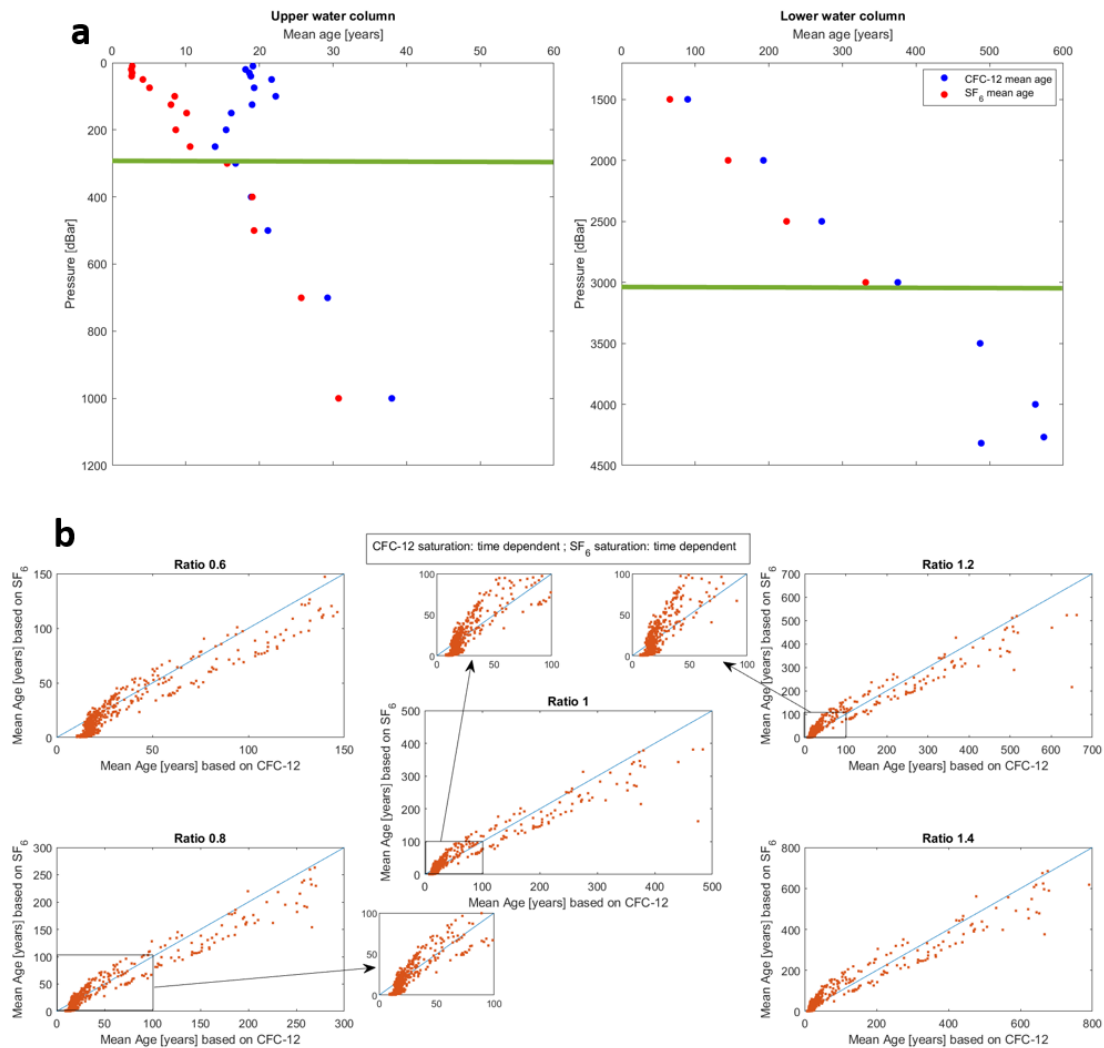
Figure S1. (a) Calculated mean age from CFC-12 and SF_6 measurements at the North Pole with the time dependent saturation and a Δ/Γ-ratio of 1. The green horizontal lines express increased uncertainty of the calculated mean age via CFC-12 concentrations in the upper 250m, due to the decreasing atmospheric concentrations and the bottom layer below 2000m for small SF_6 concentrations. (b) Calculated mean age from CFC-12 and SF_6 with different Δ/Γ-ratio compared. The saturations for each tracer were assumed to be time dependent and mean ages were compared for different ratios (0.6 until 1.4).
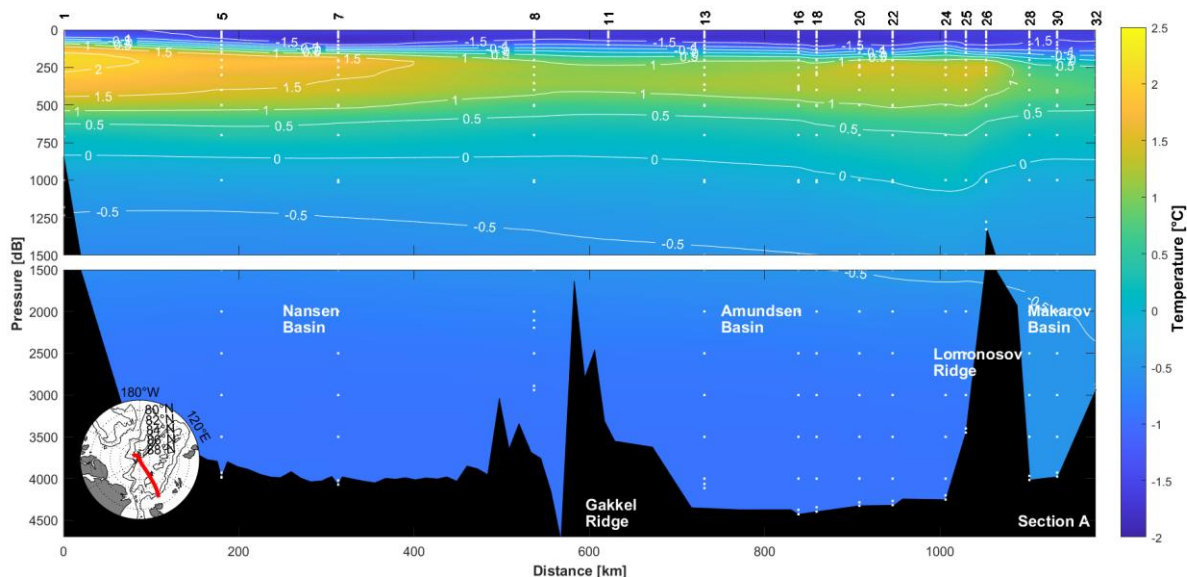
Figure S2. Distribution of Temperature [°C] along section A during the 2021 cruise. The upper panel shows the upper 1500m, while depths below 1500m are shown in the lower panel. The station numbers are displayed on top in black and the white dots below each number represent the sampling depths.
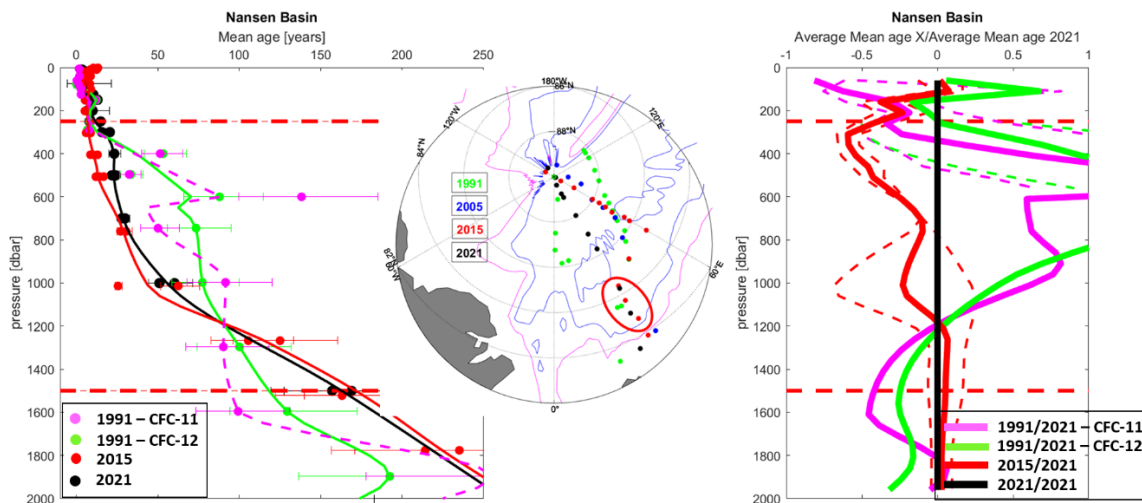

Figure S3. Mean age comparison of stations from year X: 1991 (green), 2015 (red) and 2021 (black) in the Nansen Basin from CFC-12 measurements and 1991 (magenta) from CFC-11 measurements. The left figure show data points from each station and depth

_____

above 2000 m in the respective basin, with the mean values demonstrated by the thin lines. The right figure shows the average relative mean age difference with respect to the data from 2021, with the dashed lines showing the standard deviation of the crossover analysis used for computing the mean values. The dashed red lines represent the focus area of this study, the intermediate layer (250-1500m).

4. Manuscript II

Changing composition of the
Gulf of St. Lawrence Inflow Waters

L. Gerke[1], T. Tanhua[1], W. A. Nesbitt[2], S. W. Stevens[3], D. W. R. Wallace[2]

1 GEOMAR Helmholtz Centre for Ocean Research Kiel, Kiel, Germany
2 Department of Oceanography, Dalhousie University, Halifax, Nova Scotia, Canada
3 Department of Earth and Ocean Sciences, The University of British Columbia, Vancouver, British Columbia, Canada

1 **Changing composition of the Gulf of St. Lawrence Inflow Waters**

2

3 **Lennart Gerke[1*]** (https://orcid.org/0000-0002-5783-1070)**, Toste Tanhua[1]**

4 **(**https://orcid.org/0000-0002-0313-2557**), William A. Nesbitt[2]** (https://orcid.org/0000-0002-

5 5217-3267**), Samuel W. Stevens[3]** (https://orcid.org/0000-0003-1108-6578**), Douglas W. R.**

6 **Wallace[2]** (https://orcid.org/0000-0001-7832-3887)

7

8 [1] GEOMAR Helmholtz Centre for Ocean Research Kiel, Kiel, Germany

9 [2] Department of Oceanography, Dalhousie University, Halifax, Nova Scotia, Canada

10 [3] Department of Earth and Ocean Sciences, The University of British Columbia, Vancouver,
11 British Columbia, Canada

12

13 * Corresponding author: Lennart Gerke (lgerke@geomar.de)

14

15 **Key Points:**

16 • The deep water age in the Laurentian Channel is younger near the Estuary head, in apparent
17 contradiction of regional circulation patterns

18 • The observed deep water age distributions confirm a recent shift in source water
19 composition towards entry of older Atlantic waters

20 • Deoxygenation of the deep water of the St. Lawrence Estuary and Gulf is expected to
21 amplify progressively.

22

_____

23 **Abstract**

24 The deep water of the Gulf of St. Lawrence has experienced a significant reduction in dissolved

25 oxygen content during the past decades. One suggested driver of this decrease is a change in the

26 composition of the deep inflowing water that ventilates the Gulf, consisting of a mix of warmer,

27 less-oxygenated North Atlantic Central Waters (NACW) and cooler, more-oxygenated Labrador

28 Current Waters (LCW). In this study, we use transient tracer measurements from two 2022 surveys

29 to estimate ages of water using the transit time distribution concept. These are used to examine

30 ventilation changes in the Gulf's deep waters and suggest that "older" water is present near the

31 Gulf entrance, indicating the presence of a larger proportion of NACW whereas "younger" water

32 is present further inshore, indicating a larger LCW proportion. The overall age distribution

33 suggests a recent shift in source water composition (NACW-dominated) and highlights the

34 potential for further deoxygenation.

35

36 **Plain Language Summary**

37 The Gulf of St. Lawrence is located on the east coast of Canada. Over the last several decades, a

38 decrease in dissolved oxygen has been observed in the deep water layers in this region, and hypoxic

39 conditions are intensifying and expanding within the most landward regions of the Gulf. As the

40 Gulf continues to be supplied with an inflow of water from the Atlantic Ocean, the continued drop

41 in oxygen has been attributed to changes in the composition of this inflowing water. We measured

42 man-made dissolved gases whose concentrations in subsurface water provide information about

43 how long the water has been removed from contact with the atmosphere, or the water's 'age'. The

44 observations show an age gradient within the Gulf, with older waters found close to the inflow

45 area and younger waters found further along its flow path into the Gulf. This confirms that there

46 has been a recent change in the age of water entering the Gulf from the Atlantic Ocean, with

47 'older', oxygen-depleted water now progressively replacing 'younger', more oxygenated water.

48 The transient tracer measurements show that the replacement with older water mass is not yet

49 complete, so that intensification and expansion of hypoxia is likely to continue.

50

51

52

_____

53 **1 Introduction**

54 The Gulf of St. Lawrence (GSL) is a large, semi-enclosed sea that connects to the North Atlantic

55 Ocean through the Cabot Strait to the Southeast and Strait of Belle Isle to the Northeast.

56 In recent years, this region has garnered attention due to a significant decline in dissolved oxygen

57 (DO) concentrations within the deep layer (e.g. Blais et al., 2023; Gilbert et al., 2010; Jutras et al.,

58 2020), leaving a growing area persistently hypoxic (DO < 62.5 µM) (Blais et al., 2023; Jutras et

59 al., 2023). Among other things, it was reported that the annual average of DO in the Estuary of the

60 Gulf dropped to 36 µM in 2022 (12 % saturation) (Blais et al., 2023). This phenomenon has been

61 observed increasingly in coastal zones worldwide during the past few decades, mainly due to

62 eutrophication triggered by the burning of fossil fuels and runoff of fertilizers (Diaz & Rosenberg,

63 2008). In the well-studied region at the head of the Lower St. Lawrence Estuary (LSLE), deep

64 layer DO values decreased from 130 µM to 60 µM between 1930 and 1984 where they then

65 remained stable until 2019. In 2020, concentrations rapidly decreased to a minimum of 35 µM

66 (Jutras et al., 2023), with further decline observed by Blais et al. (2023) in 2022. Following

67 extensive measurements in this region, the hypoxic zone was first documented in the LSLE

68 (Gilbert et al., 2005). Two-thirds of this decrease is estimated to be caused by a change in the

69 composition of the deep water mass entering the Gulf from the North Atlantic and one third being

70 due to eutrophication (Gilbert et al., 2005; Mucci et al., 2011). The development of persistently

71 hypoxic areas has a huge impact on the biology and ecosystem in such regions, e.g. on the

72 distribution of fish, as some are more tolerant to hypoxia than others (e.g. Brown-Vuillemin et al.,

73 2022; Dupont-Prinet et al., 2013; Petersen & Gamperl, 2010).

74 In this study, we use transient tracer measurements to examine the deep water and infer possible

75 changes in the regional ventilation. The term ventilation is understood as the transport of surface

76 waters to the interior of the ocean, and the age of the water refers to the time since it was last in

77 contact with the atmosphere. Ventilation is a measurable and quantifiable parameter that transports

78 atmosphere-ocean boundary perturbations, such as temperature or oxygen anomalies to the interior

79 ocean. Ventilation studies often rely on measurements of transient tracers, such as SF_6 and

80 CFC-12, which were measured for the first time in the Gulf during two cruises, in June and

81 November of 2022, as part of a deep tracer release experiment (TReX Deep; Stevens et al. (2024,

82 accepted for publication)) to understand circulation timescales. The transient tracers reported on

83 in this study were measured simultaneously to the tracer that was deliberately injected for the

84   TReX experiment. These measurements suggest that the deep water inflow, which, historically,

85   consisted of a mix of low-oxygenated, old North Atlantic Central Waters (NACW) and high-

86   oxygenated Labrador Current Waters (LCW), is now composed of almost entirely the NACW

87   endmember at the entrance point. However, some influence of the LCW is observed further

88   landward, different to what was reported by Jutras et al. (2023). As this NACW dominated source

89   water progressively transits along the Laurentian Channel towards the head of the Estuary, hypoxia

90   is expected to continue to develop in the coming years. This is in line with the observations by

91   Blais et al. (2023) who reported a continued decline in DO between 2020 and 2022 all throughout

92   the Estuary and Gulf.

93

94   **2 Hydrography**

95   The St. Lawrence Estuary and Gulf is one of the largest semi-enclosed Estuaries in the world and

96   is composed of three components: the Upper Estuary ranging from Ile d'Orleans to Tadoussac, the

97   LSLE spanning from Tadoussac to Pointe-des-Monts, and finally the GSL. The GSL is a large

98   marginal sea (approximate area of 240 000 km^2) located at the east coast of North America, and is

99   connected to the Atlantic Ocean through Cabot Strait, found between Nova Scotia and

100   Newfoundland in the Southeast, and to the Newfoundland and Labrador Shelf via the Strait of

101   Belle Isle in the Northeast (see Figure 1). Due to its width and depth, the Cabot Strait is the main

102   entry point for North Atlantic water, which enters as a deep inflow (Koutitonsky & Budgen, 1991).

103   The GSL includes itself three channels (darker blue areas in Figure 1), one south of Anticosti

104   Island (Laurentian Channel), one north of the Island (Anticosti Channel) and one channel towards

105   the Strait of Belle Isle (Esquiman Channel), all bordered by extensive shelf areas.
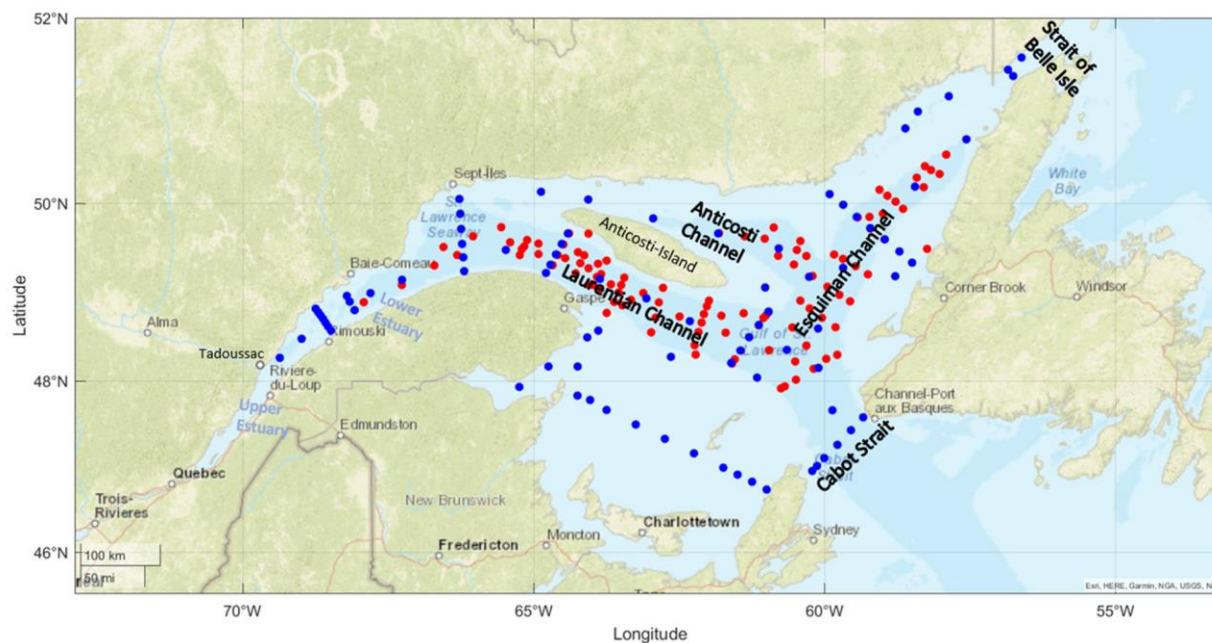
106

107 Figure 1: Display of the Gulf of St. Lawrence, with its Channels, Straits, the Lower and Upper Estuary and

108 the sampled station from the expeditions in June 2022 (TReX 2 – red dots) and November 2022 (DFO's

109 AZMP survey/TReX 4 – blue dots).

110

111 Two major currents feed the Gulf of St Lawrence with water masses from the Atlantic Ocean. The

112 two constituents are LCW and NACW, which enter at depths exceeding 200 m through the wide

113 and deep Cabot Strait, forming the relatively warm (2 °C to 7 °C) and saline (33 to 35) deep water

114 of the GSL (Lauzier & Trites, 1958; McLellan, 1957). This deep water is transported to the surface

115 at the terminus of the Laurentian Channel and head of the LSLE near Tadoussac, and at the end

116 and edges of each channel by bottom-boundary mixing processes (Cyr et al., 2015; Ingram, 1983;

117 Saucier et al., 2003).

118

119 In addition to the deep water entering the Gulf through the Cabot Strait, the water column structure

120 consists of an intermediate layer and a surface layer. The cold (-1.5 °C to 2 °C) and saline (31.5 to

121 33) intermediate layer (CIL-Cold Intermediate Layer), is mainly formed locally during winter due

122 to deep water mixing when cooling and formation of sea ice increase the density of the surface

123 water (Galbraith, 2006). A small fraction of the CIL also originates from the inflow of cold water

124 from the Labrador Shelf through the Strait of Belle Isle (Galbraith, 2006; Shaw & Galbraith, 2023).

125 The intermediate water mass in the LSLE and Upper St. Lawrence Estuary consists of less salty

126 water, which is renewed annually by saltier CIL water moving inward from the Gulf in spring

127 (Galbraith, 2006). The warm ($> 2\,°C$) and low salinity (27 to 31.5) surface water flows mainly

128 seaward, thereby transporting the upwelled deep water, the continental runoff freshwater from the

129 Estuary, and water from the north shore rivers towards the Atlantic (Galbraith, 2006; Gilbert &

130 Pettigrew, 1997). This outflow leaves the Gulf through the Cabot Strait on top of the more dense,

131 deep and intermediate-depth waters that are transported into the GSL (Dickie & Trites, 1983; Jutras

132 et al., 2020).

133

3 Data and Method

135 3.1 Data

136 The data analyzed and discussed in this study was obtained during two field campaigns, one in

137 June 2022 (TReX 2) and one in November 2022 (DFO's AZMP Survey/TReX 4), both carried out

138 on the Canadian research vessel '*R/V Coriolis II*'. The main focus of the TReX 2 field campaign

139 was to trace the previously released tracer trifluoromethyl sulphur pentafluoride (SF_5CF_3), as part

140 of a deep water tracer release experiment (TRE) aiming at monitoring the transport pathways for

141 the deep water in the GSL. The released tracer and the tracers focused on in this study, CFC-12

142 and SF_6, were measured simultaneously. The cruises sampled sections in the Laurentian Channel,

143 the Anticosti Channel, and the Esquiman Channel (see Figure 1 – red dots). The later cruise was

144 organized by the Department of Fisheries and Oceans, Canada (DFO) as part of the Atlantic Zone

145 Monitoring Program (AZMP). We were able to collect transient tracer samples on this cruise as

146 well, some also in Cabot Strait close to the Atlantic Ocean (Blais et al., 2023).

147

148 3.2 Methods

149 We use observations of the chronological transient tracers (CFC-12 and SF_6) from the two cruises

150 in 2022 to estimate water mass mean ages in the LSLE and GSL. Due to their increasing historical

151 concentration in the atmosphere and conservative behavior in seawater, these transient tracers are

152 useful to help quantify water mass ventilation time-scales. Given an assumed saturation state for

153 equilibrium between surface water and atmosphere, and knowing the tracers' atmospheric

154   concentration as a function of time, the historical input functions for each tracer at the sea surface

155   are known (Bullister, 2015; Bullister et al., 2002; Fine, 2011; Walker et al., 2000; Warner & Weiss,

156   1985; Weiss et al., 1985). Since the concentration of SF_6 continues to increase in the atmosphere,

157   it can be used to estimate ventilation over approximately the last 40 years. CFC-12, on the other

158   hand, is more appropriate for slightly older water masses, as its production started around 1940,

159   but its atmospheric concentration has decreased since 2002 (see Figure S3). Nevertheless, both

160   tracers used in combination as a tracer couple are needed to provide information on ventilation

161   patterns (e.g. Stöven et al., 2015).

162   The tracers were measured simultaneously on board of the research vessel with a gas

163   chromatographic – electron capture detector system attached to a custom purge and trap unit (GC-

164   ECD/PT5) (Bullister et al., 2002; Gerke et al., 2024, accepted for publication; Tanhua et al., 2005;

165   Tanhua et al., 2004). For details on calibration, see the supplemental material.

166   The transit time distribution (TTD) is a well-established concept to represent ventilation and allows

167   calculation of various characteristics of the age distribution for a parcel of water in the ocean,

168   including its mean age (Hall & Plumb, 1994; Shao et al., 2016; Trossman et al., 2012). As

169   described in detail in the supplemental material, we constrained the most suitable TTD for this

170   region using our measured tracers' concentrations in combination with a time dependent saturation

171   estimated by Raimondi et al. (2021) and a Δ/Γ-ratio of 1.2. Note that in this study, the term "age"

172   refers to the time elapsed since a water mass was last in contact with the atmosphere, i.e. since it

173   was ventilated. Here, we use temperature and salinity imprint to infer the composition of the Gulf

174   inflow waters, and the transient tracers to infer the ventilation timescale of these waters.

175   To obtain information on the properties of the inflowing deep water consisting of LCW and

176   NACW, we included data from the data product GLODAPv2.2022 (Global Ocean Data Analysis

177   Project version 2) (Lauvset et al., 2022), analyzing data after 2010 in the region close to the

178   entrance point for deep water, at the Cabot Strait.

179

180   4 Results

181   During both cruises, all three water masses of the GSL, the surface, intermediate and deep waters,

182   were clearly present (see Figure 2).

183

_____
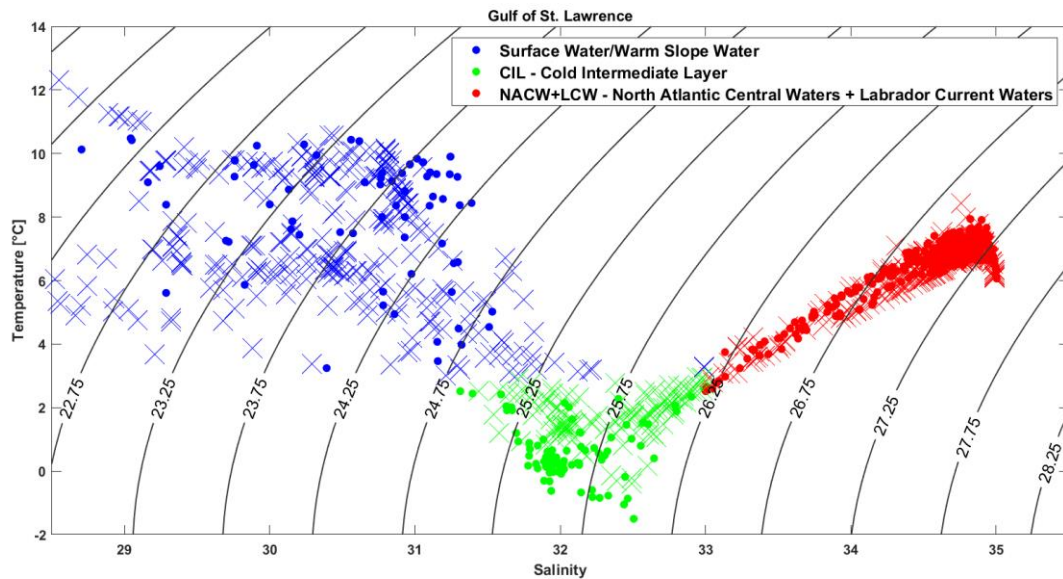
184

185   Figure 2: Potential temperature vs practical salinity plot, showing the three main layers of the GSL, as

186   indicated by different colors with density lines of σ_Θ from measurements of both cruises (TReX 2 – dots;

187   DFO's AZMP survey/TReX 4 – crosses). Note that the deep water (red) represents a mixture of warmer

188   and saltier NACW and colder and fresher LCW.

189

190   Both cruises showed a similar temperature vs. salinity structure throughout the water column. As

191   our study pertains to the region's deep layer, we concentrate on properties in the core of the deep

192   water mass on the $\sigma_\Theta = 27.26$ kg/m^3 isopycnal (see Figure 3). This focus is due to the high

193   abundance of measurements around this isopycnal, as the tracer was injected on this density

194   surface during the TReX Deep tracer injection cruise.

_____
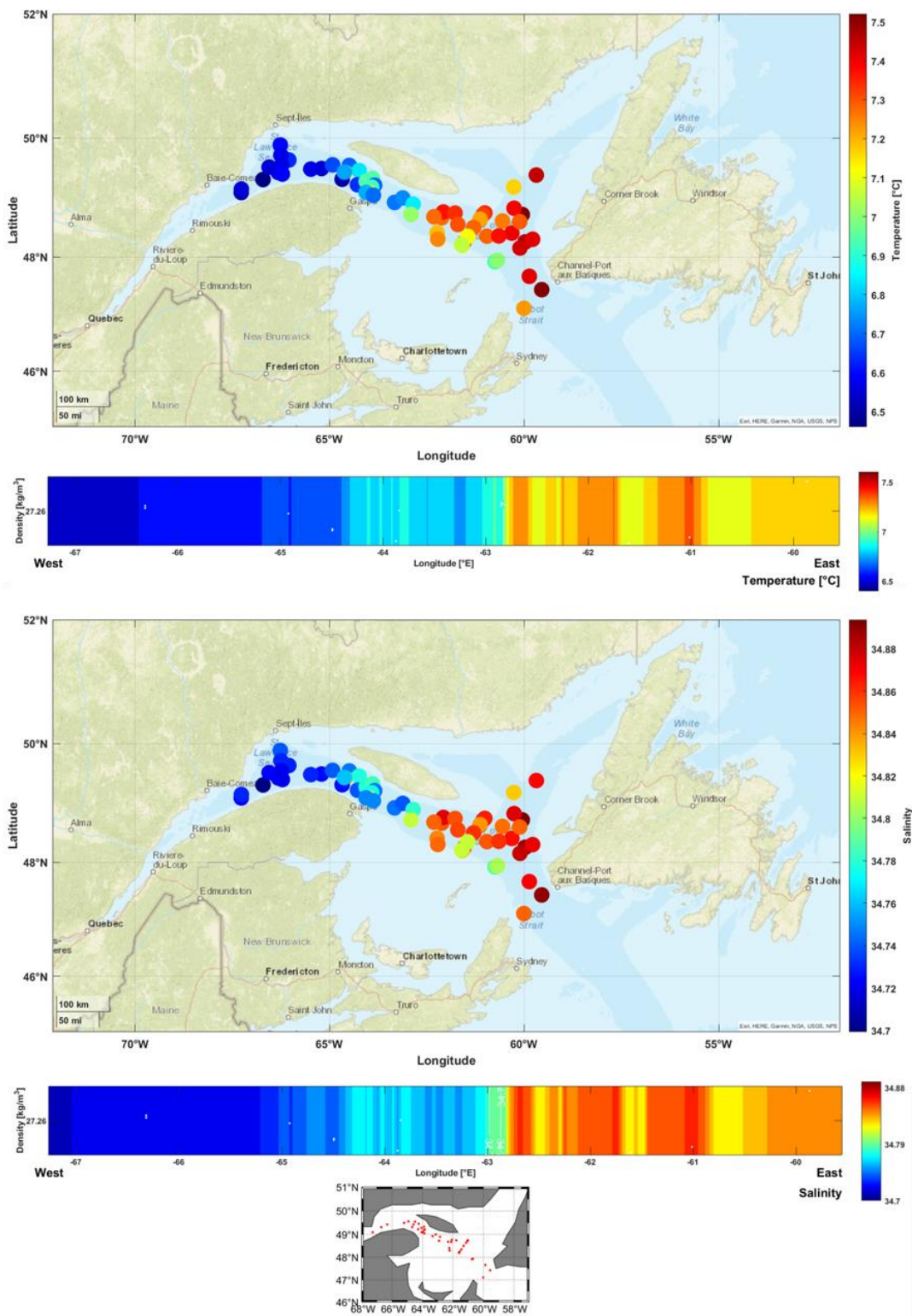
Figure 3: Potential Temperature (top) and Salinity (bottom) measured on the $\sigma_\Theta = 27.26$ kg/m^3 isopycnal in the Laurentian Channel and plotted against the longitude and latitude.

198

199   The results show the presence of colder and less saline waters on this isopycnal in the western end

200   of the Laurentian Channel compared to the eastern end, near the Cabot Strait. As described above,

201   the deep water represents a mixture of two water masses, LCW (salinity 33.4-35 and temperature

202   -0.7 °C to 3.2 °C) and NACW (salinity > 35 and temperature > 4 °C) (Jutras et al., 2020), which

203   flow from the Atlantic Ocean through Cabot Strait into the Gulf. Our results show a sudden

204   discontinuity in both variables at 62.8 °W, which predicts the influence of the warmer, more saline

205   NACW being more pronounced in the east.

206   When examining the mean age of water, as determined via SF_6 and CFC-12 tracer concentrations

207   in data collected since 2010 within the Atlantic region outside the Gulf of St. Lawrence, and at a

208   density of $\sigma_\Theta = 27.26$ kg/m^3 (see Figure 4), we observe oldest water to be located southwest of

209   Cabot Strait with considerably younger water located to the northeast.
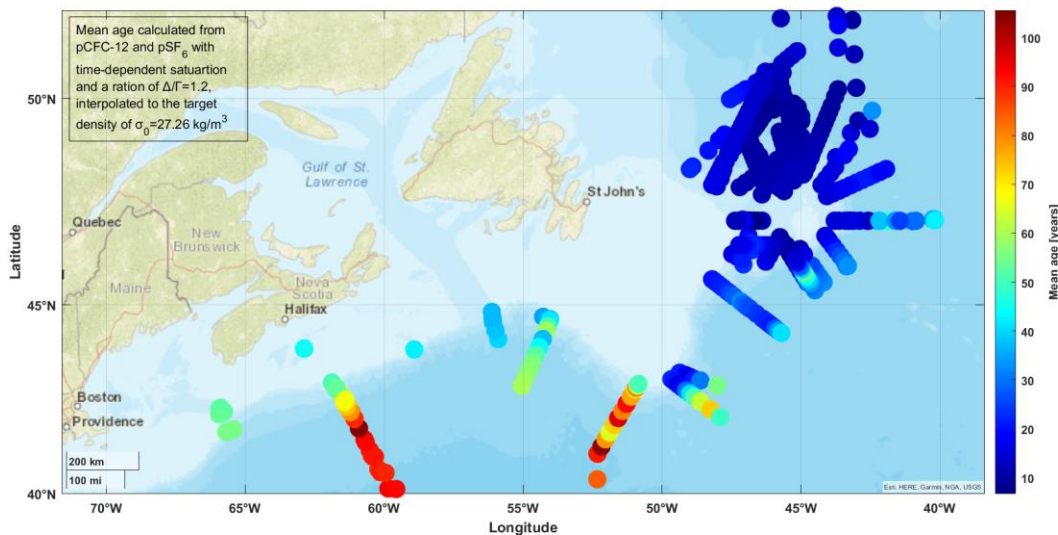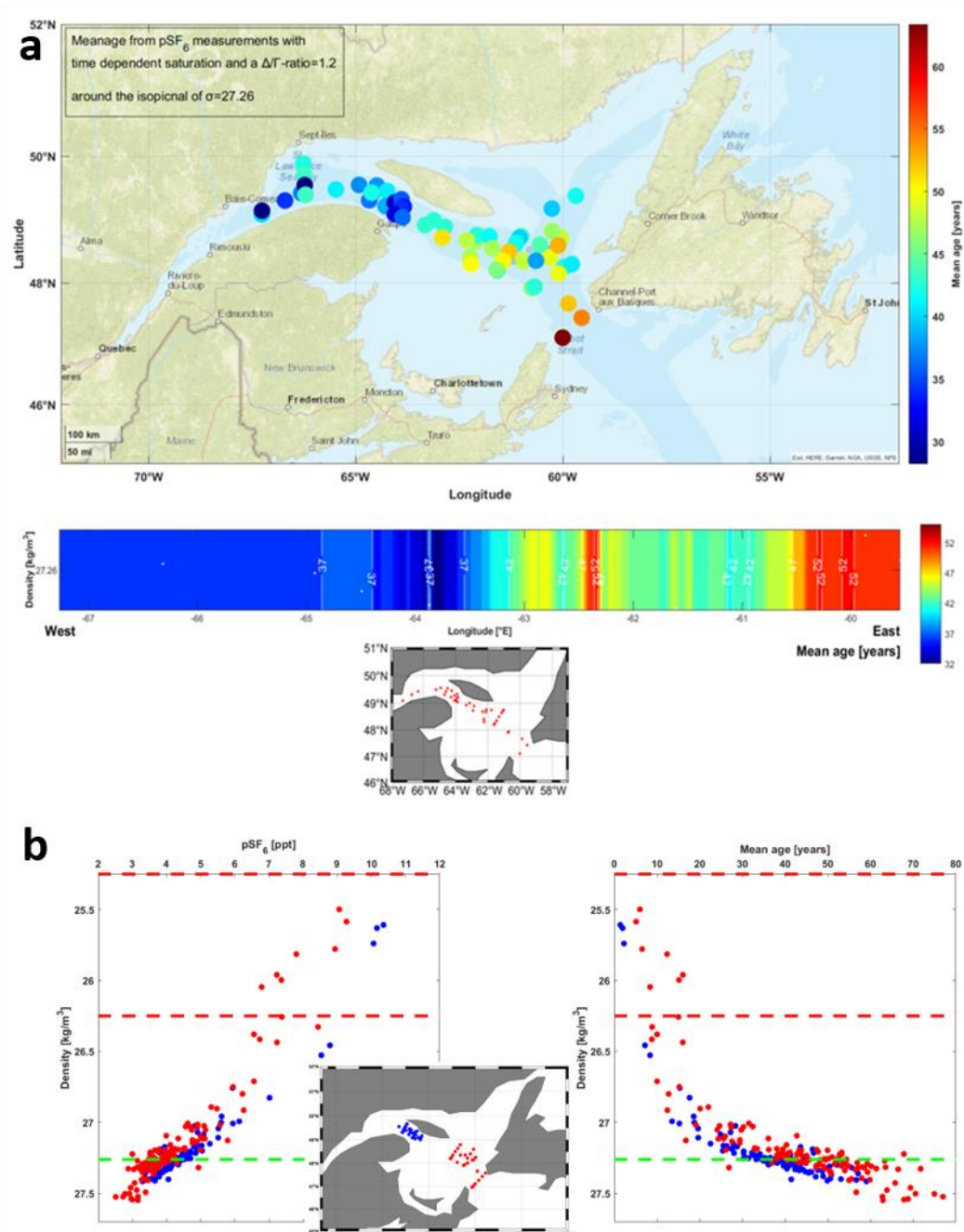

210

211   Figure 4: Interpolated mean age calculations from SF_6 and CFC-12 measurements to the target density of

212      $\sigma_\Theta = 27.26$ kg/m^3 after 2010 outside the Gulf of St. Lawrence.

213

214   This reflects the distribution of more recently ventilated LCW in the northeast and the older

215   NACW in the southwest. At the mouth of the Laurentian Channel, the waters tend to show

216   relatively old values (40 – 50 years), but the influence of the younger LCW is visible. The ages

217   are lower compared to measurements to the southwest of the inflow location.

_____

218   The mean age of the GSL deep water shows that the water close to the Cabot Strait is older
219   compared to that found in the Lower Estuary (see Figure 5a) which is consistent with the
220   distributions of temperature and salinity (see Figure 3). "Younger" waters will tend to have higher
221   LCW composition and "older" waters have higher NACW composition.

222

223   Figure 5: a) Mean age calculations from pSF$_6$ measurements at depths on the isopycnal of $\sigma_\Theta = 27.26$ kg/m^3
224   in the Laurentian Channel plotted against the longitude and latitude. b) Display of measured concentrations

225 in the CIL and the entire deep layer of the Laurentian Channel. The red dots display samples measured
226 further east and the blue dots the data from stations westward. The green line represents the isopycnal of
227 $\sigma_\Theta = 27.26$ and the red dotted lines the isopycnals of $\sigma_\Theta = 25.25$ and $\sigma_\Theta = 26.25$ marking the different water
228 layers.

229

230 This indicates a pronounced influence of older NACW on the deep water at the eastern end of the
231 Laurentian Channel with younger water, showing stronger influence of LCW, being found further
232 to the west along the channel. As the mean age progressively increases from west to east while the
233 prevailing direction of deep water flow being from east to west, this influence may to amplify over
234 time.
235 As mentioned previously, the sampling strategy primarily focused on the $\sigma_\Theta = 27.26$ kg/m^3
236 isopycnal. However, samples collected around this isopycnal in the deep layer show comparable
237 results, with higher tracer concentrations, resulting in younger water, observed further landward
238 in the entire deep layer compared to measurements taken closer to Cabot Strait (see Figure 5b). In
239 the intermediate layer, above the $\sigma_\Theta = 26.25$ kg/m^3 isopycnal, similar trends were observed,
240 although the data coverage here is rather scarce. The surface layer is not considered, due to the
241 absence of measured samples.

242

243 **5 Discussion**

244 Our observations of water mass age suggest a recent change in composition of the Gulf of St.
245 Lawrence's deep inflow. The along-channel property gradients show relatively young, cooler, and
246 fresher water in the Lower Estuary and western Gulf, with older, warmer and more saline water
247 entering through Cabot Strait (Figures 3 and 5a). This is the opposite pattern of water mass age as
248 would be expected if water is transported along the Laurentian Channel, westwards, from the
249 Atlantic inflow region in the east (Dickie & Trites, 1983). Therefore, these distributions show clear
250 evidence for a recent influx of water with increased NACW composition. Given the timing of our
251 sampling in 2022 and estimated transit times of 1-2 years from Cabot Strait to Anticosti Island
252 (Stevens et al., 2024, accepted for publication), the mid-channel transition from older to younger
253 water (around 63 °W; Figures 3 and 5a) would suggest that a significant shift in inflow composition
254 took place around 2020, as was evidenced by a dramatic decrease of bottom water oxygen content
255 around this time (Jutras et al., 2023).

_____

256 A further circulation feature evident in the property and age distributions is the cross-channel
257 variability, with older, warmer, more saline water entering along the northern boundary of the
258 Laurentian Channel and younger, cooler, less saline water being found along the southern
259 boundary (Figures 3 and 5a), indicative of a cyclonic circulation in the Laurentian Channel (Han
260 et al., 1999).

261

262 Given that the deep waters of the LSLE and GSL are composed of a mixture of NACW and LCW,
263 our results imply that the mixing proportions for this deep layer have changed significantly since
264 2020. An extended optimum multiparameter (eOMP) analyses of water mass properties has shown
265 that the influence of NACW in bottom water composition has grown in recent years (Jutras et al.,
266 2023). Our observations of transient tracers and water mass age distributions in the GSL are
267 consistent with this conclusion and reveal the signal of older, warmer, more saline water near the
268 Gulf entrance, whereas a significant younger, LCW component remains further inshore along the
269 Laurentian Channel. Whereas the eOMP analysis by Jutras et al. (2023) indicated that deep waters
270 in the Lower Estuary were comprised solely of NACW during 2022, we find evidence in the age
271 distributions for a remaining contribution of LCW to the deep water within the Lower Estuary.
272 This implies that further deoxygenation is likely to occur as this preexisting LCW contributions to
273 the deeper water continues to decline.

274

6 Conclusions

276 This study estimated mean ages for the bottom water in the Gulf of St. Lawrence from transient
277 tracer measurements. The observations show older water being present at the eastern end close to
278 the Cabot Strait and younger water being located landward, closer to the Estuary. The observed
279 pattern is counterintuitive, as the regional estuarine circulation would imply increasing mean age
280 moving further inshore. We show that this age distribution is the result of a change in the water
281 mass composition of Atlantic-derived water, whereby the relative contribution of older NACW
282 and younger LCW have changed over time. We postulate a ventilation change, resulting in the
283 weakening influence of the LCW on the deep waters of the GSL since 2020 showing a significant
284 mean age increase. As this shift is observed at the longitude of the eastern tip of Anticosti Island
285 in the Laurentian Channel, with younger waters still present inland, indicates that newer water has

286 not yet been completely flushed out of the GSL. Our observations of transient tracers provide direct
287 evidence for this change, supporting the findings of previous work that has focused on decreasing
288 oxygen concentrations in the Estuary (e.g. Blais et al., 2023; Jutras et al., 2023). Modelling studies
289 have attributed these recent changes in the deep water entering the Gulf of St. Lawrence to a slow-
290 down of the Atlantic Meridional Overturning Circulation driven by climate change (Caesar et al.,
291 2021; Caesar et al., 2018; Claret et al., 2018). This phenomenon could shift the Gulf Stream
292 northward (Joyce & Zhang, 2010), contract the subpolar gyre (Lohmann et al., 2009; Taylor &
293 Stephens, 1998) and thereby reduce the transport of LCW southwest towards the Cabot Strait. This
294 northward shift of the Gulf Stream is partly visibly in the mean age results presented outside the
295 Gulf (see Figure 4), where older water is found around the entry point into the Gulf, representing
296 the NACW mainly present at these latitudes since 2010 (Gonçalves Neto et al., 2021).

297

7 Outlook

299 Continued observations of transient tracers and oxygen inside the Lower St. Lawrence Estuary and
300 Gulf in the upcoming years are of importance, as these measurements could indicate if the deep
301 water continues to get older, and therefore further accentuates the hypoxia in this semi enclosed
302 sea, or alternatively, if the influence of NACW has already peaked. Further analysis of the transport
303 time of the bottom water from the Cabot Strait to the Lower Estuary (e.g., Stevens et al., 2024,
304 accepted for publication) will also be useful for prediction of the arrival time for NACW-dominant
305 deep water in the lower Estuary.

306

314 Oceans program and the Department of Fisheries and Oceans. SWS's participation was supported

315 by a TReX Graduate Award and a UBC Four-Year fellowship. We would also like to thank other

316 researchers on board for their support, especially Adriana Reitano, Marshal Thrasher, and Jeshua

317 Becker who analyzed tracer samples during DFO's AZMP survey/TReX4. Additionally, we would

318 like to acknowledge the work of all scientists and technicians who contributed to the data in

319 GLODAPv2.2022.

320

Open Research

321

322 The transient tracer and CTD data of the two cruises examined in this study will be made available

323 on the open research repository 'Canadian Integrated Ocean Observing System – St. Lawrence

324 Global Observatory' (CIOOS-SLGO) via (link will follow). Regarding the peer review process,

325 the data is temporarily uploaded as supporting information.

326 Historical transient tracer data used from the GLODAPv2.2022 data product can be found at

327 https://www.ncei.noaa.gov/access/ocean-carbon-acidification-data-

328 system/oceans/GLODAPv2_2022/.

329

References

330

331 Blais, M., Galbraith, P. S., Plourde, S., & Lehoux, C. (2023), Chemical and Biological Oceanographic Conditions in
332 the Estuary and Gulf of St. Lawrence during 2022, *Can. Tech. Rep. Hydrogr. Ocean Sci.*, *357*, v + 70 p.
333 Brown-Vuillemin, S., Chabot, D., Nozères, C., Tremblay, R., Sirois, P., & Robert, D. (2022), Diet composition of
334 redfish (Sebastes sp.) during periods of population collapse and massive resurgence in the Gulf of St. Lawrence,
335 *Frontiers in Marine Science*, *9*, doi:https://doi.org/10.3389/fmars.2022.963039.
336 Bullister, J. L. (2015), Atmospheric CFC-11, CFC-12, CFC-113, CCl4 and SF6 Histories*Rep.*, Carbon Dioxide
337 Information Analysis Center, http://cdiac.ornl.gov/ftp/oceans/CFC_ATM_Hist/CFC_ATM_Hist_2011.
338 Bullister, J. L., Wisegarver, D. P., & Menzia, F. A. (2002), The solubility of sulfur hexafluoride in water and
339 seawater, *Deep-Sea Res. I*, *49*(1), 175-187.
340 Caesar, L., McCarthy, G. D., Thornalley, D. J. R., Cahill, N., & Rahmstorf, S. (2021), Current Atlantic Meridional
341 Overturning Circulation weakest in last millennium, *Nature Geoscience*, doi:10.1038/s41561-021-00699-z.
342 Caesar, L., Rahmstorf, S., Robinson, A., Feulner, G., & Saba, V. (2018), Observed fingerprint of a weakening
343 Atlantic Ocean overturning ciruclation, *Nature*, *566*, 191-196, doi:https://doi.org/10.1038/s41586-018-0006-5.
344 Claret, M., Galbraith, E. D., Palter, J. B., Bianchi, D., Fennel, K., Gilbert, D., & Dunne, J. P. (2018), Rapid coastal
345 deoxygenation due to ocean circulation shift in the northwest Atlantic, *Nat Clim Change*, *8*(10), 868-872,
346 doi:10.1038/s41558-018-0263-1.
347 Cyr, F., Bourgault, D., Galbraith, P. S., & Gosselin, M. (2015), Turbulent nitrate fluxes in the Lower St. Lawrence
348 Estuary, Canada, *Journal of Geophysical Research: Oceans*, *120*(3), 2308-2330, doi:10.1002/2014jc010272.
349 Diaz, R. J., & Rosenberg, R. (2008), Spreading Dead Zones and Consequences for Marine Ecosystems, *Science*,
350 *321*(5891), 926-929, doi:DOI: 10.1126/science.1156401.
351 Dickie, L., & Trites, R. (1983), The Gulf of St. Lawrence, in: Ecosystems of the World: Estuaries and enclosed seas,
352 *edited by: Ketchum, B., New York, NY, Elsevier*, 403-425.
353 Dupont-Prinet, A., Pillet, M., Chabot, D., Hansen, T., Tremblay, R., & Audet, C. (2013), Northern shrimp (Pandalus
354 borealis) oxygen consumption and metabolic enzyme activities are severely constrained by hypocia in the Estuary

and Gulf of St. Lawrence, *Journal of Experimental Marine Biology and Ecology*, *448*, 298-307, doi:http://dx.doi.org/10.1016/j.jembe.2013.07.019.

Fine, R. A. (2011), Observations of CFCs and SF(6) as Ocean Tracers, *Annual Review of Marine Science, Vol 3*, *3*, 173-195, doi:10.1146/annurev.marine.010908.163933.

Galbraith, P. S. (2006), Winter water masses in the Gulf of St. Lawrence, *J. Geophys. Res.*, *111*(C6), doi:10.1029/2005jc003159.

Gerke, L., Arck, Y., & Tanhua, T. (2024), Temporal Variability of Ventilation in the Eurasian Arctic Ocean, edited.

Gilbert, D., & Pettigrew, B. (1997), Interannual variability (1948 - 1994) of the CIL core temperature in the Gulf of St. Lawrence, *Can. J. Fish. Aquat. Sci.*, *54*, 57-67.

Gilbert, D., Rabalais, N. N., Díaz, R. J., & Zhang, J. (2010), Evidence for greater oxygen decline rates in the coastal ocean than in the open ocean, *Biogeosciences*, *7*(7), 2283-2296, doi:10.5194/bg-7-2283-2010.

Gilbert, D., Sundby, B., Gobeil, C., Mucci, A., & Tremblay, G.-H. (2005), A seventy-two-year record of diminishing deep-water oxygen in the St. Lawrence estuary: The northwest Atlantic connection, *Limnol. Oceanogr.*, *50*(5), 1654-1666, doi:10.4319/lo.2005.50.5.1654.

Gonçalves Neto, A., Langan, J. A., & Palter, J. B. (2021), Changes in the Gulf Stream preceded rapid warming of the Northwest Atlantic Shelf, *Communications Earth & Environment*, *2*(1), doi:10.1038/s43247-021-00143-5.

Hall, T. M., & Plumb, R. A. (1994), Age as a diagnostic of stratospheric transport, *Journal of Geophysical Research: Atmospheres*, *99*(D1), 1059-1070, doi:10.1029/93JD03192.

Han, G., Loder, J. W., & Smith, P. C. (1999), Seasonal-Mean Hydrography and Circulation in the Gulf of St. Lawrence and on the Eastern Scotian and Southern Newfoundland Shelves, *Journal of Physical Oceanograohy*, *29*, 1279-1301, doi:https://doi.org/10.1175/1520-0485(1999)029<1279:SMHACI>2.0.CO;2.

Ingram, R. G. (1983), Vertical Mixing at the Head of the Laurentian Channel, *Estuarine, Coastal and Shelf Science*, *16*, 333-338, doi:https://doi.org/10.1016/0272-7714(83)90150-6.

Joyce, T. M., & Zhang, R. (2010), On the Path of the Gulf Stream and the Atlantic Meridional Overturning Circulation, *J Climate*, *23*(11), 3146-3154, doi:10.1175/2010jcli3310.1.

Jutras, M., Dufour, C. O., Mucci, A., Cyr, F., & Gilbert, D. (2020), Temporal Changes in the Causes of the Observed Oxygen Decline in the St. Lawrence Estuary, *Journal of Geophysical Research: Oceans*, *125*(12), doi:10.1029/2020jc016577.

Jutras, M., Mucci, A., Chaillou, G., Nesbitt, W. A., & Wallace, D. W. R. (2023), Temporal and spatial evolution of bottom-water hypoxia in the St Lawrence estuarine system, *Biogeosciences*, *20*(4), 839-849, doi:10.5194/bg-20-839-2023.

Koutitonsky, V. G., & Budgen, G. L. (1991), The physical oceanography of the Gulf of St. Lawrence: a review with emphasis on the synoptic variability of the motion, *Can. Spec. Publ. Fish. Aquat. Sci.*, *113*, 57-90.

Lauvset, S. K., et al. (2022), GLODAPv2.2022: the latest version of the global interior ocean biogeochemical data product, *Earth Syst. Sci. Data*, *14*(12), 5543-5572, doi:10.5194/essd-14-5543-2022.

Lauzier, L. M., & Trites, R. W. (1958), The deep waters of the Laurentian Channel, *J. Fish. Res. Board Can.*, *15*, 1247-1257.

Lohmann, K., Drange, H., & Bentsen, M. (2009), Response of the North Atlantic subpolar gyre to persistent North Atlantic oscillation like forcing, *Climate Dynamics*, *32*, 273-285, doi:https://doi.org/10.1007/s00382-008-0467-6.

McLellan, H. J. (1957), On the distinctness and origin of the slope water off the Scotian Shelf and its easterly flow south of the Grand Banks, *J. Fish. Res. Board Can.*, *14*, 213-239.

Mucci, A., Starr, M., Gilbert, D., & Sundby, B. (2011), Acidification of Lower St. Lawrence Estuary Bottom Waters, *Atmos.-Ocean*, *49*, 206-218, doi:10.1080/07055900.2011.599265.

Petersen, L. H., & Gamperl, A. K. (2010), Effect of acute and chronic hypoxia on the swimming performance, metabolic capacity and cardiac function of Atlantic cod (<i>Gadus morhua</i>), *Journal of Experimental Biology*, *213*(5), 808-819, doi:10.1242/jeb.033746.

Raimondi, L., Tanhua, T., Azetsu-Scott, K., Yashayaev, I., & Wallace, D. W. R. (2021), A 30 -Year Time Series of Transient Tracer-Based Estimates of Anthropogenic Carbon in the Central Labrador Sea, *Journal of Geophysical Research: Oceans*, *126*(5), e2020JC017092, doi:https://doi.org/10.1029/2020JC017092.

Saucier, F. J., Roy, F., Gilbert, D., Pellerin, P., & Ritchie, H. (2003), Modeling the formation and circulation processes of water masses and sea ice in the Gulf of St. Lawrence, Canada, *J. Geophys. Res.*, *108*, doi:https://doi.org/10.1029/2000JC000686.

Shao, A. E., Mecking, S., Thompson, L., & Sonnerup, R. E. (2016), Evaluating the use of 1-D transit time distributions to infer the mean state and variability of oceanic ventilation, *Journal of Geophysical Research: Oceans*, *121*(9), 6650-6670, doi:10.1002/2016jc011900.

_____

410   Shaw, J. L., & Galbraith, P. S. (2023), Climatology of Transport in the Strait of Belle Isle, *Journal of Geophysical*
411   *Research: Oceans*, *128*(2), doi:10.1029/2022jc019084.
412   Stevens, S. W., Pawlowicz, R., Tanhua, T., Gerke, L., Nesbitt, W. A., Drozdowski, A., Chassé, J., & Wallace, D. W.
413   R. (2024), A subsurface tracer release experiment in the Gulf of St. Lawrence, an increasingly hypoxic marginal sea,
414   edited.
415   Stöven, T., Tanhua, T., Hoppema, M., & Bullister, J. L. (2015), Perspectives of transient tracer applications and
416   limiting cases, *Ocean Sci.*, *11*(5), 699-718, doi:10.5194/os-11-699-2015.
417   Tanhua, T., Bulsiewicz, K., & Rhein, M. (2005), Spreading of overflow water from the Greenland to the Labrador
418   Sea, *Geophys. Res. Letters*, *32*(10), L10615, doi:10.1029/2005GL022700.
419   Tanhua, T., Olsson, K. A., & Fogelqvist, E. (2004), A first study of SF_6 as a transient tracer in the Southern Ocean,
420   *Deep-Sea Res. II*, *51*, 2683-2699.
421   Taylor, A. H., & Stephens, J. A. (1998), The North Atlantic Oscillation and the latitude of the Gulf Stream, *Tellus A:*
422   *Dynamic Meteorology and Oceanography*, *50*(1), 134, doi:10.3402/tellusa.v50i1.14517.
423   Trossman, D. S., Thompson, L., Mecking, S., & Warner, M. J. (2012), On the formation, ventilation, and erosion of
424   mode waters in the North Atlantic and Southern Oceans, *Journal of Geophysical Research: Oceans*, *117*(C9),
425   C09026, doi:10.1029/2012jc008090.
426   Walker, S. J., Weiss, R. F., & Salameh, P. K. (2000), Reconstructed histories of the annual mean atmospheric mole
427   fractions for the halocarbons CFC-11, CFC-12, CFC-113 and carbon tetrachloride, *J. Geophys. Res.*, *105*(C6),
428   14285-14296.
429   Warner, M. J., & Weiss, R. F. (1985), Solubilities of chlorofluorocarbons 11 and 12 in water and sea water, *Deep-*
430   *Sea Res.*, *32*(12), 1485-1497.
431   Weiss, R. F., Bullister, J. L., Gammon, R. H., & Warner, M. J. (1985), Atmospheric chlorofluoromethanes in the
432   deep equatorial Atlantic, *Nature*, *314*(6012), 608-610.
433

4.1 Supplemental Material Manuscript II

Changing composition of the
Gulf of St. Lawrence Inflow Waters

L. Gerke[1], T. Tanhua[1], W. A. Nesbitt[2], S. W. Stevens[3], D. W. R. Wallace[2]

1 GEOMAR Helmholtz Centre for Ocean Research Kiel, Kiel, Germany
2 Department of Oceanography, Dalhousie University, Halifax, Nova Scotia, Canada
3 Department of Earth and Ocean Sciences, The University of British Columbia, Vancouver, British Columbia, Canada

Geophysical Research Letters

Supporting Information for

Changing composition of the Gulf of St. Lawrence Inflow Waters

Lennart Gerke[1], Toste Tanhua[1], William A. Nesbitt[2], Samuel W. Stevens[3], Douglas W. R. Wallace[2]

[1]GEOMAR Helmholtz Centre for Ocean Research Kiel, Kiel, Germany

[2]Department of Oceanography, Dalhousie University, Steele Ocean Science Building, Halifax, Nova Scotia, Canada

[3]Department of Earth and Ocean Sciences, The University of British Columbia, Vancouver, British Columbia, Canada

Contents of this file

Text S1. _Analysis Method_

The gas chromatographic – electron capture detector (GC-ECD) system consisted of a precolumn packed with 30cm Porasil C and 60cm Molesieve 5A, followed by a main column packed with 200cm Carbograph 1AC and 20cm Molsieve 5A. Throughout the measurement, these components were kept at a constant temperature of 50°C. The function of these columns was to separate the various analytes before their concentration was determined with the electron capture detector.

Before the analysis, the purge and trap unit extracted the analytes from the water sample by bubbling N_2 gas though the sample and trapping them on a column of 100cm 1/16" tubing, packed with 70cm Heysep D. To ensure efficient trapping, this column was cooled

to -60 to -70°C using liquid nitrogen and subsequently heated to 100°C to desorb the analytes onto the precolumn.

Water samples were collected in 250mL glass syringes directly from the Niskin bottles. After temporary storage in a 0°C water bath, 200mL of the sample volume was injected into the purge and trap unit.

The system was calibrated by measuring precise volumes of a calibrated gaseous standard containing known concentrations of the analytes. A calibration curve was recorded at the beginning of each cruise and to determine any drift in the detector, point calibration was carried out daily.

The system has a detection limit of 0.04 fmol/kg and 0.2 fmol/kg for SF_6 and CFC-12, respectively and ideally a purge efficiency of above 95%. Due to high variations and very high concentrations reported during the TreX 4 expedition, we compared these results to measured samples during TreX 2 at similar density and location. This resulted in a shift of the CFC-12 measurements by -20% and SF_6 by -14% in order to achieve more plausible values (see Figure S1). We conclude that the measured values from TreX 2 are more accurate, as they show tracer concentrations in the surface layer, close to 100% saturation with the atmospheric values from 2022.
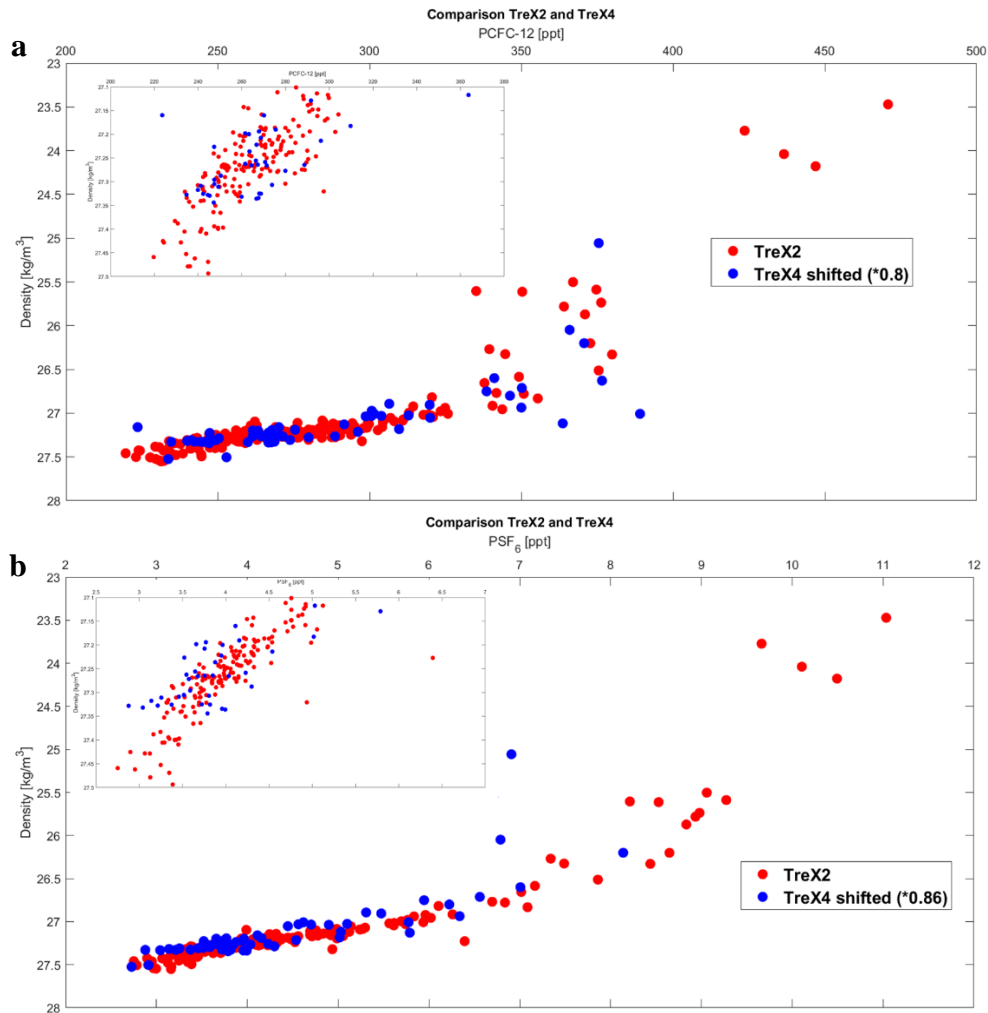
Figure S1: Display of the TreX 2 and shifted TreX4 data of (a) CFC-12 concentrations and (b) SF$_6$ concentrations. Each with a zoom into the area around the σ_Θ=27.26 kg/m^3 isopycnal, showing a large amount of comparable datapoints.

Text S2. *Estimated saturation and ratio of Δ/Γ*

The transit time distribution (TTD) is a well-established concept looking at ventilation timescales via mean age calculation using measured transient tracer concentrations. Thereby, one also achieves knowledge on the ratio between advective and diffusive transport of water masses from the surface into the interior ocean (e.g. Stöven & Tanhua, 2014; Waugh et al., 2003). TTD determination is possible using a tracer couple sampled at

the same location and time with significant different input functions, as being the case for SF_6 and CFC-12 during the two cruises analyzed in this study.

The method is based on a function describing the concentration of a single tracer at a certain location ($c(t_s,r)$), calculated using boundary concentrations of this tracer, related to their input function, and Green's function ($G(t,r)$) (see Equation 1).

$$c(t_s,r) = \int_0^\infty c_0(t_s - t)e^{-\lambda t} \times G(t,r)dt \qquad \textbf{1}$$

Applying four assumptions, being (1) a steady state, (2) a single source region, (3) no inner water interactions affecting the concentration of the tracer and (4) a one-dimensional flow and assuming an inverse Gaussian (IG) distribution for the age distribution, the Inverse Gaussian Transit Time Distribution (IG-TTD) provides one solution for the TTD. Since only distinct sampling points of a tracer are under consideration here, Green's function ($G(t)$) at a particular time can now be characterized by the mean age (Γ) and the width of the distribution (Δ), excluding the location (see Equation 2). (Schneider et al., 2012; Sonnerup et al., 2013; Stöven & Tanhua, 2014; Waugh et al., 2002).

$$G(t) = \sqrt{\frac{\Gamma^3}{4\pi\Delta^2 t^3}} \times \exp(\frac{-\Gamma(t-\Gamma)^2}{4\Delta^2 t}) \qquad \textbf{2}$$

The ratio of width to mean age (Δ/Γ), describes the above-mentioned relationship of advective to diffusive flow. A Δ/Γ-ratio of 1.0 is the unity ratio, Δ/Γ-ratio > 1 indicate a diffusive dominating process and a Δ/Γ-ratio < 1 a more advective ventilation of a water parcel.

The initial attempt to constrain the TTD involved comparing mean ages derived from CFC-12 to SF_6 measurements at the same location and time (see Figure S2a). However, this method did not yield nice results, as optimal outcomes would align the data points on top or close to the linear line. One potential reason for this discrepancy could be the estimate of a steady state in ventilation, which is not the case in the Gulf, see main part of the paper.

Additionally, uncertainties may arise from the assumption of an inverse Gaussian shape for the TTD, which might not be practical to use in this area and the presence of only rather young water, affecting the calculations from CFC-12 measurements, given their atmospheric history has been declining since 2002.

Trying to rule out this last uncertainty, we followed a different approach in taking only the SF_6 concentrations and calculating mean ages using varying ratios. From the resulting

mean ages, the assumed CFC-12 concentrations were determined by backwards calculation, and these values were then compared to the actual measured concentrations.
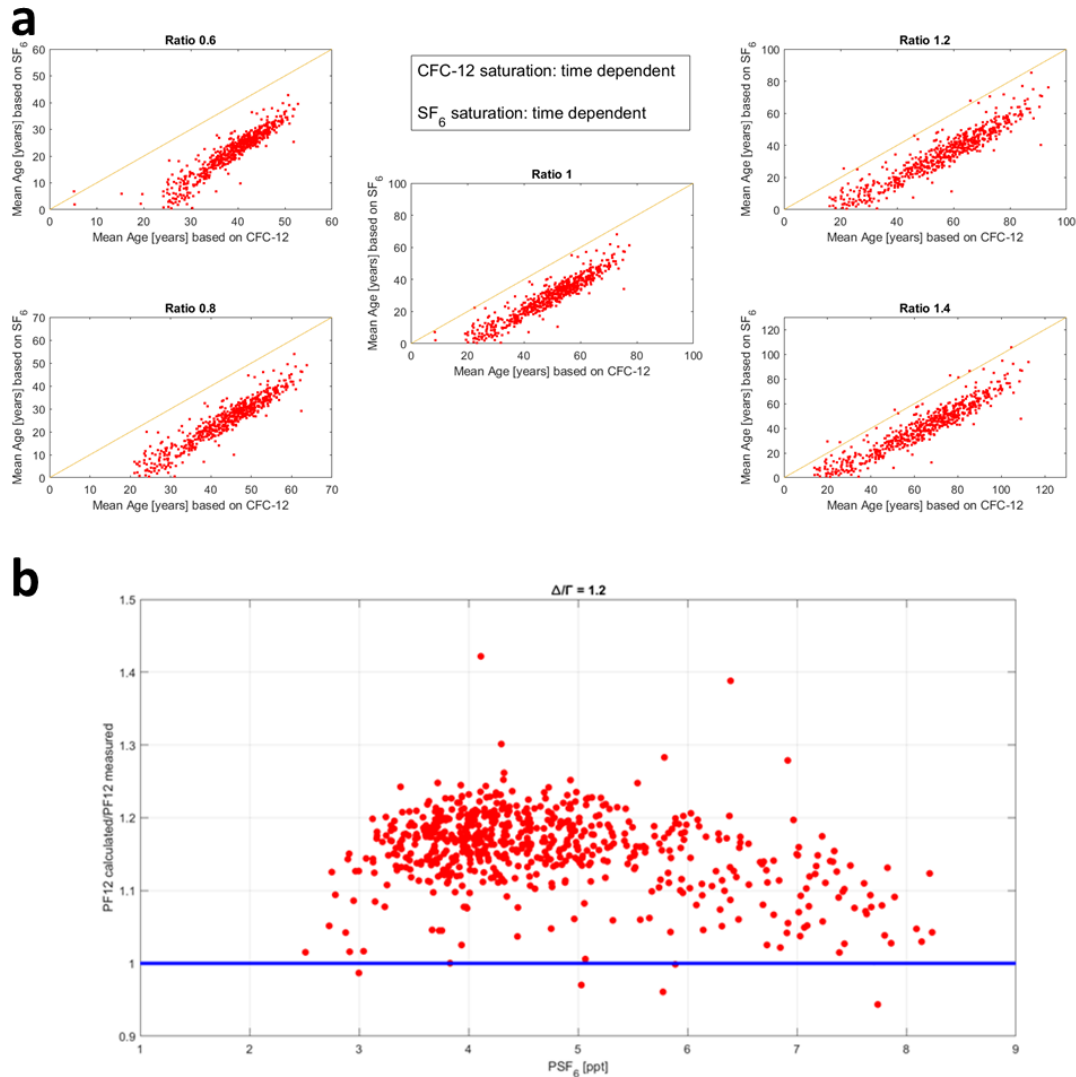

Figure S2: a) Comparison of calculated mean ages from CFC-12 and SF_6 with different Δ/Γ-ratio compared. The saturations for each tracer were assumed to be time dependent. b) Display of the relationship between calculated and measured PCFC-12 against PSF_6 concentrations using a ratio of $\Delta/\Gamma=1.2$ for the calculations.

Figure S2b shows the difference in the expected to measured concentrations of CFC-12 as a function of the SF_6 concentrations. As previously observed in the classical approach, the

best results are achieved when using a Δ/Γ-ratio of 1.8 (see Figure S2a and S5), indicated by datapoints being close to the strait blue line. Even for lower pSF_6 concentrations, the ratio of calculated to measured pCFC-12 is similar as for high concentrations, which indicates that the influence of the decreasing pCFC-12 in the atmosphere is not very pronounced in the calculation and that the difficulty in constraining the TTD results mainly from the assumptions made for the calculation. Being the steady state, the single source region and the inverse Gaussian shape.

Nonetheless, as the uncertainty is displayed from a variety of different uncertainties, we conclude in using a Δ/Γ-ratio of 1.2, thereby a slightly diffusive dominated flow, plus the time dependent saturation by (Raimondi et al., 2021) for the calculation of mean ages in this study. This conclusion is drawn from the results, which indicate satisfying solutions when employing a Δ/Γ-ratio of 1.2, with negligible difference to the best results obtained from using a Δ/Γ-ratio of 1.8. Additionally, it should be noted that with increasing Δ/Γ-ratio, the calculated mean ages become more sensitive to deviations in saturation and tracer age (Stöven et al., 2015).

For the data inside the Gulf of St. Lawrence we primarily focus on the mean ages calculated from SF_6 concentrations due to rather young waters, but for the data outside the Gulf we also include data from CFC-12 concentrations due to the larger quantity of available measurements.
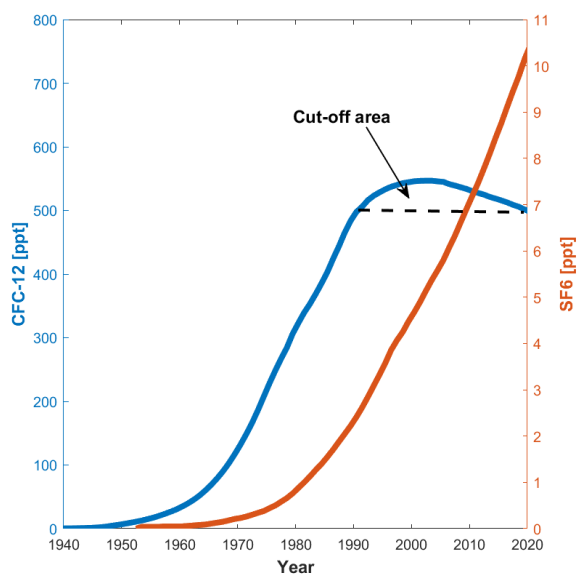
_____

Additional Supplemental Figures

Figure S3: Atmospheric concentrations of the two transient tracers used in this study. CFC-12 (blue) with its by now decreasing atmospheric concentration and SF_6 (red) with steadily increasing concentrations since 1960. Both tracer concentrations are represented in ppt (parts per trillion) here.
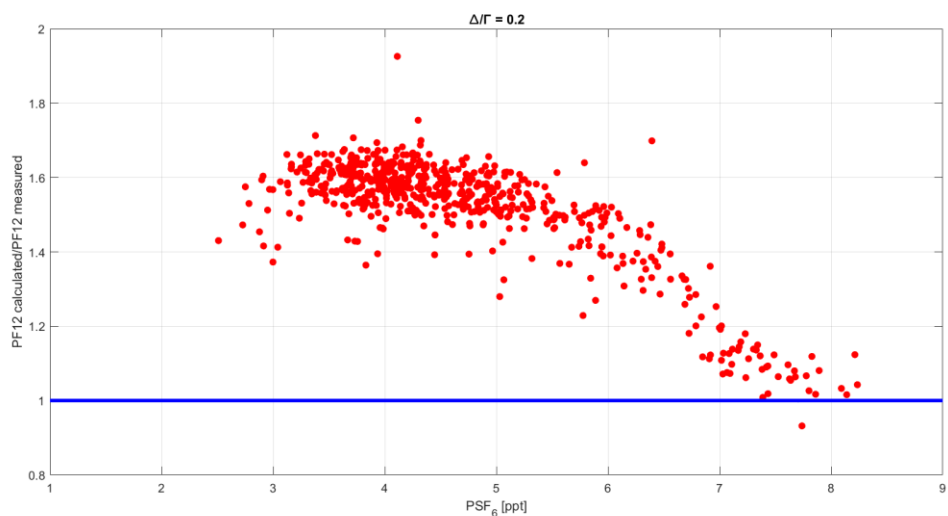

Figure S4: Display of the relationship between calculated and measured CFC-12 against PSF_6 concentrations using a ratio of $\Delta/\Gamma=0.2$ for the calculation of the CFC-12 concentrations.
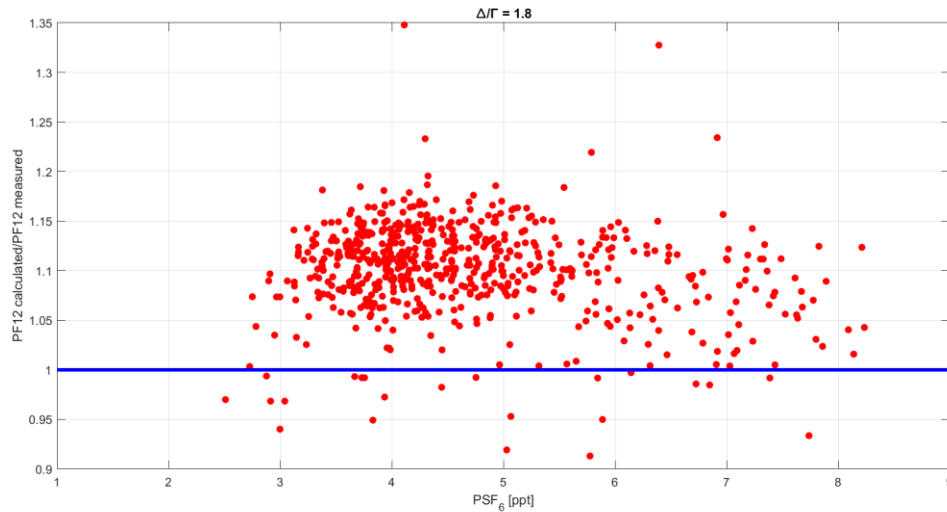
Figure S5: Display of the relationship between calculated and measured CFC-12 against PSF_6 concentrations using a ratio of Δ/Γ=1.8 for the calculation of the CFC-12 concentrations.

References

Raimondi, L., Tanhua, T., Azetsu-Scott, K., Yashayaev, I., & Wallace, D. W. R. (2021), A 30 -Year Time Series of Transient Tracer-Based Estimates of Anthropogenic Carbon in the Central Labrador Sea, *Journal of Geophysical Research: Oceans*, *126*(5), e2020JC017092, doi:https://doi.org/10.1029/2020JC017092.

Schneider, A., Tanhua, T., Körtzinger, A., & Wallace, D. W. R. (2012), An evaluation of tracer fields and anthropogenic carbon in the equatorial and the tropical North Atlantic, *Deep Sea Research Part I: Oceanographic Research Papers*, *67*(0), 85-97, doi:10.1016/j.dsr.2012.05.007.

Sonnerup, R. E., Mecking, S., & Bullister, J. L. (2013), Transit time distributions and oxygen utilization rates in the Northeast Pacific Ocean from chlorofluorocarbons and sulfur hexafluoride, *Deep Sea Research Part I: Oceanographic Research Papers*, *72*, 61-71, doi:http://dx.doi.org/10.1016/j.dsr.2012.10.013.

Stöven, T., & Tanhua, T. (2014), Ventilation of the Mediterranean Sea constrained by multiple transient tracer measurements, *Ocean Sci.*, *10*(3), 439-457, doi:10.5194/os-10-439-2014.

Stöven, T., Tanhua, T., Hoppema, M., & Bullister, J. L. (2015), Perspectives of transient tracer applications and limiting cases, *Ocean Sci.*, *11*(5), 699-718, doi:10.5194/os-11-699-2015.

Waugh, D. W., Hall, T. M., & Haine, T. W. N. (2003), Relationship among tracer ages, *J. Geophys. Res.*, *108*(C5), doi:doi:10.1029/2002JC001325.

Waugh, D. W., Vollmer, M. K., Weiss, R. F., Haine, T. W. N., & Hall, T. M. (2002), Transit time distributions in Lake Issyk-Kul, *Geophysical Research Letters*, *29*(24).

5. Manuscript III

Multiple tracer approach to analyze Arctic Ocean Ventilation

L. Gerke[1], T. Tanhua[1]

1 GEOMAR Helmholtz Centre for Ocean Research Kiel, Kiel, Germany

This chapter is a manuscript in preparation

Multiple tracer approach to analyze Arctic Ocean Ventilation

Lennart Gerke[1*] (https://orcid.org/0000-0002-5783-1070**), Toste Tanhua[1]**

(https://orcid.org/0000-0002-0313-2557**)**

[1] GEOMAR Helmholtz Centre for Ocean Research Kiel, Kiel, Germany

* Corresponding authors: Lennart Gerke (lgerke@geomar.de) ; Toste Tanhua (ttanhua@geomar.de)

Key points:

- HCFC's and HFC's can serve as efficient gaseous ocean tracers in the Arctic region
- Advective flow of water masses in the Atlantic layer, shifting to more diffusive characteristics at greater depths
- Presence of two distinct water masses mixing in specific areas of the Arctic Ocean

Abstract

In this study we analyzed the applicability of new chronological transient tracers in observing ventilation patterns in the rapidly changing environment of the Arctic Ocean. The limited amount of data currently available, which rely mainly on the two well-established tracers CFC-12 and SF_6, restricts the precision in the analysis of ventilation dynamics in this region. By including hydrochlorofluorocarbons and hydrofluorocarbons (referred to as 'Medusa'-tracers), collected during the SAS-Oden 2021 expedition at six Transient Tracer Super Stations, alongside the commonly used CFC-12 and SF_6, we introduce a unique set of tracers for the ventilation analysis. The results demonstrate the suitability and effectiveness including 'Medusa'-tracers in the observations. The inclusion helped to constrain parameters such as mean age and width of age distributions more precisely and thereby increased the accuracy in the analysis. Using the precisely measured tracer concentrations and applying the transit time distribution (TTD) method, we could show that ventilation is dominated by adjective flow within the Atlantic layer (above 1000 m) and that this is shifted to more diffusive characteristics at greater depths. The introduction of multiple different tracer pairs, which were employed to analyze the ventilation characteristics, identified regions where two water masses with similar densities, but distinct mean ages mix within the Arctic Ocean. In these cases, the extensive range of tracer measurements allowed an expansion from the assumption of a one-inverse Gaussian to a two-inverse Gaussian distribution of ages representing the TTD, thereby taking into account a mixing of two water masses. The multi-tracer approach also identified regions, specifically the Makarov Basin, where the assumption of a one-inverse Gaussian distribution to represent the TTD is practicable, as the results from all tracer pairs are in line. Thus, the inclusion of hydrochlorofluorocarbon and hydrofluorocarbon data helps to increase accuracy in the calculation of water mass ages and ventilation patterns.

Plain Language Summary

Ventilation analysis in the ocean is often based on transient tracer measurements that permit the use of the transit time distribution (TTD) method to describe age parameters of a given water mass in the ocean's interior. In this study, we introduce a novel multiple tracer approach to determine ventilation parameters in the Arctic Ocean, a region of high interest due to the increasing impact of climate change-related influences. The tracer samples were collected

during a research expedition on the icebreaker Oden in 2021 at six, so called Transient Tracer Super Stations, producing an exclusive collection of tracers sampled at the same locations and times. The measured concentrations of the new tracers, several different hydrochlorofluorocarbons and hydrofluorocarbons, in combination with the well-established tracers CFC-12 and SF_6, were used to constrain age parameters by employing the TTD method and assuming a one-inverse Gaussian distribution. The results, using different tracer pairs, show an advective-dominated flow of water masses in the Atlantic layer of the Arctic Ocean (above 1000 m), changing to more diffusive characteristics at lower depths. In addition, the multiple tracer analysis identified certain areas in the Arctic Ocean which are affected by two water masses with similar densities but different ventilation characteristics. Here, results for the individual tracer pairs differed, but because data of multiple tracers were available, the TTD method could be expanded to be represented by a two-inverse Gaussian distribution of ages which takes into account the presence of two different water masses that eventually mix in the respective region.

1. Introduction

Transient tracers represent a powerful tool to assess ocean ventilation. They are particularly well suited for tracking water movements because their atmospheric histories and their solubilities in seawater are often well documented, and because they typically experience no inner water interactions (Bullister & Warner, 2017; Bullister et al., 2002; Warner & Weiss, 1985). Consequently, when measured within a water parcel, transient tracers serve as reliable age indicators, i.e. they report the time a water parcel was last in contact with the atmosphere. Well known tracers often used in oceanography are anthropogenic gaseous tracers, such as CFC-12 (chlorofluorocarbon-12) and SF_6 (sulphur hexafluoride) (e.g. Bullister et al., 2006; Stöven, 2011; Tanhua et al., 2013). However, due to environmental issues the production of these gases was reduced or even banned, limiting their use as oceanographic age tracers (e.g. Stöven et al., 2015). Therefore, the search for new ocean tracers attracts increasing attention on one hand, to replace CFC-12 and on the other hand, to increase accuracy in the age determination based on tracer measurements. Already used and well-studied are radionuclide tracers, such as Iodine-129, Uranium-236 (Casacuberta et al., 2018; Casacuberta et al., 2016; Wefing, 2021) and Argon-39, the latter being especially valuable for deep water analyses. However, in particular, concentrations of Argon-39 are difficult to determine with high accuracy (Lu et al., 2014; Ritterbusch et al., 2014). Thus, other gaseous compounds are also tested for their applicability as tracers in ocean ventilation analyses. These include hydrofluorocarbons (HFC's) and hydrochlorofluorocarbons (HCFC's) (Li et al., 2019).

Ocean ventilation is a physical process which describes the interplay between the atmosphere and the ocean's interior, specifically, the transfer of water masses from the surface mixed layer to the deep ocean. It is the primary pathway of transporting surface water, which due to air-sea gas exchange itself is affected by atmospheric perturbations, such as changes in temperature and gas concentrations, into the ocean's interior (e.g. Azetsu-Scott et al., 2005; Krysell & Wallace, 1988; Talley et al., 2016; Tanhua et al., 2009; Thiele & Sarmiento, 1990; Wallace et al., 1987). Understanding ventilation in different parts of the world's oceans is essential to interpret possible fluctuations in ocean dynamics caused, e.g., by climate change or seasonal variability. Processes affecting ventilation dynamics range from wind-driven and tidal mixing, to subduction, deep water convection, brine enhanced deep water mixing and deep-water circulation, as well as deep water upwelling (e.g. D'Asaro, 1985; Ferrari & Wunsch, 2009; Rainville et al., 2011). Together, these processes define the ocean ventilation, thus the

transport of water masses via advective and diffusive pathways, as well as their mixing within the interior of the ocean (Khatiwala et al., 2001).

Among others, anthropogenic carbon (C_{ant}) is also subject to this process of transporting atmospheric perturbations into the interior ocean, where it is stored long-term. C_{ant} defines human activities emitting carbon dioxide into the atmosphere (e.g. by fossil fuel burning or cement production) and causing the atmospheric concentration to increase since preindustrial times, exceeding 280 parts per million (ppm atmospheric concentration before industrialization) (e.g. Rajasakaren et al., 2019). One region storing notable amounts of C_{ant} is the Arctic Ocean (AO). Here, a significant portion (up to 2%) of the total C_{ant} (2.5 to 3.3 Pg-C (pentagrams of carbon), normalized to 2005 (Tanhua et al., 2009)) is stored due to unique ventilation and circulation patterns (e.g. Fabry et al., 2009; MacGilchrist et al., 2014; Terhaar et al., 2020). Moreover, recent studies report an even higher CO_2 storage capacity of the AO, accounting for 4-8 % of the global storage and thus indicating a pivotal role of the AO in counteracting climate change (DeVries et al., 2023; Yasunaka et al., 2023). Previous investigations also showed that the majority of the C_{ant} is stored within the surface and intermediate layers (Anderson et al., 1998; Tanhua et al., 2009), with a significant influx by Atlantic Waters (AW) entering the AO through the Fram Strait and the Barents Sea (Ulfsbo et al., 2018).

The AO is of particular interest not only due to its lateral and vertical transport of C_{ant}, but also because of its vulnerability to the impacts of climate change. This reflects itself in the declining sea ice coverage, decreasing at a rate of 12.8 ± 2.4 % per decade since 1979 (Meredith et al., 2019; Nghiem et al., 2006), and the pronounced warming trend, attributed partially also to increasingly warmer AW entering at intermediate depths. These rapid changes likely affect the C_{ant} storage capacity and more generally, might influence ventilation and circulation patterns in the AO (Gerke et al., 2024, accepted for publication). Together, this underscores the need to investigate and understand these processes in the AO in more detail.

Ventilation itself is difficult to quantify precisely as it is affected by a complexity of the various mechanisms and cannot be measured directly. Studies often rely on transient tracer measurements and employ the transit time distribution (TTD) method to obtain information on the ventilation within certain regions (e.g. Olsen et al., 2010; Sonnerup et al., 2013; Stöven & Tanhua, 2014). Nonetheless, due to a variety of assumptions required to constrain the TTD, and the currently limited amount of tracer measurements in the AO, the ventilation in this

area remains poorly described. In this study, we exploit a unique set of multiple transient tracer measurements, collected at various location throughout the AO, to gain more insights into the ventilation patterns. This is achieved by applying the TTD method, constraining 'ages' of water masses, defined as the time since a particular water parcel was last in contact with the atmosphere, and by characterizing the advective and diffusive flow characteristics.

A set of different transient tracers with significantly different input functions is ideally suited to derive age-related data that describe ventilation. By measuring concentrations of such multiple tracers at the same location and time, more information can be obtained to constrain the most probable TTD. Following this approach, we examined data from multiple gaseous transient tracer measurements in different regions of the AO, focusing on the intermediate water column (100 – 1500 m). These tracers encompass six chronological tracers described in detail below, and we show and discuss their advantages and disadvantages in analyzing ocean ventilation dynamics. These analyses reveal advective to diffusive characteristics in the ventilation patterns at different depths. Furthermore, we calculated mean and mode ages of the respective water masses employing the local concentrations of the variety of different tracer pair combinations to constrain the TTD. The novel approach of using multiple tracers to obtain the most probable TTD underscores the value of sampling more than two tracers simultaneously for ventilation analyses.

2. Transient tracers

CFC-12 is an anthropogenic tracer with well documented atmospheric concentrations since the 1940s (see Figure 1a). Its production history is well described in Stöven et al. (2015) and due to its atmospheric lifespan, CFC-12 concentrations still show sustained high values, even though the concentration started to decline since 2002 (Fine, 2011; Stöven et al., 2015). Therefore, CFC-12 can be employed as an ocean tracer for intermediate water masses, whereas its use is increasingly limited for young water masses as the measured concentrations are inconclusive, represented by the cut-off area in Figure 1a.

Atmospheric data of SF_6, were first measured at the beginning of the 20th century, and are also well documented showing exponentially increasing concentrations since the 1960s (see Figure 1a). The anthropogenic tracer history of SF_6 is again described in detail by Stöven et al. (2015) revealing that it serves as an appropriate tracer for surface and partly also intermediate

water masses. However, its use is limited due to the overall rather low concentrations, resulting in detection difficulties at deeper levels where lower concentrations are met.

CFC-12 and SF_6 are not only well-suited oceanographic tracers because of their atmospheric concentration history, they also have established solubility functions in sea water. The solubility, a function of temperature, salinity and the physical nature of the molecule, is extremely relevant when examining the air-sea gas exchange, considering the degree of saturation and the atmospheric variation over time. As these parameters are all well-known for CFC-12 and SF_6, both tracers have proven extremely useful in the analysis of ventilation and ocean circulation as well as accompanying mixing processes (Fine, 2011). Moreover, both tracers have been measured multiple times in various regions of the world's oceans providing strong historical data sets (Sonnerup et al., 2013; Stöven & Tanhua, 2014; Tanhua et al., 2009).
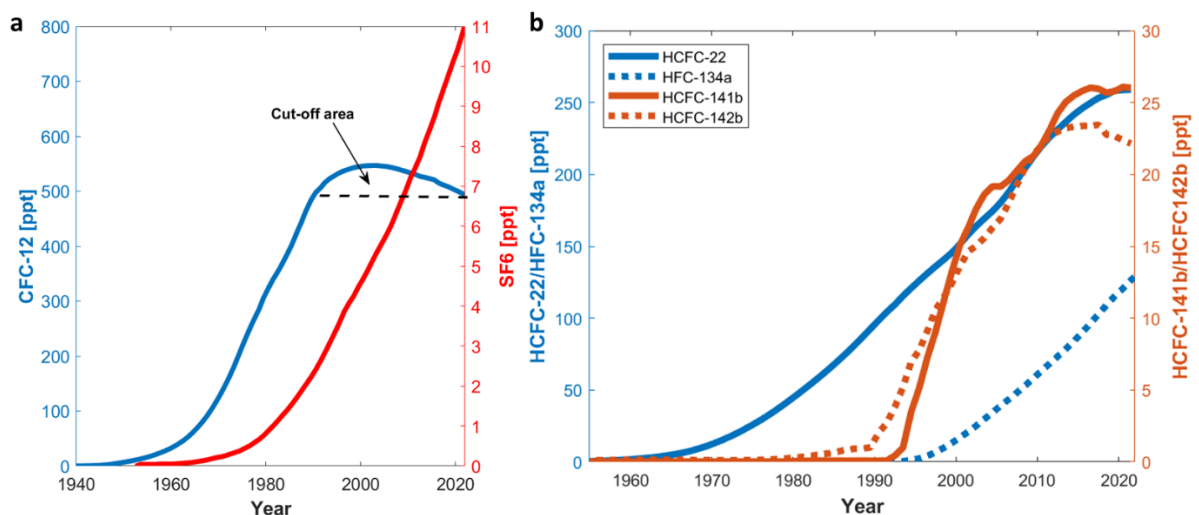

Figure 1: Atmospheric concentrations of (a) the two transient tracers CFC-12 (blue) and SF_6 (red) (Bullister & Warner, 2017), and (b) of the 'Medusa'-tracers HCFC-22 (solid blue), HFC-134a (dotted blue), HCFC-141b (solid red) and HCFC-142b (dotted red) (Montzka et al., 2009) (https://gml.noaa.gov/aftp/data/hats/hcfcs/; https://gml.noaa.gov/aftp/data/hats/hfcs/). All tracer concentrations are given in partial pressure values (ppt - parts per trillion).

Other ocean tracers that might help to replace CFC-12 for the analysis of young water masses in the future and could aid in a more detailed ventilation analysis are HCFC's, such as HCFC-22 (Chlorodifluoromethane), HCFC-141b (1,1-Dichloro-1-fluoroethane) and HCFC-142b (1-Chloro-1,1-difluoroethane), and HFC's (HFC-134a – 1,1,1,2-tetrafluoroethane). These so called 'Medusa'-tracers also show well established atmospheric concentration records (see Figure 1b), have no natural background and can be measured precisely, making them appropriate

candidates as ocean tracers (Li et al., 2019). They were initially produced in the mid-1900s and show increasing atmospheric concentrations since then. HCFC-22 increased since 1965, and HCFC-142b and HCFC-141b since 1980 and 1990, respectively. HFC-134a is the tracer with the most recent appearance in the atmosphere, starting to increase exponentially since 1995. In recent years, the measured concentrations of HCFC-142b decreased slightly and HCFC-141b seems to have reached a plateau since 2015. A more detailed explanation of each of these tracers and their atmospheric history can be found in Li et al. (2019).

3. Data collection and analysis

3.1. Study region

Transient tracer data analyzed in this study were collected in different areas of the AO during the 'SAS-Oden 2021' expedition on the Swedish icebreaker Oden (see the cruise track in Figure 2a). Along the cruise, so called Transient Tracer Super Stations (TTSS) were set up in various basins of the AO (see Figure 2b) collecting water samples for measurement of the concentrations of a unique set of transient tracers. Due to the cruise covering mainly the Eurasian side of the Lomonosov Ridge, most samples were collected there, but one TTSS was also located on the Amerasian side. Specifically, one station was placed in the Nansen Basin (Station 5), one station around the Gakkel Ridge (Station 8), three stations in the Amundsen Basin (Stations 16, 20 and 46) and one in the Makarov Basin (Station 28). Within the Amundsen Basin one station was located at an area close to the north Greenland shoreline, and the other two close to the North Pole. Hereby, different basins and areas possibly affected differently by water mass movements, were covered. In addition to these TTSS, data for CFC-12 and SF_6 were also collected at 34 stations located along the cruise track of the expedition (see Figure 2a, (Gerke et al., 2024)).
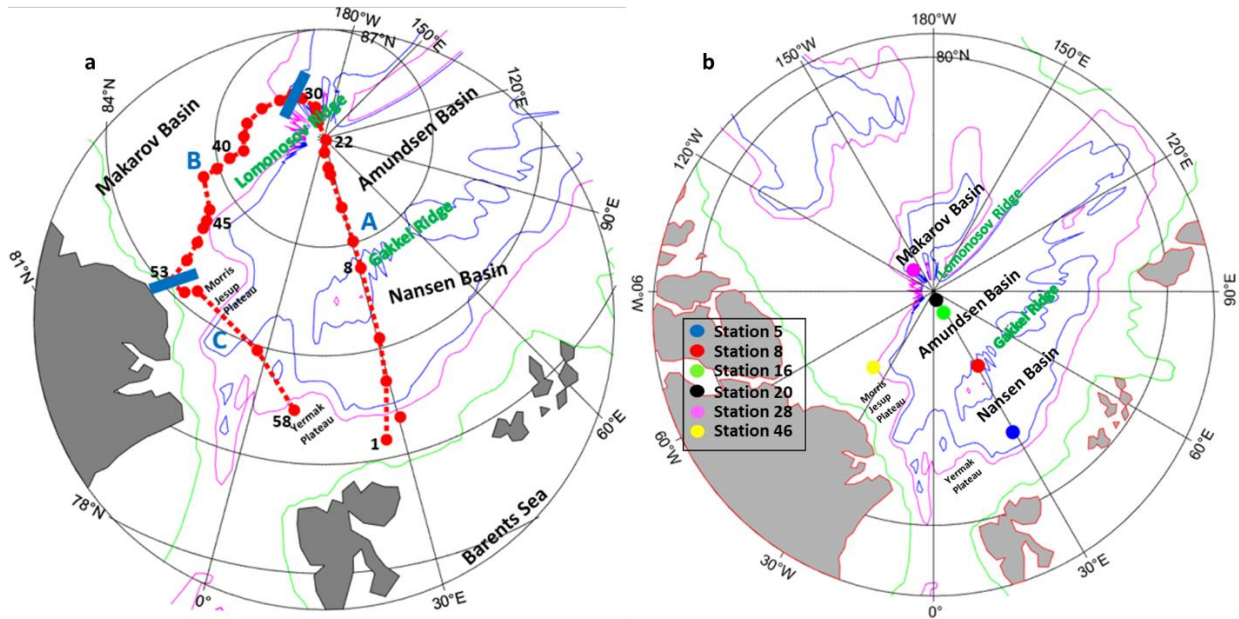
Figure 2: (a) Map outlining the cruise track of the 'SAS-Oden 2021' expedition. (b) Transient Tracer Super Station (TTSS) set up during the cruise.

3.2. Water masses in the Arctic Ocean

This study focusses on the intermediate layer (between 100 and 1500m). In its upper parts this water mass includes the Atlantic layer, which describes water entering from the Atlantic Ocean. It is often divided into two branches, the Fram Strait Branch Water (FSBW) and the Barents Sea Branch Water (BSBW). The FSBW enters the AO through the Fram Strait and is typically found at depths between ≈ 100 – 500 m (27.70 kg/m^3 ≤ σ_Θ ≤ 27.97 kg/m^3) (Rudels et al., 2012). It is considered the most representative water mass within the Atlantic layer (Raimondi et al., 2023) and in this study referred to as the Arctic Atlantic Water (AAW) (Ulfsbo et al., 2018). The BSBW enters the central AO, after moving though the Barents Sea at the St. Anna Trough. Due to intensive cooling and increasing density, it sinks below the FSBW and is typically found at depths of ≈ 500 to 700 m (σ_Θ ≥ 27.97 kg/m^3; $\sigma_{0.5}$ ≤ 30.44 kg/m^3; temperature ≥ 0 °C) (Raimondi et al., 2023; Rudels et al., 2012). It is also referred to as dense Arctic Atlantic Water (dAAW) (Ulfsbo et al., 2018). The water found below the BSBW at depths between ≈ 700 and 1500 m (σ_Θ ≥ 27.97 kg/m^3; $\sigma_{0.5}$ ≤ 30.44 kg/m^3; temperature ≤ 0 °C), still considered part of the intermediate layer, is referred to as the upper Polar Deep Water (uPDW) (Rudels et al., 2012; Ulfsbo et al., 2018).

The other three water masses present in the AO are the wind driven surface, the halocline and the deep water masses. The surface water circulates mainly horizontally and is the water mass mostly affected by increasing temperatures, decreasing sea-ice coverage and increasing

freshwater input. It is characterized by near freezing temperatures and a high fresh water content from river runoff, precipitation and iceberg calving (Aagaard et al., 1981; Ekwurzel et al., 2001; Haine, 2021). The halocline is formed via vertical movement of saline shelf water produced during freezing and acts as a barrier between the surface water above and the AAW below, preventing upward heat flux (Aagaard et al., 1981; Bauch et al., 2014). In this study, these two water masses are treated combined as surface waters (SW), representing all water above the intermediate layer (above ≈ 100 m). Deep water masses (DW) are present below 1500 m. They ventilate to these depths via boundary convection processes, which transport brine-enriched water formed at the shelfs into the deep basins (Anderson et al., 1999; Wallace et al., 1992). This water is present below the $\sigma_{0.5}$ = 30.444 kg/m^3 isopycnal (Rudels et al., 2012; Ulfsbo et al., 2018), and includes the deep water present on the Eurasian and the Amerasian side.

3.3. Data

At the six TTSS, samples for the analysis of multiple tracers were collected. These included chronological gaseous transient tracers such as the commonly sampled SF$_6$ and CFC-12, as well as less established gaseous tracers of potential interest for future use in ocean research, namely HCFC-22 (hydrochluorofluorocarbon-22), HCFC-141b (hydrochluorofluorocarbon-141b), HCFC-142b (hydrochluorofluorocarbon-142b) and HFC-134a (hydrofluorocarbon-134a) (hereafter referred to as 'Medusa'-tracers). In addition, radionuclide tracers were sampled, these included ^{129}I and ^{236}U, which serve as well-established tracers in the AO for AW analysis (Casacuberta et al., 2018; Casacuberta et al., 2016), and ^{14}C and ^{39}Ar for deep water analysis. The results obtained using these tracers will be covered in future studies. In this study, we focus solely on the chronological gaseous tracers (tracers with no sinks and sources in the ocean's interior (Stöven & Tanhua, 2014)) and on the intermediate water layer (100 – 1500 m), as these tracers are best suited at the age range expected in these water masses.

3.3.1. CFC-12 & SF$_6$

Concentrations of the chronological transient tracers CFC-12 and SF$_6$ were measured directly on board using a gas chromatographic system equipped with electron capture detector combined with a purge and trap unit (PT-GC-ECD) (Bullister et al., 2002; Gerke et al., 2024; Tanhua et al., 2005). During the 'SAS-Oden 2021' expedition, 709 samples were measured,

with a precision of 2.6 % and 1.5 % for SF$_6$ and CFC-12, respectively, which could be calculated due to duplicates measured throughout the cruise. The samples covered depths from the surface to the bottom of the ocean.

3.3.2. 'Medusa'-tracers

At the six TTSS, samples for the 'Medusa'-tracers were collected from 7 different depths in the intermediate layer which were measured later in the laboratory (GEOMAR, Kiel). Samples were drawn in 1.3 L glass ampoules and measured using the 'Medusa-Aqua'-system, a gas chromatograph mass spectrometer (Li & Tanhua, 2021; Miller et al., 2008). A total of 41 samples were collected and 27 of these were measured successfully. The precisions in concentration determination for each of the tracers on the 'Medusa-Aqua'-system are given in Li & Tanhua (2021), with HCFC-22: 3.1 %; HCFC-141b: 6.1 %; HCFC-142b: 1.8 % and HFC-134a: 9.7 %. In contrast to the commonly used tracers CFC-12 and SF$_6$, the solubilities of the 'Medusa'-tracers in seawater have not been determined experimentally so far. Only mathematical calculations have been carried out and are displayed as Ostwald-solubility functions (Li et al., 2019). These functions were used to determine the partial pressure values of the tracers in the seawater samples used in this study. The resulting partial pressure values of HCFC-22 and HFC- 134a were additionally adjusted to known atmospheric histories, aligning the surface water sample values to the atmospheric concentrations measured in the northern hemisphere in 2021. Detailed information on the sampling and measuring procedure as well as the concentration analysis are described in detail in the supplemental material. Measurement of the 'Medusa'-tracers is currently only possible in the laboratory using a specially designed system that cannot easily be used on-board. The sampling and measurement procedures require long times, which limits the quantity of samples.

3.4.   Transit Time Distribution

The Transit Time Distribution (TTD) is a well-established method to assess ventilation timescales and rates (Hall & Plumb, 1994; Khatiwala et al., 2001; Schneider et al., 2012; Sonnerup et al., 2013; Stöven & Tanhua, 2014; Waugh et al., 2002). Using transient tracer measurements and their respective input functions, the TTD describes an age distribution for individual water parcels within the ocean's interior.

The TTD method does not assume distinct ages for the transit time, but considers a distribution of ages by applying the Green's function ($G(t',r)$), which itself describes the propagation of a tracer boundary condition into the interior ocean. Multiplying this function with each tracer's input function ($c_0(t)$), yields simulated concentrations of the respective tracer at a certain location and time ($c(t,r)$) (see equation 1) (Hall & Plumb, 1994; Holzer & Primeau, 2010).

$$c(t,r) = \int_0^\infty c_0(t-t')e^{-\lambda t'} * G(t',r)\, dt' \qquad\qquad \textbf{1}$$

Here, the input function of each tracer is known due to its atmospheric history and characteristics concerning air-sea gas exchange and solubility in seawater. The unknown is Green's function, which is commonly described by an inverse Gaussian shape of the distribution, providing a probability density function (PDF) (see equation 2 and Figure S7).

$$G(t) = \sqrt{\frac{\Gamma^3}{4\pi\Delta^2 t^3}} * \exp(\frac{-\Gamma(t-\Gamma)^2}{4\Delta^2 t}) \qquad\qquad \textbf{2}$$

The solution to the Green's function includes the assumptions of (1) a steady state, (2) a single surface source region dominating, (3) no changes in the tracer concentration due to inner water interactions and (4) a one-dimensional flow (Khatiwala et al., 2001; Schneider et al., 2012; Sonnerup et al., 2013; Stöven & Tanhua, 2014; Waugh et al., 2002).

In equation 2, Γ describes the mean age, whereas Δ represents the width of the distribution. The relationship between these two parameters provides information on the advective and diffusive flow characteristics within a water parcel. A Δ/Γ-ratio < 1 indicates dominance of advective processes, and a Δ/Γ-ratio > 1 characterizes a more diffusive flow.

To determine the parameters mean age (Γ), width of the distribution (Δ), as well as the Δ/Γ-ratio, it is possible to follow 'Smith's' approach to constrain the TTD or to calculate the most probable TTD with the help of the one-inverse Gaussian (1-IG) TTD approach (Raimondi et al., 2023; Smith et al., 2011; Stöven & Tanhua, 2014). Both applications use at least two transient tracers with significantly different input functions as a tracer pair to determine the TTD and assume inverse Gaussian distribution. Using multiple tracers and assuming a mixing of two

water masses with individual Green functions, the two-inverse Gaussian (2-IG) TTD approach can be implemented to constrain the most probable TTD (Stöven & Tanhua, 2014).

3.4.1. Smith's approach

Smith's TTD approach calculates the most likely solution for the TTD for each data point individually. Therefore, it compares the measured concentrations of a tracer pair to modelled tracer concentrations, which are based on their input functions and pre-designed Γ and Δ values (Raimondi et al., 2023; Smith et al., 2011). Thus, to determine Γ and Δ for each individual data point, a matrix of all conceivable concentrations is constructed, ranging for mean ages and widths of the distribution between 0 and 2000 years and permitting only combinations of Γ/Δ-ratios between 0.2 and 1.8. Hereby, multiple solutions of TTDs are obtained. Considering the input functions of the two tracers and all possible PDFs yields a domain of modelled tracer concentrations (see Figure 5, below). The measured sample concentrations are then plotted on top of this domain/grid and the most probable result for Γ and Δ, along with the Γ/Δ-ratio for each data point, is obtained by choosing the closest point in the underlying grid. Additionally, the parameter 'mode age' can be determined, which represents the most probably solution of each PDF (see Figure S7). Thus, for each tracer concentration measured this approach yields the respective mode age, Γ, Δ values and a Γ/Δ-ratio (Raimondi et al., 2023).

To constrain the most probable TTD for each region in the AO, we compared multiple tracer grids and measured tracer concentrations from a variety of different tracer pair combinations. Furthermore, to determine the saturation of each tracer in the AO, we fitted the surface water concentrations to concentrations modelled from recent atmospheric values. This revealed that all tracers, except for CFC-12 (85 %), reached full saturation (100 %) upon entering the AO.

The individual results of each tracer pair are then also compared to each other to obtain the most probable data set and examine where the 'Medusa'-tracers, which were included in several tracer pairs, provide additional information on the TTD of specific regions. Variations in the results obtained for the Γ/Δ-ratios and mean ages from different tracer pairs are utilized in the 2-IG TTD approach (see below).

3.4.2. 1-IG TTD approach

Similar to the 'Smith's' approach, the 1-IG TTD approach (Stöven & Tanhua, 2014) also assumes inverse gaussian distribution and predetermines a range of mean ages (e.g. 0 – 2000 years). However it then considers a fixed Δ/Γ-ratio, ranging from 0.2 and 1.8, to determine the width of the distribution (Δ). Subsequently, the PDFs are obtained across all ranges of mean ages, and considering the input function of each tracer, all possible simulated concentrations are generated, taking into account the defined mean ages and fixed Δ/Γ-ratio. Correlating the measured concentrations within all water samples to the simulated concentration using a fixed Δ/Γ-ratio, the respective mean ages are computed. Comparing computed mean ages of two tracers with significantly different input functions to each other, then determines the most probable TTD, when showing similar values. Thus, the 1-IG TTD approach can constrain the most probable TTD based on a fixed Δ/Γ-ratio for the respective region. In this study, we employed this approach to constrain mean ages based on the CFC-12 and SF_6 data collected throughout the 'SAS-Oden 2021' cruise. A prior investigation had constrained the most probable TTD using parts of the data, employing a Δ/Γ-ratio = 1 and using a time dependent saturation from the Greenland Sea (Gerke et al., 2024; Jeansson et al., 2023). Consequently, we continued to employ these assumptions across all samples collected during the cruise.

The 1-IG TTD as well as 'Smith's' approach both rely on the assumption of a one-inverse Gaussian distribution, but differ in the way to determine the most probably TTD. 'Smith's' approach considers each individual data point and determines individual parameters like mean age and Δ/Γ-ratio for each measurement. In contrast, the 1-IG approach determines the TTD from and for a series of measurements, including those carried out in different regions and depths. Both approaches have certain advantages, specifically more detail with respect to individual ventilation parameters (Smith's approach) and the possibility to handle a big set of data and excluding uncertainties more easily (1-IG approach).

3.4.3. 2-IG TTD approach

This study utilized measurements of multiple tracers. Therefore, a range of tracer pair combinations could be employed to calculate ventilation parameters. The resulting mean ages and Δ/Γ-ratios show variabilities at certain regions and depths (see section 3.4). This variability

can be attributed to the inadequate assumption of the one-inverse Gaussian distribution, which assumes that only one water mass dictates the ventilation of each area. To address this point and the possibly underlying inaccuracy, a two-inverse Gaussian distribution, which includes the presence of a second water mass, was applied. This approach considers a mix of two water masses with similar densities but different age histories (one younger, one older) and relies on measurements of multiple tracers, each characterized by an unique input function. The 2-IG TTD approach combines two distributions (Green functions) for the two water masses and assumes a linear combination of those by including a percentage factor (α), which fixes the ratio between the two distributions but can be varied (Stöven & Tanhua, 2014; Waugh et al., 2003) (see equation 3).

$$c(t,r) = \int_0^\infty c_0(t - t')e^{-\lambda t'} * [\alpha * G(\Gamma_1, \Delta_1, t', r) + (1 - \alpha) * G(\Gamma_2, \Delta_2, t', r)]\, dt' \qquad \textbf{3}$$

Employing each designated α yields a matrix of mean ages for each tracer in combination with their respective input functions (see Figure 3), providing results for the two mean ages at the respective measured concentrations.
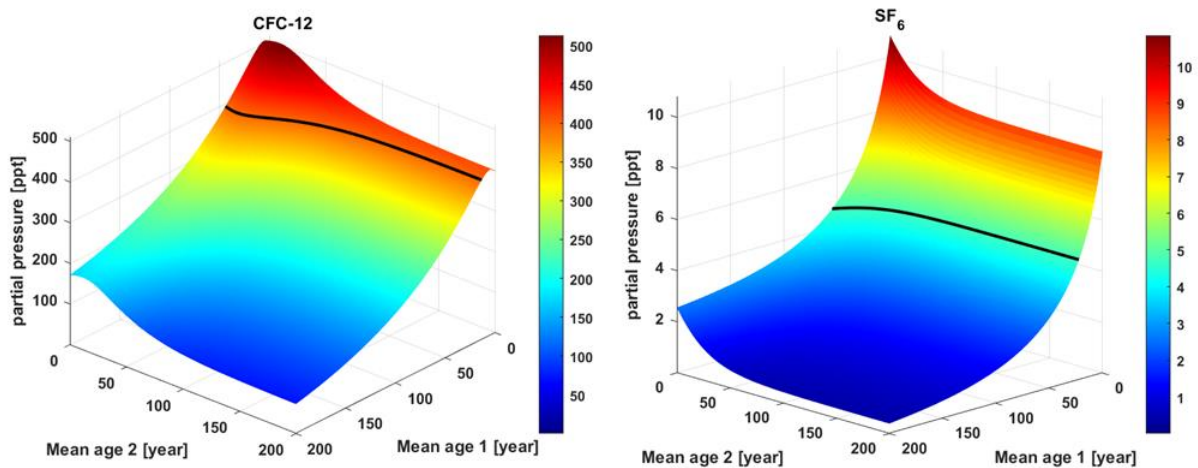

Figure 3: Examples of mean age matrices for CFC-12 and SF$_6$ with Δ_1/Γ_1-ratio = 0.9 and Δ_2/Γ_2-ratio = 0.4 and α = 80 %. The black line represents a concentration of 393 ppt and 4.7 ppt for CFC-12 and SF$_6$, respectively. These represent the concentrations measured at 500 m depth at station 8, as an example.

The resulting partial mean ages (Γ_1, Γ_2) of each Green function (black line in Figure 3) are then multiplied by the respective distribution factor α to obtain the mean age (Γ) of the water mass analyzed which includes a mix of the two water masses (see equation 4).

$$\Gamma = \alpha * \Gamma_1 + (1 - \alpha) * \Gamma_2 \qquad\qquad \textbf{4}$$

The 2-IG TTD approach thereby analyses the mean age of a water parcel under the assumption of an older and a younger water mass mixing, each having distinct mean ages and Δ/Γ-ratios. Boundary conditions for the 2-IG TTD can be derived by applying 'Smith's' approach and assuming a 1-IG TTD. The variability in the Δ/Γ-ratios and resulting mean ages compiled from varying tracer pair combinations are then addressed and yield the boundary conditions using the 2-IG TTD.

For instance, at station 8 the Δ/Γ-ratios within the AAW range from 0.4 to 0.9 which would set the lower and upper boundaries for the two water masses mixing, yielding specific Δ_1/Γ_1 and Δ_2/Γ_2 ratios. Utilizing the range of mean ages (Γ-boundary), which is also derived from 'Smith's' approach, assuming that the total mean age of the water mass is within this range, and varying α in 10% increments from 0.1 to 1, yields different Γ_1 and Γ_2 values using equation 4. For example, with a total mean age of 30 and α set to 0.5, Γ_1 and Γ_2 are calculated each to be 15 years. Δ_1 and Δ_2 are subsequently computed using the Δ/Γ-ratio boundaries. This produces a set of Γ_1, Γ_2, Δ_1, Δ_2 and α values.

With these parameters and the respective input functions for each tracer, modelled concentrations for each set of Γ_1, Γ_2, Δ_1, Δ_2 and α values are calculated using equation 3. These modelled concentrations of all six tracers are then compared to the measured values at each station and depth, determining the closest match using an Euclidean distance error calculation (Dokmanic et al., 2015). In this error determination, the tracer values of CFC-12 and SF_6 are weighted double, as these tracers were measured with higher precision and accuracy and have well known solubility functions. The closest result yields the actual values for alpha and the total mean age of the water parcel, which in turn can be used to compute the individual mean ages of each water mass using equation 4.

4. Results and Discussion

4.1. Multiple tracer measurements

Transient tracer concentrations measured at the different TTSS show similar general trends at each station and depth (see Figure 4a). All display decreasing values with increasing depth, consistent with established patterns. Below 1500 to 2000 m, all tracers show very low or

undetectable concentrations suggesting that the tracers are primarily detectable within the AAW, dAAW and uPDW, with no significant presence in the deeper layers of the AO yet. The consistent decrease in concentrations from the surface to the interior confirms the general trend seen in the AO, with the absence of any more recently ventilated water mass in the deeper interior of the basins (Gerke et al., 2024). One exception is station 20 where increased tracer concentrations are detected at depths of 500 and 700 m (see Figure 4a – black dots). These slightly elevated concentrations at intermediate depths can be attributed to more recently ventilated, younger water with higher tracer concentrations, showing the influence of recirculating AW at these latitudes (Gerke et al., 2024; Rudels et al., 1999; Wefing, 2021).
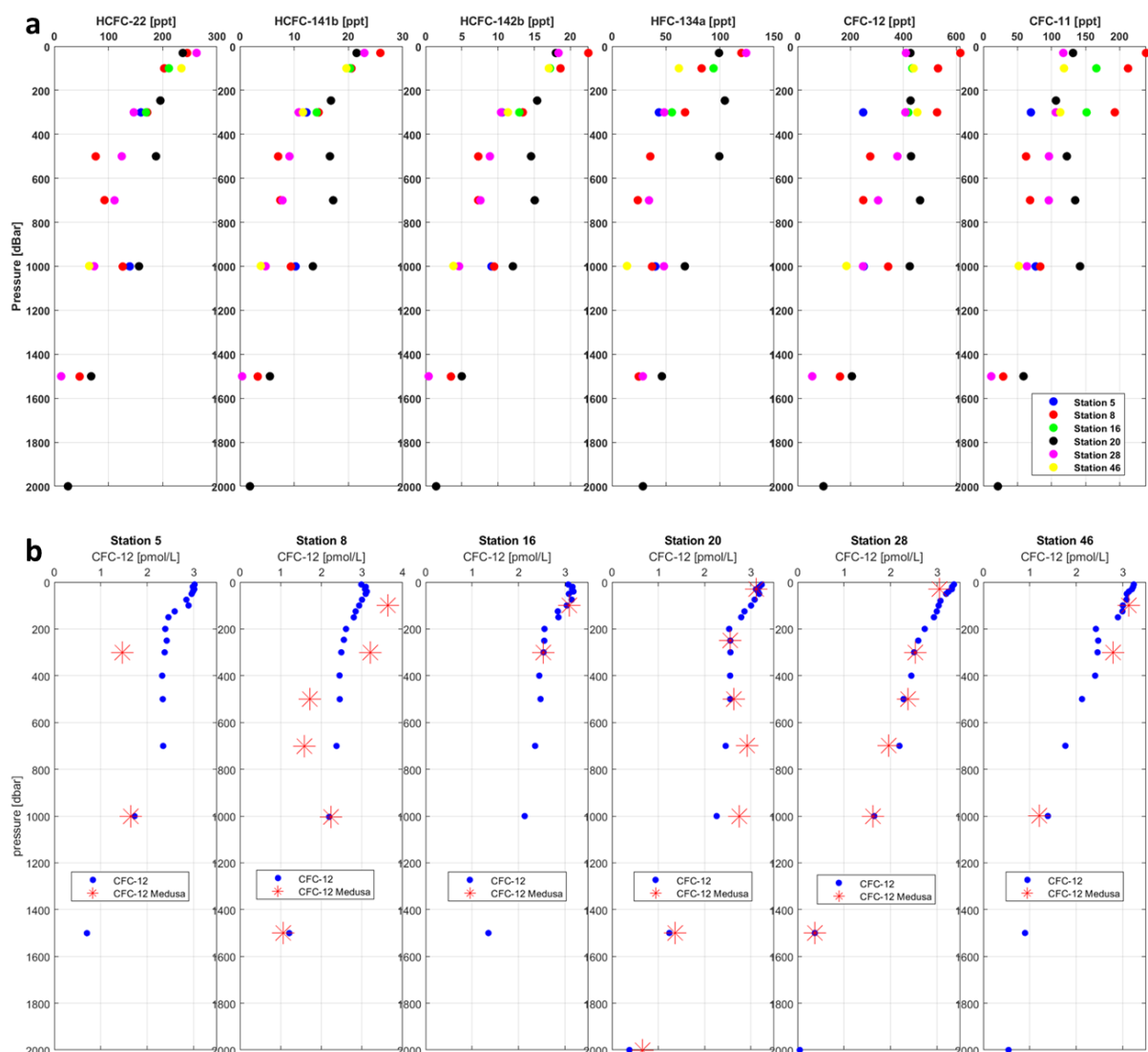

Figure 4: (a) Display of the calculated partial pressure (ppt) values based on tracer concentrations measured using the 'Medusa-Aqua'-system. The colors represent the TTSS, where the samples were collected. (b) Comparison of the CFC-12 (pmol/L) concentrations at each TTSS measured either by the 'Medusa-Aqua'-system (red) and once using the PT-GC-ECD technique (blue).

Figure 4b shows a comparison of the CFC-12 concentrations measured at the same station using either the 'Medusa-Aqua'-system or the PT-GC-ECD set up during the cruise. The results show a good agreement revealing accuracy of the Medusa measurements. Some variations can be seen at stations 5 and 8, which likely could be attributed to uncertainties in both sampling and measuring. The slightly higher level of uncertainties at these stations will likely also apply to the other tracers measured in the respective samples using the 'Medusa'-system. This is taken into consideration in the following analyses. Given the higher consistency observed using the PT-GC-ECD procedure, we used this CFC-12 dataset in the subsequent analyses.

4.2. 'Medusa' data validation

To decipher whether the 'Medusa'-tracers can serve as valid tools for ventilation analyses in the AO, different tracer pairs were used to determine the most probable solutions of the TTD at the respective TTSS. These tracer pairs, specifically CFC-12&SF_6, CFC-12&HCFC-22, CFC-12&HCFC-141b, CFC-12&HCFC142b and CFC-12&HFC134a, were chosen because they have significantly different input functions and thereby produce the most promising and widely stretched grids when applying 'Smith's' TTD approach (see Figure 5), and because most of the concentrations measured in the samples are present within the grids. Here, the uncertainties (represented by error bars) arise from precision in the concentration analysis of each individual tracer, as described in sections 2.3.1 and 2.3.2.
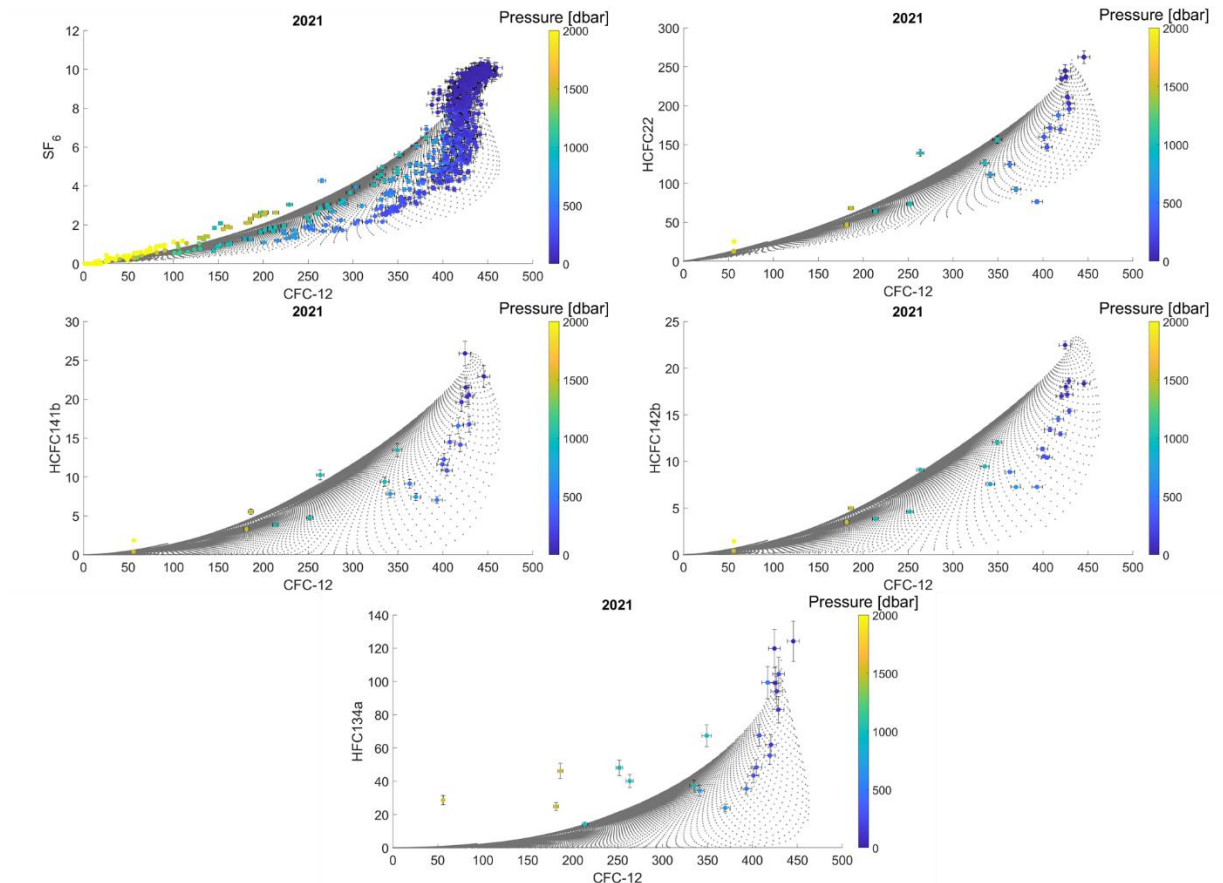
Figure 5: Δ-Γ grids obtained following 'Smith's' approach for different tracer pairs. The respective saturations used for each tracer are 100 % for SF$_6$ and the 'Medusa'-tracers and 85 % for CFC-12. Each of the grey grid points correspond to a tracer pair concentration calculated using one combination of Γ and Δ. Measured tracer gas concentrations are plotted on top of the respective grid with the color-coding representing the pressure at which the respective sample was collected (see color bar on the right of each graph). Error bars indicate the error arising from the precision of the concentration measurements. All tracer concentrations are displayed as partial pressure values (ppt – parts per trillion).

The concentrations measured for each tracer pair in the different water samples fit well into the designated Δ-Γ grid, particularly within the depth range of 100 – 1000 meters. Concentrations at these depths fall within the most extensively stretched region of each grid, where the modelled tracer concentrations, based on the parameters Δ-Γ-ratio, mean age and width of the distribution, can be most accurately derived with minimal uncertainty. However, due to uncertainties associated with the concentration determination of each tracer, the closest grid point, used to represent the most probable TTD, varies. Consequently, the constrained parameters (Γ, Δ and Δ-Γ-ratio) obviously bear uncertainties for each data point. This uncertainty increases for data present at the edge of each grid.

Nonetheless, all tracer pair combinations used yield widely stretched grids and the measured data coincide with the respective grid used to constrain the TTD. This indicates that the 'Medusa'-tracers are well suited for the analysis of age distributions in AO waters.

Next, to validate the ventilation parameters, which were computed using 'Smith's' approach incorporating the 'Medusa'-tracers, the mean ages were compared to mean ages calculated using the well-established tracers CFC-12 and SF_6 in combination with the 1-IG TTD approach. In addition to compare the results at the six TTSS to those obtained at the regions nearby, stations from the 'SAS-Oden 2021' cruise located next to each TTSS were included in the mean age analysis using CFC-12 and SF_6 data and the 1-IG approach (see Figure 6, bottom map). This comparison yielded similar mean age results throughout each region, and therefore demonstrates the effectiveness of using 'Medusa'-tracers to constrain TTD parameters within the AO.

The two approaches used to constrain the mean ages in the TTD ('Smith' and 1-IG TTD) rely on the same assumption of an inverse gaussian distribution, but vary in terms of saturation and Δ/Γ-ratio. The 1-IG-TTD approach fixed a Δ/Γ-ratio = 1 and applied a time dependent saturation of the tracers, whereas 'Smith's' approach permits variations in the ratio but chooses fixed saturations. As the results show similar mean age values, we can conclude that within the intermediate water column of the AO, the mean age calculation is not dependent on the choice of the approach used to derive the TTD.
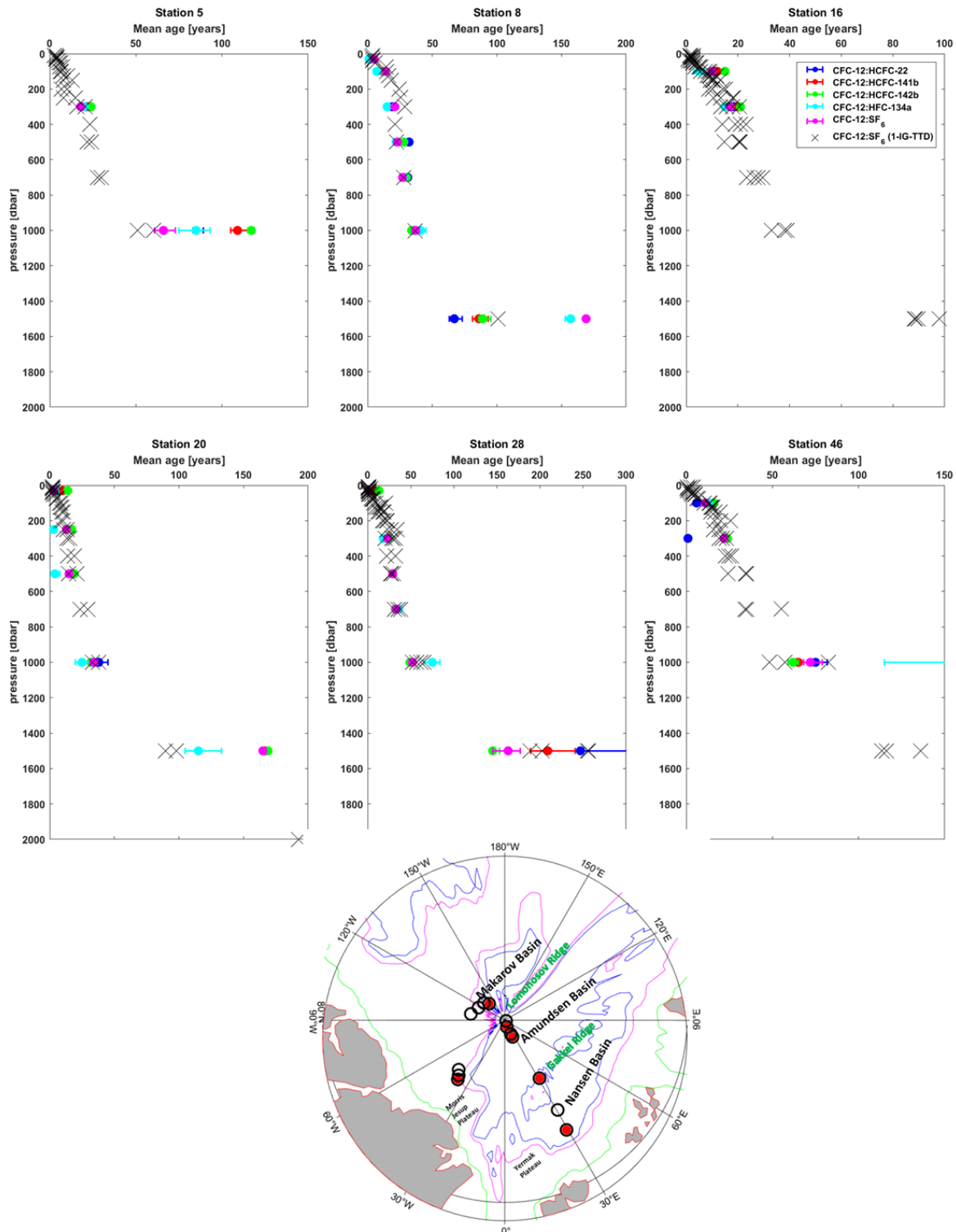
Figure 6: Comparison of mean ages calculated using 'Smith's' approach and the various tracer pairs measured at each TTSS to mean ages constrained at nearby stations within the respective region using CFC-12 and SF₆ data and the 1-IG TTD approach. The color coding represents the different tracer pairs given in the legend. Error bars show the lowest and highest possible parameter constrained from matching the measured datapoint with the underlying grid with errors resulting from the precision of concentration determination of each tracer. The black crosses show the results obtained when using

the 1-IG TTD approach. The map at the bottom shows the respective data sampling stations, with the red points representing the TTSS and the black circles showing the nearby stations included in the 1-IG TTD approach.

4.3. Variability of ventilation in different water masses

Concentrations of the different tracer pairs (see Figure 5) at each individual data point can be employed to calculate values for the parameters Δ/Γ-ratio, Γ and mode age and the results can then be compared for the different tracer pairs (see Figures 7, 8 and 9). The data reveal a strong correlation between the tracer combinations used, when comparing the mean ages, which consistently increase with depth (see Figure 7). Slightly more variations are observed when examining the mode ages (see Figure 8). These variations increase especially at greater depths, which most likely can be attributed to the potential increase of diffusive-dominated flow of water masses at these depths.

The range of advective- and diffusive-dominated flow can be examined by careful analysis of the Δ/Γ-ratios (see Figure 9). The results indicate predominately advective flow (Δ/Γ-ratios < 1) in water masses such as the AAW and dAAW, transitioning towards more diffusive characteristics (increasing Δ/Γ-ratios) in the deeper ocean (uPDW & DW). However, because the modelled tracer grids show a compression at lower concentrations, typically met in the deep water samples, these values are associated with higher levels of uncertainty. In the surface layer, the Δ/Γ-grids also narrows, leading to increased uncertainty, evidenced by larger error bars observed in the SW samples (see Figure 9 – blue dots). Some variations could also arise from errors associated with the solubility functions of the 'Medusa' gases, because these were only determined mathematically, and from uncertainties arising from the measurement precision using the 'Medusa-Aqua'-system. In case of CFC-12, the high level of uncertainty in the surface water samples possibly is due to decreasing concentrations in the atmosphere and as a consequence, the difficulty to obtain a wider Δ/Γ-grid.

Some minor discrepancies between the data calculated using different tracer pairs across all depths exist in terms of Δ/Γ-ratios. Consistently higher ratios are obtained, when a combination of CFC-12&SF$_6$, CFC-12&HCFC-22 or CFC-12&HFC-134a is employed, as opposed to including one of the other 'Medusa'-tracers (HCFC-141b or HCFC-142b) in the analysis. The tracer pair of CFC-12&HFC-134a shows the largest scatter and uncertainties and thus the least

comparable results. This most likely arises from the difficulty to plot the measured concentrations onto the modelled grid, especially for deeper water samples.
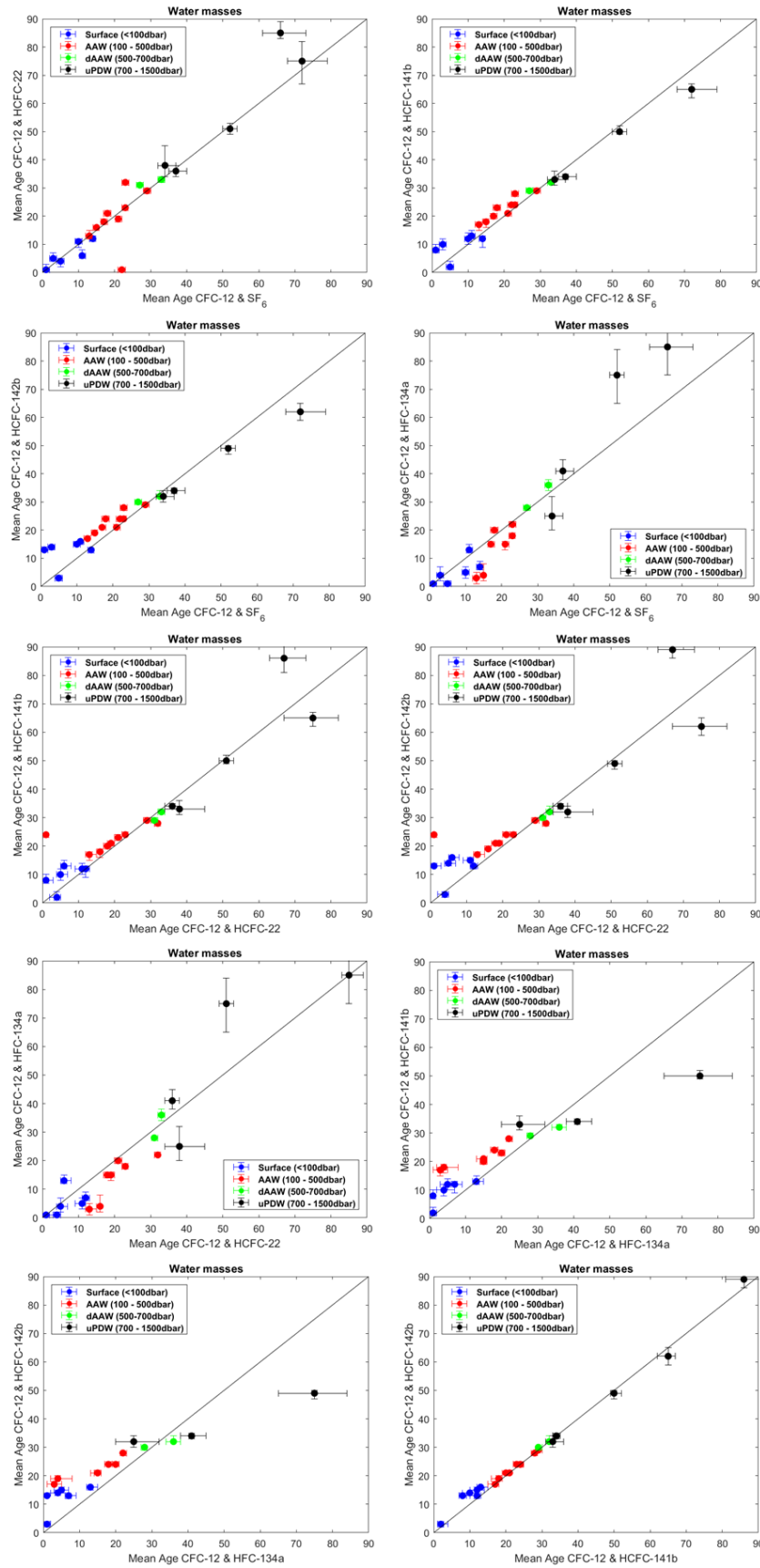
143

Figure 7: 1:1-comparison of mean ages which were calculated based on measured concentrations of different tracer pairs. The color coding represents the different water masses (surface, AAW, dAAW and uPDW). The deep water is not included as this would hinder the comparison for younger waters.
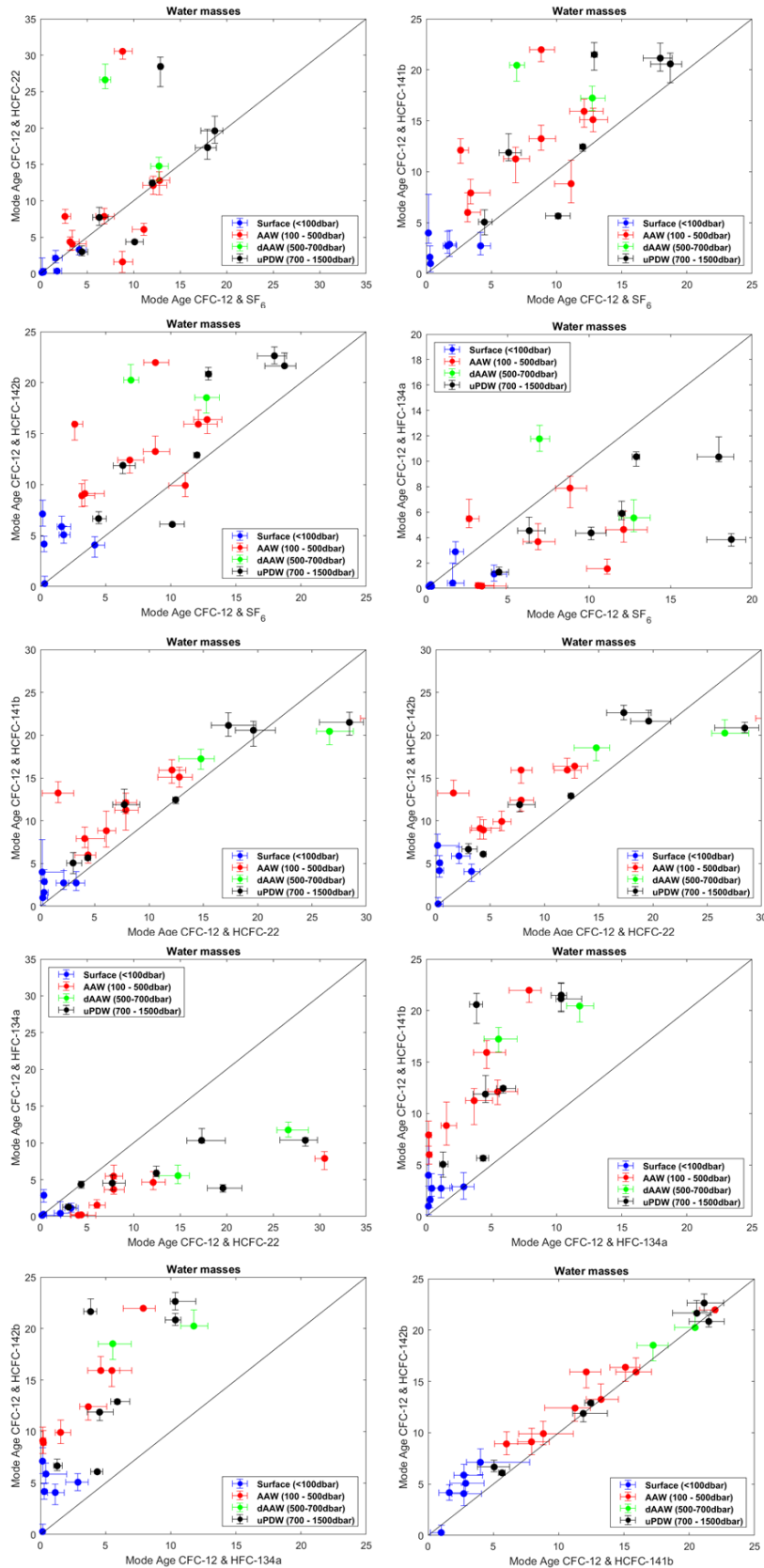
Figure 8: 1:1-comparison of mode ages which were calculated based on concentrations measured for the different tracer pairs. The color coding represents the different water masses (surface, AAW, dAAW and uPDW). The deep water is not included as this would hinder the comparison for younger waters.
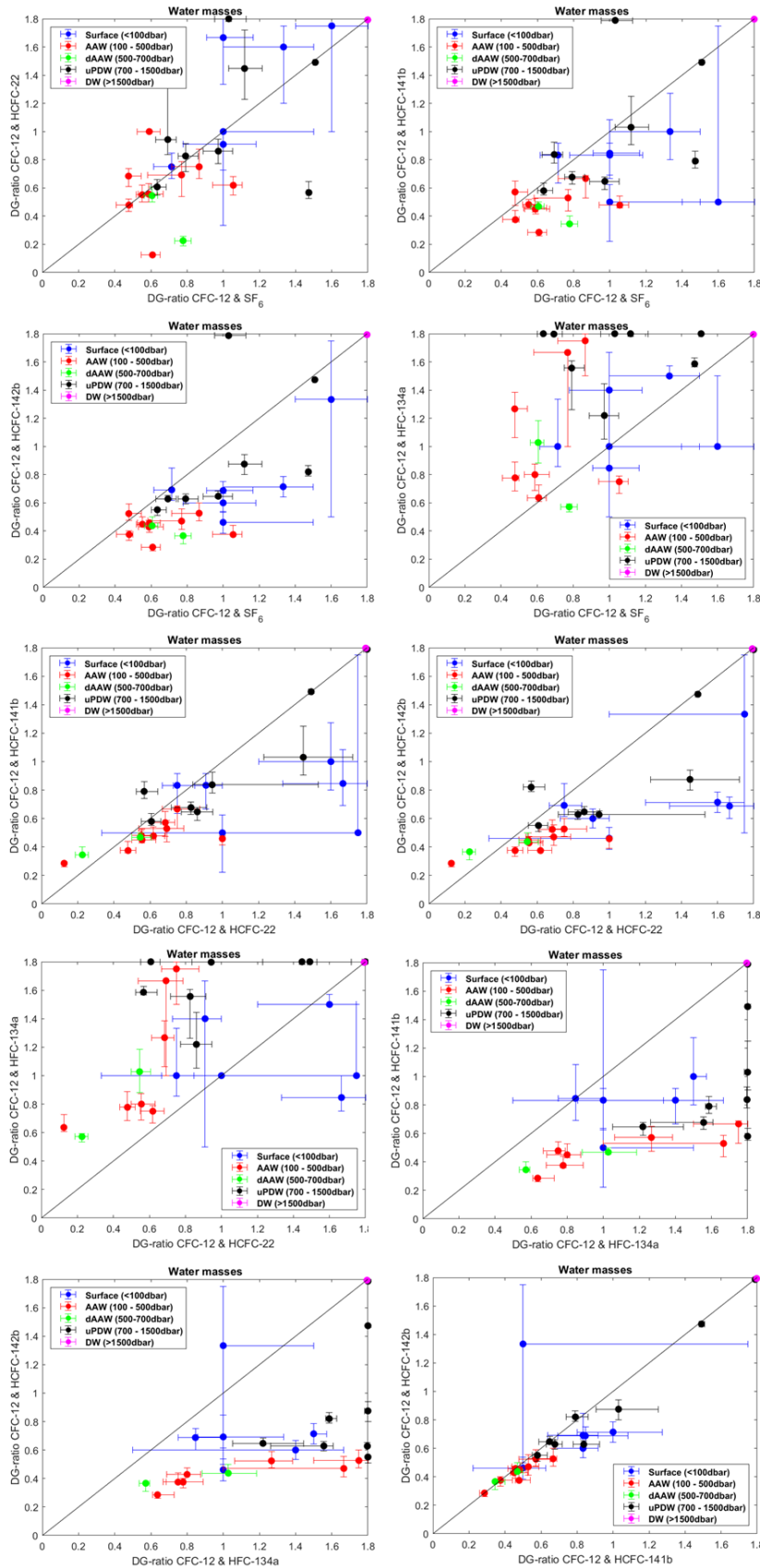
Figure 9: 1:1-comparison of D/G (Δ/Γ)-ratios which were calculated based on the concentrations of different tracer pairs. The color coding represents the different water masses (surface, AAW, dAAW, uPDW and DW).

4.4. Improvement of ventilation analysis using 'Medusa'-tracers

Due to the distribution of the TTSS across various basins and regions within the AO (see Figure 2b), and by applying multiple tracer pairs in the analysis of ventilation dynamics, we were able to examine discrepancies of Δ/Γ-ratios and mean ages in and between the distinct regions. As discussed above, we observed advective-dominated flow patterns at depths between 200 and 1000 m (Δ/Γ ratio < 1), with diffusive characteristics becoming more pronounced at greater depths. Notably, in the Makarov Basin (Station 28) the advective-dominated flow extends below 1000 m (see Figure 10a), whereas other stations already showed a transition towards a more diffusively influenced ventilation (Δ/Γ ratio > 1) at these depths.

Figure 10: Comparison of (a) Δ/Γ-ratios and (b) mean ages calculated using 'Smith's' approach and the different tracer pair concentrations measured at each TTSS. The color coding represents the different tracer pairs and the error bars cover the lowest and highest possible parameter constrained within each underlying grid with errors resulting from imprecision in each tracer measurement.

The mean ages derived from the analyses of the different tracer combinations yield consistent findings for all regions and depths. A comparison of the various regions reveals slightly higher mean ages within the Makarov Basin (Station 28) in the intermediate layer at depths of 1000 m, relative to the other regions. This trend is visible across all combinations of tracers used for the calculation and is in line with earlier results employing only CFC-12 and SF_6 (e.g. Gerke et al., 2024).

Larger discrepancies are visible in the Δ/Γ-ratios, with standard deviations exceeding 20 % at certain stations (Figure S8). Notably, the tracer combination of CFC-12&HFC-134a consistently shows higher Δ/Γ-ratios throughout the water column at each of the TTSS. Additionally, the mean age data derived from this tracer combination display slightly higher variations compared to results obtained by employing the other tracer pairs. As discussed above, this discrepancy can primarily be attributed to the challenges of plotting the measured concentrations onto the modelled tracer grid using 'Smith's' approach. Consequently, we calculated standard deviations including and excluding this tracer pair. Excluding this tracer pair, the remaining demonstrate sufficient comparability at station 28 (Std-dev < 15 %; see Figure S8 (red and magenta dots)), suggesting that the assumption of a 1-IG distribution appears reasonable in this region (the Makarov Basin). However, at the other stations Δ/Γ-ratio values exhibit higher variability across all tracer pair combination (Std-dev > 20 %). This discrepancy could stem from measurement or sampling uncertainties, especially at stations 5 and 8 (see section 3.1) (marked yellow in Table S1). However, the variations in the Δ/Γ-ratios could also arise from the mixing of different water masses with different Δ/Γ-ratios, indicating that the assumption of a 1-IG distribution may not be suitable for the description of the distribution within these areas.

Therefore, we applied the 2-IG TTD approach to all samples showing standard deviations > 20 %. For this analysis, the boundary conditions (Δ/Γ-ratio and mean age) were chosen from the varying results of using 'Smith's' TTD approach. The 2-IG TTD approach assumes the presence of an older and a more recently ventilated water mass, each characterized by distinct Δ/Γ-ratios.

At station 8, the values were therefore set to Δ/Γ-ratios of 0.4 and 0.9 in the AAW, 0.1 and 1 in the dAAW, and 0.5 and 1.5 in the uPDW, as the computed values from the individual tracer pairs using 'Smith's' approach vary in between these ranges. At station 20, we considered AAW and dAAW Δ/Γ-ratios of 0.4 and 0.9 and those in the uPDW of 0.5 and 1.5. The ranges of

the mean ages (Γ-boundaries), also derived from the individual results of the tracer pairs, at these two stations as well as the boundary conditions for Δ/Γ-ratios and mean ages for stations 5, 16 and 46 are given in Table S1.

Applying the 2-IG TTD approach (see chapter 2.4.3) and utilizing these boundary conditions, computed the mean age results for the two different water masses (see Tables S1 and Figure 11).

Stations 8 and 20, where the intermediate water layer was effectively sampled show an interesting and consistent pattern, with some exceptions. Throughout the upper 700 m the water masses are primarily influenced by the water mass with the higher Δ/Γ-ratio ($Δ_1/Γ_1$-ratio), whereas below 1000 m the influence reverses and the effect of the water mass with the lower Δ/Γ-ratio ($Δ_2/Γ_2$-ratio) becomes predominant. Nonetheless, as the set values for the $Δ_1/Γ_1$ and $Δ_2/Γ_2$-ratios in the upper parts both show advective-dominated characteristics, i.e. Δ/Γ-ratios < 1, it appears likely that advective-dominated flow prevails at intermediate depths in the AO.

The mean age values obtained following the 2-IG TTD approach at these selected stations, fall within the upper range of the predetermined Γ-boundary above 700 m. Below this depth, the computed mean age tends to be in the middle of the Γ-boundary. The overall mean age results are displayed in Figure 11 next to the results obtained using only single tracer pairs for the analysis.
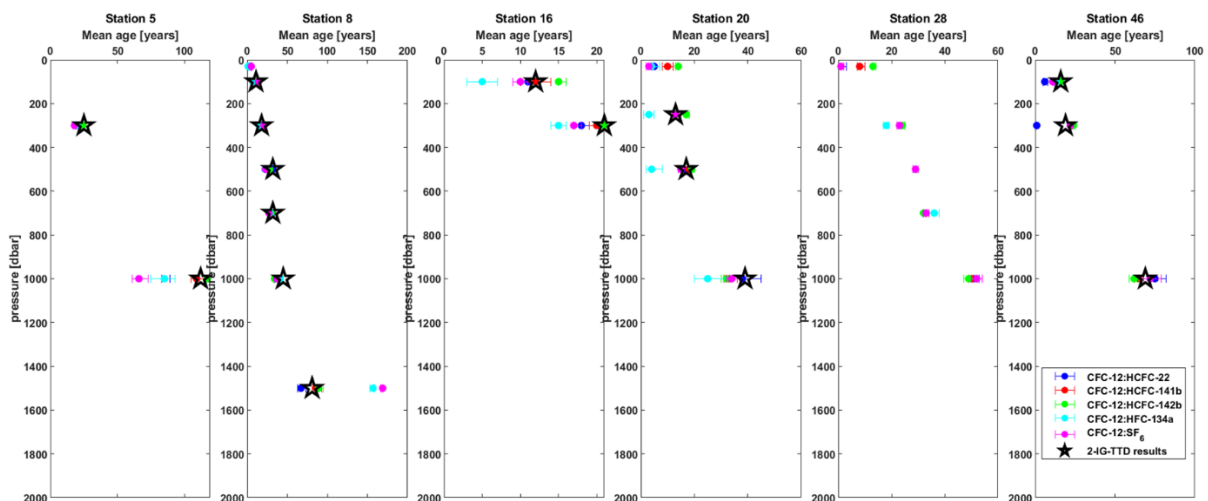

Figure 11: Comparison of mean ages calculated using the different tracer pair concentrations measured at the respective TTSS to the mean age results obtained via calculations employing the 2-IG TTD approach. The color coding represents the different tracer pairs used in 'Smith's' approach and

the error bars cover the lowest and highest possible parameter constrained within the underlying grid with errors resulting from imprecision in each tracer measurement. The black star represents the mean age calculated with the 2-IG TTD.

5. Conclusions

The multi-tracer approach introduced in this study provides valuable insights into ocean ventilation in the AO. We show that concentrations of the so called 'Medusa'-tracers can be used to effectively analyze water mean and mode ages as well as constrain Δ/Γ-ratios in this region. Unlike previous measurements of these tracers in the Mediterranean Sea (Li & Tanhua, 2021), where the 'Medusa'-tracers exhibited a reduced stability, our measurements reveal reasonable results for these tracers in the cold AO. Furthermore, we show that different analytical approaches (Smith's and 1-IG) can be used to characterize ventilation in the AO, their efficiency is demonstrated and individual advantages and disadvantages are discussed.

We analyzed multiple ventilation parameters within the intermediate layer (0 - 1500 m) across various regions of the AO, employing a range of transient tracers. The tracer pairs evaluated using 'Smith's' approach, CFC-12&HCFC-22; CFC-12&HCFC-141b; CFC-12&HCFC-142b; CFC-12&HFC134a and CFC-12&SF_6, all produce comparable results for the different ventilation parameters, Δ/Γ-ratio, mean and mode age of water masses, and thus show that the 'Medusa'-tracers can be used for the analysis of ventilation dynamics in the AO. The results demonstrate more advective flow in the Atlantic layer, which transitions to increased diffusive characteristics at greater depths and reveal increasing mean ages with increasing depths. This transition is less apparent in the Makarov Basin, where below 1500 m the Δ/Γ-ratios determined still show values below 1. In regions on the Eurasian side of the AO the Δ/Γ-ratios exceed 1 at increasing depths, expressing the diffusive influence here.

Despite the overall comparability, some variations in the computed Δ/Γ-ratios are evident among the different tracer pairs in certain regions of the AO. This suggests that assuming a single inverse Gaussian distribution may not be feasible in these regions and indicates that the respective water parcels are influenced by two distinct water masses with similar densities but distinct mean ages, one characterized by a larger Δ/Γ-ratio as compared to the other. With the exception of Station 28, located in the Makarov Basin, all other five TTSS exhibit high standard deviations in the values computed for the Δ/Γ-ratios using different tracer pair combinations. This indicates that the assumption of a single inverse Gaussian distribution is

valid in the Makarov Basin but probably not in the other regions analyzed here. These regions are likely characterized by the presence of two water masses with distinct Δ/Γ-ratios. Therefore the 2-IG TTD approach was introduced to calculate the ventilation parameters here. This approach revealed that the water mass with the higher Δ/Γ-ratio prevails at depths above 700 m, transitioning to the water mass with lower Δ/Γ-ratio at depths below.

6. Outlook

This study constitutes one of the first efforts to analyze ventilation in the AO using multiple tracers, with 'Medusa'-tracers being analyzed the first time in this region. Given the reproducible results obtained using different tracer pairs and because 'Medusa'-tracers can provide important information in particular on the intermediate water layer, future sampling programs should consider measurements of these tracers. As the solubility functions are still unknown, experimental data deciphering these functions would be beneficial to enhance the applicability of these tracers in the future.

Our analysis employing these multiple tracers was limited to samples from six stations covering different Arctic regions. Therefore, additional sampling efforts are required to obtain more detailed information on this rapidly changing region.

Acknowledgments

References

Aagaard, K., Coachman, L. K., & Carmack, E. C. (1981), On the halocline of the Arctic Ocean, *Deep Sea Research*, *28*, 529-545.

Anderson, L. G., Jones, E. P., & Rudels, B. (1999), Ventilation of the Arctic Ocean estimated by a plume entrainment model constrained by CFCs, *J. Geophys. Res.*, *104*(C6), 13423-13429.

Anderson, L. G., Olsson, K., Jones, E. P., Chierici, M., & Fransson, A. (1998), Anthropogenic carbon dioxide in the Arctic Ocean: Inventory and sinks, *J. Geophys. Res.*, *103*(C12), 27707-27716.

Azetsu-Scott, K., Jones, E. P., & Gershey, R. M. (2005), Distribution and ventilation of water masses in the Labrador Sea inferred from CFCs and carbon tetrachloride, *Mar. Chem.*, *94*(1-4), 55-66.

Bauch, D., Torres-Valdes, S., Polyakov, I., Novikhin, A., Dmitrenko, I., McKay, J., & Mix, A. (2014), Halocline water modification and along-slope advection at the Laptev Sea continental margin, *Ocean Science*, *10*(1), 141-154, doi:10.5194/os-10-141-2014.

Bullister, J., & Warner, M. J. (2017), Atmoshperic Histories (1765-2022) for CFC-11, CFC-12, CFC-113, CCl4, SF6, N2O (NCEI Accession 0164584). An update to Bullister (2015) NDP-09, *NOAA Nathional Centers for Environmental Information. Dataset*, doi:https://doi.org/10.3334/cdiac/otg.cfc_atm_hist_2015.

Bullister, J. L., Wisegarver, D. P., & Menzia, F. A. (2002), The solubility of sulfur hexafluoride in water and seawater, *Deep-Sea Res. I*, *49*(1), 175-187.

Bullister, J. L., Wisegarver, D. P., & Sonnerup, R. E. (2006), Sulfur hexafluoride as a transient tracer in the North Pacific Ocean, *Geophys. Res. Letters*, *33*(18), doi:doi:1029/2006GL026514.

Casacuberta, N., Christl, M., Vockenhuber, C., Wefing, A.-M., Wacker, L., Masqué, P., Synal, H.-A., & Rutgers van der Loeff, M. (2018), Tracing the Three Atlantic Branches Entering the Arctic Ocean With 129I and 236U, *Journal of Geophysical Research: Oceans*, *123*(9), 6909-6921, doi:10.1029/2018jc014168.

Casacuberta, N., Masqué, P., Henderson, G., Rutgers van-der-Loeff, M., Bauch, D., Vockenhuber, C., Daraoui, A., Walther, C., Synal, H. A., & Christl, M. (2016), First 236U data from the Arctic Ocean and use of 236U/238U and 129I/236U as a new dual tracer, *Earth and Planetary Science Letters*, *440*, 127-134, doi:https://doi.org/10.1016/j.epsl.2016.02.020.

D'Asaro, E. A. (1985), The energy flux from the wind to near inertial motions in the surface mixed layer, *Journal of Physical Oceanograohy*, *15*(1), 1043-1059, doi:https://doi.org/10.1175/1520-0485(1985)015<1043:TEFFTW>2.0.CO;2.

DeVries, T., et al. (2023), Magnitude, Trends, and Variability of the Global Ocean Carbon Sink From 1985 to 2018, *Global Biogeochem Cycle*, *37*(10), doi:10.1029/2023gb007780.

Dokmanic, I., Parhizkar, R., Ranieri, J., & Vetterli, M. (2015), Euclidean Distance Matrices: Essential theory, algorithms, and applications, *IEEE Signal Processing Magazine*, *32*(6), 12-30, doi:10.1109/msp.2015.2398954.

Ekwurzel, B., Schlosser, P., Mortlock, R. A., Fairbanks, R. G., & Swift, J. H. (2001), River runoff, sea ice meltwater, and Pacific water distribution and mean residence times in the Arctic Ocean, *J. Geophys. Res.*, *106*(C5), 9075-9092.

Fabry, V. J., McClintock, J. B., Mathis, J. T., & Grebmeier, J. M. (2009), Ocean acidification at high latitudes: The Bellwether, *Oceanography*, *22*, 160-171, doi:https://doi.org/10.5670/oceanog.2009.105.

Ferrari, R., & Wunsch, C. (2009), Ocean Circulation Kinetic Energy: Reservoirs, Sources, and Sinks, *Annual Review of Fluid Mechanics*, *41*(1), 253-282, doi:10.1146/annurev.fluid.40.111406.102139.

Fine, R. A. (2011), Observations of CFCs and SF(6) as Ocean Tracers, *Annual Review of Marine Science, Vol 3*, *3*, 173-195, doi:10.1146/annurev.marine.010908.163933.

Gerke, L., Arck, Y., & Tanhua, T. (2024), Temporal Variability of Ventilation in the Eurasian Arctic Ocean, edited.

Haine, T. W. N. (2021), A Conceptual Model of Polar Overturning Circulations, *J. Phys. Oceanogr.*, *51*(3), 727-744, doi:10.1175/jpo-d-20-0139.1.

Hall, T. M., & Plumb, R. A. (1994), Age as a diagnostic of stratospheric transport, *Journal of Geophysical Research: Atmospheres*, *99*(D1), 1059-1070, doi:10.1029/93JD03192.

Holzer, M., & Primeau, F. W. (2010), Improved constraints on transit time distributions from argon 39: A maximum entropy approach, *J. Geophys. Res.*, *115*(C12), C12021, doi:10.1029/2010jc006410.

Jeansson, E., Tanhua, T., Olsen, A., Smethie, W. M., Rajasakaren, B., Ólafsdóttir, S. R., & Ólafsson, J. (2023), Decadal Changes in Ventilation and Anthropogenic Carbon in the Nordic Seas, *Journal of Geophysical Research: Oceans*, *128*(3), doi:10.1029/2022jc019318.

Khatiwala, S., Visbeck, M., & Schlosser, P. (2001), Age tracers in an ocean GCM, *Deep-Sea Res. I*, *48*(6), 1423-1441.

Krysell, M., & Wallace, D. W. R. (1988), Arctic Ocean ventilation studied with a suite of anthropogenic halocarbon tracers, *Science*, *242*, 746-749.

Li, P., Mühle, J., Montzka, S. A., Oram, D. E., Miller, B. R., Weiss, R. F., Fraser, P. J., & Tanhua, T. (2019), Atmospheric histories, growth rates and solubilities in seawater and other natural waters of the potential transient tracers HCFC-22, HCFC-141b, HCFC-142b, HFC-134a, HFC-125, HFC-23, PFC-14 and PFC-116, *Ocean Sci.*, *15*(1), 33-60, doi:10.5194/os-15-33-2019.

Li, P., & Tanhua, T. (2021), Medusa–Aqua system: simultaneous measurement and evaluation of novel potential halogenated transient tracers HCFCs, HFCs, and PFCs in the ocean, *Ocean Sci.*, *17*(2), 509-525, doi:10.5194/os-17-509-2021.

Lu, Z. T., et al. (2014), Tracer applications of noble gas radionuclides in the geosciences, *Earth-Science Reviews*(0), doi:doi.org/10.1016/j.earscirev.2013.09.002.

MacGilchrist, G. A., Naveira Garabato, A. C., Tsubouchi, T., Bacon, S., Torres-Valdés, S., & Azetsu-Scott, K. (2014), The Arctic Ocean carbon sink, *Deep Sea Research Part I: Oceanographic Research Papers*, *86*(0), 39-55, doi:http://dx.doi.org/10.1016/j.dsr.2014.01.002.

Meredith, M., et al. (2019), Polar Regions. In: IPCC Special Report on the Ocean and Cryosphere in a Changing Climate.

Miller, B. R., Weiss, R. F., Salameh, P. K., Tanhua, T., Greally, B. R., Muhle, J., & Simmonds, P. G. (2008), Medusa: A sample preconcentration and GC/MS detector system for in situ measurements of atmospheric trace halocarbons, hydrocarbons, and sulfur compounds, *Anal. Chem.*, *80*(5), 1536-1545.

Montzka, S. A., Hall, B. D., & Elkins, J. W. (2009), Accelerated increases observed for hydrochlorofluorocarbons since 2004 in the global atmosphere, *Geophys. Res. Letters*, *36*(3), doi:10.1029/2008gl036475.

Nghiem, S. V., Chao, Y., Neumann, G., Li, P., Perovich, D. K., Street, T., & Clemente-Colón, P. (2006), Depletion of perennial sea ice in the East Arctic Ocean, *Geophys. Res. Letters*, *33*(17), doi:10.1029/2006gl027198.

Olsen, A., Omar, A. M., Jeansson, E., Anderson, L. G., & Bellerby, R. G. J. (2010), Nordic seas transit time distributions and anthropogenic CO_2, *J. Geophys. Res.*, *115*(C5), C05005.

Raimondi, L., Wefing, A. M., & Casacuberta, N. (2023), Anthropogenic Carbon in the Arctic Ocean: Perspectives From Different Transient Tracers, *Journal of Geophysical Research: Oceans*, *129*(1), doi:https://doi.org/10.1029/2023JC019999.

Rainville, L., Lee, C. M., & Woodgate, R. A. (2011), Impact of Wind-Driven Mixing in the Arctic Ocean, *Oceanography*, *24*(3), 136-145.

Rajasakaren, B., Jeansson, E., Olsen, A., Tanhua, T., Johannessen, T., & Smethie, W. M. (2019), Trends in anthropogenic carbon in the Arctic Ocean, *Prog. Oceanogr.*, *178*, 102177, doi:https://doi.org/10.1016/j.pocean.2019.102177.

Ritterbusch, F., Ebser, S., Welte, J., Reichel, T., Kersting, A., Purtschert, R., Aeschbach-Hertig, W., & Oberthaler, M. K. (2014), Groundwater dating with Atom Trap Trace Analysis of 39Ar, *Geophys. Res. Letters*, *41*(19), 6758-6764, doi:10.1002/2014gl061120.

Rudels, B., Anderson, L., Eriksson, P., Fahrbach, E., Jakobsson, M., & Jones, E. P. (2012), Observations in the ocean, in *Arctic Climate Change*, edited by H.-W. J. (Ed.), pp. 117-198, Dordrecht: Springer, Atmospheric and Oceanographic Sciences Library, doi:https://doi.org/10.1007/978-94-007-2027-5_4.

Rudels, B., Friedrich, H. J., & Quadfasel, D. (1999), The Arctic Circumpolar Boundary Current, *Deep-Sea Res. II*, *46*(6-7), 1023-1062.

Schneider, A., Tanhua, T., Körtzinger, A., & Wallace, D. W. R. (2012), An evaluation of tracer fields and anthropogenic carbon in the equatorial and the tropical North Atlantic, *Deep Sea Research Part I: Oceanographic Research Papers*, *67*(0), 85-97, doi:10.1016/j.dsr.2012.05.007.

Smith, J. N., McLaughlin, F. A., Smethie Jr., W. M., Moran, S. B., & Lepore, K. (2011), Iodine-129, 137Cs, and CFC-11 tracer transit time distributions in the Arctic Ocean, *Journal of Geophysical Research: Oceans*, *116*(C4), doi:10.1029/2010jc006471.

Sonnerup, R. E., Mecking, S., & Bullister, J. L. (2013), Transit time distributions and oxygen utilization rates in the Northeast Pacific Ocean from chlorofluorocarbons and sulfur hexafluoride, *Deep Sea Research Part I: Oceanographic Research Papers*, *72*, 61-71, doi:http://dx.doi.org/10.1016/j.dsr.2012.10.013.

Stöven, T. (2011), Ventilation processes of the Mediterranean Sea based on CFC-12 and SF$_6$ measurements, Christian-Albrecht-Universität zu Kiel, Kiel.

Stöven, T., & Tanhua, T. (2014), Ventilation of the Mediterranean Sea constrained by multiple transient tracer measurements, *Ocean Sci.*, *10*(3), 439-457, doi:10.5194/os-10-439-2014.

Stöven, T., Tanhua, T., Hoppema, M., & Bullister, J. L. (2015), Perspectives of transient tracer applications and limiting cases, *Ocean Sci.*, *11*(5), 699-718, doi:10.5194/os-11-699-2015.

Talley, L. D., et al. (2016), Changes in Ocean Heat, Carbon Content, and Ventilation: A Review of the First Decade of GO-SHIP Global Repeat Hydrography, *Annual Review of Marine Science*, *8*(1), doi:doi:10.1146/annurev-marine-052915-100829.

Tanhua, T., Bulsiewicz, K., & Rhein, M. (2005), Spreading of overflow water from the Greenland to the Labrador Sea, *Geophys. Res. Letters*, *32*(10), L10615, doi:10.1029/2005GL022700.

Tanhua, T., Jones, E. P., Jeansson, E., Jutterstrom, S., Smethie, W. M., Wallace, D. W. R., & Anderson, L. G. (2009), Ventilation of the Arctic Ocean: Mean ages and inventories of anthropogenic CO$_2$ and CFC-11, *J. Geophys. Res.*, *114*(C1), C01002, doi:doi:10.1029/2008JC004868.

Tanhua, T., Waugh, D. W., & Bullister, J. L. (2013), Estimating changes in ocean ventilation from the early 1990s CFC-12 and late 2000s SF$_6$ measurements, *Geophys. Res. Lett*, *40*, 1-6, doi:10.1002/grl.50251.

Terhaar, J., Kwiatkowski, L., & Bopp, L. (2020), Emergent constraint on Arctic Ocean acidification in the twenty-first century, *Nature*, *582*(7812), 379-383, doi:10.1038/s41586-020-2360-3.

Thiele, G., & Sarmiento, J. L. (1990), Tracer dating and ocean ventilation, *J. Geophys. Res.*, *95*(C6), 9377-9391.

Ulfsbo, A., Jones, E. M., Casacuberta, N., Korhonen, M., Rabe, B., Karcher, M., & van Heuven, S. M. A. C. (2018), Rapid Changes in Anthropogenic Carbon Storage and Ocean Acidification in the Intermediate Layers of the Eurasian Arctic Ocean: 1996–2015, *Global Biogeochem Cycle*, *32*(9), 1254-1275, doi:10.1029/2017gb005738.

Wallace, D. W. R., Moore, R. M., & Jones, E. P. (1987), Ventilation of the Arctic Ocean cold halocline: rates of diapycnal isopycnal transport, oxygen utilization and primary production inferred using chlorofluoromethane distributions, *Deep Sea Research I*, *34*(12), 1957-1979.

Wallace, D. W. R., Schlosser, P., Krysell, M., & Bönisch, G. (1992), Halocarbon ratio and tritium/3He dating of water masses in the Nansen Basin, Arctic Ocean, *Deep Sea Research I*, *39*(S2A), 435-458.

Warner, M. J., & Weiss, R. F. (1985), Solubilities of chlorofluorocarbons 11 and 12 in water and sea water, *Deep-Sea Res.*, *32*(12), 1485-1497.

Waugh, D. W., Hall, T. M., & Haine, T. W. N. (2003), Relationship among tracer ages, *J. Geophys. Res.*, *108*(C5), doi:10.1029/2002JC001325.

Waugh, D. W., Vollmer, M. K., Weiss, R. F., Haine, T. W. N., & Hall, T. M. (2002), Transit time distributions in Lake Issyk-Kul, *Goephysical Research Letters*, *29*(24).

Wefing, A. M. (2021), 129I and 236U as a new tracer pair to study water mass circulation in the Arctic Ocean and Fram Strait, ETH Zurich.

Yasunaka, S., et al. (2023), An Assessment of CO2 Uptake in the Arctic Ocean From 1985 to 2018, *Global Biogeochem Cycle*, *37*(11), doi:10.1029/2023gb007806.

5.1 Supplemental Material Manuscript III

Multiple tracer approach to analyze Arctic Ocean Ventilation

L. Gerke[1], T. Tanhua[1]

1 GEOMAR Helmholtz Centre for Ocean Research Kiel, Kiel, Germany

Supplemental Material

Multiple tracer approach to analyze Arctic Ocean Ventilation

Supplemental Methods

Analysis of 'Medusa'-Tracers

At the six Transient Tracer Super Stations (TTSS) water samples for analyzing HCFC's and HFC's were collected using 1.3 L glass ampoules. The ampoules were connected to the Niskin bottles via a stainless steel mounting system (Stöven, 2011). While filling each ampoule, water was overflowed at least twice the volume of the ampoule to ensure removal of any previous contaminations. Directly after sampling, nitrogen gas was connected to the mounting system, which provided a headspace of pure nitrogen gas before flame-sealing the ampoule.

Samples collected at the TTSS for analyzing HCFC's and HFC's were measured using a specially designed purge and trap system in combination with a gas chromatograph mass spectrometer (GC-MS), referred to as the 'Medusa-Aqua' analytical system (Li & Tanhua, 2021).

The 'Medusa'-GC-MS system was developed at the Scripps Institute of Oceanography and enables high precision and simultaneous measurements of approximately 40 atmospheric compounds, including CFC's, HCFC's and HFC's (Miller et al., 2008). The system uses two differently packed traps, kept at controlled low temperature (≈ -165 °C), to separate the less volatile analytes from the most volatile ones in the sample. By individually heating each trap to 100 °C for desorption, the compounds are transferred into the GC and separated within a pre and a main column. The analysis is then performed by a quadrupole mass spectrometer (see Figure S1).
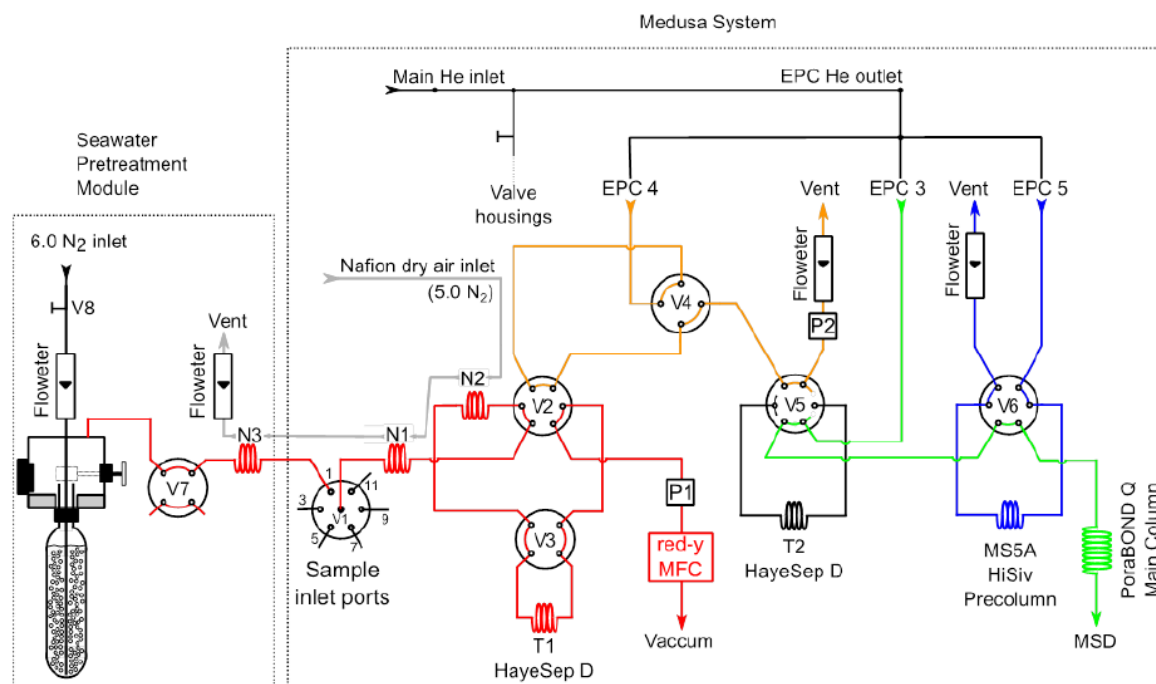
Figure S1: Display of the 'Medusa-Aqua'-system flow scheme, showing the seawater pretreatment module and the analyzing 'Medusa'-GC-MS system (Li & Tanhua, 2021).

The 'Medusa'-system was equipped with an Ampoule-Cracker-System (Li & Tanhua, 2021; Stöven, 2011; Vollmer & Weiss, 2002), which permits to crack and purge the water samples within ampoules. The analytes are absorbed with pure nitrogen gas bubbling through the water sample and transported onto the two traps described previously. The final design is called, 'Medusa-Aqua' analytical system (Li & Tanhua, 2021).

Before the measurement, each ampoule was placed in a 65 °C water bath for a minimum of 24h. This increased the purge efficiency as more gas would previously enter the gas phase. Despite this enrichment of analytes in the gas phase, each sample was measured at least four times to ensure optimal purge efficiency. For exact volume determination each ampoule was weight with and without water following the measurement.

Measurements of a gaseous standard were employed to generate standard curves, used to determine the concentration of each gas within every sample and to identify any potential detector drifts.

The concentrations obtained in the initial measurements required some corrections. First, the measured standard curves had to be adjusted as they did not fully cover the range of concentrations found in the measured samples. To overcome this issue, previously measured

standard curves on the 'Medusa' encompassing higher amounts of tracers-analytes were also considered. These curves were adjusted to align closely with values measured from standard curves during the actual sample analysis, especially at low area values (see Figure S2a, S4a, S5a and S6a). This enabled an extension of the standard curves to cover a wider concentration range, accommodating larger amounts of gaseous standard (see Figure S2b, S3b, S4b and S5b). The corrected standard curves were then used to calculate concentrations of each tracer.
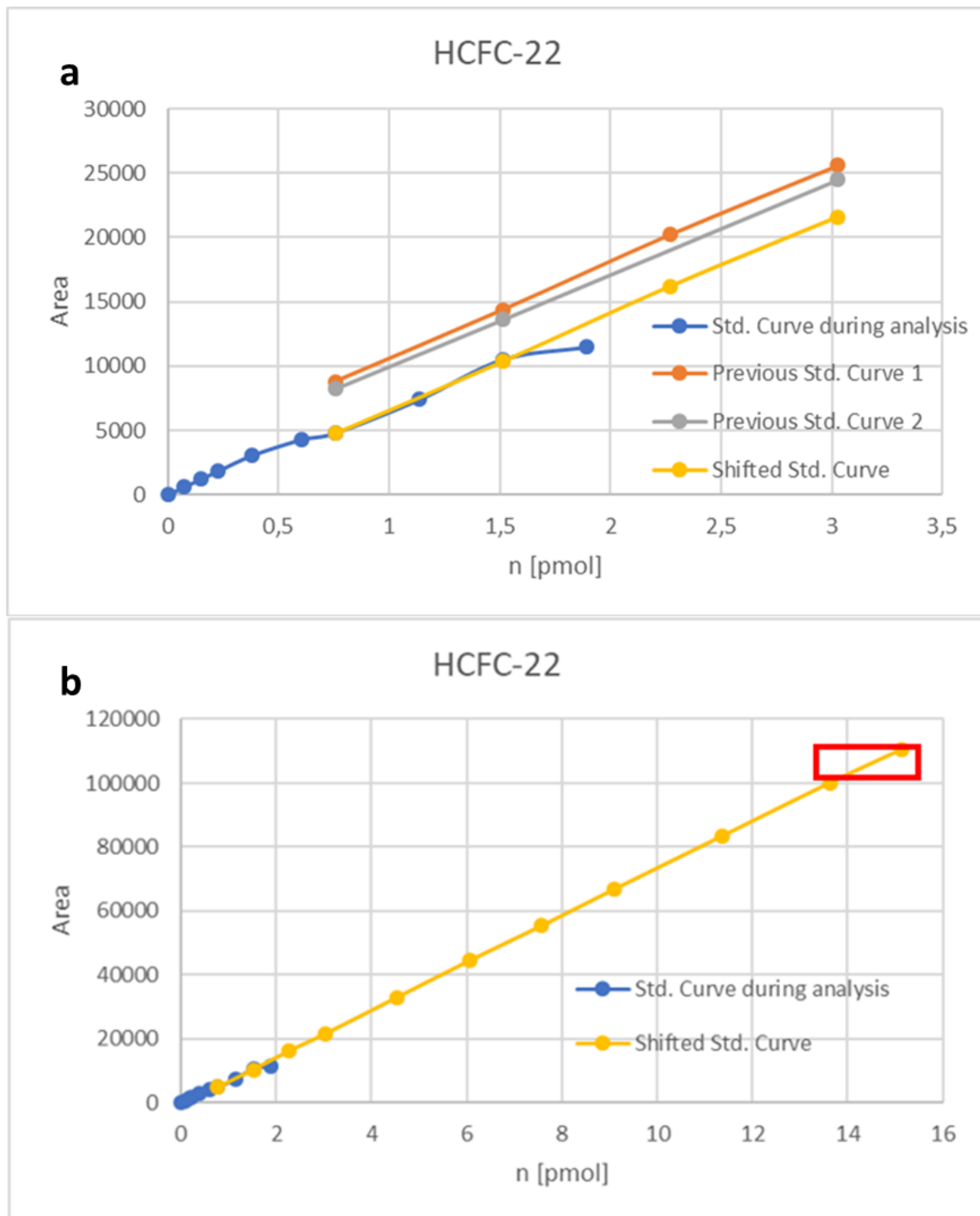
Figure S2: Graph of the shift (a) and extension (b) of the standard curve used to determine HCFC-22 concentrations. The shifted standard curve in the top graph only shows the lower concentration ranges to fit it more precisely to the standard curve measured during the actual sample analysis. The actual concentrations measured in the ocean surface water samples are found in the high concentration range shown in the red box.

Second, the HCFC-22 and HFC-134a concentrations obtained needed to be multiplied by a factor of 1.5 and 0.9, respectively. This aligned the surface water sample values with the atmospheric concentrations measured in the corresponding year (2021) in the northern hemisphere. To compare these values, the measured concentrations were converted from mol/L to partial pressure (ppt - parts per trillion) values, which is typically used for atmospheric values. Following these corrections all tracer concentrations measured in the surface water samples were found to be consistent with the respective atmospheric concentrations observed in 2021 (see Figure S3).
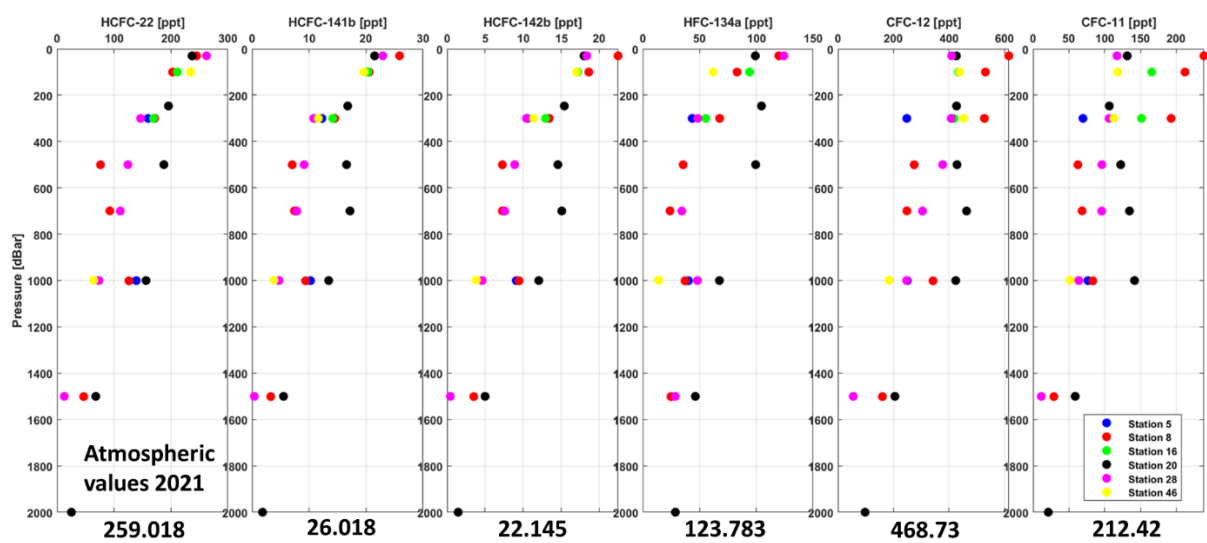

Figure S3: Display of the calculated partial pressures of all samples using the Ostwald solubility of each tracer (Li et al., 2019) after implementing the adjustments. The different colors represent the samples collected at each of the six stations. The atmospheric partial pressures of each tracer in the northern hemisphere in 2021 of each tracer are displayed at the bottom.
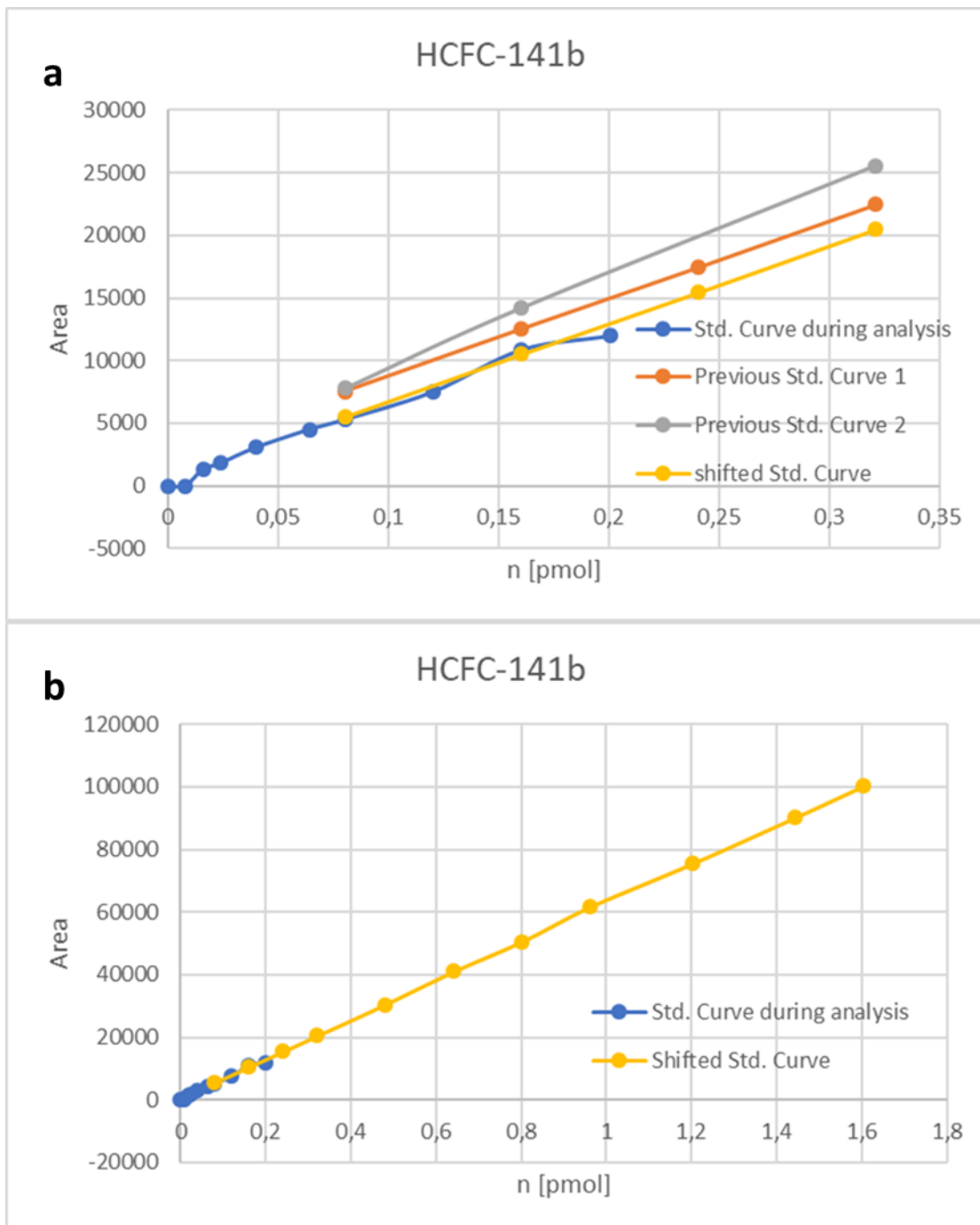
Additional Supplemental Figures

Figure S4: Graph of the shift (a) and extension (b) of the standard curve used to determine HCFC-141b concentrations. The shifted standard curve in the top graph only shows the lower concentration ranges to fit it more precisely to the standard curve measured during the actual sample analysis.
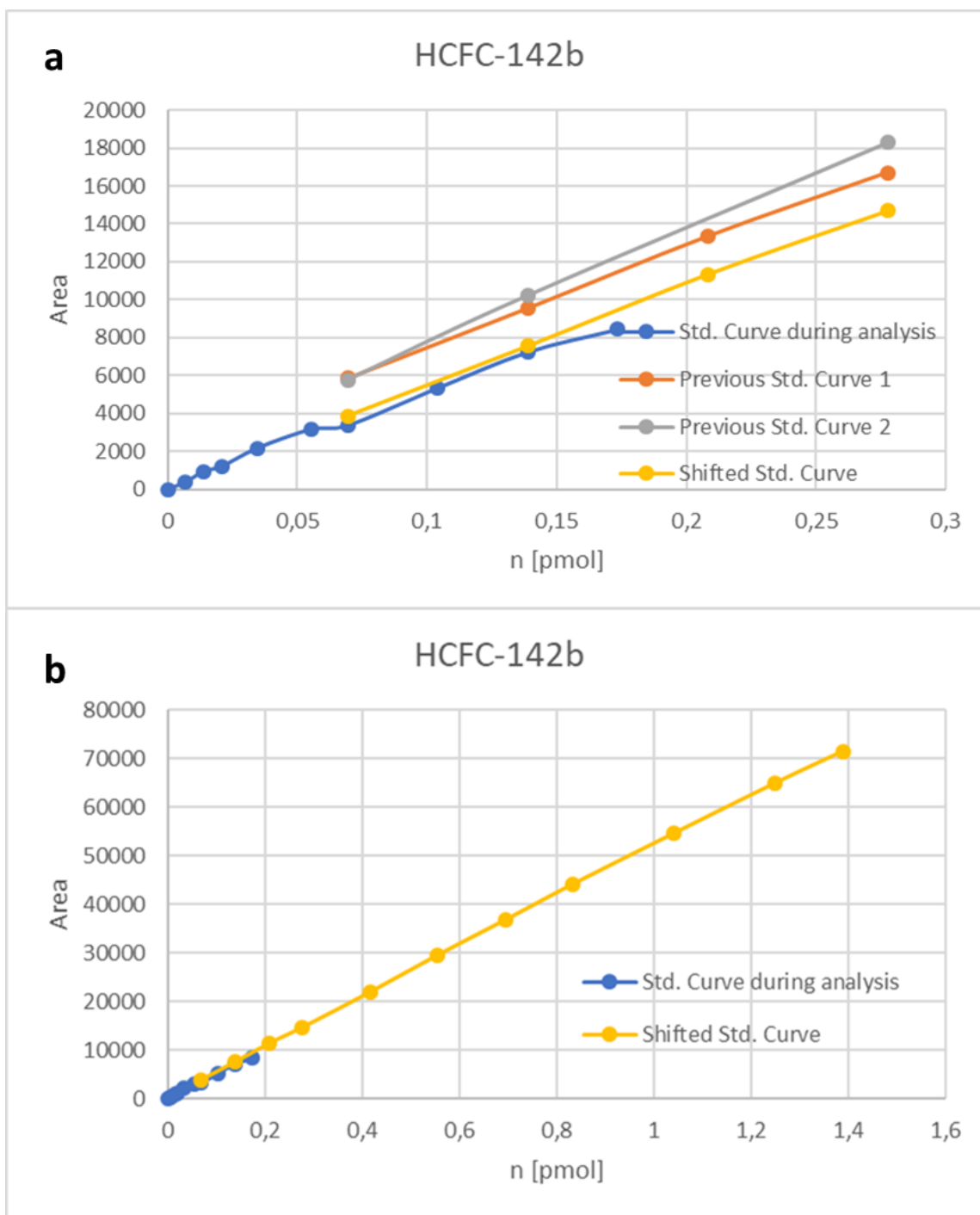
Figure S5: Graph of the shift (a) and extension (b) of the standard curve used to determine HCFC-142b concentrations. The shifted standard curve in the top graph only shows the lower concentration ranges to fit it more precisely to the standard curve measured during the actual sample analysis.

Figure S6: Graph of the shift (a) and extension (b) of the standard curve used to determine HFC-134a concentrations. The shifted standard curve in the top graph only shows the lower concentration ranges to fit it more precisely to the standard curve measured during the actual sample analysis.
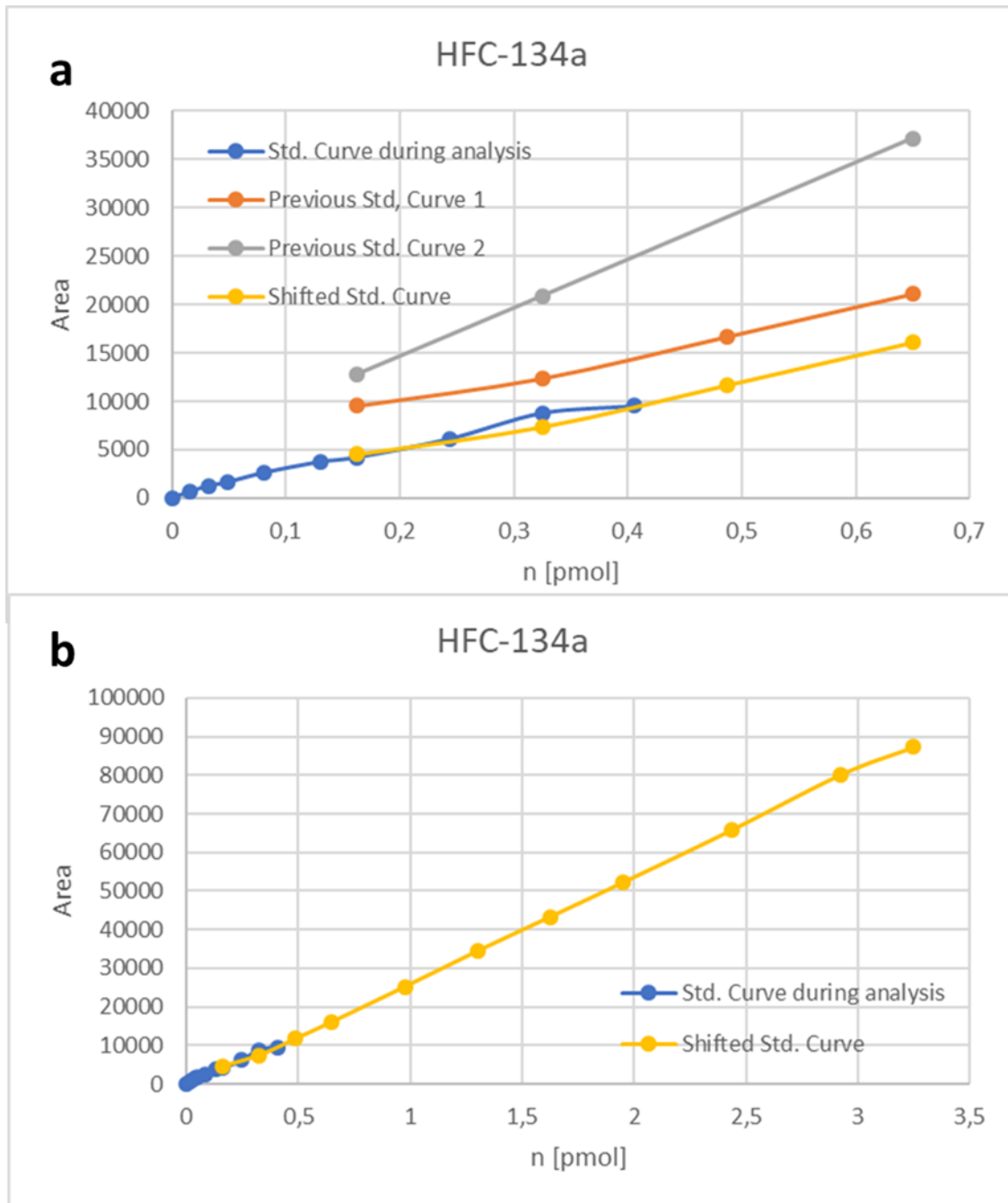
_____
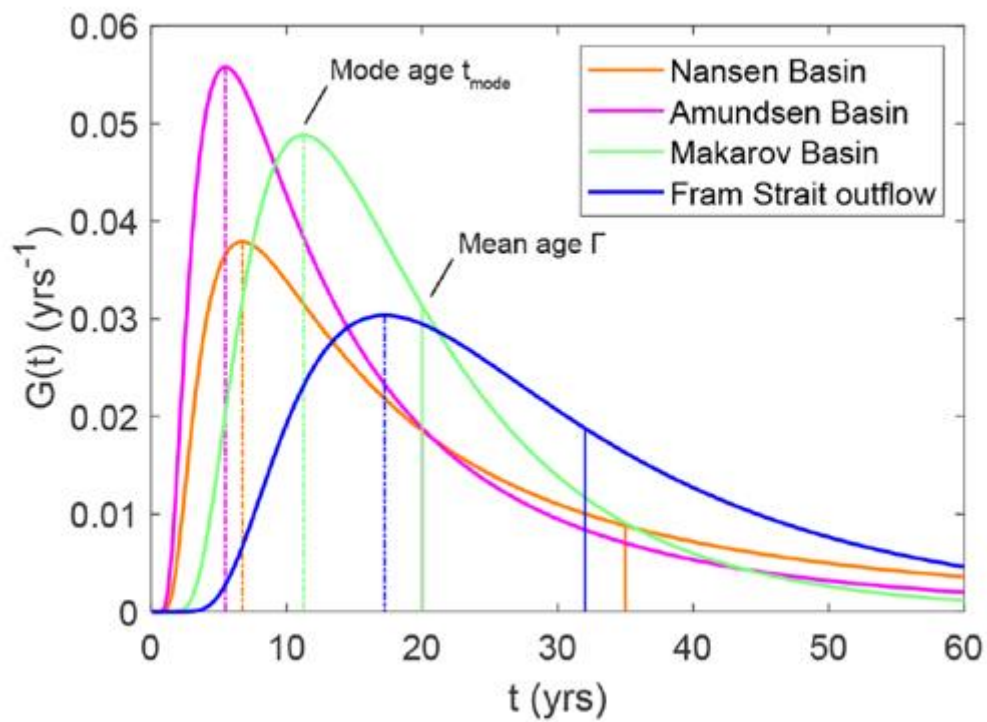
Figure S7: Inverse Gaussian TTDs, showing the distribution of ages for a water parcel with the mean age and mode age displayed. The most probable functions for different basins in the Arctic Ocean are shown (Wefing et al., 2021).

Figure S8: Display of the relative standard deviations of the parameters (a) Δ/Γ-ratio and (b) mean age. The different colors represent the deviations in the calculations including or excluding the results from the tracer pair CFC-12&HFC-134a. They also depict if the min and max values, which result from the errors in concentration measurements, are included or not.

Additional Supplemental Tables

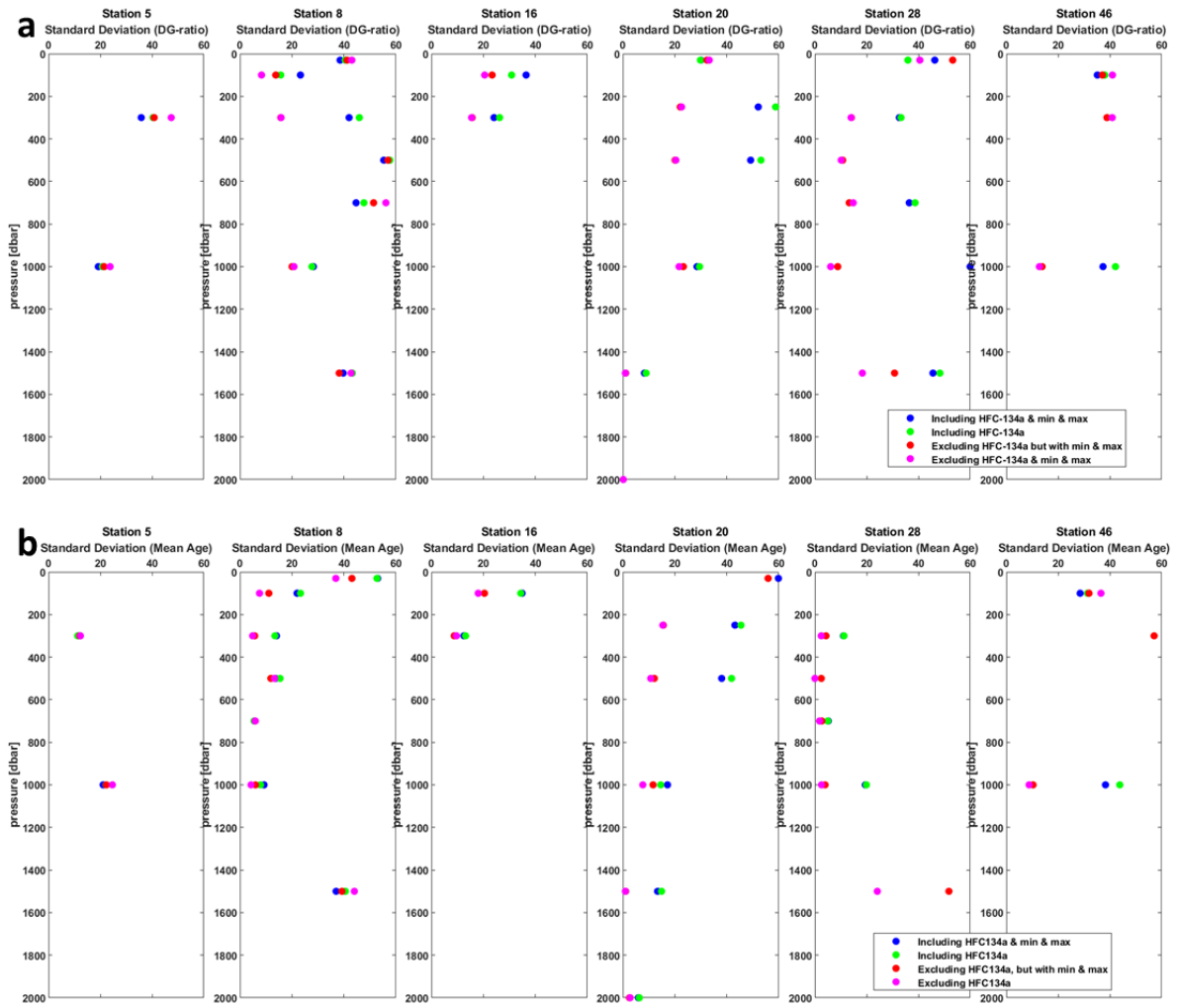**Table S1:** Calculated results of the overall mean age (Γ), as well as the individual mean ages of the two water masses mixing (Γ_1, Γ_2) and the determined α at the stations 5, 8, 16, 20 and 46. Also displayed are the predetermined boundary conditions for Δ/Γ-ratios and overall mean age of the two water masses. Results marked in yellow represent the stations, where measurement uncertainties are likely to cause standard deviations above 20 %, not the presence of two water masses.

Station	Depth	Δ_1/Γ_1-ratio	Δ_2/Γ_2-ratio	Γ-boundary	α	Γ_1	Γ_2	Γ
5	300	1.0	0.4	17-25	0.1	2.5	22.5	25
5	1000	1.8	1.0	61-119	1	112	NaN	112
8	100	0.9	0.4	6-14	1	11	NaN	11
8	300	0.9	0.4	13-22	1	18	NaN	18
8	500	1.0	0.1	22-32	0.1	3.2	28.8	32
8	700	1.0	0.1	26-32	1	32	NaN	32
8	1000	1.5	0.5	33-45	0.2	9	36	45
8	1500	1.5	0.5	63-169	0.1	8.1	72.9	81
16	100	0.9	0.4	3-16	0.9	10.8	1.2	12
16	300	0.9	0.4	14-21	0.1	2.1	18.9	21
20	250	0.9	0.4	1-18	0.9	11.7	1.3	13
20	500	0.9	0.4	2-20	0.9	15.3	1.7	17
20	1000	1.5	0.5	20-45	1	39	NaN	39
20	1500	1.5	0.5	105-169	0.3	36.3	84.7	121
46	100	0.9	0.4	5-16	0.8	12.8	3.2	16
46	300	0.9	0.4	1-24	1	19	NaN	19
46	1000	1.5	0.5	59-82	0.1	6.9	62.1	69

References

Li, P., Mühle, J., Montzka, S. A., Oram, D. E., Miller, B. R., Weiss, R. F., Fraser, P. J., & Tanhua, T. (2019), Atmospheric histories, growth rates and solubilities in seawater and other natural waters of the potential transient tracers HCFC-22, HCFC-141b, HCFC-142b, HFC-134a, HFC-125, HFC-23, PFC-14 and PFC-116, *Ocean Sci.*, *15*(1), 33-60, doi:10.5194/os-15-33-2019.

Li, P., & Tanhua, T. (2021), Medusa–Aqua system: simultaneous measurement and evaluation of novel potential halogenated transient tracers HCFCs, HFCs, and PFCs in the ocean, *Ocean Sci.*, *17*(2), 509-525, doi:10.5194/os-17-509-2021.

Miller, B. R., Weiss, R. F., Salameh, P. K., Tanhua, T., Greally, B. R., Muhle, J., & Simmonds, P. G. (2008), Medusa: A sample preconcentration and GC/MS detector system for in situ measurements of atmospheric trace halocarbons, hydrocarbons, and sulfur compounds, *Anal. Chem.*, *80*(5), 1536-1545.

Stöven, T. (2011), Ventilation processes of the Mediterranean Sea based on CFC-12 and SF_6 measurements, Christian-Albrecht-Universität zu Kiel, Kiel.

Vollmer, M. K., & Weiss, R. F. (2002), Simultaneous determination of sulfur hexafluoride and three chlorofluorocarbons in water and air, *Mar. Chem.*, *78*(2-3), 137-148.

Wefing, A. M., Casacuberta, N., Christl, M., Gruber, N., & Smith, J. N. (2021), Circulation timescales of Atlantic Water in the Arctic Ocean determined from anthropogenic radionuclides, *Ocean Sci.*, *17*(1), 111-129, doi:10.5194/os-17-111-2021.

6. Summary, Discussion and Outlook

This chapter presents a discussion and summary of the major findings of this thesis (chapters 3, 4 and 5), and gives an outlook on possible future research directions. The first emphasis was on ventilation in the Arctic Ocean (AO), focusing on the general ventilation and circulation patterns observed during the 'SAS-Oden 2021' expedition, and a temporal variability identified through comparison with historical data. The second focus concerned the application of novel transient tracers also sampled in the AO and their usefulness to improve the ventilation analysis. In the third major aim, transient tracer measurements and ventilation analyses were carried out to obtain information on the deep water masses entering the Gulf of St. Lawrence (GSL) and identify possible changes in ventilation within the deep water inflow into the Gulf from the Atlantic Ocean.

6.1 Arctic Ocean

Using data obtained from transient tracer (CFC-12 and SF_6) measurements collected during the 'SAS-Oden 2021' expedition aboard the icebreaker Oden, an analysis of ventilation and circulation was conducted. Samples were measured onboard and from the concentrations determined, the transit time distribution (TTD) was derived. The comparison of mean age results obtained for each of the two tracers enabled the determination of the most probable TTD, characterized by a time dependent saturation and a Δ/Γ-ratio of 1. The time dependent saturation of the tracers was determined by Jeansson et al. (2023) from measurements in the Greenland Sea, a region where surface water subducts and enters the AO.

The general ventilation analysis revealed increasing mean ages (lower tracer concentrations) from the surface to the interior. The oldest water (lowest concentrations) was found at the bottom of the Makarov Basin, whereas somewhat younger ages were observed in the Nansen and Amundsen Basins. This indicates the presence of poorly ventilated older deep water on the Amerasian side of the Lomonosov Ridge in comparison to the Eurasian side, as previously also noted by Macdonald & Carmack (1991) and Jones et al. (1995). In each case this regional deep water is most likely formed by boundary convection processes that transport local brine enriched water formed at the shelfs into the deep basins (Aagaard & Carmack, 1989; Anderson et al., 1999; Tanhua et al., 2009; Wallace et al., 1992).

Slightly elevated tracer concentrations (younger water masses) were observed in the upper and intermediate layers at latitudes near the North Pole, close to the Lomonosov Ridge, compared to analogous depths within the central Nansen and Amundsen Basins. These were detected using the well-established tracers CFC-12 and SF_6, but also by the newly introduced, so called 'Medusa'-tracers (HCFC-22, HCFC-141b, HCFC-142b and HFC-134a) which all show elevated tracer concentrations at a station near the North Pole. The higher tracer concentrations signify the presence of the Arctic Ocean Boundary Current (AOBC). This current represents a boundary circulation of Atlantic Water (AW), which enters at the Fram Strait and through the Barents Sea, and circulates around the AO, primarily along the ocean ridges before returning to the Fram Strait. Water movement via the AOBC could explain the calculated mean ages, which at intermediate depths showed values of approximately 20 years at the North Pole and 10 years at stations near the Svalbard shelf, where the AW enters. This mean age difference of approximately 10 years fits precisely with the AW transport rates reported by Smith et al. (2011).

The analysis of temporal changes in the ventilation focused on the intermediate water layer (250-1500 m), which was chosen due to the optimal representation of the age spectrum by the two tracers CFC-12 and SF_6 at these depths. It included data from historical cruises conducted in 1991, 2005 and 2015. In addition to the transient tracer data, changes in AOU (Apparent Oxygen Utilization) rates and water properties (temperature and salinity) throughout the years were included in the analysis, which focused on the Eurasian Arctic Ocean. The comparison identified a decrease in the ventilation from 2005 through 2015 until 2021 in all regions analyzed (Nansen and Amundsen Basins), which most likely can be attributed to changes in the AW entering the AO. Correspondingly, the computed mean ages increased from 2005 over 2015 until 2021. The water properties measured also showed variability, with increased temperatures observed in 2005 and 2015 at intermediate depths and AOU data displaying the same pattern as the mean ages, i.e. higher values in 2021 compared to 2005 and 2015.

Notably, mean age data from 1991 showed even slightly higher values compared to those observed in 2021 in all regions, apart from the northern Amundsen Basin. This suggests reduced ventilation in 1991 and 2021 relative to 2005 and 2015 and implies the presence of a multidecadal variability in the ventilation. The minor discrepancy in the AOU data, which showed comparable results in 1991 and 2021, and no elevation in 1991, potentially can be

attributed to measurement uncertainties in the 1991 data and possible changes in the respiration rates affecting the AOU values. A decline in respiration rates may have shifted the 2005, 2015 and 2021 data towards higher AOU values, thereby closer to those observed in 1991, thus resulting in similar values for 1991 and 2021. In contrast to other parts of the AO, the multidecadal variability was not observed in the North Pole region, where the AOBC is present. Here the 1991 mean ages were comparable to those observed in 2005. Given that the boundary current transports water masses from the Fram Strait to the North Pole within approximately 12 years (Smith et al., 2011), and considering the 14-year interval between 1991 and 2005, multidecadal-scale changes do not significantly impact intermediate waters at these latitudes. Furthermore, the observations around the North Pole suggest a slowdown in the boundary current over the past 16 years, as the mean ages increased from 2005 until 2021.

The inclusion of multiple tracers in the ventilation analysis of the AO (manuscript III), provided more detailed information and permitted a more comprehensive and precise assessment of ventilation parameters. Given the age spectrum of the tracers used for the analysis, the focus remained on the intermediate layer until a depth of 1500 m. Employing six different tracers and comparing a variety of different tracer pairs under the assumption of a one-inverse Gaussian (1-IG) distribution of ages to represent the transit time distribution (TTD), revealed that advective flow (Δ/Γ-ratio < 1) dominates the ventilation within the upper parts of the intermediate layer. Diffusive characteristics, however, exhibit an increasing influence at the depths below. The intermediate layer of the Makarov Basin, showed the most pronounced advective flow at these depths, with only a slight diffusive influence as depth increased. As all tracer pairs displayed similar and meaningful results, this analysis demonstrated the suitability of 'Medusa'-tracers for ventilation analyses in the AO region. Nevertheless, in certain regions of the AO, such as the Nansen and Amundsen Basins, some small difference in the mean age and especially the Δ/Γ-ratio were observed between the tracer pairs. Assuming that these discrepancies occurred due to the presence of two water masses mixing in the respective areas, the TTD analysis in these regions was extended from a 1-IG to a two-inverse Gaussian (2-IG) distribution to represent the TTD. This could account for the mixing of two water masses with distinct age histories and similar densities and could be carried out due to the unique suit of multiple tracers measured. The 2-IG TTD analyses employing multiple tracers indeed showed that the intermediate water layer in many areas of the Eurasian AO represents a

mixture of water masses with similar densities but distinct ages. Possibly this is due to a mixing of the AW, which enters the AO from the Atlantic, with water regionally formed at the shelf areas. However, the situation in the Makarov Basin is different. Here the results for mean age and Δ/Γ-ratio, calculated under the assumption of a 1-IG distribution of ages, were almost identical for different tracer pairs, suggesting a more homogeneous water distribution.

Together, the analyses demonstrated that ocean ventilation and circulation patterns can be described using transient tracer measurements combined with the TTD method assuming a one- or two-inverse Gaussian age distribution. Important insights into the water mass ages and the interplay between advective and diffusive flow characteristics were obtained. The data emphasize the importance of continued sampling of well-established tracers, such as CFC-12 and SF$_6$, in future campaigns and show the effectiveness of the 'Medusa'-tracers in improving ventilation analysis in the cold AO region.

6.2 Gulf of St. Lawrence

Possible ventilation changes in the deep water of the GSL were assessed using a collection of transient tracer data which were obtained during two research expeditions in 2022. Previous studies had revealed that the deep water entering the Gulf comprises a mix of older North Atlantic Central Water (NACW) and younger Labrador Current Water (LCW) and had proposed a transition towards an increased influence of NACW. To further assess this possible trend, the transient tracer data were used to derive the most probable TTD for the ventilation analysis, incorporating a time dependent saturation of the tracers determined from measurements in the Labrador Sea (Raimondi et al., 2021) and a Δ/Γ-ratio of 1.2.

The analysis identified the presence of relatively young, cooler, and fresher water in the Lower St. Lawrence Estuary and western Gulf. Older, warmer and more saline water on the other hand, was found entering through Cabot Strait. This distribution of water mass ages is opposite to what would be expected from the deep water flow pattern, which transports water from the east to the west at these depths, normally resulting in aging waters along the way (Dickie & Trites, 1983). Therefore, the distributions observed now provide clear evidence for a recent change in the composition of the GSL's deep water inflow. They imply that the mixing proportions for this deep layer have changed significantly with the deep water

increasingly dominated by older NACW and less influenced by younger LCW. Jutras et al. (2023) also reported such a recent shift using an extended optimum multiparameter (eOMP) analysis of water mass properties. However, in contrast to the eOMP analysis by Jutras et al. (2023), which indicated that deep waters in the Lower Estuary were comprised solely of NACW in 2022, our calculations of age distributions based on transient tracer measurements in 2022 provide evidence for a remaining contribution of LCW to the deep water within the Lower Estuary.

In recent years, the GSL waters showed a trend towards decreasing oxygen concentration, partly being attributed to a shift in the deep water composition. Our analysis supports this view because due to the increased NACW influence, less oxygen is transported into the Gulf. The older NACW has been shielded from the atmosphere for longer and therefore has been subject to respiration processes in the water column for a longer time, resulting in lower oxygen levels relative to the younger LCW. Our analysis furthermore indicates that the LCW contribution to deep water entering the Gulf will continue to decline in the future. Therefore, further deoxygenation in the Lower Estuary of the GSL can be expected.

Given the timing of our sampling in 2022 and estimated transit times of 1-2 years for water moving from Cabot Strait to Anticosti Island (S. W. Stevens, personal communication), the herein documented mid-channel transition from younger to older water suggests that a significant shift in inflow composition took place around 2020. This is in line with a drastic decrease of bottom water oxygen content observed around this time (Jutras et al., 2023).

Another circulation feature observed by analyzing properties and age distribution of GSL deep waters is the cross-channel variability. Older, warmer and more saline water enters along the northern boundary of the Laurentian Channel, while younger, cooler and less saline water is found along the southern boundary. This is indicative of the presence of a cyclonic circulation in the Laurentian Channel (Han et al., 1999).

6.3 Outlook

6.3.1 General aspects

As demonstrated in this thesis, the multiple tracer approach is a valuable tool to improve precision in the determination of the TTD for the analysis of ventilation in the AO. The use of

more than two tracers with significantly different input functions yields valuable information needed to constrain the most suitable TTD and this should be considered in planning future campaigns. However, this should not happen at the expense of sampling the well-established tracers CFC-12 and SF_6 as their recordings will continue to yield important information on ventilation patterns in the intermediate water column.

6.3.2 Arctic Ocean

The analysis conducted in this study revealed variability in the ventilation and indicated a multidecadal change in the ventilation patterns. This emphasizes the need for further investigations, including transient tracer measurements in future campaigns. Preferably, the use of CFC-12 and SF_6 should be continued, but measurements should also be expanded by sampling of 'Medusa' or other age tracers. Together, this should yield a more comprehensive understanding of ventilation dynamics in the rapidly changing environment of the AO.

During the 'SAS-Oden 2021' expedition, water sampling was carried out not only to measure CFC-12, SF_6 and 'Medusa' tracers but also to eventually determine concentrations of radioactive tracers such as Iodine-129, Uranium-236, Carbon-14, and Argon-39. As sampling occurred at the same location and time, these additional tracers hold the potential to further increase accuracy in the ventilation analysis. Considering the age spectrum of each tracer, a particular focus could be placed on the surface and intermediate waters utilizing ^{129}I and ^{236}U, while deep waters could be analyzed with the help of ^{14}C and ^{39}Ar data. Together, this would permit a comprehensive ventilation analysis spanning the entire water column in the AO.

In addition to analyzing the most probable TTD for each region and depth, this information can be used to obtain detailed information on the anthropogenic carbon storage within the AO. Anthropogenic carbon can be treated as a tracer with increasing atmospheric concentrations since preindustrial times. Once the age distribution of a water parcel is known, it becomes feasible to calculate the anthropogenic carbon content within this given water parcel.

6.3.3 Gulf of St. Lawrence

By analyzing transient tracer data this study has confirmed a recent change in the composition of the deep water in the GSL. This underscores the necessity for future expeditions to monitor these dynamics in the next years and thereby answer, among others, the following questions: Does the deep water continue to get older? And, does the older water in the eastern Gulf indeed move towards the western end, potentially reducing the oxygen supply to the Estuary? Addressing these questions through ongoing observations and analyses will be crucial for obtaining a comprehensive understanding of the evolving deep water dynamics in the Gulf.

References Main Text

Aagaard, K. (1989), A synthesis of the Arctic Ocean circulation, *Rapports et Proces-verbaux Reunion Conseil Internationale Exploration de la Mer*, *188*, 11-22, doi:10.17895/ices.pub.19279133.

Aagaard, K., & Carmack, E. (1989), The role of sea ice and fresh water in the Arctic circulation, *J. Geophys. Res.*, *94*(14), 485-498.

Aagaard, K., Coachman, L. K., & Carmack, E. C. (1981), On the halocline of the Arctic Ocean, *Deep Sea Research*, *28*, 529-545.

Aksenov, Y., Ivanov, V. V., Nurser, A. J. G., Bacon, S., Polyakov, I. V., Coward, A. C., Naveira Garabato, A. C., & Beszczynska-Möller, A. (2011), The arctic circumpolar boundary current, *Journal of Geophysical Research: Oceans*, *116 (C9)*, doi:https://doi.org/10.1029/2010JC006637.

Anderson, L. G., Jones, E. P., & Rudels, B. (1999), Ventilation of the Arctic Ocean estimated by a plume entrainment model constrained by CFCs, *J. Geophys. Res.*, *104*(C6), 13423-13429.

Azetsu-Scott, K., Jones, E. P., & Gershey, R. M. (2005), Distribution and ventilation of water masses in the Labrador Sea inferred from CFCs and carbon tetrachloride, *Mar. Chem.*, *94*(1-4), 55-66.

Bauch, D., Torres-Valdes, S., Polyakov, I., Novikhin, A., Dmitrenko, I., McKay, J., & Mix, A. (2014), Halocline water modification and along-slope advection at the Laptev Sea continental margin, *Ocean Science*, *10*(1), 141-154, doi:10.5194/os-10-141-2014.

Beaird, N., Fer, I., Rhines, P., & Eriksen, C. (2012), Dissipation of Turbulent Kinetic Energy Inferred from Seagliders: An Application to the Eastern Nordic Seas Overflows, *J. Phys. Oceanogr.*, *42*(12), 2268-2282, doi:10.1175/jpo-d-12-094.1.

Bowden, K. F. (1963), The mixing process in a Tidal Estuary, in *Air and Water Polution Annual Report*, edited, Pergamon Press.

Brandt, P., Funk, A., Czeschel, L., Eden, C., & Böning, C. W. (2006), Ventilation and Transformation of Labrador Sea Water and Its Rapid Export in the Deep Labrador Current, *J. Phys. Oceanogr.*, *37*, 946-961, doi:DOI: 10.1175/JPO3044.1.

Bullister, J., & Warner, M. J. (2017), Atmoshperic Histories (1765-2022) for CFC-11, CFC-12, CFC-113, CCl4, SF6, N2O (NCEI Accession 0164584). An update to Bullister (2015) NDP-09, *NOAA Nathional Centers for Environmental Information. Dataset*, doi:https://doi.org/10.3334/cdiac/otg.cfc_atm_hist_2015.

Bullister, J. L., Wisegarver, D. P., & Menzia, F. A. (2002), The solubility of sulfur hexafluoride in water and seawater, *Deep-Sea Res. I*, *49*(1), 175-187.

Casacuberta, N., Masqué, P., Henderson, G., Rutgers van-der-Loeff, M., Bauch, D., Vockenhuber, C., Daraoui, A., Walther, C., Synal, H. A., & Christl, M. (2016), First 236U data from the Arctic Ocean and use of 236U/238U and 129I/236U as a new dual tracer, *Earth and Planetary Science Letters*, *440*, 127-134, doi:https://doi.org/10.1016/j.epsl.2016.02.020.

Chen, C. Y., Li, Y. M., Bailey, K., O'Connor, T. P., Young, L., & Lu, Z. T. (1999), Ultrasensitive Isotope Trace Analyses with a Magneto-Optical Trap, *Science*, *286*(5442), 1139-1141, doi:10.1126/science.286.5442.1139.

Christl, M., Casacuberta, N., Vockenhuber, C., Elsässer, C., Bailly Du Bois, P., Herrmann, J., & Synal, H. A. (2015), Reconstruction of the 236U input function for the Northeast Atlantic Ocean: Implications for 129I/236U and 236U/238U-based tracer ages, *Journal of Geophysical Research: Oceans*, *120*(11), 7282-7299, doi:10.1002/2015jc011116.

Clarke, R. A., & Gascard, J. C. (1983), The formation of Labrador Sea-Water. Part 1: Large-scale processes, *J. Phys. Oceanogr.*, *13*(10), 1764-1778.

Collon, P., et al. (2004), Development of an AMS method to study oceanic circulation characteristics using cosmogenic 39Ar, *Nucl. Instrum. Methods Phys. Res. Sect. B-Beam Interact. Mater. Atoms*, *223-224*, 428-434, doi:https://doi.org/10.1016/j.nimb.2004.04.081.

Cyr, F., Bourgault, D., Galbraith, P. S., & Gosselin, M. (2015), Turbulent nitrate fluxes in the Lower St. Lawrence Estuary, Canada, *Journal of Geophysical Research: Oceans*, *120*(3), 2308-2330, doi:10.1002/2014jc010272.

D'Asaro, E. A. (1985), The energy flux from the wind to near inertial motions in the surface mixed layer, *Journal of Physical Oceanograohy*, *15*(1), 1043-1059, doi:https://doi.org/10.1175/1520-0485(1985)015<1043:TEFFTW>2.0.CO;2.

Dickie, L., & Trites, R. (1983), The Gulf of St. Lawrence, in: Ecosystems of the World: Estuaries and enclosed seas, *edited by: Ketchum, B., New York, NY, Elsevier*, 403-425.

Dincer, S., Tezcan, S. S., Duzkaya, H., & Dincer, M. S. (2018), Insulation and Molecular Properties of Alternative Gases to SF6, in *2nd International Symposium on Multidisciplinary Studies and Innovative Technologie*, edited, Ankara, Turkey, doi:10.1109/ISMSIT.2018.8566680.

Dokmanic, I., Parhizkar, R., Ranieri, J., & Vetterli, M. (2015), Euclidean Distance Matrices: Essential theory, algorithms, and applications, *IEEE Signal Processing Magazine*, *32*(6), 12-30, doi:10.1109/msp.2015.2398954.

Ebser, S., Kersting, A., Stöven, T., Feng, Z., Ringena, L., Schmidt, M., Tanhua, T., Aeschbach, W., & Oberthaler, M. K. (2018), 39Ar dating with small samples provides new key constraints on ocean ventilation, *Nature Communications*, *9*(1), 5046, doi:10.1038/s41467-018-07465-7.

Edmonds, H. N., Zhou, Z. Q., Raisbeck, G. M., Yiou, F., Kilius, L. R., & Edmond, J. M. (2001), Distribution and behaviour of anthropogenic 129I in water masses ventilating the North Atlantic Ocean, *J. Geophys. Res.*, *106*(C4), 6881-6894.

Ekwurzel, B., Schlosser, P., Mortlock, R. A., Fairbanks, R. G., & Swift, J. H. (2001), River runoff, sea ice meltwater, and Pacific water distribution and mean residence times in the Arctic Ocean, *J. Geophys. Res.*, *106*(C5), 9075-9092.

Feldman, G. C., & McClain, C. R. (2012), Ocean Color Web, MODIS Reprocessing R2009, NASA Goddard Space Flight Center, http://oceancolor.gsfc.nasa.gov.

Ferrari, R., & Wunsch, C. (2009), Ocean Circulation Kinetic Energy: Reservoirs, Sources, and Sinks, *Annual Review of Fluid Mechanics*, *41*(1), 253-282, doi:10.1146/annurev.fluid.40.111406.102139.

Fine, R. A. (2011), Observations of CFCs and SF(6) as Ocean Tracers, *Annual Review of Marine Science, Vol 3*, *3*, 173-195, doi:10.1146/annurev.marine.010908.163933.

Flato, G. M. (2011), Earth system models: an overview, *WIREs Climate Change*, *2*(6), 783-800, doi:10.1002/wcc.148.

Frolov, I. E., Gudkovich, Z. M., Radionov, V. F., Shirochkov, A. V., & Timokhov, L. A. (2005), The Arctic Basin, *Springer Praxis Books*, doi:10.1007/3-540-37665-8.

Galbraith, P. S. (2006), Winter water masses in the Gulf of St. Lawrence, *J. Geophys. Res.*, *111*(C6), doi:10.1029/2005jc003159.

Gascard, J.-C., Watson, A. J., Messias, M.-J., Olsson, K. A., Johannessen, T., & Simonsen, K. (2002), Long-lived vortices as a mode of deep ventilation in the Greenland Sea, *Nature*, *416*(6880), 525-527.

Gascard, J. C., & Clarke, R. A. (1983), The formation of Labrador Sea-Water. Part 2: Mesoscale and smaller-scale processes, *J. Phys. Oceanogr.*, *13*(10), 1779-1797.

Gascard, J. C., Raisbeck, G., Sequeira, S., Yiou, F., & Mork, K. A. (2004), The Norwegian Atlantic Current in the Lofoten basin inferred from hydrological and tracer data (129-I) and its interaction with the Norwegian Coastal Current, *Geophys. Res. Letters*, *31*(1), doi:10.1029/2003gl018303.

Gilbert, D., & Pettigrew, B. (1997), Interannual variability (1948 - 1994) of the CIL core temperature in the Gulf of St. Lawrence, *Can. J. Fish. Aquat. Sci.*, *54*, 57-67.

Gilbert, D., Rabalais, N. N., Díaz, R. J., & Zhang, J. (2010), Evidence for greater oxygen decline rates in the coastal ocean than in the open ocean, *Biogeosciences*, *7*(7), 2283-2296, doi:10.5194/bg-7-2283-2010.

Golovko, V. V. (2023), Application of the most frequent value method for 39Ar half-life determination, *The European Physical Journal C*, *83*(10), doi:10.1140/epjc/s10052-023-12113-6.

Gordon, A. L. (1981), South Atlantic thermocline ventilation, *Deep Sea Research Part A. Oceanographic Research Papers*, *28*(11), 1239-1264, doi:https://doi.org/10.1016/0198-0149(81)90033-9.

Grassl, H. (2001), Chapter 1.1 Climate and oceans, in *Ocean Circulation and Climate*, edited by G. Siedler, J. Church and J. Gauld, pp. 3-9, Academic Press, International Geophyiscs, doi://doi.org/10.1016/S0074-6142(01)80108-X.

Griffin, D. A., & LeBlond, D. A. (1990), Estuary/ocean exchange controlled by spring-neap tidal mixing, *Estuarine, Coastal and Shelf Science*, *30*(3), 275-297, doi:https://doi.org/10.1016/0272-7714(90)90052-S.

Haine, T. W. N. (2021), A Conceptual Model of Polar Overturning Circulations, *J. Phys. Oceanogr.*, *51*(3), 727-744, doi:10.1175/jpo-d-20-0139.1.

Hall, T. M., & Plumb, R. A. (1994), Age as a diagnostic of stratospheric transport, *Journal of Geophysical Research: Atmospheres*, *99*(D1), 1059-1070, doi:10.1029/93JD03192.

Han, G., Loder, J. W., & Smith, P. C. (1999), Seasonal-Mean Hydrography and Circulation in the Gulf of St. Lawrence and on the Eastern Scotian and Southern Newfoundland Shelves, *Journal of Physical Oceanograohy*, *29*, 1279-1301, doi:https://doi.org/10.1175/1520-0485(1999)029<1279:SMHACI>2.0.CO;2.

Hanawa, K., & Talley, L. D. (2001), Mode Waters, in *Circulation and Climate, Observing and Modelling the Global Ocean.* , edited by G. Siedler, J. Church and J. Gould, pp. 373-386, Academic Press, London.

Holzer, M., & Primeau, F. W. (2010), Improved constraints on transit time distributions from argon 39: A maximum entropy approach, *J. Geophys. Res.*, *115*(C12), C12021, doi:10.1029/2010jc006410.

Ingram, R. G. (1983), Vertical Mixing at the Head of the Laurentian Channel, *Estuarine, Coastal and Shelf Science*, *16*, 333-338, doi:https://doi.org/10.1016/0272-7714(83)90150-6.

Jeansson, E., Tanhua, T., Olsen, A., Smethie, W. M., Rajasakaren, B., Ólafsdóttir, S. R., & Ólafsson, J. (2023), Decadal Changes in Ventilation and Anthropogenic Carbon in the Nordic Seas, *Journal of Geophysical Research: Oceans*, *128*(3), doi:10.1029/2022jc019318.

Jiang, W., et al. (2011), (39)Ar Detection at the 10(-16) Isotopic Abundance Level with Atom Trap Trace Analysis, *Physical Review Letters*, *106*(10).

Jones, E. P. (2001), Circulation in the Arctic Ocean, *Polar Res.*, *20*(2), 139-146, doi:10.1111/j.1751-8369.2001.tb00049.x.

Jones, E. P., Rudels, B., & Anderson, L. G. (1995), Deep waters of the Arctic Ocean: origins and circulation, *Deep-Sea Res. I*, *42*(5), 737-760.

Jutras, M., Dufour, C. O., Mucci, A., Cyr, F., & Gilbert, D. (2020), Temporal Changes in the Causes of the Observed Oxygen Decline in the St. Lawrence Estuary, *Journal of Geophysical Research: Oceans*, *125*(12), doi:10.1029/2020jc016577.

Jutras, M., Mucci, A., Chaillou, G., Nesbitt, W. A., & Wallace, D. W. R. (2023), Temporal and spatial evolution of bottom-water hypoxia in the St Lawrence estuarine system, *Biogeosciences*, *20*(4), 839-849, doi:10.5194/bg-20-839-2023.

Karcher, M., Smith, J. N., Kauker, F., Gerdes, R., & Smethie, W. M. (2012), Recent changes in Arctic Ocean circulation revealed by iodine-129 observations and modeling, *Journal of Geophysical Research: Oceans*, *117*(C8), doi:10.1029/2011jc007513.

Khatiwala, S., Visbeck, M., & Schlosser, P. (2001), Age tracers in an ocean GCM, *Deep-Sea Res. I*, *48*(6), 1423-1441.

Krysell, M., & Wallace, D. W. R. (1988), Arctic Ocean ventilation studied with a suite of anthropogenic halocarbon tracers, *Science*, *242*, 746-749.

Kuhlbrodt, T., Griesel, A., Montoya, M., Levermann, A., Hofmann, M., & Rahmstorf, S. (2007), On the driving processes of the Atlantic meridional overturning circulation, *Rev. Geophys.*, *45*(2), doi:https://doi.org/10.1029/2004RG000166.

Lauvset, S. K., et al. (2022), GLODAPv2.2022: the latest version of the global interior ocean biogeochemical data product, *Earth Syst. Sci. Data*, *14*(12), 5543-5572, doi:10.5194/essd-14-5543-2022.

Lauvset, S. K., et al. (2021), An updated version of the global interior ocean biogeochemical data product, GLODAPv2.2021, *Earth Syst. Sci. Data Discuss.*, *2021*, 1-32, doi:10.5194/essd-2021-234.

Li, P., Mühle, J., Montzka, S. A., Oram, D. E., Miller, B. R., Weiss, R. F., Fraser, P. J., & Tanhua, T. (2019), Atmospheric histories, growth rates and solubilities in seawater and other natural waters of the potential transient tracers HCFC-22, HCFC-141b, HCFC-142b, HFC-134a, HFC-125, HFC-23, PFC-14 and PFC-116, *Ocean Sci.*, *15*(1), 33-60, doi:10.5194/os-15-33-2019.

Li, P., & Tanhua, T. (2021), Medusa–Aqua system: simultaneous measurement and evaluation of novel potential halogenated transient tracers HCFCs, HFCs, and PFCs in the ocean, *Ocean Sci.*, *17*(2), 509-525, doi:10.5194/os-17-509-2021.

Loosli, H. H. (1983), A dating method with 39Ar, *Earth and Planetary Science Letters*, *63*(1), 51-62, doi:https://doi.org/10.1016/0012-821X(83)90021-3.

Lu, Z. T., et al. (2014), Tracer applications of noble gas radionuclides in the geosciences, *Earth-Science Reviews*(0), doi:doi.org/10.1016/j.earscirev.2013.09.002.

Macdonald, R. W., & Carmack, E. C. (1991), Age of Canada Basin Deep Waters - a Way to Estimate Primary Production for the Arctic-Ocean, *Science*, *254*(5036), 1348-1350.

Macrander, A., Käse, R. H., Send, U., Valdimarsson, H., & Jónsson, S. (2007), Spatial and temporal structure of the Denmark Strait Overflow revealed by acoustic observations, *Ocean Dynamics*, *57*(2), 75-89, doi:10.1007/s10236-007-0101-x.

Marshall, J., & Schott, F. (1999), Open-ocean convection: observations, theory and models, *Rev. Geophys.*, *37*, 1-64, doi:https://doi.org/10.1029/98RG02739.

Matthes, K., et al. (2020), The Flexible Ocean and Climate Infrastructure version 1 (FOCI1): mean state and variability, *Geoscientific Model Development*, *13*(6), 2533-2568, doi:10.5194/gmd-13-2533-2020.

McCartney, M. S., & Talley, L. D. (1982), The Subpolar Mode Water of the North Atlantic Ocean, *J. Phys. Oceanogr.*, *12*(11), 1169-1188, doi:10.1175/1520-0485(1982)012<1169:TSMWOT>2.0.CO;2.

McWilliams, J. C. (1988), Vortex generation through balanced adjustment, *J. Phys. Oceanogr.*, *18*, 1178-1192, doi:10.1175/1520-0485(1988)018.

Mecking, S., Warner, M. J., & Bullister, J. L. (2006), Temporal changes in pCFC-12 ages and AOU along two hydrographic sections in the eastern subtropical North Pacific, *Deep-Sea Res. I*, *53*(1), 169-187.

Meredith, M., et al. (2019), Polar Regions. In: IPCC Special Report on the Ocean and Cryosphere in a Changing Climate.

Miller, B. R., Weiss, R. F., Salameh, P. K., Tanhua, T., Greally, B. R., Muhle, J., & Simmonds, P. G. (2008), Medusa: A sample preconcentration and GC/MS detector system for in situ measurements of atmospheric trace halocarbons, hydrocarbons, and sulfur compounds, *Anal. Chem.*, *80*(5), 1536-1545.

Nansen, F. (1902), The oceanography of the North Polar Basin. The Norwegian North Polar Expedition 1893-1896, *Scientific Results 3*.

NOAA (2023), What is upwelling?, National Ocean Service website, https://oceanservice.noaa.gov/facts/upwelling.html, 20.03, 2024.

Papadopoulos, V. P., et al. (2015), Factors governing the deep ventilation of the Red Sea, *Journal of Geophysical Research: Oceans*, *120*(11), 7493-7505, doi:10.1002/2015jc010996.

Pfirman, S. (2004), Variability in Arctic sea ice drift, *Geophys. Res. Letters*, *31*(16), doi:10.1029/2004gl020063.

Polyakov, I., Ingvaldsen, R. B., Pnyushkov, A. V., Bhatt, U. S., Francis, J. A., Janout, M., Kwok, R., & Skagseth, O. (2023), Fluctuating Atlantic inflows modulate Arctic atlantification, *Science*, *381*(6661), 972-979, doi:DOI: 10.1126/science.adh5158.

Rahmstorf, S. (2006), Thermohaline Ocean Circulation, *Encyclopedia of Quaternary Sciences*, *5*.

Raimondi, L., Tanhua, T., Azetsu-Scott, K., Yashayaev, I., & Wallace, D. W. R. (2021), A 30 -Year Time Series of Transient Tracer-Based Estimates of Anthropogenic Carbon in the Central Labrador Sea, *Journal of Geophysical Research: Oceans*, *126*(5), e2020JC017092, doi:https://doi.org/10.1029/2020JC017092.

Raimondi, L., Wefing, A. M., & Casacuberta, N. (2023), Anthropogenic Carbon in the Arctic Ocean: Perspectives From Different Transient Tracers, *Journal of Geophysical Research: Oceans*, *129*(1), doi:https://doi.org/10.1029/2023JC019999.

Rainville, L., Lee, C. M., & Woodgate, R. A. (2011), Impact of Wind-Driven Mixing in the Arctic Ocean, *Oceanography*, *24*(3), 136-145.

Raitsos, D. E., Hoteit, I., Prihartato, P. K., Chronis, T., Triantafyllou, G., & Abualnaja, Y. (2011), Abrupt warming of the Red Sea, *Geophys. Res. Letters*, *38*(14), doi:10.1029/2011gl047984.

Ravishankara, A. R., Solomon, S., Turnipseed, A. A., & Warren, R. F. (1993), Atmospheric Lifetimes of Long-Lived Halogenated Species, *Science*, *259*(5092), 194-199.

Rigor, I. G., Wallace, J. M., & Colony, R. L. (2002), Response of Sea Ice to the Arctic Oscillation, *J Climate*, *15*(18), 2648-2663.

Ritterbusch, F., Ebser, S., Welte, J., Reichel, T., Kersting, A., Purtschert, R., Aeschbach-Hertig, W., & Oberthaler, M. K. (2014), Groundwater dating with Atom Trap Trace Analysis of 39Ar, *Geophys. Res. Letters*, *41*(19), 6758-6764, doi:10.1002/2014gl061120.

Rudels, B., Anderson, L., Eriksson, P., Fahrbach, E., Jakobsson, M., & Jones, E. P. (2012), Observations in the ocean, in *Arctic Climate Change*, edited by H.-W. J. (Ed.), pp. 117-198, Dordrecht: Springer, Atmospheric and Oceanographic Sciences Library, doi:https://doi.org/10.1007/978-94-007-2027-5_4.

Rudels, B., Anderson, L. G., & Jones, E. P. (1996), Formation and evolution of the surface mixed layer and halocline of the Arctic Ocean, *J. Geophys. Res.*, *101*(C4), 8807-8821.

Rudels, B., Friedrich, H. J., & Quadfasel, D. (1999), The Arctic Circumpolar Boundary Current, *Deep-Sea Res. II*, *46*(6-7), 1023-1062.

Rudels, B., Jones, E. P., Anderson, L. G., & Kattner, G. (1994), On the Intermediate Depth Waters of the Arctic Ocean, in *The Polar Oceans and Their Role in Shaping the Global Environment*, edited by R. Muench and O. M. Johannesson, pp. 33-46, American Geophysical Union, Washington D.C.

Sallée, J.-B., Matear, R. J., Rintoul, S. R., & Lenton, A. (2012), Localized subduction of anthropogenic carbon dioxide in the Southern Hemisphere oceans, *Nature Geoscience*, *5*(8), 579-584, doi:10.1038/ngeo1523.

Saucier, F. J., Roy, F., Gilbert, D., Pellerin, P., & Ritchie, H. (2003), Modeling the formation and circulation processes of water masses and sea ice in the Gulf of St. Lawrence, Canada, *J. Geophys. Res.*, *108*, doi:https://doi.org/10.1029/2000JC000686.

Schlosser, P., Kromer, B., Weppernig, R., Loosli, H. H., Bayer, R., Bonani, G., & Suter, M. (1994), The distribution of 14C and 39Ar in the Weddell Sea, *J. Geophys. Res.*, *99*, 10275-10287, doi:10.1029/94JC00313.

Schneider, A., Tanhua, T., Körtzinger, A., & Wallace, D. W. R. (2012), An evaluation of tracer fields and anthropogenic carbon in the equatorial and the tropical North Atlantic, *Deep Sea Research Part I: Oceanographic Research Papers*, *67*(0), 85-97, doi:10.1016/j.dsr.2012.05.007.

Shao, A. E., Mecking, S., Thompson, L., & Sonnerup, R. E. (2016), Evaluating the use of 1-D transit time distributions to infer the mean state and variability of oceanic ventilation, *Journal of Geophysical Research: Oceans*, *121*(9), 6650-6670, doi:10.1002/2016jc011900.

Smith, G. C., Saucier, F. J., & Straub, D. (2006), Formation and circulation of the cold intermediate layer in the Gulf of Saint Lawrence, *J. Geophys. Res.*, *111*(C6), doi:10.1029/2005jc003017.

Smith, J. N., McLaughlin, F. A., Smethie Jr., W. M., Moran, S. B., & Lepore, K. (2011), Iodine-129, 137Cs, and CFC-11 tracer transit time distributions in the Arctic Ocean, *Journal of Geophysical Research: Oceans*, *116*(C4), doi:10.1029/2010jc006471.

Snoeijs-Leijonmalm, P., & Party, S.-O. S. (2022), Expedition Report SWEDARCTIC Synoptic Arctic Survey 2021 with icebreaker Oden*Rep.*, 300 pp.

Sonnerup, R. E., Mecking, S., & Bullister, J. L. (2013), Transit time distributions and oxygen utilization rates in the Northeast Pacific Ocean from chlorofluorocarbons and sulfur hexafluoride, *Deep Sea Research Part I: Oceanographic Research Papers*, *72*, 61-71, doi:http://dx.doi.org/10.1016/j.dsr.2012.10.013.

Stöven, T. (2011), Ventilation processes of the Mediterranean Sea based on CFC-12 and SF_6 measurements, Christian-Albrecht-Universität zu Kiel, Kiel.

Stöven, T., & Tanhua, T. (2014), Ventilation of the Mediterranean Sea constrained by multiple transient tracer measurements, *Ocean Sci.*, *10*(3), 439-457, doi:10.5194/os-10-439-2014.

Stöven, T., Tanhua, T., Hoppema, M., & Bullister, J. L. (2015), Perspectives of transient tracer applications and limiting cases, *Ocean Sci.*, *11*(5), 699-718, doi:10.5194/os-11-699-2015.

Swift, J. H., & Aagaard, K. (1981), Seasonal transitions and water mass formation in the Iceland and Greenland seas, *Deep-Sea Res. A*, *28*(A10), 1107-1129.

Talley, L. D., et al. (2016), Changes in Ocean Heat, Carbon Content, and Ventilation: A Review of the First Decade of GO-SHIP Global Repeat Hydrography, *Annual Review of Marine Science*, *8*(1), doi:doi:10.1146/annurev-marine-052915-100829.

Tanhua, T., Jones, E. P., Jeansson, E., Jutterstrom, S., Smethie, W. M., Wallace, D. W. R., & Anderson, L. G. (2009), Ventilation of the Arctic Ocean: Mean ages and inventories of anthropogenic CO_2 and CFC-11, *J. Geophys. Res.*, *114*(C1), C01002, doi:doi:10.1029/2008JC004868.

Tanhua, T., & Olsson, K. A. (2005), Removal and bioaccumulation of anthropogenic, halogenated transient tracers in an anoxic fjord, *Mar. Chem.*, *94*(1-4), 27-41, doi:doi:10.1016/j.marchem.2004.07.009.

Tanhua, T., Olsson, K. A., & Fogelqvist, E. (2004), A first study of SF_6 as a transient tracer in the Southern Ocean, *Deep-Sea Res. II*, *51*, 2683-2699.

Tanhua, T., Olsson, K. A., & Jeansson, E. (2005), Formation of Denmark Strait Overflow Water and its hydro-chemical composition, *J. Mar. Systems*, *57*, 264-288, doi:10.1016/j.jmarsys.2005.05.003.

Thiele, G., & Sarmiento, J. L. (1990), Tracer dating and ocean ventilation, *J. Geophys. Res.*, *95*(C6), 9377-9391.

Thomson, R. E., Spear, D. J., Krassovski, M. V., Hourston, R. A. S., Juhász, T. A., & Mihály, S. F. (2017), Buoyancy-driven coastal current blocks ventilation of an anoxic fjord on the Pacific coast of Canada, *Journal of Geophysical Research: Oceans*, *122*(4), 2976-2998, doi:10.1002/2016jc012512.

Ulfsbo, A., Jones, E. M., Casacuberta, N., Korhonen, M., Rabe, B., Karcher, M., & van Heuven, S. M. A. C. (2018), Rapid Changes in Anthropogenic Carbon Storage and Ocean Acidification in the Intermediate Layers of the Eurasian Arctic Ocean: 1996–2015, *Global Biogeochem Cycle*, *32*(9), 1254-1275, doi:10.1029/2017gb005738.

Vollmer, M. K., & Weiss, R. F. (2002), Simultaneous determination of sulfur hexafluoride and three chlorofluorocarbons in water and air, *Mar. Chem.*, *78*(2-3), 137-148.

Wallace, D. W. R., Moore, R. M., & Jones, E. P. (1987), Ventilation of the Arctic Ocean cold halocline: rates of diapycnal isopycnal transport, oxygen utilization and primary production inferred using chlorofluoromethane distributions, *Deep Sea Research I*, *34*(12), 1957-1979.

Wallace, D. W. R., Schlosser, P., Krysell, M., & Bönisch, G. (1992), Halocarbon ratio and tritium/3He dating of water masses in the Nansen Basin, Arctic Ocean, *Deep Sea Research I*, *39*(S2A), 435-458.

Warner, M. J., & Weiss, R. F. (1985), Solubilities of chlorofluorocarbons 11 and 12 in water and sea water, *Deep-Sea Res.*, *32*(12), 1485-1497.

Warren, B. A., & Owens, B. (1987), Deep Curretns in the Central Subarctic Pacific Ocean, *J. Phys. Oceanogr.*, *18*, doi:10.1175/1520-0485(1988)018.

Wassmann, P. (2015), Overarching perspectives of contemporary and future ecosystems in the Arctic Ocean, *Prog. Oceanogr.*, *139*, 1-12, doi:https://doi.org/10.1016/j.pocean.2015.08.004.

Watson, A. J., et al. (1999), Mixing and convection in the Greenland Sea from a tracer-release experiment, *Nature*, *401*(6756), 902-904.

Waugh, D. W., Vollmer, M. K., Weiss, R. F., Haine, T. W. N., & Hall, T. M. (2002), Transit time distributions in Lake Issyk-Kul, *Goephysical Research Letters*, *29*(24).

Wefing, A. M. (2021), 129I and 236U as a new tracer pair to study water mass circulation in the Arctic Ocean and Fram Strait, ETH Zurich.

Wefing, A. M., Casacuberta, N., Christl, M., Gruber, N., & Smith, J. N. (2021), Circulation timescales of Atlantic Water in the Arctic Ocean determined from anthropogenic radionuclides, *Ocean Sci.*, *17*(1), 111-129, doi:10.5194/os-17-111-2021.

Williams, R. (2001), Ocean Subduction, *Encyclopedia of Ocean Sciences*, 1982-1993, doi:10.1016/B978-012374473-9.00109-0.

Woodgate, R. A. (2013), Arctic Ocean Circulation: Going Around the Top Of the World, *Nature Education Knowledge*, *4*.

Appendix A

Temporal Variability of Ventilation in the Makarov Basin and the Svalbard Shelf area (extension to Chapter 3)

The analysis of temporal variability in Arctic Ocean ventilation reported in manuscript 1 focused solely on three regions: the Nansen Basin, the southern Amundsen Basin, and the northern Amundsen Basin. These regions were chosen due to the large number of comparable sampling stations set up within the respective areas over the 30-year time period. However, data from 1991, 2005, 2015 and 2021 were also available for the Makarov Basin, although more spatially dispersed. Furthermore, samples were also collected at one station in the Svalbard shelf area each for the years 2005, 2015 and 2021. The limited number of comparable stations in these two regions and the relatively low quantity of samples collected introduces uncertainties in the comparative analysis. Therefore, the data were excluded from the main manuscript, however, as they show some interesting and to some extend comparable results they are briefly summarized in this appendix.

A.1 Makarov Basin

The Makarov Basin is present on the Amerasian side of the Lomonosov Ridge. Here, data were available for the analysis of ventilation patterns from a total of 11 sampling stations over the 30-year time period (1991, 2005, 2015 and 2021). Notably, the stations of the earlier cruises (1991 and 2005) were located further east and on the edge of the Lomonosov Ridge, while in 2015, transient tracer data were collected at only 2 stations spread over the entire basin (see Figure A1).

The data show results similar to those obtained for the ventilation patterns in the Eurasian AO (see Chapter 3). Again, the highest mean ages were computed from the 1991 data throughout the intermediate water column, followed by slightly younger water in 2021, and the youngest being present in 2005 and 2015 (see Figure A1a). Thus, water masses of the Makarov Basin are most likely also subject to temporal variability in ventilation over the last 30 years. Moreover, the data, suggest that the AW also affects the intermediate water on this side of the Lomonosov Ridge in the Central AO. The main differences compared to the results obtained for the Eurasian side of the Lomonosov Ridge are the mean age values below 1000 m,

which show less variation between the years 2005, 2015 and 2021. The variability in ventilation is significant only in the top 1000 meters of the water column over the past 16 years, whereas slower ventilation was observed throughout the entire intermediate water column in 1991.

The AOU comparison (see Figure A1b) of water masses in the Makarov Basin again shows results which are similar but less pronounced, as also observed on the Eurasian side. Compared to the mean age results the AOU data from 2021 and 1991 are more aligned in this analysis, but still show higher values compared to the data from 2005 and 2015. This supports the finding of a slower ventilation in 1991 and 2021 compared to 2005 and 2015. While the mean age data indicate that significant variability is observed in the upper 1000 m when comparing 2005, 2015 and 2021 data, the AOU differences are only evident in the upper 800 m. This reduced variability in ventilation might be due to an influence of Pacific water entering though the Bering Strait on this side of the Lomonosov Ridge.
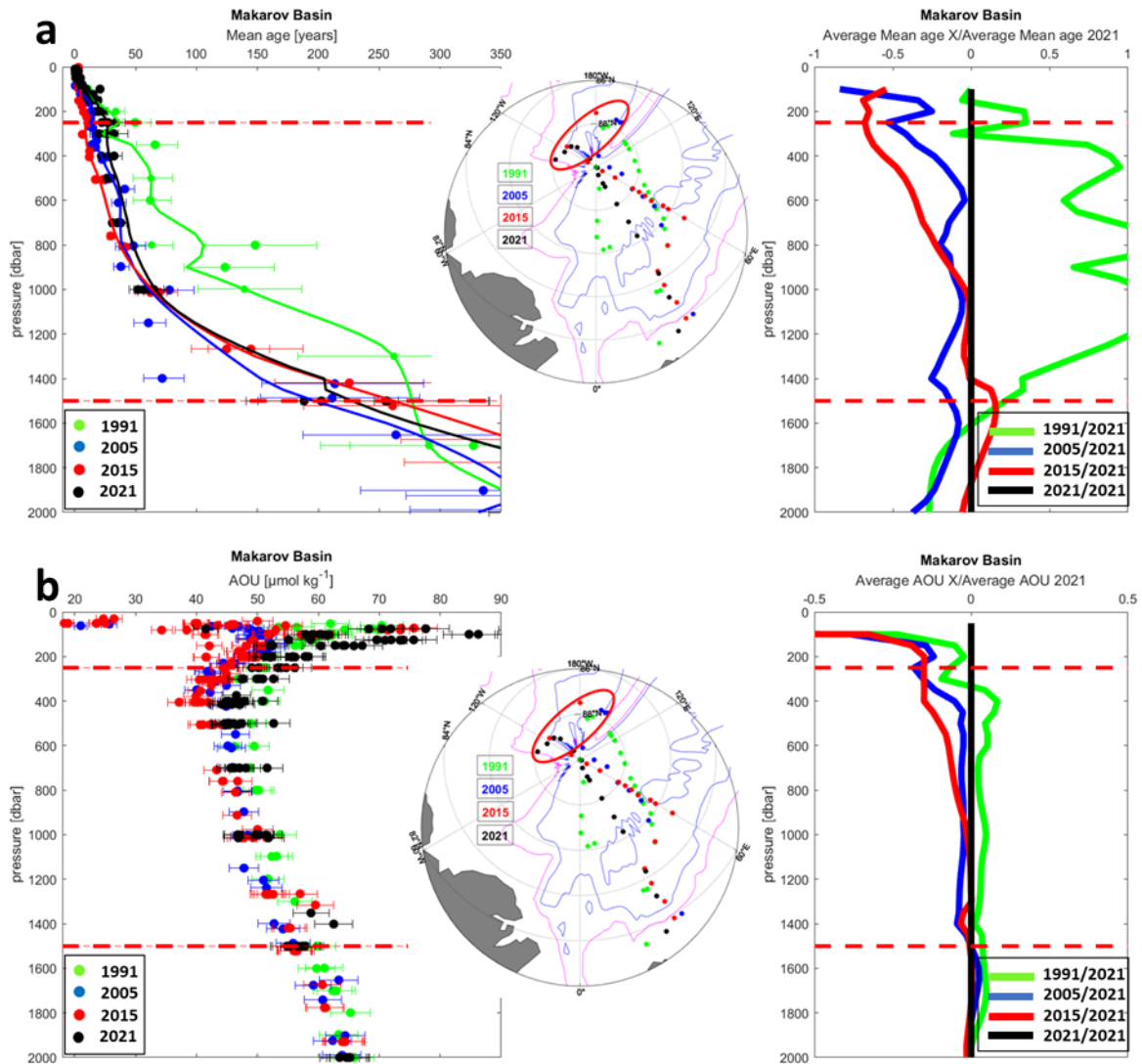
Figure A1: (a) Mean age comparison and (b) AOU comparison of stations in the Makarov Basin in year X: 1991 (green), 2005 (blue), 2015 (red) and 2021 (black). The left panels show data points from each station and depth above 2000 m, with the mean values depicted by the solid lines in (a). The right panels show the (a) average relative mean age and (b) average relative AOU difference with respect to the data from 2021. The dashed red lines represent the focus area of this study, the intermediate layer (250-1500 m).

A.2 Svalbard Shelf area

At the shelf close to Svalbard, the opportunity to compare data from one station of the Oden cruise in 2021 to stations sampled in 2005 and 2015 (see Figure A2) was utilized to analyze an area dominated by the inflow of the AW below the halocline.

The mean age data from 2005 and 2015 are comparable to each other and show slightly younger mean ages at a depth between 400 and 1200 m compared to 2021. This indicates a general decrease in the ventilation, which suggests reduced or slower supply of younger water at this depth. While it has to be considered that this variability could also be due to the somewhat different locations of the stations, it should be noted that stations from the cruises in 2005 and 2015 were situated further east. Therefore, tracer samples collected here should, in theory, indicate older water at intermediate depths because the FSBW would have travelled further to reach this location after subducting in the Fram Strait.

The AOU data indicate no major variability in ventilation of the intermediate layer. Slightly lower AOU values were measured in samples of the upper waters column in 2021 (above 400 m), but this difference could also be due to measurement uncertainties as only data from one station could be taken into consideration.
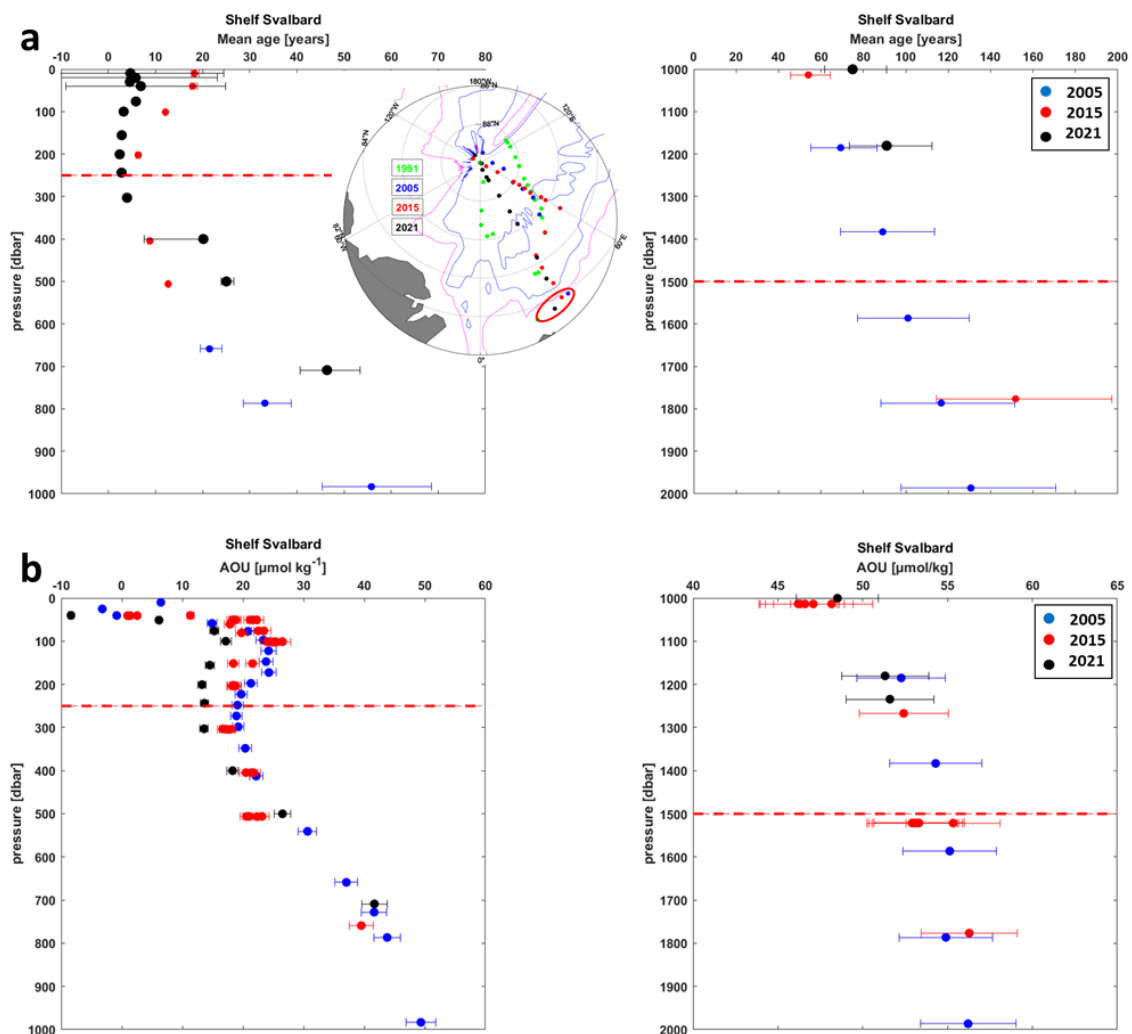
Figure A2: (a) Mean age comparison and (b) AOU comparison of stations from year X: 2005 (blue), 2015 (red) and 2021 (black) at the shelf area near Svalbard. The left and right panels of the figures show the upper 1000 m and the data from depths between 1000 and 2000 m, respectively. The dashed red lines represent the focus area of this study, the intermediate layer (250-1500 m).

Appendix B

Evidence of SF$_6$ tracer release experiment in the Arctic Ocean

Considering all transient tracer data collected during the SAS-Oden 2021 expedition and employing 'Smith's' approach to analyze the ventilation patterns via the TTD, it was evident that at lower SF$_6$ concentration (0.5 – 4 ppt), the measured values exceeded the modelled concentrations within the tracer grid (see Figure B1a – blue dots). A detailed examination of this feature revealed that these elevated values occurred at potential densities between $\sigma_\theta > 28.045$ kg/m^3 and $\sigma_\theta <= 28.07$ kg/m^3. Tanhua et al. (2005) documented that within a potential density interval of 28.045 to 28.06, increased SF$_6$ tracer concentrations spread within the overflow water from the Greenland Sea to the Labrador Sea. This was related to a SF$_6$ tracer release experiment carried out in August 1996 in the Greenland Sea (Watson et al., 1999). As this density interval closely aligns with the interval where elevated SF$_6$ values were measured in 2021 in the AO, the difference between modelled and measured SF$_6$ concentrations most likely can be attributed to this release experiment. The extended density interval to values of up to $\sigma_\theta = 28.07$ kg/m^3 most likely can be explained by the longer time that has passed since the release and to slow mixing with colder ambient water masses present in the AO.
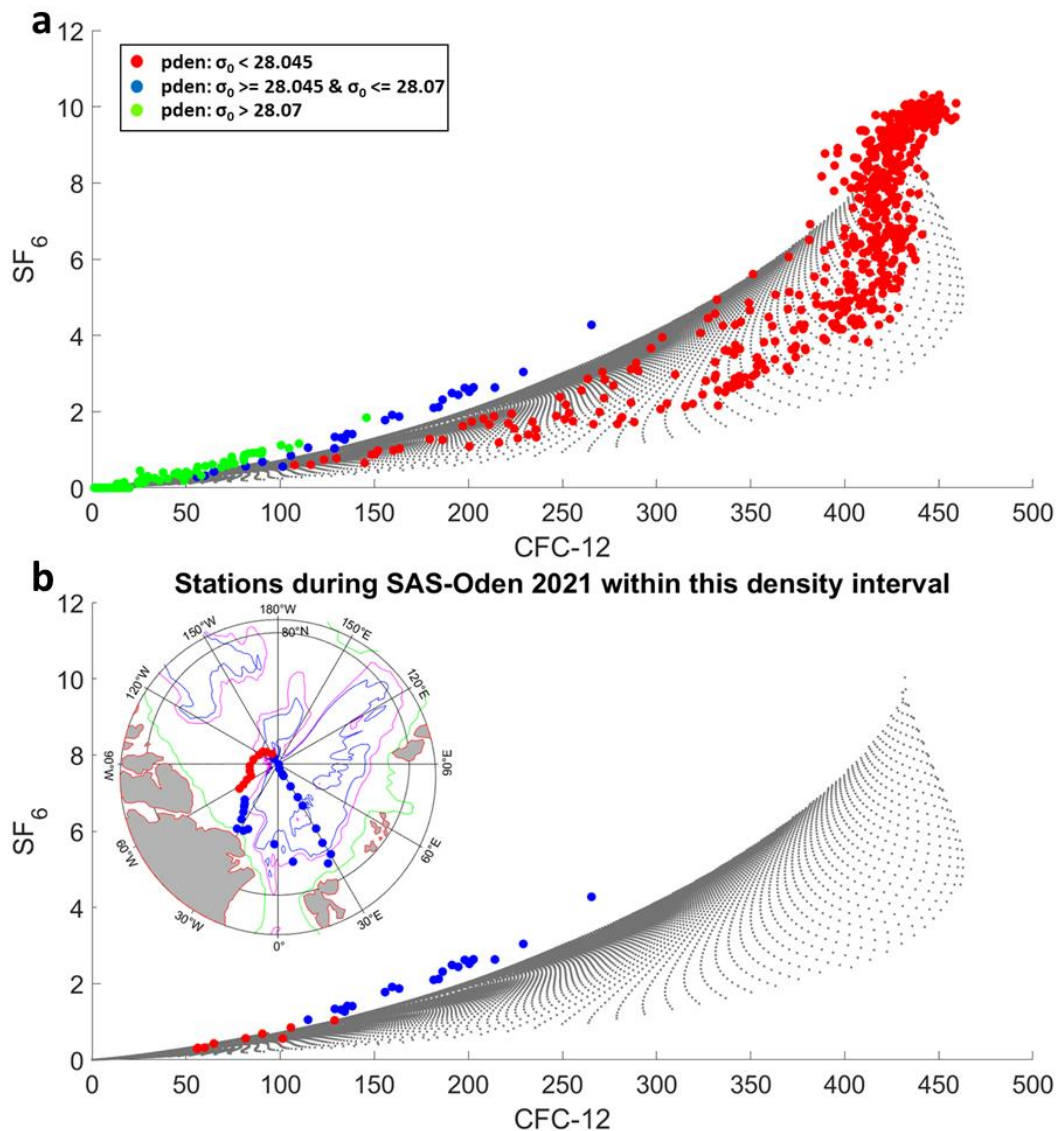
Figure B1: (a) Δ-Γ grid obtained following Smith's approach for the CFC-12 – SF$_6$ tracer combinations. The respective saturations used to obtain the modelled concentrations were 85% for CFC-12 and 100% for SF$_6$. Measured tracer gas concentrations are plotted on top of the grid with the color-coding representing different potential density intervals. (b) Display of the same Δ-Γ grid with concentrations measured within the density interval of σ_θ >= 28.045 kg/m^3 to σ_θ <= 28.07 kg/m^3 plotted on top. The color coding represents the respective sampling position during the SAS-Oden 2021 cruise displayed on the top left. All tracer concentrations are given as partial pressure values (ppt – parts per trillion).

Since the elevated concentrations within this density interval are only present on the Eurasian side of the AO (see Figure B1b), it appears that the influence of the SF$_6$ tracer release experiment has not yet reached the Makarov Basin. However, the enhanced SF$_6$ concentrations expanded and spread since the release in 1996 within the Nansen and

Amundsen Basins. Overall, this indicates that deep tracer release experiments can significantly impact ventilation analysis and potentially cause misleading data if not properly considered in the analysis.

References

Tanhua, T., Bulsiewicz, K., & Rhein, M. (2005), Spreading of overflow water from the Greenland to the Labrador Sea, *Geophys. Res. Letters*, *32*(10), L10615, doi:10.1029/2005GL022700.

Watson, A. J., et al. (1999), Mixing and convection in the Greenland Sea from a tracer-release experiment, *Nature*, *401*(6756), 902-904.

Appendix C

Preliminary results on Argon-39 measurements in the Arctic Ocean during the SAS-Oden 2021 expedition

(In cooperation with Yannis Arck, University of Heidelberg)

For the deep water analysis within the Arctic Ocean (AO), the tracers CFC-12 and SF_6 as well as the 'Medusa'-tracers are not suitable. Due to their limited age range, these tracers can only be employed to analyze ventilation patterns in relatively recently ventilated waters, present in the upper and intermediate layers of the AO. Below approximately 2000 m, concentrations of these tracers are very low or undetectable. To improve deep water ventilation analysis, radioactive tracers, such as Argon-39, are more effective. During the 'SAS- Oden 2021' expedition, samples for this tracer were collected at the six transient tracer super stations (TTSS), covering the entire water column from the surface to the seafloor. Following the cruise, samples from so far three of these six sampling stations were measured at the University of Heidelberg using the ATTA system (see chapter 2.2.3 for description of the method).

The isotope ^{39}Ar is measured relative to its coexisting stable isotope (^{40}Ar), ensuring that the analysis is not affected by to factors like ice cover or seasonality in the air-sea gas exchange process (Gu et al., 2022). The measured ratios are then compared to the constant atmospheric radioactive isotope ratio, expressed as percent of modern Argon (pmAr). A value of 100 pmAr represents 100% modern Argon, meaning that the $^{39}Ar/^{40}Ar$ ratio in the sample matches that of the atmosphere. Higher values are not possible and can only stem from measurement and statistical uncertainties. The age computed from the measured $^{39}Ar/^{40}Ar$ ratios is based on the radioactive decay of the isotope, having a half life of 268 years (Golovko, 2023) . For example, a measurement of 50 pmAr corresponds to an age of 268 years, equivalent to one half life.

The data of the upper 1000 m show results indistinguishable from modern atmospheric values, i.e. around 100 pmAr. However, at depths below 1500 m, where this tracer is preferably used to analyze deep water masses, the measured values decrease. In the deep waters of the Makarov Basin, at depths between 1500 and 3000 m, values range from 30 to 40 % modern indicating ages of up to 500 years (see Figure C1). This represents the oldest deep water in this basin, consistent with findings by Schlosser et al. (1994) and also in line with

calculations based on the tracer data of CFC-12 and SF_6 from the 'SAS-Oden 2021' cruise. The analysis of mean ages via the TTD using these conventional tracers suggests that deep water masses in the Makarov Basin could be older than 700 years, though with high uncertainties due to low and almost undetectable concentrations (see Figure 4c in manuscript I).

Based on the ^{39}Ar analysis, the youngest deep water is found at station 46, close to the north coast of Greenland, displaying values of around 200 years. In contrast, station 20 though also located in the Amundsen Basin shows older deep waters between 2500 and 3500 m. This suggests that the deep water at station 46 might be influenced by more recently ventilated waters mixing with ambient water in the Amundsen Basin. These potentially enter from the Amerasian side through a channel between the Greenland coast and the Lomonosov Ridge.

Interestingly, the ^{39}Ar data from the bottom water of the Makarov Basin (4000 m) show increased concentrations, indicating younger water compared to measurements above (2000 – 3000 m). This could be caused by a regional deep water formation event which involves boundary convection of extensively brine-enriched waters near to the Makarov Basin transporting waters directly into the deep layer at the bottom. However, as there is only one sample analyzed at this depth, measurement uncertainties have to be taken into account and the interpretation has to be considered preliminary.
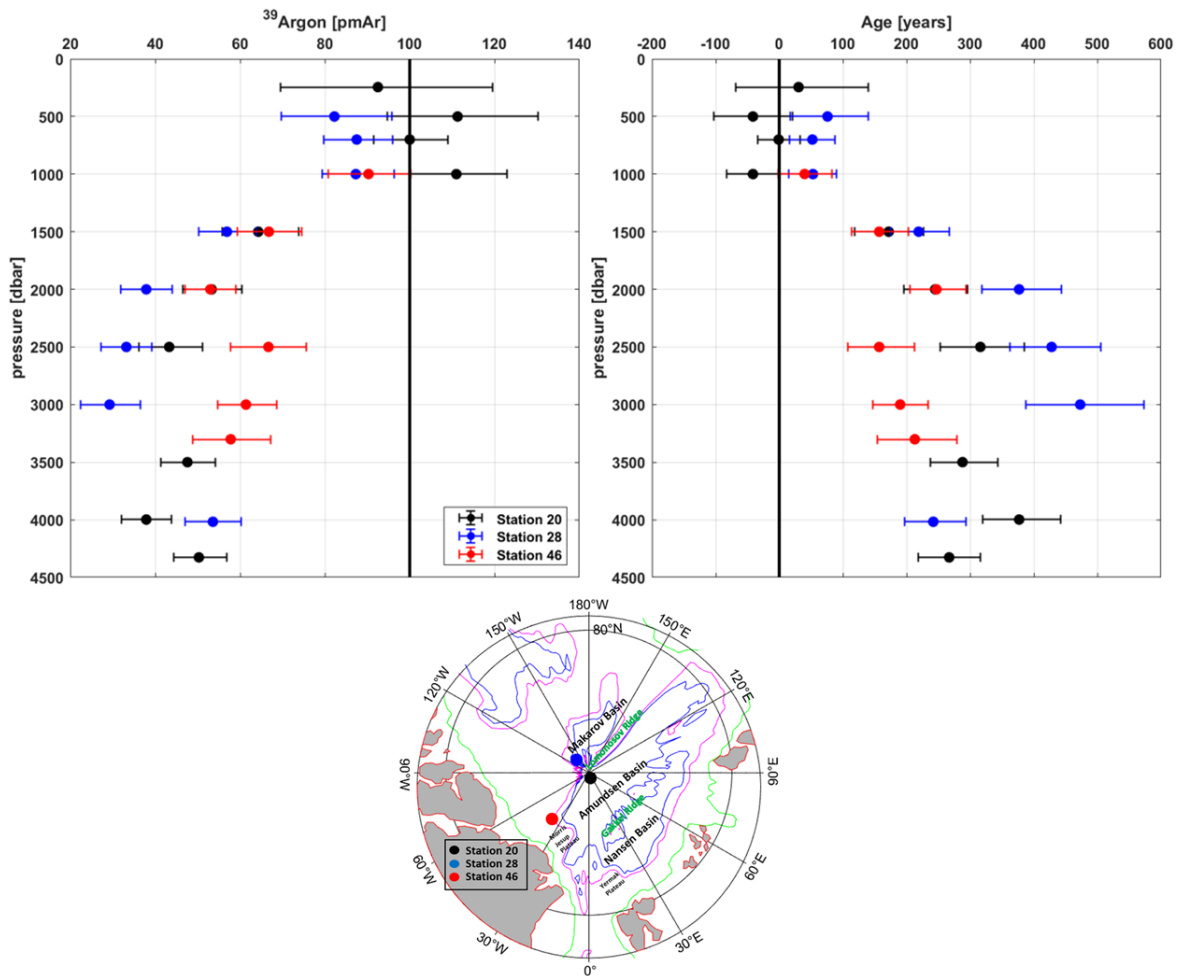
Figure C1: Display of the Argon-39 values in pmAr (^{39}Ar/^{40}Ar ratio in percent of modern Argon) and ages of water masses at different depths calculated based on the pmAr data collected at three of the six TTSS. The map showing the locations of the stations is displayed at the bottom.

The future analysis of all ^{39}Ar samples from the six TTSS is likely to provide valuable insights on the deep water ventilation within the AO. Combining ^{39}Ar values with CFC-12 measurements will also benefit the TTD analysis of deep water masses. In combination with multiple tracers used in the upper and intermediate water layers, this will help to constrain the most probable TTD for each region and throughout the entire water column in the AO.

References

Golovko, V. V. (2023), Application of the most frequent value method for 39Ar half-life determination, *The European Physical Journal C*, *83*(10), doi:10.1140/epjc/s10052-023-12113-6.

Gu, J.-Q., Jiang, W., Tong, A. L., Yang, G.-M., Dong, X.-Z., Ritterbusch, F., Wang, F., & Wang, J. (2022), Estimation of the Ventilation Transit Time Distribution at the Yap–Mariana Junction Using 39Ar, 85Kr

_____

and 14C Tracers, *Journal of Geophysical Research: Oceans*, *127*(7), e2022JC018417, doi:https://doi.org/10.1029/2022JC018417.

Schlosser, P., Kromer, B., Ostlund, G., Ekwurzel, B., Bonisch, G., Loosli, H. H., & Purtschert, R. (1994), On the C-14 and Ar-39 distribution in the central Arctic-Ocean - Implications for deep-water formation, *Radiocarbon*, *36*(3), 327-343.

Appendix D

Supplemental Material Chapters 1 & 2

D.1 Supporting figures for the concentration determination of 'Medusa'-tracer samples

The concentration analysis of the 'Medusa'-tracers using the 'Medusa-Aqua'-system required corrections of the standard curves recorded during the analysis (see Data and Methods, chapter 2.2.2). This involved shifting previously measured standard curves to match with those measured at a later time during the analysis. The figures below (see Figures D1 – D3) display the corrections and corrected standard curves used for determining the concentration of the tracers HCFC-141b, HCFC-142b and HFC-134a.
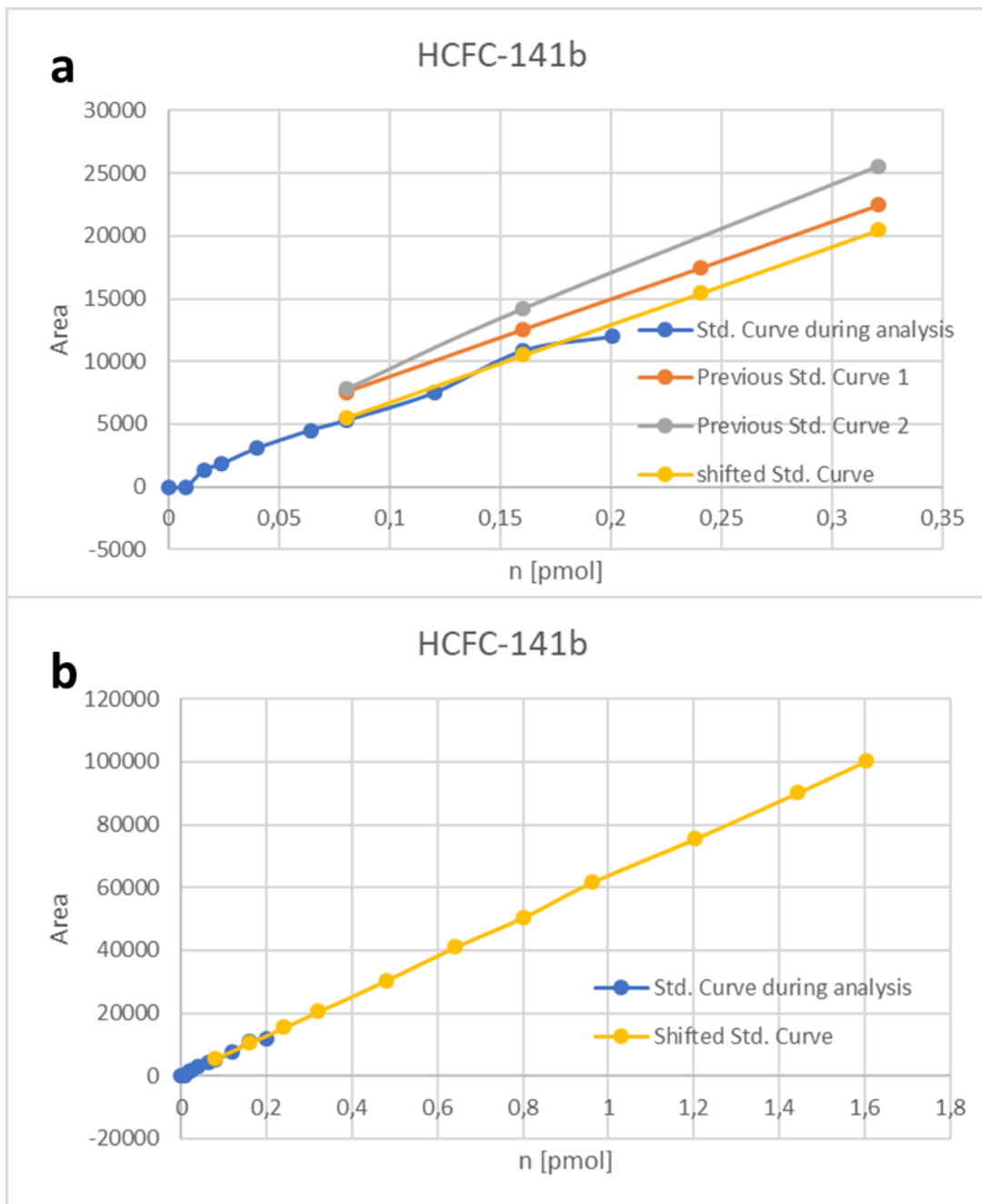
Figure D1: Graph of the shift (a) and extension (b) of the standard curve used to determine HCFC-141b concentrations. The shifted standard curve in the top graph only shows the lower concentration ranges to fit it more precisely to the standard curve measured during the actual sample analysis.
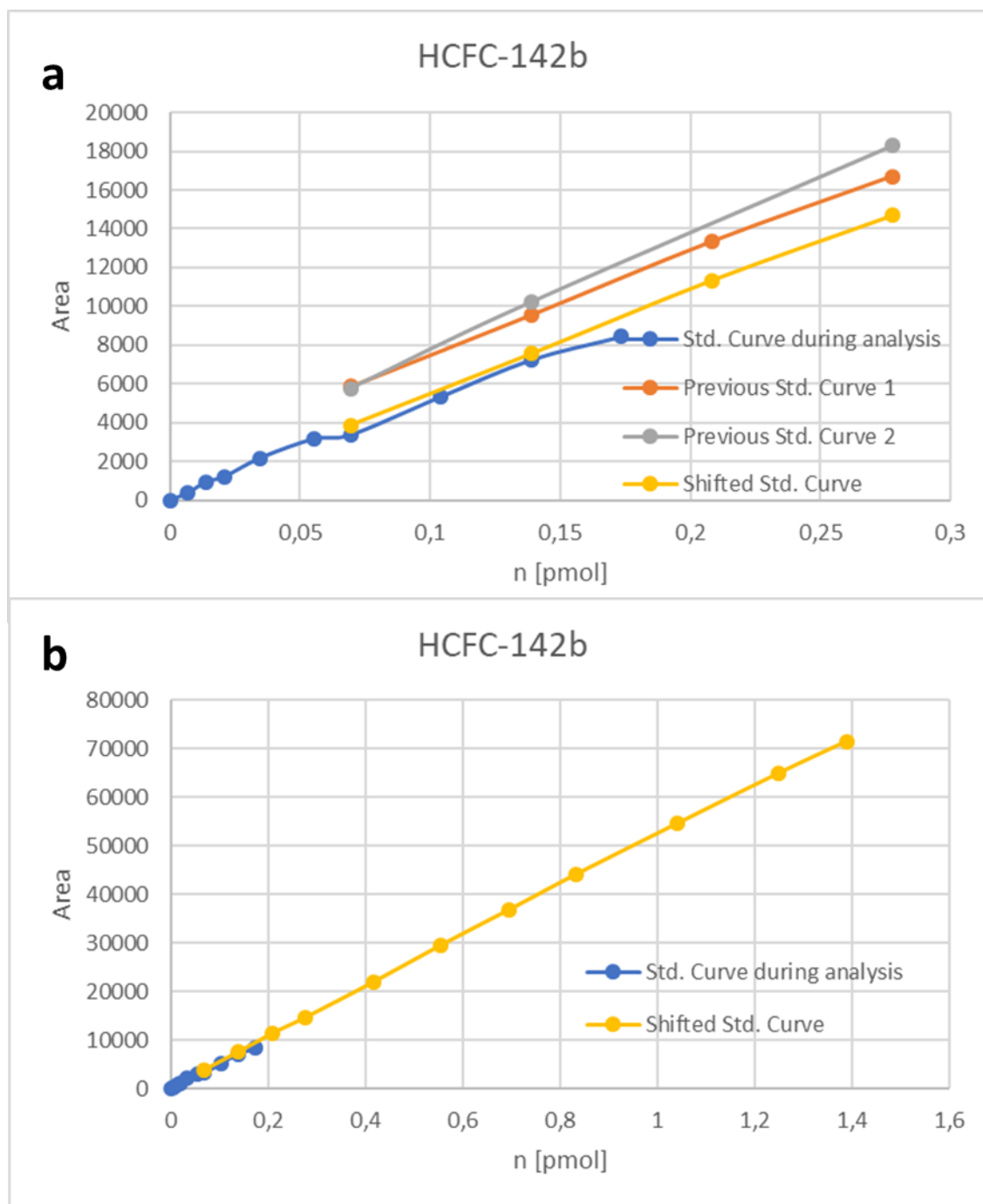
Figure D2: Graph of the shift (a) and extension (b) of the standard curve used to determine HCFC-142b concentrations. The shifted standard curve in the top graph only shows the lower concentration ranges to fit it more precisely to the standard curve measured during the actual sample analysis.

Figure D3: Graph of the shift (a) and extension (b) of the standard curve used to determine HFC-134a concentrations. The shifted standard curve in the top graph only shows the lower concentration ranges to fit it more precisely to the standard curve measured during the actual sample analysis.
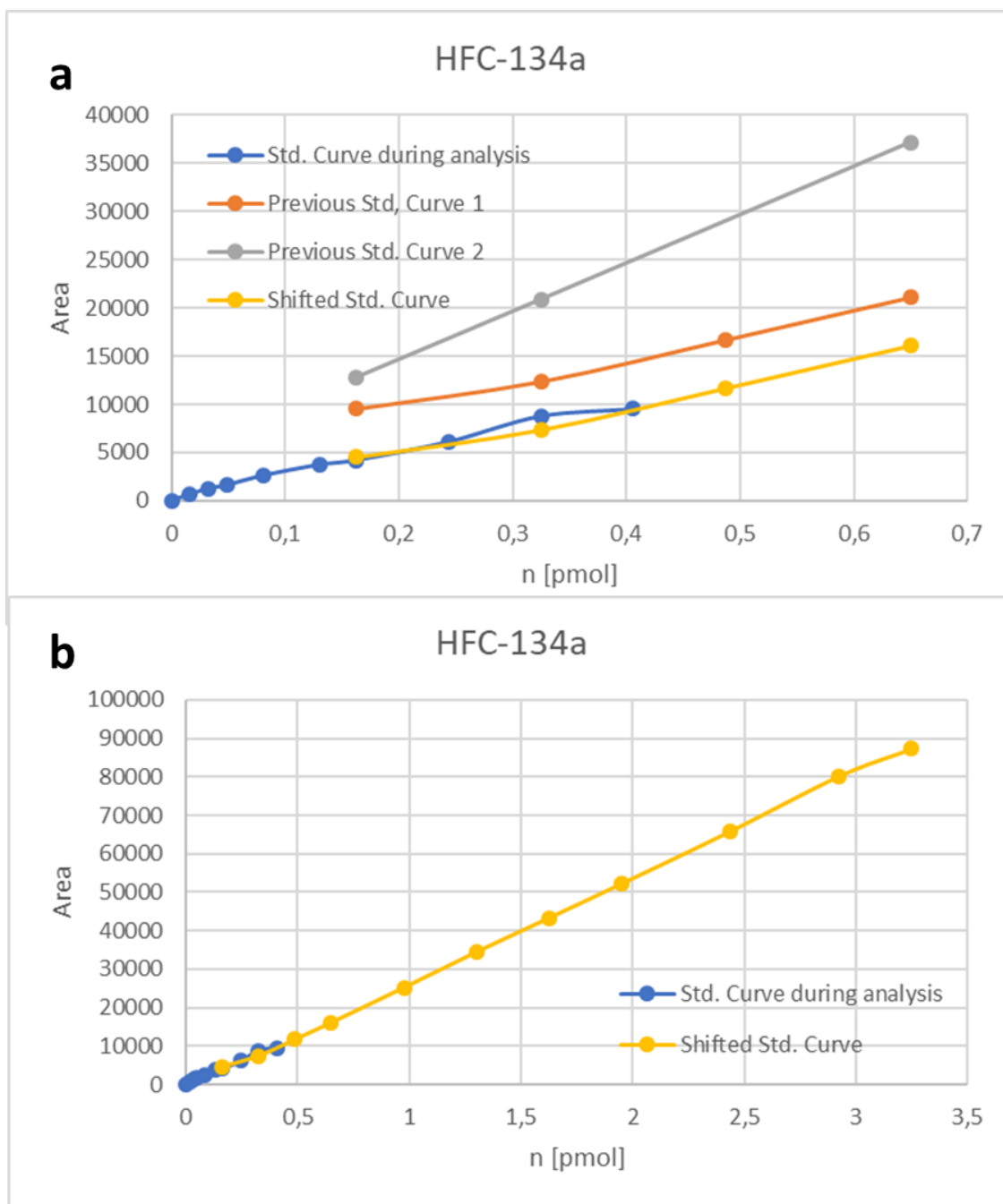
D.2 Supporting figures for the experimental assessment of 'Medusa'-tracer solubilities

In the solubility experiment, measured and expected fractions of dissolved tracer in a given volume of water were determined for each of the following tracers: CFC-12, SF$_6$, HCFC-22, and HFC-134a, in waters of varying salinity and temperature (see Data and Methods, chapter 2.2.2.1). The comparisons of measured to expected fractions are shown in the figures below (see Figures D4 – D9). These comparisons were used to assess the accuracy of the experiment (CFC-12 and SF$_6$) and to attempt to determine solubility functions for the 'Medusa'-tracers HCFC-22 and HFC-134a.
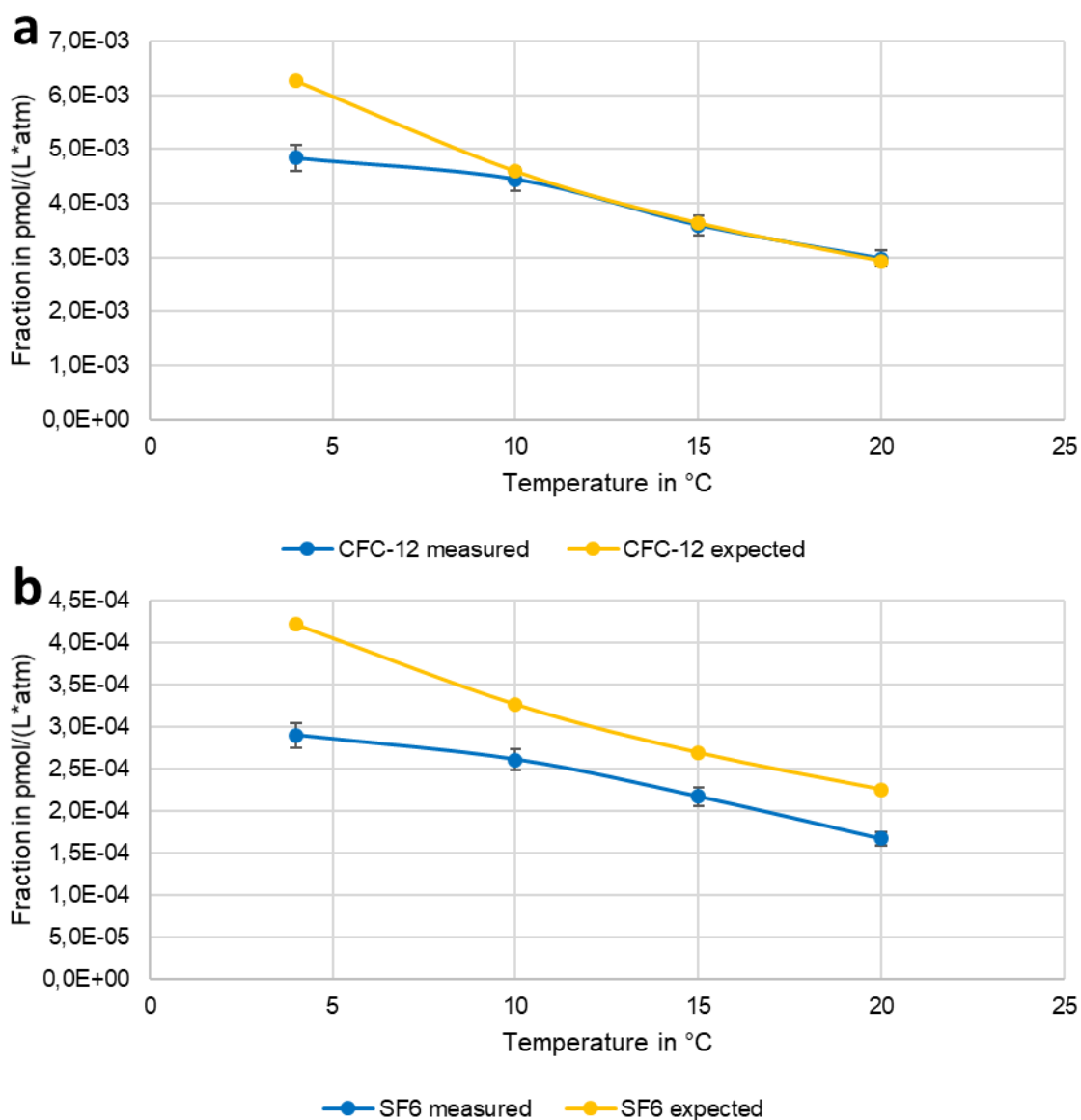
Figure D4: Solubility of (a) CFC-12 and (b) SF$_6$ in 18 psu water. Comparison of the measured results (CFC-12 and SF$_6$ measured) to those calculated using the solubility functions from Warner & Weiss (1985) and Bullister et al. (2002) (CFC-12 and SF$_6$ expected).

Figure D5: Solubility of (a) CFC-12 and (b) SF$_6$ in 26.2 psu water. Comparison of the measured results (CFC-12 and SF$_6$ measured) to those calculated using the solubility functions from Warner & Weiss (1985) and Bullister et al. (2002) (CFC-12 and SF$_6$ expected).

Figure D6: Solubility of (a) CFC-12 and (b) SF$_6$ in 34.4 psu water. Comparison of the measured results (CFC-12 and SF$_6$ measured) to those calculated using the solubility functions from Warner & Weiss (1985) and Bullister et al. (2002) (CFC-12 and SF$_6$ expected).

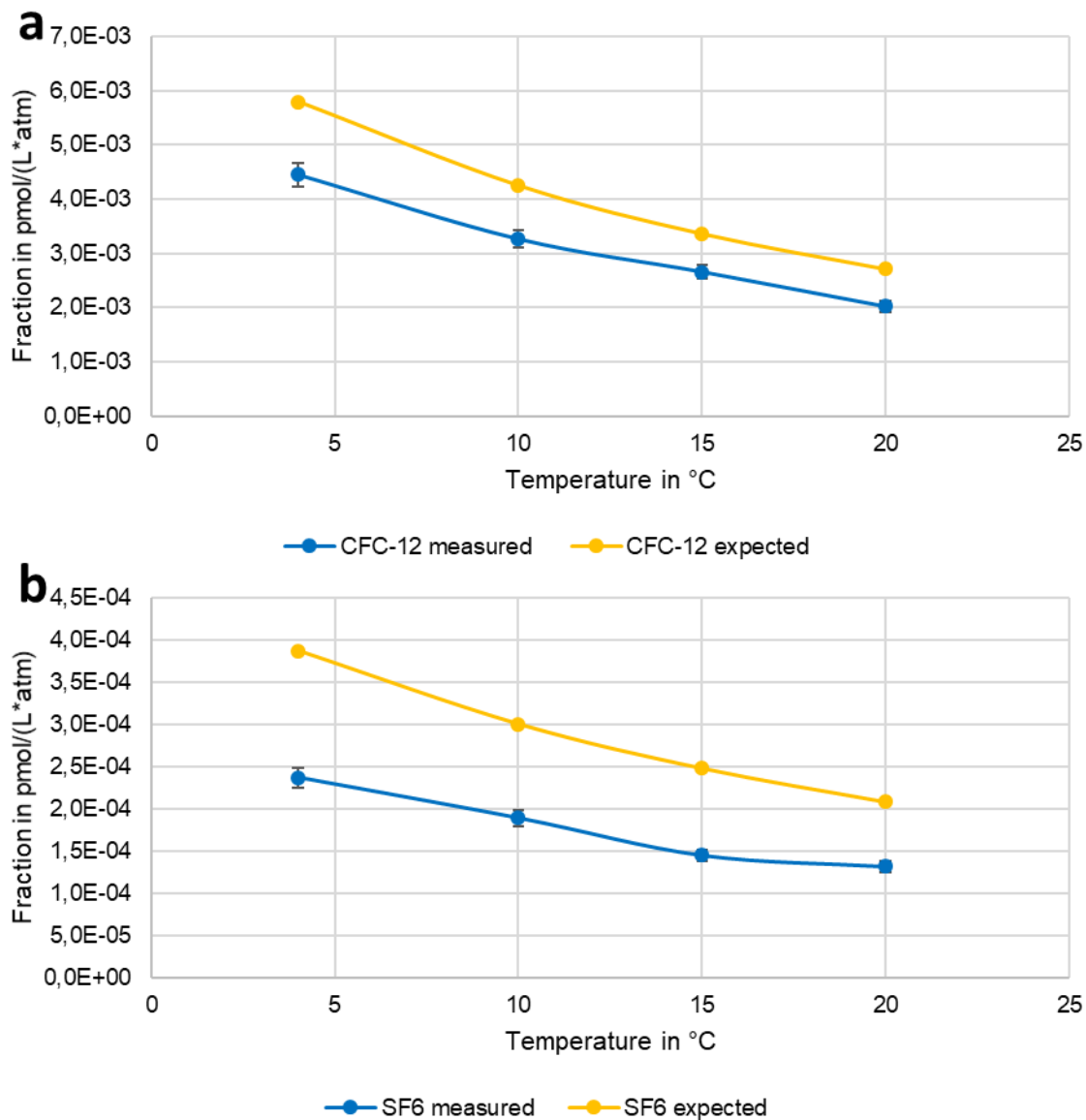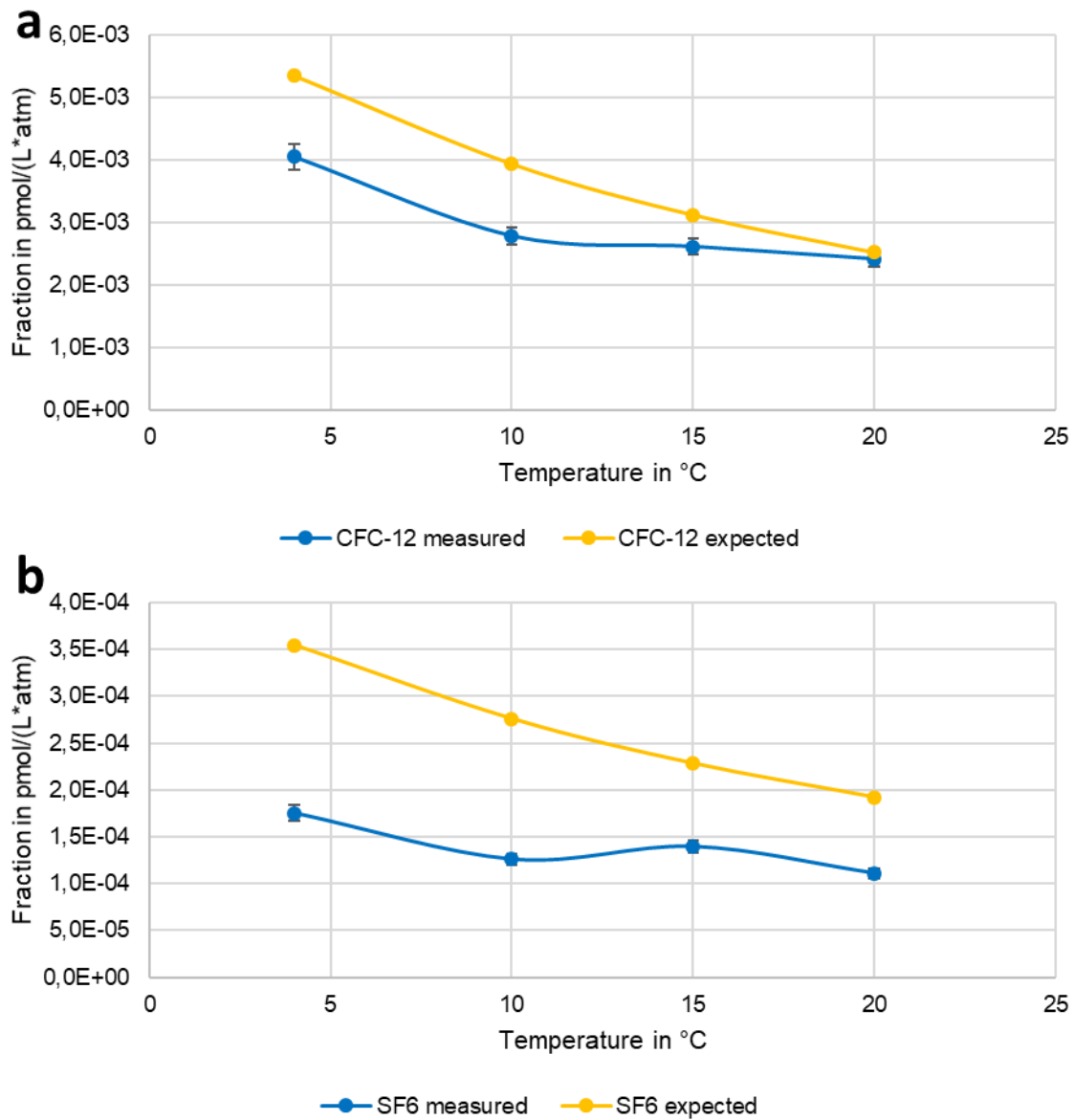**Figure D7:** Solubility fraction of HCFC-22 in (a) 18 psu water and (b) 26.2 psu water. Shown is a comparison of the results measured (blue) to those calculated using the solubility function determined (yellow).
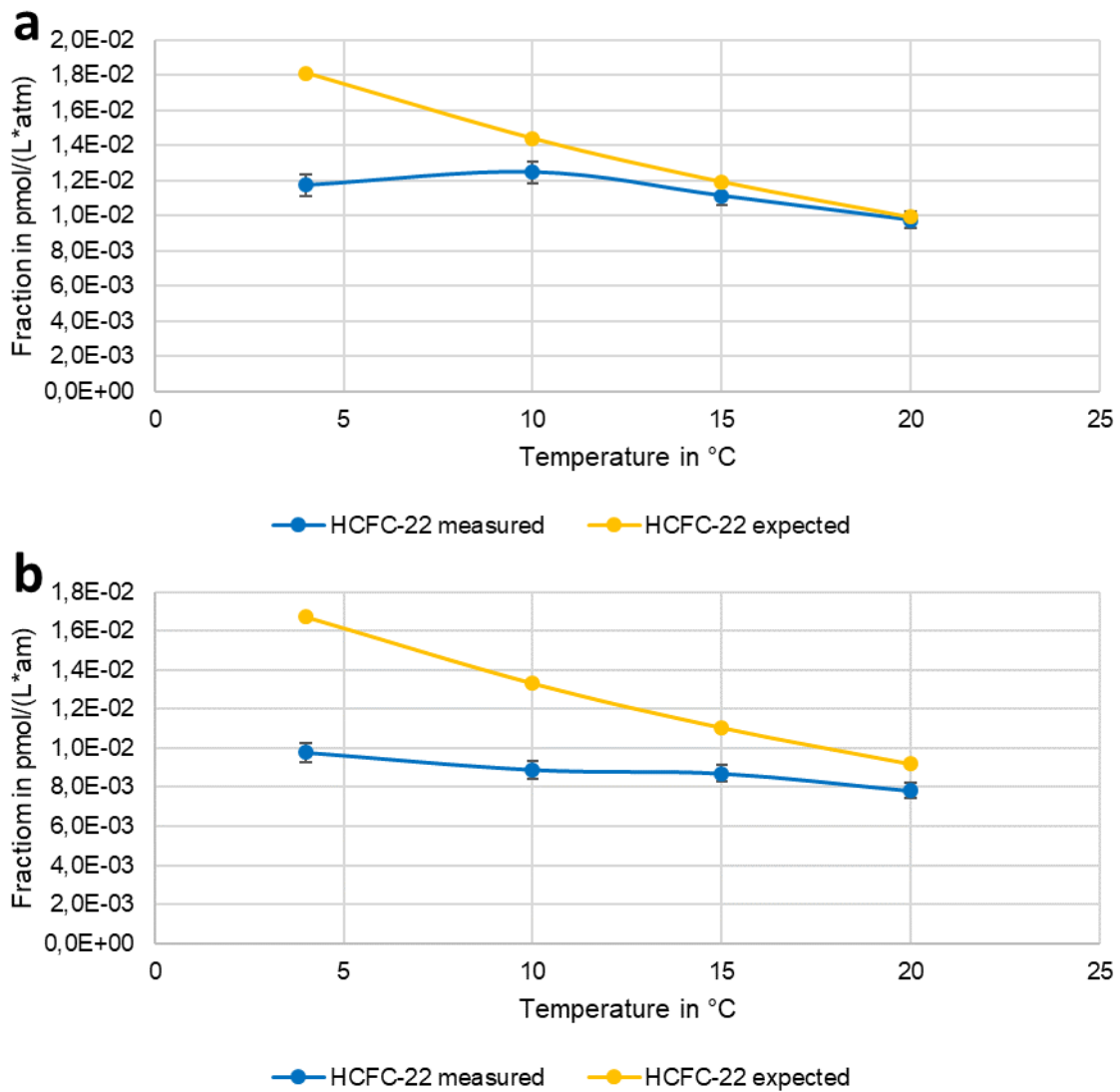
Figure D8: Solubility fraction of HFC-134a in (a) 18 psu water and (b) 26.2 psu water. Shown is a comparison of the results measured (blue) to those calculated using the solubility function determined (yellow).

Figure D9: Solubility fraction of HFC-134a in (a) MilliQ water (0 psu) and (b) 34.4 psu water. Shown is a comparison of the results measured (blue) to those calculated using the solubility function determined (yellow).
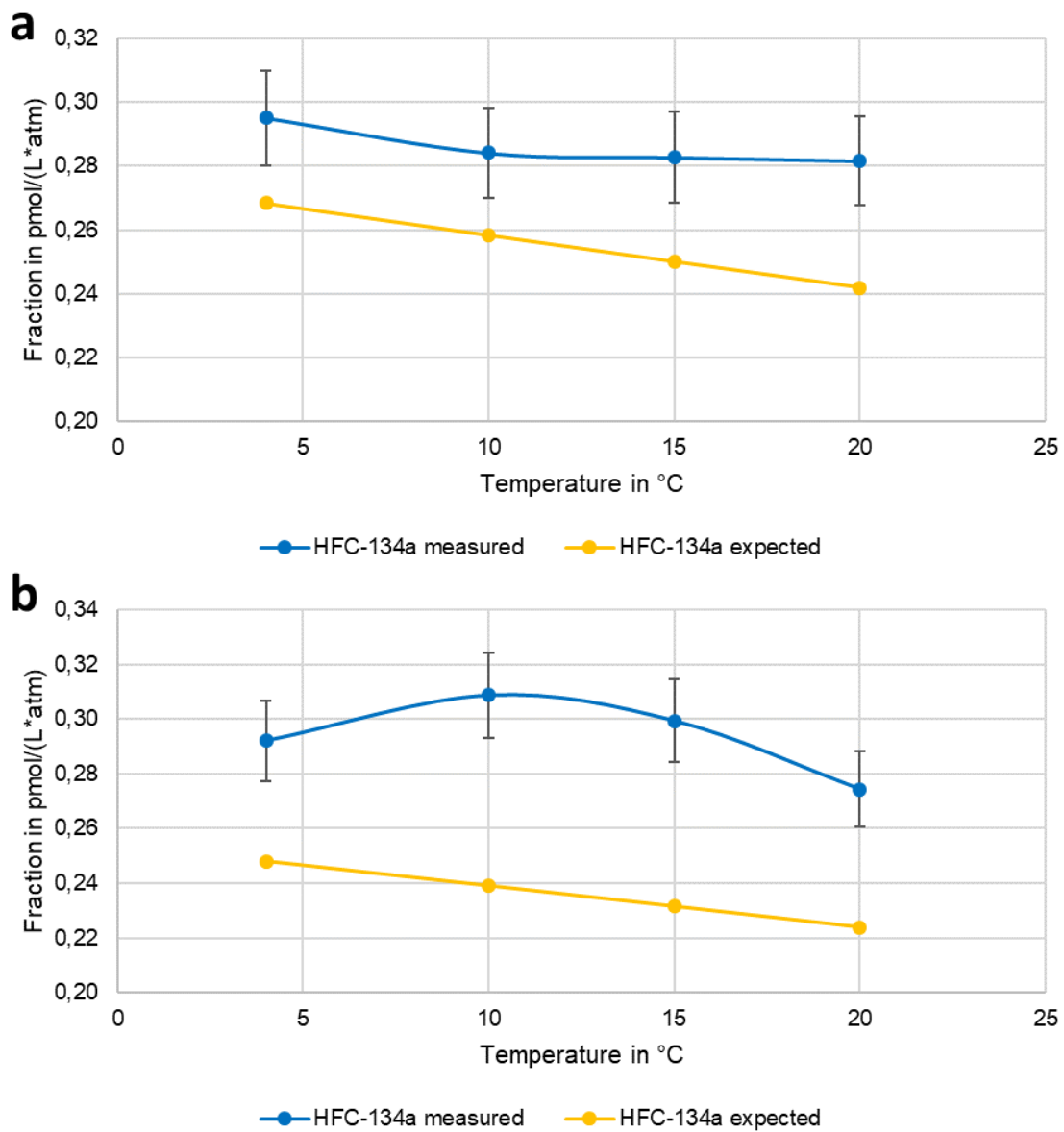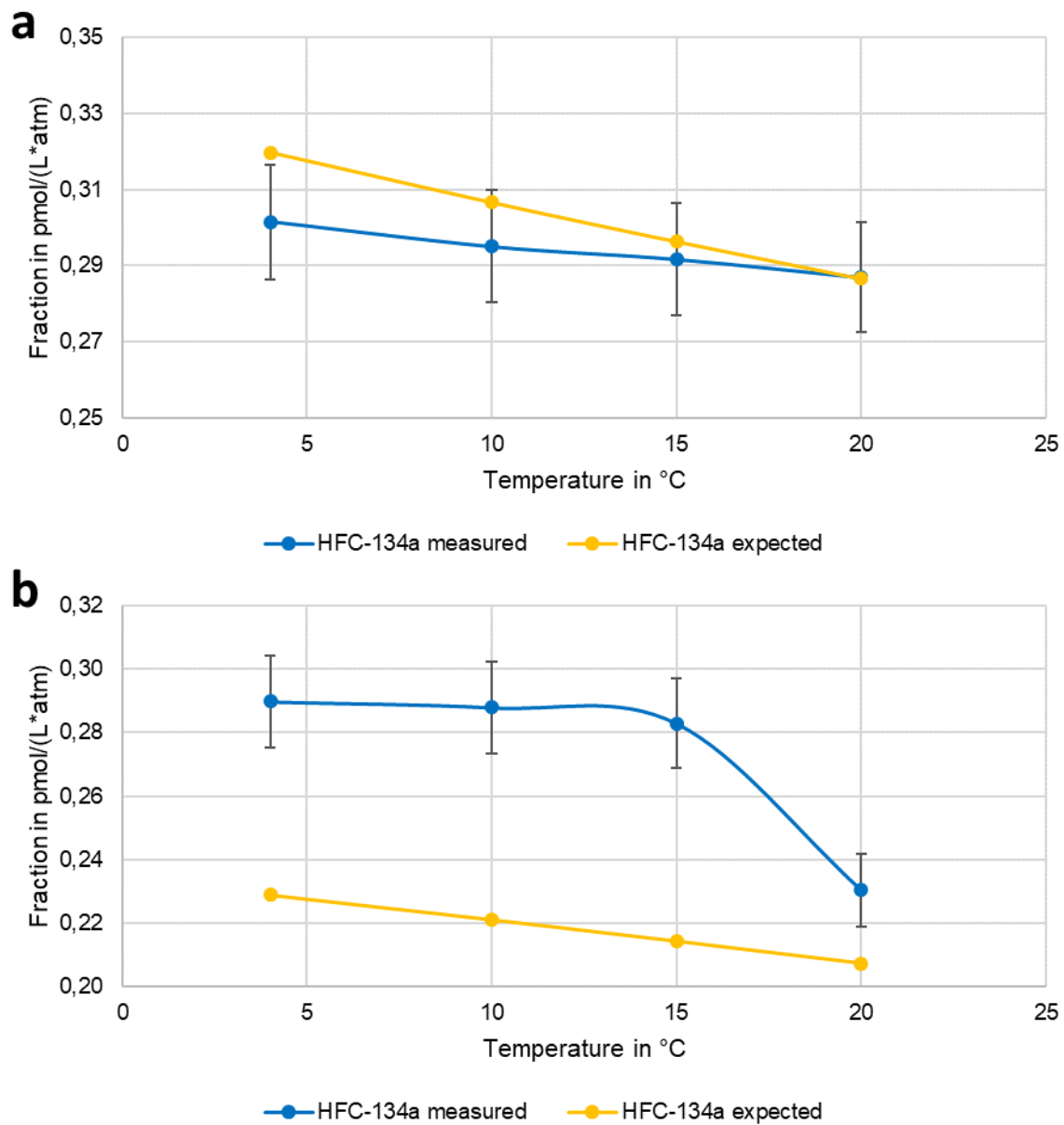
D.3 Standards used

The table below displays the predetermined partial pressure values for each of the standard gas bottles used throughout this thesis. The bottle 'DS3' was used to provide standard curves for the concentration analysis of CFC-12 and SF_6 during the research expeditions (SAS-Oden 2021, TReX 2 and TReX 4). 'DS4' and the 'Gold' standard were used in the solubility experiment and for analysing 'Medusa'-tracer concentrations in the laboratory from samples collected during the 'SAS-Oden 2021' cruise.

Table D1: Partial pressure values of each tracer present in the used standard gas bottles.

Tracer	DS3	DS4	Gold
CFC-12	826.76 ppt	400 ppt	544.61 ppt
SF_6	2.36 ppt	90 ppt	5.71 ppt
HCFC-22	/	15 ppt	180.01 ppt
HCFC-141b	/	/	19.08 ppt
HCFC-142b	/	/	16.5 ppt
HFC-134a	/	13 ppt	38.63 ppt

List of Abbreviations

AMS	Accelerator Mass Spectrometry	
ADCP	Acoustic Doppler Current Profiler	
C_{ant}	anthropogenic carbon	
AOU	Apparent Oxygen Utilization	
AAW	Arctic Atlantic Water	
AO	Arctic Ocean	
AOBC	Arctic Ocean Boundary Current	
ARICE	Arctic Research Icebreaker Consortium	
AMOC	Atlantic Meridional Overturning Circulation	
AW	Atlantic Water	
ATTA	Atom Trap Trace Analysis	
BSBW	Barents Sea Branch Water	
CIOOS-SLGO	Canadian Integrated Ocean Observing System – St. Lawrence Global Observatory	
CFC's	Chlorofluorocarbons	
CFC-12	Chlorofluorocarbon-12	
CIL	Cold Intermediate Layer	
DW	Deep Water	
DSOW	Denmark Strait Overflow Water	
dAAW	dense Arctic Atlantic Water	
DFG	Deutsche Forschungsgesellschaft	
DO	Dissolved Oxygen	
ESM	Earth System Model	
ECD	Electron Capture Detector	
eOMP	extended optimum multiparameter analyses	
FOCI	Flexible Ocean and Climate Infrastructure	
FSBW	Fram Strait Branch Water	
GC	Gas Chromatograph	
GLODAP	Global Ocean Data Analysis Project	
GSL	Gulf of St. Lawrence	

_____

HCFC's	Hydrochluorofluorocarbons
HCFC-141b	Hydrochluorofluorocarbon-141b
HCFC-142b	Hydrochluorofluorocarbon-142b
HCFC-22	Hydrochluorofluorocarbon-22
HFC's	Hydrofluorocarbons
HFC-134a	Hydrofluorocarbon-134a
IHG	Interhemispheric Gradient
IG	Inverse Gaussian
LCW	Labrador Current Water
LLC	Low Level Counting
LSLE	Lower St. Lawrence Estuary
MOT	Magneto-Optical Trap
MEOPAR	Marine Environmental Observation, Prediction and Response network
MS	Mass Spectrometer
NACW	North Atlantic Central Water
NCC	Norwegian Coastal Current
1-IG-TTD	one-inverse Gaussian Transit Time Distribution
2-IG-TTD	two-inverse Gaussian Transit Time Distribution
ppm	part per million
ppt	parts per trillion
PDF	Probability Density Function
PT5	Purge and Trap system 5
SIO	Scripps Institution of Oceanography
Std-dev	Standard deviation
SF_6	Sulphur hexafluoride
SW	Surface Water
SPRS	Swedish Polar Research Secretariat
SAS	Synoptic Arctic Survey
TReX	Tracer Release Experiment
TReX2	Tracer Release Experiment 2
TReX4	Tracer Release Experiment 4

TTSS	Transient Tracer Super Stations	
TTD	Transit Time Distribution	
SF_5CF_3	trifluoromethyl sulphur pentafluoride	215
uPDW	upper Polar Deep Water	
USLE	Upper St. Lawrence Estuary	
Γ	Mean age	
Δ	Width of the distribution	

Lennart Gerke

Date of birth: 18.01.1994, Goettingen (Germany)
Nationality: German

Knooper Weg 169
24118 Kiel
Germany

Tel.: +49 17632409300
E-Mail: lgerke@geomar.de

Education

GEOMAR Helmholtz Centre for Ocean Research, Kiel (Germany)   01/2021 - present
PhD candidate | Chemical Oceanography
   - PhD thesis: Ventilation of the Arctic Ocean and the Gulf of St. Lawrence

Christian-Albrechts-University, Kiel (Germany)   10/2017 – 09/2020
Master of Science | Chemistry
   - Master Thesis: pCO_2 in the Mediterranean Sea during the cruise MSM72

Christian-Albrechts-University, Kiel (Germany)   10/2013 – 10/2017
Bachelor of Science | Chemistry
   - Bachelor Thesis: Transient Tracers and Eddies along GO-SHIP section A10.5

High School Education:

Pascal-Gymnasium, Muenster (Germany) | High School Diploma   08/2004 – 07/2013

Scientific research and academic work experience

GEOMAR, Kiel (Germany) | Research Assistant   10/2020 – 01/2021

KM Contros GmbH, Kiel (Germany) | Internship   04/2019 – 06/2019

GEOMAR, Kiel (Germany) | Student Assistant   08/2016 – 11/2016

Participation in scientific cruises

Cruise 'BELS' (GEOMAR, Germany) | Research Assistant   11/2023 – 12/2023
Labrador Sea

Cruise 'TReX5' (GEOMAR, Germany) | Research Assistant   07/2023 – 07/2023
Gulf of St. Lawrence

Cruise 'TReX2' (GEOMAR, Germany) | Research Assistant   06/2022 – 07/2022
Gulf of St. Lawrence

Cruise 'SAS-2021' (GEOMAR, Germany) | WP-Leader   07/2021 – 10/2021
Arctic Ocean

Cruise 'MSM94' (GEOMAR, Germany) | Student Assistant   07/2020 – 09/2020
Labrador Sea

Cruise 'MSM72' (GEOMAR, Germany) | Student Assistant   03/2018 – 04/2018
Mediterranean Sea

Conferences

Ocean Science Meeting 2024, New Orleans | Oral Presentation   02/2024

Nansen Legacy Symposium 2023, Tromsø | Oral Presentation   11/2023

Arctic Science Summit Week 2023, Vienna | Oral Presentation   02/2023

Arctic Research Icebreaker Cons. Conference, Brussels | Poster Presentation   12/2022

Arctic Science Summit Week 2022, Tromsø | Early Career Co-Chair   02/2023

Publications

Gerke, L., Arck, Y., Tanhua, T. (2024), Temporal Variability of Ventilation in the Eurasian Arctic Ocean, *Journal of Geophysical Research – Oceans*, 2024 (accepted for publication).

Gerke, L., Nesbitt, W. A., Stevens, S. W., Wallace, D. W. R., Tanhua, T. (2024), Changing composition of the Gulf of St. Lawrence Inflow Waters (manuscript in revision for publication in *Geophysical Research Letters*).

Stevens, S. W., Pawlowicz, R., Tanhua, T., **Gerke, L.,** Nesbitt, W. A., Drozdowski, A., Chassé, J., Wallace, D. W. R., (2024), A subsurface tracer release experiment in the Gulf of St. Lawrence, an increasingly hypoxic marginal sea, *Commun. Earth Environ.*, 2024 (accepted for publication).

Guo, H., Koeve, W., He, Y.-C., Oschlies, A., Kemena, T. P., **Gerke, L.,** Kriest, I. (2024), Evaluation of the Inverse Gaussian Transit Time Distribution Method for inferring mean state and temporal change of ocean ventilation age: A model study (manuscript submitted to *Journal of Geophysical Research – Oceans*).

Eidesstattliche Erklärung

Hiermit versichere ich, Lennart Gerke, an Eides statt, dass ich die vorliegende Doktorarbeit zum Thema ‚Ventilation of the Arctic Ocean and the Gulf of St. Lawrence' selbstständig und ausschließlich mit den angegeben Quellen, Hilfsmitteln, sowie durch die Beratungen meiner Betreuer angefertigt habe.

Die Arbeit wurde unter Einhaltung der Regeln guter wissenschaftlicher Praxis der Deutschen Forschungsgemeinschaft verfasst.

Sie hat weder ganz, noch in Teilen, einer anderen Stelle im Rahmen eines Prüfungsverfahrens vorgelegt, ist nicht veröffentlicht und auch nicht zur Veröffentlichung eingereicht.

Außerdem wurde kein akademischer Grad entzogen.

Kiel, _____

gez. Lennart Gerke